

Understanding the structure of minerals at the  
atomic scale: a new perspective enabled by  
advanced microscopy

A thesis submitted in fulfilment of the requirements for the degree of

Doctor of Philosophy

Alexandre La Fontaine

Department of Engineering /

Australian Centre for Microscopy and Microanalysis

The University of Sydney

2016



---

# 1 Abstract

From oxides to ores and rocks, minerals are the most prevalent materials on Earth. The majority of their properties are the direct result of their microstructure. The investigation of their structure at the nano and micron scale is routinely carried out using techniques such as optical and electron microscopy, X-ray diffraction or secondary ion mass spectrometry. However, these techniques are usually limited in resolution, either spatially or chemically. More recently, atom probe tomography (APT) has emerged as a powerful microscopy technique that can provide 3D maps showing the position and atomic mass of individual atoms with sub-nanometre resolution. The non-conductive character of most minerals, both thermally and electrically, makes their investigation by APT challenging, from sample preparation to data interpretation. However, with the relatively recent development of focused ion beam sample preparation techniques and ultra-violet laser-assisted local electrode atom probe, the APT study of large band gap materials such as oxides has become more successful in the last decade. Advanced microscopy techniques such as transmission Kikuchi diffraction (TKD) or electron backscattered diffraction (EBSD) can also be used in combination with APT, and bring a new perspective to the investigation of the atomic scale structure of minerals, leading to a better understanding of their structure – properties relationships.

The overall purpose of this thesis is to develop and apply new methods and techniques for the characterization of the structure of minerals at the atomic scale. This is achieved by means of various advanced microscopy techniques, which are applied to a selection of important scientific questions. By using a combination of APT, TKD, EBSD and transmission electron microscopy we investigate intergranular corrosion in stainless steels, the atomic structure of dental enamel and the robustness of zircon as a geological dating accessory.

In this work, intergranular corrosion mechanisms in a commercial austenitic stainless steel (ASS) were revealed using EBSD and correlative TKD/TEM. Characterization by APT of the intergranular iron-chromium spinel formed during corrosion of the ASS revealed new insights at the atomic scale on its role towards the fast corrosion rate of the ASS. With the combined use of EBSD, TKD and APT, the atomic scale distribution of trace elements within dislocations in deformed mineral zircons was investigated for the first time to review the robustness of zircon for radiogenic dating. By using APT and TEM, new structural and elemental analysis of human dental enamel at the atomic scale provided unprecedented information for our understanding of human tooth decay.

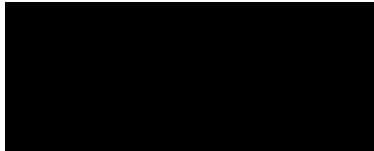
---

## **2 Prefatory material**

### **2.1 Certificate of originality**

I hereby declare that this submission is my own work and to the best of my knowledge it contains no materials previously published or written by another person, nor material which to a substantial extent has been accepted for the award of any other degree or diploma at The University of Sydney or any other educational institution, except where due acknowledgment is made in this thesis. Any contribution made to the research by others, with whom I have worked at The University of Sydney or elsewhere, is explicitly acknowledged in the thesis.

I also declare that the intellectual content of this thesis is the product of my own work, except to the extent that assistance from others in the project's design and conception or in style, presentation and linguistic expression is acknowledged.



Signed by Alexandre La Fontaine

---

## 2.2 Authors' contributions

### 1) Martensitic transformation in an intergranular corrosion area of austenitic stainless steel during thermal cycling

Authors: Alexandre La Fontaine, Hung-Wei Yen, Patrick Trimby, Steven Moody, Sarah Miller, Martin Chensee, Simon P. Ringer, Julie M. Cairney

Published in Corrosion Science, Volume 85, Pages 1-6 (2014)

DOI: 10.1016/j.corsci.2014.04.048

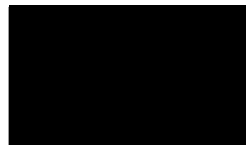
The content of this published letter is largely the product of the work of Alexandre La Fontaine under the supervision of Julie Cairney, Simon Ringer and Sarah Miller. Hung-Wei Yen revised the manuscript, contributed to the theoretical background of this letter and contributed to the experimental work. Patrick Trimby carried out the EBSD and TKD experiments together with Alexandre La Fontaine and Hung-Wei Yen. He has also significantly contributed to the interpretation of results. Steven Moody assisted in the sample preparation. Martin Chensee provided the material for this investigation.



Hung-Wei Yen



Patrick Trimby



Steven Moody



Sarah Miller



Martin Chensee



Simon P. Ringer



Julie M. Cairney

---

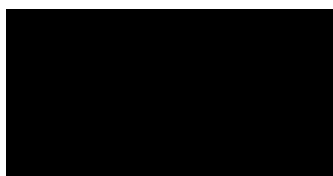
## 2) Interpreting atom probe data from chromium oxide scales

Authors: Alexandre La Fontaine, Baptiste Gault, Andrew Breen, Leigh Stephenson, Anna Ceguerra, Limei Yang, Thuan Dinh Nguyen, Jianqiang Zhang, David J. Young, Julie M. Cairney

Published in Ultramicroscopy, Volume 159, Pages 354-359 (2015)

DOI: 10.1016/j.ultramic.2015.02.005

The content of this published article is largely the product of the work of Alexandre La Fontaine under the supervision of Julie Cairney, Jianqiang Zhang and David Young. Baptiste Gault significantly contributed to the interpretation of results. Andrew Breen, Anna Ceguerra and Leigh Stephenson assisted in the data processing. Limei Yang carried out the chromia sample preparation. Thuan Dinh Nguyen produced and provided the chromia sample.



Baptiste Gault



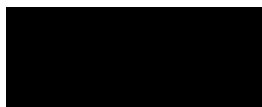
Andrew Breen



Leigh Stephenson



Anna Ceguerra



Limei Yang



Thuan Dinh Nguyen



Jianqiang Zhang



David J. Young



Julie M. Cairney

## 3) Atom probe study of chromium oxide spinels formed during intergranular corrosion

Authors: Alexandre La Fontaine, Hung-Wei Yen, Peter J. Felfer, Simon P. Ringer, Julie M. Cairney

Published in Scripta Materialia, Volume 99, Pages 1-4 (2015)

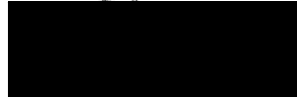
DOI: 10.1016/j.scriptamat.2014.09.028

---

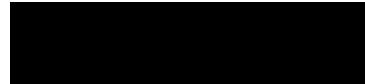
The content of this published article is largely the product of the work of Alexandre La Fontaine under the supervision of Julie M. Cairney and Simon P. Ringer. Hung-Wei Yen revised the manuscript and significantly contributed to the interpretation of results. Peter Felfer carried out the sample preparation for one of the specimens used in this study.



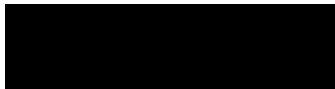
Hung-Wei Yen



Peter Felfer



Simon P. Ringer



Julie M. Cairney

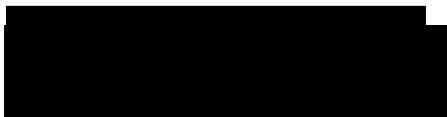
#### **4) Laser-assisted atom probe tomography of deformed minerals: a zircon case study**

Authors: Alexandre La Fontaine, Sandra Piazzolo, Patrick Trimby, Limei Yang, Julie M. Cairney

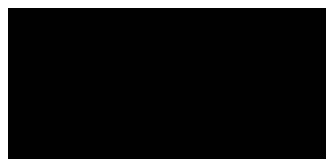
Submitted the 15<sup>th</sup> of March 2016 to the journal *Microscopy and Microanalysis* in June 2016.

DOI: not yet available

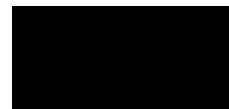
The content of this article is largely the product of the work of Alexandre La Fontaine under the supervision of Julie M. Cairney. Sandra Piazzolo and Patrick Trimby contributed to the interpretation of results and assisted in the writing. Limei Yang carried out the sample preparation.



Sandra Piazzolo



Patrick Trimby



Limei Yang



Julie M. Cairney

---

## 5) Deformation-induced trace element redistribution in zircon revealed using atom probe tomography

Authors: Sandra Piazzolo, Alexandre La Fontaine, Patrick Trimby, Simon Harley, Limei Yang, Richard Armstrong, Julie M. Cairney

Published in Nature Communications

DOI: 10.1038/ncomms10490

Sandra Piazzolo initiated this project, selected samples, assisted in data reduction and interpretation, and wrote the majority of the paper. Alexandre La Fontaine performed data analysis and data reduction of atom probe tomography data and assisted in interpretation. Patrick Trimby conducted EBSD and TKD analyses and SEM imaging and assisted in interpretation and rewriting. Limei Yang prepared samples by focused ion beam. Simon Harley provided the sample, field and sample description and assisted in SHRIMP data interpretation. Richard Armstrong dated the zircon by SHRIMP. Julie M. Cairney assisted in data reduction, interpretation and rewriting. All authors reviewed and approved this paper.



Sandra Piazzolo



Patrick Trimby



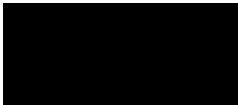
Simon Harley



Limei Yang



Richard Armstrong



Julie M. Cairney

## 6) Atomic scale compositional mapping reveals Mg-rich amorphous calcium phosphate in human dental enamel

Authors: Alexandre La Fontaine, Alexander Zavgorodniy, Hongwei Liu, Rongkun Zheng, Michael Swain, Julie M. Cairney

Alexandre La Fontaine initiated this project, prepared the APT samples, performed data analysis and data reduction of APT data, assisted in TEM data interpretation, and wrote the majority of the paper.



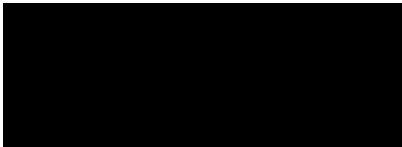
---

Alexander Zavgorodniy sourced the samples, prepared the samples for optical and TEM, conducted optical microscopy and assisted in interpretation and writing. Hongwei Liu conducted TEM imaging and performed TEM data reduction and interpretation. Rongkun Zheng participated in the project initiation, assisted in interpretation and rewriting. Michael Swain participated in the project initiation, assisted in data reduction and interpretation and assisted in writing. Julie M. Cairney assisted in data reduction, interpretation and writing. All authors reviewed and approved this paper.

This article has been submitted to Science Advances on the 31<sup>st</sup> of March 2016.

Submitted to Science Advances

DOI: not yet available



Alexander Zavgorodniy



Hongwei Liu



Rongkun Zheng



Michael Swain



Julie Cairney

---

## 2.3 Previously published materials and manuscript in preparation

The following publications are not to be assessed in this thesis.

### Published materials:

#### **“Influence of Surface Migration on the Spatial Resolution of Pulsed Laser Atom Probe Tomography”**

B. Gault · M. Müller · A. La Fontaine · M. P. Moody · A. Shariq · A. Cerezo · S. P. Ringer · G. D. W. Smith

Journal of Applied Physics 108(4):044904-044904-6 · August 2010

DOI: 10.1063/1.3462399

#### **“Impact of laser pulsing on the reconstruction in an atom probe tomography”**

Baptiste Gault · Alex La Fontaine · Michael P Moody · Simon P Ringer · Emmanuelle A Marquis

Ultramicroscopy 110(9):1215-22 · August 2010

DOI: 10.1016/j.ultramic.2010.04.017

#### **“Elemental partitioning of platinum group metal containing Ni-base superalloys using electron microprobe analysis and atom probe tomography”**

J.S. Van Sluytman · A. La Fontaine · J.M. Cairney · T.M. Pollock

Acta Materialia 58(6):1952-1962 · April 2010

DOI: 10.1016/j.actamat.2009.11.038

#### **“Effect of Al and Gd Solutes on the Strain Rate Sensitivity of Magnesium Alloys”**

N. Stanford · I. Sabirov · G. Sha · A. La Fontaine · S. P. Ringer · M. R. Barnett

Metallurgical and Materials Transactions A 41(3):734-743 · March 2010

DOI: 10.1007/s11661-009-0107-8

#### **“Spatial Resolution in Atom Probe Tomography”**

Baptiste Gault · Michael P Moody · Frederic De Geuser · Alex La Fontaine · Leigh T Stephenson · Daniel Haley · Simon P Ringer

Microscopy and Microanalysis 16(1):99-110 · February 2010

DOI: 10.1017/S1431927609991267

#### **“Atom Probe Tomography of Solute Distributions in Mg-Based Alloys”**

N. Stanford · G. Sha · A. La Fontaine · M.R. Barnett · S.P. Ringer

Metallurgical and Materials Transactions A 40(10):2480-2487 · October 2009

DOI: 10.1007/s11661-009-9937-7

---

**“Effect of pre-straining and bake hardening on the microstructure and mechanical properties of CMnSi TRIP steels”**

Elena V. Pereloma · I. B. Timokhina · P. D. Hodgson · L. C. Zhang · S P Ringer · A. La Fontaine  
La Metallurgia Italiana 101(6) · June 2009

**“Advances in the calibration of atom probe tomographic reconstruction”**

Baptiste Gault · Michael P. Moody · Frederic de Geuser · Guy Tsafnat · Alexandre La Fontaine · Leigh T. Stephenson · Daniel Haley · Simon P. Ringer  
Journal of Applied Physics 105(3):034913 - 034913-9 · March 2009  
DOI: 10.1063/1.3068197

**“Correlation between film structures and potential limits for hydrogen and oxygen evolutions at a-C:N film electrochemical electrodes”**

Aiping Zeng · Marcela M.M. Bilek · David R. McKenzie · Peter A. Lay · Alexandre La Fontaine · Vicki J. Keast  
Carbon 46(4):663-670 · April 2008  
DOI: 10.1016/j.carbon.2008.01.022

**“Variability in the segregation of bismuth between grain boundaries in copper”**

V. J. Keast · A. La Fontaine · J. du Plessis  
Acta Materialia 55(15):5149-5155 · September 2007  
DOI: 10.1016/j.actamat.2007.05.034

**“Compositional distributions in classical and lead-free brasses”**

A. La Fontaine · V.J. Keast  
Materials Characterization 57(4-5):424-429 · December 2006  
DOI: 10.1016/j.matchar.2006.02.005

Manuscript in preparation:

**“Atom probe study of grain boundary segregation of carbon, iron, and silicon inside chromia scales grown in CO<sub>2</sub> gas”**

Thuan Dinh Nguyen, Alexandre L. Fontaine, Limei Yang , Julie M. Cairney, Jianqiang Zhang, David J. Young  
(To be submitted in Acta Materialia)

---

## 2.4 Acknowledgements

When I first came to Sydney in 2004, I started working as a research assistant at the Australian Centre for Microscopy and Microanalysis (ACMM), formerly known as the Electron Microscope Unit. And here I am today, eleven years later, writing the acknowledgements section of my PhD, after five years working at the ACMM, one and half years travelling the world with my beloved Aude, 8 months teaching science in a Cambodian high school and finally the three best years of my research career so far... There are of course many people to thank, some of whom I include here.

I would first like to give a very special thank you to my supervisor Prof. Julie M. Cairney. I am extremely grateful for your continuous support, guidance and for the numerous skills I have learnt from you. You are truly inspirational and I am privileged to have you as my supervisor and friend. I would like to thank you for all the opportunities you gave me to pursue my own path in research as well as to travel around the world and disseminate my research work.

I want to thank Prof. Simon P. Ringer, my co-supervisor, not only for his support during my PhD but also for the trust he had in me from the very beginning of my research career at the ACMM. I will never forget.

I would like to thank my external supervisor Dr. Sarah Miller from CSIRO for her help throughout my PhD.

My friend Dr. Hung-Wei Yen has greatly contributed to this PhD. He is a talented scientist, a committed researcher and one of the best steel experts I have ever met. I am also lucky to count Dr. Baptiste Gault as one of my friend and even luckier that he is one of the best atom probe tomography experts in the world. Merci Bat for teaching me the ways of atom probe tomography and for your unconditional help when I needed it. I am grateful to have worked closely with Dr. Patrick Trimby who graciously shared his knowledge of minerals and skills in scanning electron microscopy. Also I would like to thank Dr. Sandra Piazzolo for the fruitful ongoing collaboration.

I would like to acknowledge the technical support of the ACMM staff especially Dr. Limei Yang, Steven Moody, Dr. Takanori Sato, Toshi Arakawa, Adam Sikorsky, Dr. Hongwei Liu, Dr. Matthew Foley, Dr. Thomson Chow.

---

I would like to thank my amazing colleagues at the ACMM for the scientific, social and sportive interactions: Dr. Andrew Breen, Dr. Leigh Stephenson, Dr. Anna Ceguerra, Mehdi Eizadjou, Katja Eder, Ingrid McCaroll, Delfine Cheng, Jeffrey Henriquez, Glenn Sneddon, Joshua Watts.

I would also like to acknowledge the financial support of the Australian Renewable Energy Agency.

I am also grateful to my good friends here in Australia, amongst them Conor, Olivier, Aurelie, Lucas, Mathieu, Marianne, Camille, Nick, Katrina, Zara, Maeve, Fred, Pearl, Laurent, Sandrine and many more.

Last but not least I would like to specially thank Aude, my love and my best friend, for her 17 years of unconditional support. You are the most amazing person on this Earth and the most beautiful mother to our son Théo. I am dedicating this thesis to both of you.

A mes sœurs Karine et Aurore et mon frère Arnaud. A mes parents, Françoise et Pierre. Merci pour avoir su créer les conditions de mon épanouissement intellectuel et personnel.

---

## 2.5 Table of Contents and Figures

### Table of Contents

<b>1</b>	<b>Abstract.....</b>	<b>i</b>
<b>2</b>	<b>Prefatory material.....</b>	<b>ii</b>
2.1	Certificate of originality.....	ii
2.2	Authors' contributions.....	iii
2.3	Previously published materials and manuscript in preparation .....	viii
2.4	Acknowledgements.....	x
2.5	Table of Contents and Figures.....	xii
<b>3</b>	<b>Motivation.....</b>	<b>1</b>
<b>PART A Literature review.....</b>		<b>3</b>
<b>4</b>	<b>Introduction to the minerals selected.....</b>	<b>5</b>
4.1	Iron-chromium spinel oxides.....	5
4.1.1	Concentrated solar power (CSP).....	5
4.1.2	Austenitic stainless steels .....	9
4.1.3	Sensitization and intergranular corrosion .....	14
4.2	Silicate mineral zircon .....	15
4.2.1	Mineral zircon: a uranium-lead geochronometer .....	15
4.2.2	Deformation in zircons and trace elements diffusion .....	18
4.3	Human dental enamel hydroxyapatite .....	19
4.3.1	Hierarchical structure of enamel.....	19
4.3.2	Formation of hydroxyapatite .....	20
<b>5</b>	<b>Advanced microscopy techniques .....</b>	<b>21</b>
5.1	Introduction to atom probe tomography .....	22
5.1.1	Overview of APT .....	22
5.1.2	Spatial and mass resolution of APT .....	26

---

5.1.3	Specimen preparation techniques .....	27
5.2	Introduction to transmission Kikuchi diffraction .....	31
5.2.1	Overview of EBSD and TKD.....	31
5.2.2	Complementarity with other techniques .....	34
<b>6</b>	<b>Characterization of high resistivity materials using atom probe tomography .....</b>	<b>35</b>
6.1	Laser-assisted atom probe tomography .....	35
6.1.1	Overview .....	35
6.1.2	Common challenges inherent to the APT characterization of high-resistivity materials .....	37
6.2	Laser-assisted APT of high-resistivity materials.....	39
6.2.1	State of the art.....	39
6.2.2	Laser-assisted APT of the selected minerals: a review .....	39
<b>7</b>	<b>Aims and scope of this thesis.....</b>	<b>42</b>
<b>PART B Results .....</b>		<b>44</b>
<b>8</b>	<b>New insights on intergranular corrosion of austenitic stainless steel: an oxidation-induced phase transformation.....</b>	<b>45</b>
<b>9</b>	<b>Optimization and data quality assessment of laser-assisted APT of chromium oxides.....</b>	<b>52</b>
<b>10</b>	<b>Atomic scale structure and composition of intergranular chromium oxide spinels .....</b>	<b>59</b>
<b>11</b>	<b>Laser-assisted APT analysis parameters influence on zircon minerals data quality .....</b>	<b>64</b>
<b>12</b>	<b>Laser-assisted APT investigation of the mobility of trace elements in deformed zircons .....</b>	<b>85</b>
<b>13</b>	<b>Revealing the atomic scale structure and chemistry of human dental enamel by laser-assisted APT.....</b>	<b>99</b>
<b>PART C Conclusions .....</b>		<b>126</b>
<b>14</b>	<b>Conclusions.....</b>	<b>127</b>
14.1	Advanced microscopy techniques applied to minerals.....	127
14.1.1	Specimen preparation for TKD and APT .....	127
14.1.2	Data acquisition and analysis.....	128
14.2	Analysis of selected minerals.....	129

---

---

14.2.1	Iron-chromium spinel oxides in intergranular corrosion area of austenitic stainless steel.....	129
14.2.2	Trace elements diffusion in deformed zircons .....	129
14.2.3	Human dental enamel hydroxyapatite.....	130
14.3	Future outlook.....	130
<b>15</b>	<b>Bibliography.....</b>	<b>131</b>



---

## Table of Figures

Figure 4-1 Ivanpah Solar Electric Generating System. (15).....	6
Figure 4-2 The four most common forms of CSP. (17).....	7
Figure 4-3 Basics of stainlessness.....	9
Figure 4-4 Effect of Cr content on oxidation of Fe-Cr alloys at 1000°C in 0.13 atm O <sub>2</sub> . (23) .....	10
Figure 4-5 Simplified Schaeffler diagram (26).....	11
Figure 4-6 Schematic illustration of sensitisation process and intergranular corrosion (36) .....	14
Figure 4-7 SEM image by cathodoluminescence (photon emission induced by incident electron beam) of the surface of zircon from Jack Hills, Australia. Adapted from (46) .....	16
Figure 4-8 Wetherill Concordia diagram showing Pb/U isotope ratios of zircons and how to interpret data where the two ratios are discordant. (48).....	17
Figure 4-9 Deformation in zircon imaged by foreshatter orientation contrast map in a scanning electron microscope (Courtesy Patrick Trimby).....	19
Figure 4-10 “(a) Schematic illustration of enamel’s hierarchical structure. The occlusal surface is equal to the natural tooth surface in which the cc-axis of the rods is parallel to the chewing force. (b) and (c) SEM images of different faces. (Samples were etched in 37% H <sub>3</sub> PO <sub>4</sub> for 5 s and observed by secondary electron detector.)” (61, 62).....	20
Figure 5-1 Basic schematic of a straight flight path LEAP. Note x <sub>0</sub> and y <sub>0</sub> are ions coordinates in original sample (Courtesy B. Gault and M. Moody).....	23
Figure 5-2 Typical indexed APT mass spectrum of a Zircon sample. Data obtained with laser-assisted APT.....	24
Figure 5-3 Example of an isosurface used to highlight an Al-rich particle in a zircon mineral. The variation of Al and H content within the precipitate is obtained through a proxigram analysis. ....	26
Figure 5-4 Schematic of electropolishing APT sample preparation. Adapted from (103).....	28

---

Figure 5-5 Basics of annular milling to obtain sharp APT tips. (Courtesy J. Cairney).....	28
Figure 5-6 APT tip prepared by annular milling from an electropolished blank. (a and b are ion beam images and c electron beam image) Adapted from (109).....	29
Figure 5-7 Schematic of the FIB wedge method. Adapted from (109).....	29
Figure 5-8 Illustration of the steps involved with in-situ lift out. (Courtesy Limei Yang).....	30
Figure 5-9 EBSD typical configuration in a SEM and EBSD principle. (Adapted from (118)).....	32
Figure 5-10 Image of a typical TKD configuration and schematic comparing EBSD and TKD (121, 123).....	32
Figure 5-11 “Pattern quality vs sample thickness (a) Secondary electron (SE) image of the central perforation in an Al-6060 TEM foil. The yellow line marks a transect along which diffraction patterns were stored and analysed. (b) – (d) Example diffraction patterns collected at 22 kV using SEM-TKD from the transect shown in (a).” (122).....	33
Figure 5-12 TKD data from a high pressure torsion deformed Al-6060 alloy sample. (Courtesy P. Trimby).....	34
Figure 5-13 “(a) Schematic set-up in the microscope chamber at a tilt angle of 0°. The ion source (57) is located in an angle of 52° to the electron source. The beams have their intersection point at a working distance of 10 mm; (b) schematic set-up in the microscope chamber at a tilt angle of 52°.” (128, 131).....	35
Figure 6-1 Schematic of laser-assisted APT and the two mechanism (voltage and laser) used for field evaporation of an atom at the tip. (132, 136).....	36
Figure 6-2 “(a) Temperature evolution (model response) and (b) evaporation rate of a steel tip after the interaction with the laser pulse (red line: the illuminated side of the tip; black line: the opposite side)” (132) (c) “Finite element model of an atom probe specimen showing the temperature distribution due to the laser heating from one side” (136).....	37
Figure 6-3 Temperature dependence of thermal conductivity for high purity Si. (140).....	38

---

---

Figure 6-4 “The clusters of co-localized Y and Pb in Hadean zircon a) Projections of Y and Pb from the same 1,000-nm-long segment. The tip of the specimen points upwards. b) Enlarged view of 100 nm segment of specimen 2. c) Individual Y and Pb atoms for one cluster: small red dots, Y; green dots,  $^{206}\text{Pb}$ ; and yellow dots,  $^{207}\text{Pb}$ . The volume shown in c measures  $20 \times 20$  nm in the plane of the image by 10 nm deep.” (46) ..... 40

Figure 6-5 “(A) Mg ( $^{24}\text{Mg}^{2+}$ ) ion positions in mouse outer enamel. (B) F ( $^{40}\text{Ca}^{19}\text{F}^+$ ) ion positions in fluoride-treated mouse inner enamel. (C) Fe ( $^{56}\text{Fe}^{2+}$ ) ions in pigmented rat enamel. Scale bars, 10 nm. The view direction is parallel to the long axis of the nanowires. (D to F) Representative concentration profiles across grain boundaries. (G) Isosurface (0.5 atomic %) surrounding Mg-rich multiple grain boundary in (A). (H) Isosurfaces (5 atomic %) enveloping Fe-rich multiple grain boundary in (C). Scale bars in (G) and (H), 5 nm. (I to K) Representative proxigrams of multiple grain boundaries in (I) mouse outer enamel, (J) fluoride-treated outer mouse enamel, and (K) pigmented rat enamel.” (77) ..... 41



---

### 3 Motivation

Minerals are the most abundant inorganic solids on earth. They have shaped the development of our civilizations and the interactions between societies throughout human history. From the Bronze Age to the information age, technology and industrialization were based on the capacity of man to extract elements such as iron or aluminium from mineral deposits.

There are over 5000 species of minerals with different physical and chemical properties. While ores and mineral nutrients play a fundamental role in human technological and life development, some less well-known minerals are equally important. For instance, stainless steels are protected from destructive oxidation in air by oxide minerals. Human teeth are preserved from daily wear and acid attacks by enamel, a biomaterial primarily made up of the phosphate mineral hydroxyapatite. Serving a totally different purpose, the silicate mineral zircon is a key material to date the earth's geological events.

Like most materials, the remarkable properties of these polycrystalline minerals are the result of their microstructure. It is well established that the atomic architecture of a material and the arrangement of the different species of atoms define its chemical and physical properties. A number of processes such as grain boundary segregation or phase transformation also happen at the atomic scale and influence greatly the properties of a material.

Microscopy plays a fundamental role in our ability to observe the structure of a material and to experimentally measure such processes. Optical microscopy, electron microscopy, X-ray diffraction or ion microprobe analyses are some of the techniques routinely used for minerals investigation. Yet these techniques are usually limited in resolution, either spatially or chemically. With its unique ability to determine the position of each atom and their chemical identity, atom probe tomography is an excellent technique to study the structure of minerals at a sub-nanometre level. With the recent advances in atom probe sample preparation using focused ion beam technology and the introduction of the ultra-violet laser assisted atom probe equipment, the study of non-conductive materials using atom probe tomography has become more common (2). Other advanced microscopy techniques such as transmission Kikuchi diffraction have very recently begun to be used in combination with atom probe tomography (3). However, there are still limitations and challenges associated with the non-conductive properties of minerals including electron beam damage and charging effects in the scanning electron microscope,

---

which can render the sample preparation arduous, or the difficult field evaporation of mineral samples in the atom probe, which can affect the overall data quality.

Throughout this thesis, I have developed novel techniques for the investigation of a selection of minerals by the means of a range of advanced microscopy techniques principally including atom probe tomography, transmission Kikuchi diffraction, electron backscattered diffraction and transmission electron microscopy. The three minerals investigated in this work were primarily selected for their industrial and scientific relevance.

High temperature corrosion of stainless steels is a major technological and economical drawback for a number of industries. The first objective of this thesis is to enable a new level of investigation of intergranular corrosion and protective oxide scale in stainless steel through the use of a range of advanced microscopy techniques. These new insights into corrosion processes benefit the development of more resistant stainless steels for their use in the aggressive environment of new generation energy technologies such as concentrated solar power.

The mineral zircon ( $ZrSiO_4$ ) is ideally suited for radiogenic dating of rocks. Not only does it contain trace amounts of uranium and thorium, enabling dating using radioactive decay in the U-Pb-Th system, but it is also thought to be very chemically robust. However several recent studies have suggested that zircons may not be as robust as once believed, especially on the micron and sub-micron scale (4-7). The second objective of this work is to analyze trace element distribution and mobility within dislocations and low-angle boundaries in deformed regions of zircons using a combination of electron backscattered diffraction, transmission Kikuchi diffraction and atom probe tomography.

A staggering 60-90% of children and nearly 100% of adults worldwide suffer from dental decay (caries), which occurs via the dissolution of enamel. However, the structure of enamel and the process by which decay occurs, is not well understood. Human dental enamel is primarily composed of nanowires of the phosphate mineral hydroxyapatite. The final objective of this thesis is to reveal the atomic scale structure of human dental hydroxyapatite in order to better understand enamel formation and its resistance to acid corrosion.

---

## PART A Literature review

---

This literature review is composed of three chapters: a summary of the minerals investigated; a description of the techniques of transmission Kikuchi diffraction and atom probe tomography; and review of the literature involving in the characterization of minerals by atom probe tomography.

Chapter 4 starts with a general description of stainless steels used as tubing and piping in concentrated solar power, a high temperature solar energy technology. The process of intergranular corrosion in a selected austenitic stainless steel is described with a focus on the formation of iron-chromium spinel oxides. Following this section, the rock-forming silicate mineral zircon is introduced. The need for atomic scale characterization of trace elements distribution in deformed zircons is explained. The last part of this chapter is a literature review on dental enamel hydroxyapatite and its formation *in vivo*.

Chapter 5 is a contemporary literature review of atom probe tomography and transmission Kikuchi diffraction. Atom probe tomography is described first. Then transmission Kikuchi diffraction technique is reviewed with a particular focus on its complementarity with other advanced microscopy techniques.

Chapter 6 is a literature review of the previous characterization of high resistivity materials and minerals by laser-assisted atom probe tomography.

This literature review lays the foundation for the six publications that form the core of this thesis, presented in part B.



---

## 4 Introduction to the minerals selected

Minerals are defined in geoscience as naturally occurring crystalline solids (8). There are more than 5000 known mineral species on Earth. They are classified by a unique combination of crystal structure and composition. In the following chapter we describe the three minerals selected for this PhD: iron-chromium spinel oxides, zircon and hydroxyapatite.

Iron-chromium spinels are oxide minerals with the general formulation  $\text{Fe}^{2+}(\text{Fe}, \text{Cr})^{3+}_2\text{O}^{2-}_4$ . The end members of this spinel are chromite ( $\text{FeCr}_2\text{O}_4$ ) and magnetite ( $\text{Fe}_3\text{O}_4$ ), the latest being the most abundant of the spinel group (9). They are investigated here in the context of their role in the oxide layer that forms when some stainless steels corrode. Specifically, we were investigating the type of corrosion that might be expected in high temperature concentrated solar thermal energy production.

Zircon is an orthosilicate from the silicate group with the chemical formula  $\text{ZrSiO}_4$ . The silicate minerals compose 90% of the Earth crust and are the most abundant of all mineral groups. The base unit is a  $\text{SiO}_4^{4-}$  tetrahedron.

The bio-mineral hydroxyapatite is a phosphate mineral with the chemical formula  $\text{Ca}_5(\text{PO}_4)_3(\text{OH})$ . It belongs to the apatite mineral group ( $\text{Ca}_5(\text{PO}_4)_3(\text{OH}, \text{F}, \text{Cl})$ ) which makes up most of teeth and bones of vertebrates.

### 4.1 Iron-chromium spinel oxides

#### 4.1.1 Concentrated solar power (CSP)

Concentrating the sun to produce heat is an old concept. In 212 BC Archimedes supposedly destroyed a Roman fleet concentrated the sun using polished shields (11). In 1868, John Ericson designed the first solar powered engine. Next, Aubrey Eneas produced a solar motor delivering 5 kW for water irrigation (12). In 1913, the first CSP plant was installed in Al Meadi, again for water irrigation (13). However it is only at the end of the 20th century that real progress was made in power generation. Between 1984 and 1991, the first commercial CSP plants operated in California. Since 2006, the number of CSP plants has noticeably increased, with the main contributors being the United States seconded by Spain (14). Current growth in the technology is extremely strong. In 2013, CSP plants produce a total of around 2 GW,

---

another 2.5 GW are under construction and around 17 GW of CSP projects were underway (10). With nearly 400 MW capacity of electricity generation, the largest CSP plant ever built on Earth is now fully operational in California (Figure 4.1) (15).

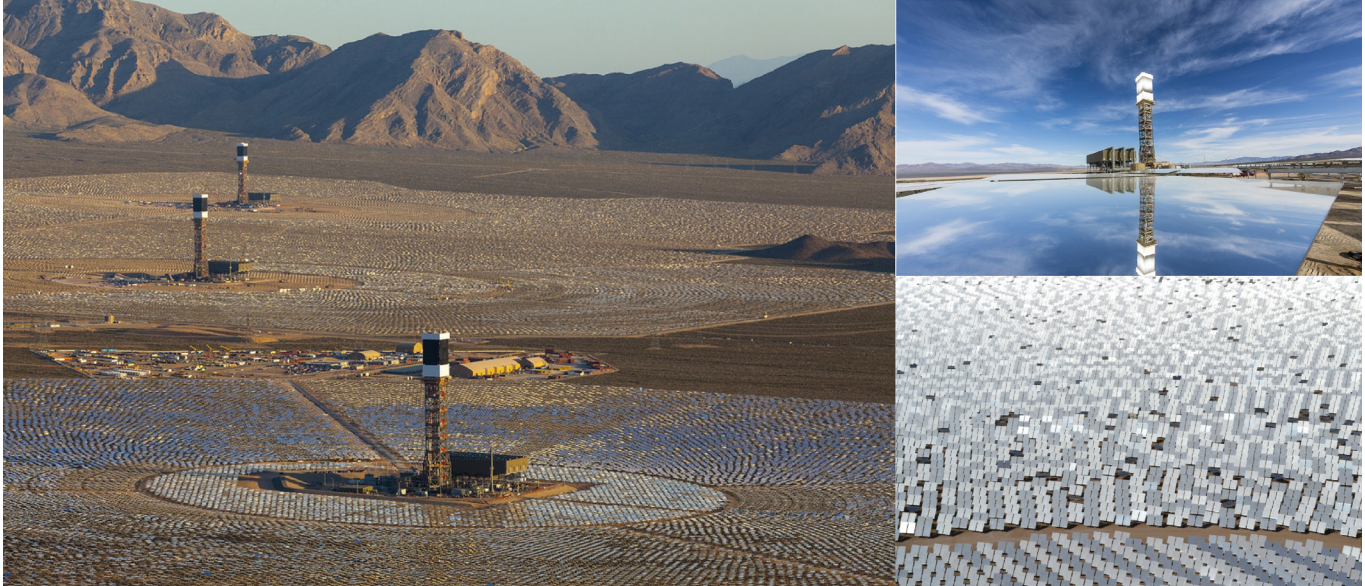


**Figure 4-1** Ivanpah Solar Electric Generating System. (15)

CSP uses mirrors to concentrate the sun direct normal irradiation (DNI) onto a receiver. The receiver heats a Heat Transfer Fluid (HTF), which generates steam. Like other thermal power station (coal or nuclear) the steam produced by the HTF powers a turbine, which generates electricity. CSP is also used for gas production. The energy provided by the concentrator drives a chemical reaction that produces solar gas, for example splitting methane into hydrogen and carbon monoxide.

CSP systems can be broken down into two different groups: line-focusing and point-focusing systems. The Linear Fresnel Reflector (16) and the Parabolic Trough Collector (PTC) are both line-focusing technologies and focus the sun's radiation along a focal line (Figure 4.2). The LFR uses a series of long flat mirrors to concentrate the DNI onto a fixed long tube receiver whereas the PTC uses arrays of curved mirrors that focus the sunlight onto a central receiver at the focal line of the collector. Both technologies use a single-axis tracking system to focus the radiation onto the receiver (1).

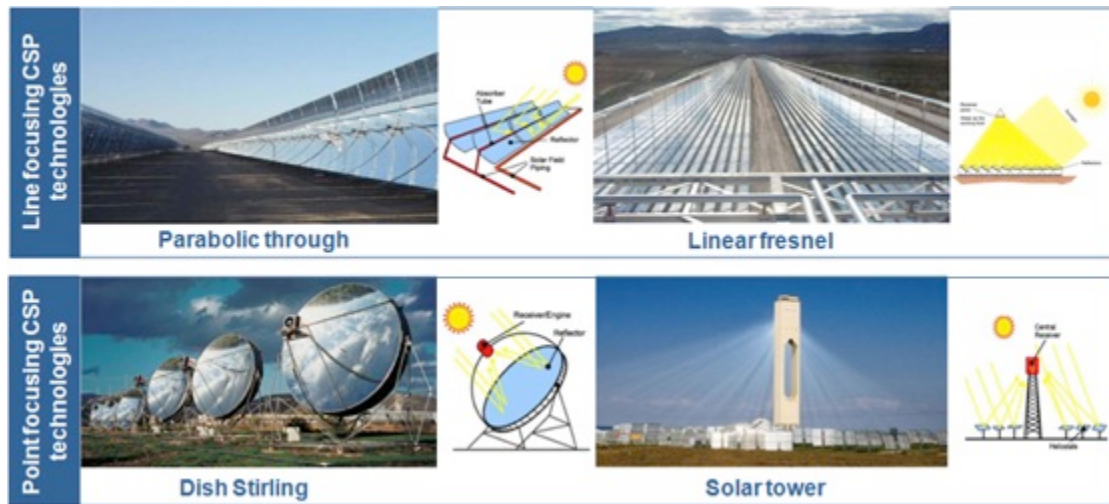


**Figure 4-2** The four most common forms of CSP. (17)

The two types of point-focusing systems, the Parabolic Dish (Stirling Dish) and the Central Receiver (Solar Tower), focus the radiation to a single focal point. The Stirling Dish technology consists of a parabolic dish that concentrates the DNI onto a receiver at the focal point of the dish. The Central receiver systems use a field of mirrors (heliostats) that focus the DNI onto a receiver mounted high on a central tower. Both technologies need a two-axis tracking system, which currently generate higher costs compared to line-focusing systems (18).

The main challenge for CSP is its commercial viability. According to IT power (19) the ‘levelized cost of energy’ (LCOE) for CSP is about \$250 per MWh, which is twice the current revenue stream for main-grid connections. To reduce the LCOE, CSP will need to increase its storage potential, a key point for evening demand peak (20). Another key point is to operate at higher temperature, which will increase the current efficiency of the solar to electricity conversion as well as the storage efficiency. Central Receiver is the most promising technology due to its development potential. Central Receivers could reach temperatures above 1000°C with new types of HTF and receivers. Some HTF in development include molten salts, air and super critical carbon Dioxide (s-CO<sub>2</sub>) (21).

Working at such high temperatures will require development of cost-effective high temperature alloys that are resistant to corrosion. For most components (heat storage, absorbers/receivers, structures, heat exchangers) it will be essential to have a good understanding of the strength, corrosion resistance, and high temperature performance of the materials used (Table 4.1).

<b>Component / System</b>	<b>Aims and Issues</b>
Absorbers / Receivers	Long-term resistance to corrosion at increased temperature
Tubing for direct steam generation	Resist high temperature, pressure and thermal cycling
Tubing for super critical-steam cycle	Resistance to temperature up to 1000°C and to high internal pressure
Heat storage Piping and tank structure	Long term resistance to internal corrosion and thermal strains
Heat exchangers	Increase temperature and reduce cost

**Table 4.1** Priorities for steel research for CSP systems. Adapted from (21)

High temperature environments have always been a challenge for materials. Stainless steels designed for high temperature use have a good combination of high temperature properties and a reasonable cost. However, like any alloy, there is a temperature limit at which the properties will drop under the effects of corrosion and ageing.

In CSP technologies, solar radiation is focused on a receiver where stainless steel tubes are used to carry a heat transfer fluid. The outer skin of these tubes can suffer high temperature atmospheric oxidation as well as attack from other gases present in the atmosphere (salts if near the ocean for instance). The inner skin of the tubes interacts with the heat transfer fluid. As described earlier, higher temperature heat transfer fluids are being developed such as molten salts, super critical CO<sub>2</sub> or direct steam generation. A good understanding of the different corrosion processes involved are therefore of great importance. Stainless steels for solar thermal applications must not only resist corrosion but also retain their mechanical properties, especially their creep resistance. Grain growth and precipitation during high temperature ageing are the main processes impacting mechanical properties of the bulk alloys.

High temperature corrosion is due to the interaction at high temperature of gases, liquids or solids with materials. The most important form of high temperature corrosion is oxidation. Air, oxygen and steam are mainly responsible for the oxidation of materials. Carburization is another form of corrosion where carbon-containing compounds such as CO<sub>2</sub>, CO and methane change the carbon composition of the surface layer of a steel, modifying its corrosion and mechanical properties. Hydrogen can be responsible for decarburization, depleting the steel of its carbon by forming methane (22).

---

Other forms of high temperature corrosion include nitridation (nitrogen), sulfidation (sulfur containing gases), halogen corrosion and ash/salt deposit corrosion (23). Molten salt corrosion can be very detrimental for steel due to the high ionic conductivity of the salts as well as the high flux at which molten salts are usually used.

As described in the next section, stainless steels generally develop a passive layer protecting the steel from detrimental corrosion. When used in extreme conditions at high temperature in an ultra-corrosive atmosphere, together with thermal cycling or high pressure, this passive layer can be destroyed and leave the steel exposed to corrosion resulting in material failure.

#### 4.1.2 Austenitic stainless steels

Stainless steels are an important and large family of steels. They are commonly used for their corrosion resistance and high temperature performance. Their corrosion resistance comes from the spontaneous formation of a thin, passive chromium oxide layer at the surface of the steel protecting it from further oxidation (Figure 4.3) (24).

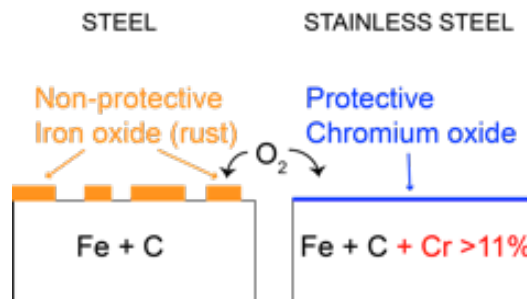


**Figure 4-3** Basics of stainlessness

According to the European standard EN10008 (25), steel is considered stainless when a minimum of 10.5% of chromium is present. The more chromium, the better the oxidation resistance. A useful property of this passive chromium oxide layer is its ability to heal when scratched or damaged. Chromium reacts rapidly with oxygen or moisture to reform a chromium oxide layer (24).

However low chromium stainless steels (12% chromium) are only passive in atmospheric conditions and will corrode extremely quickly when placed in an acidic environment. More chromium and the addition

of alloying elements improves the corrosion resistance, but also modifies the microstructure and mechanical properties of stainless steels (26). As illustrated in figure 4.4 the corrosion rate is dramatically reduced when the Cr content is high enough to form a  $\text{Cr}_2\text{O}_3$  passive layer.

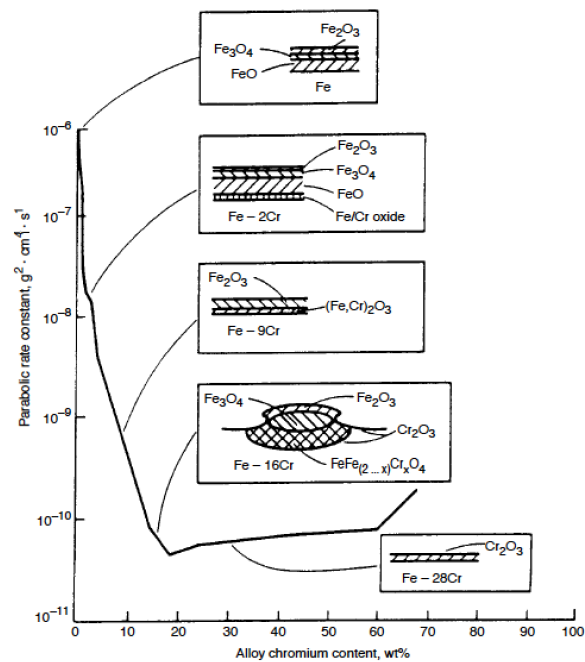


**Figure 4-4** Effect of Cr content on oxidation of Fe-Cr alloys at  $1000^{\circ}\text{C}$  in  $0.13 \text{ atm O}_2$ . (23)

Without this protective layer, iron is oxidized at a high rate forming ferrous oxide ( $\text{FeO}$ ), ferric oxide or hematite  $(\text{Fe,Cr})_2\text{O}_3$  and Fe-Cr spinels  $(\text{Fe}^{2+}(\text{Fe,Cr})^{3+}_2\text{O}^{2-}_4)$ , which do not completely cover the surface, and hence do not protect against further corrosion.

Stainless steels are generally classified into five distinct groups. The first four groups are classified based on their microstructures:

- i. austenitic stainless steels
- ii. ferritic stainless steels
- iii. martensitic stainless steels
- iv. duplex stainless steels
- v. precipitation hardened (PH) stainless steels

The fifth group, precipitation hardened (PH) stainless steels, is differentiated by their ability to be hardened by heat treatment. PH stainless steels are generally either martensitic or austenitic-martensitic (27).

Stainless steels are primarily composed of Fe, C, Cr and Ni. The microstructure of the steels will depend strongly on those elements but also on some other significant elements. Because the mechanical properties of the steels are directly related to their microstructure, it is essential to have a good understanding of the effect of alloying elements in stainless steels.

The two crystallographic forms of steels are body-centred cubic (b.c.c.) and face-centred cubic (f.c.c.). In pure iron, the f.c.c. structure exists between 900°C and 1400°C and the b.c.c. above and below this interval. Stainless steel structures vary from fully austenitic ( $\gamma$  phase – f.c.c.) to fully ferritic ( $\alpha$  phase – b.c.c.). The transition between these two phases is highly dependent on the alloying elements. Chromium is a strong ferrite stabilizer while nickel and carbon are strong austenite stabilizers (27). In order to quantify the influence of alloying elements on phase stabilization, the concept of chromium equivalent ( $\alpha$  stabilizers) and nickel equivalent ( $\gamma$  stabilizers) is widely used in conjunction with the Schaeffler diagram (figure 4.5): (26)

$$\text{Cr equivalent} = (\text{Cr}) + 2(\text{Si}) + 1.5(\text{Mo}) + 5(\text{V}) + 5.5(\text{Al}) + 1.75(\text{Nb}) + 1.5(\text{Ti}) + 0.75(\text{W}) \text{ (wt\%)}$$

$$\text{Ni equivalent} = (\text{Ni}) + (\text{Co}) + 0.5(\text{Mn}) + 0.3(\text{Cu}) + 25(\text{N}) + 30(\text{C}) \text{ (wt\%)}$$

While the Schaeffler diagram was primarily designed for use in welding it does represent a simple way of estimating the microstructure of the steel (Figure 4.5).

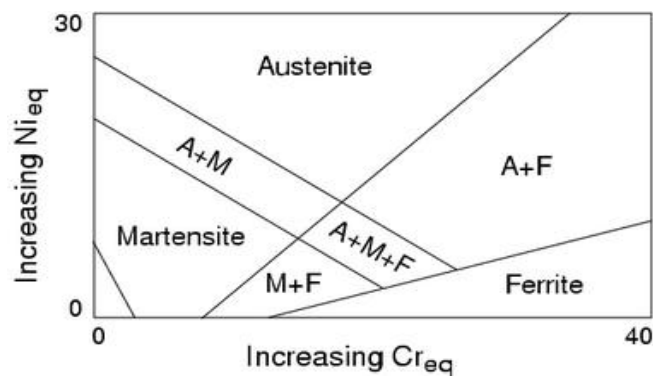


**Figure 4-5** Simplified Schaeffler diagram (26)

Alloying elements not only have an effect on the microstructure of steels but also have a strong influence on their mechanical properties, high temperature resistance, corrosion resistance, machinability and so on. The following table summarizes the effect of common alloying elements found in stainless steels:

Element	Effect
Chromium	Essential in forming the passive film. Oxidation resistance increases at Cr levels above 10.5% High Cr content can adversely affect mechanical properties, fabricability and weldability
Nickel	Stabilize the austenitic structure to enhance mechanical properties and fabrication characteristics Resistance to stress-corrosion cracking is poorest at approximately 8 to 10% Ni but is restored at levels of about 30% Ni Can minimize spalling of surface oxide during temperature cycling
Manganese	In moderate quantities and when nickel is present, performs many of the functions attributed to nickel Interacts with sulfur to form manganese sulfides which can effect corrosion resistance Can improve the adhesion of oxide film and improve oxidation resistance
Molybdenum	In combination with chromium is very effective for passive film stabilization in the presence of chlorides Especially effective in increasing resistance to the initiation of pitting and crevice corrosion
Carbon	Provides strength in the high-temperature applications Detrimental to corrosion resistance through reaction with chromium to form chromium carbides Detrimental to toughness in ferritic grades
Nitrogen	Enhances pitting resistance in austenitic grades Detrimental to the mechanical properties of the ferritic grades
Aluminum	Enhance high-temperature oxidation resistance
Niobium Titanium	Stabilizers used to preferentially combine with carbon and nitrogen to reduce the formation of chromium carbides and nitrides. This reduces the possibility of intergranular corrosion. Titanium oxide may adversely affect brazability
Silicon	Provides high-temperature oxidation resistance Provides resistance to stress corrosion cracking and to corrosion by oxidizing acids

**Table 4.2** Common alloying elements found in stainless steels and their effects. Adapted from (28)

Austenitic stainless steels have been used for several decades in high temperature applications. They have excellent high temperature tensile and creep strength and very good corrosion resistance. They are iron-based alloys containing significant amounts of chromium and nickel. As described in the previous section, ~10.5 wt% of chromium is usually required to reach a critical level of corrosion resistance.

Nickel is added to ensure the stability of the austenite phase. The composition of different austenitic heat-resistant stainless steel is shown in table 4.3.



	C max. (wt%)	Si max. (wt%)	Mn max. (wt%)	Cr (wt%)	Ni (wt%)	Mo (wt%)	Ti (wt%)	Nb (wt%)
<b>301</b>	0.15	1.00	2.00	16-18	6-8			
<b>310</b>	0.25	1.50	2.00	24-26	19-22			
<b>316</b>	0.08	1.00	2.00	16-18	10-14	2.0-3.0		
<b>321</b>	0.08	1.00	2.00	17-19	9-12		5 x %C min.	
<b>347</b>	0.08	1.00	2.00	17-19	9-13			10 x %C

**Table 4.3** The AISI 300 series. Adapted from (29)

Particular attention is placed on Sandvik 253 MA in this literature review as this specific steel was investigated in this study. Sandvik 253MA (253MA) is a full austenitic stainless steel developed for high temperature application. This grade has high creep strength and excellent corrosion resistance to isothermal and cycling oxidation. It can be used at temperatures up to 1150°C (30). Table 4.4 shows the composition of 253MA:

Fe	C	Cr	Ni	Si	Mn	Cu	Mo	N	V	P	Ti	REM (Ce/La)
Bal.	0.08	20.9	10.8	1.64	0.58	0.44	0.19	0.17	0.058	0.024	0.011	0.05

**Table 4.4** 253MA typical chemical composition (wt%). (31)

The addition of silicon and rare earth metals (cerium and lanthanum) improve the oxidation resistance as well as the adhesion of the passive layer, allowing better resistance to thermal cycling. The addition of nitrogen and carbon increases the strength and delays the formation of sigma phase providing good resistance to embrittlement (32).

Overall, 253MA is a cost effective solution for high temperature applications in most corrosive environment. However, 253MA is subject to sensitization due to the relatively high carbon content. In thermal cycling conditions it is likely that the temperature will be in the range of 400 °C to 850 °C where sensitization can occur. This might lead to intergranular corrosion, increasing the chances of stress corrosion cracking (33).

### 4.1.3 Sensitization and intergranular corrosion

Between 480 °C and 815 °C formation of chromium carbides can occur, usually taking place at the austenitic grain boundaries (34). This process is referred to as sensitization. The chromium carbides formed at the grain boundaries induce a chromium-depleted zone around the grain boundaries. If the chromium content of those areas drops below 11% - 12% these zones are no longer corrosion resistant and oxidation will occur (Figure 4.6) (26). In corrosive environment a sensitized stainless steel will suffer intergranular corrosion potentially leading to complete failure of the material (35).

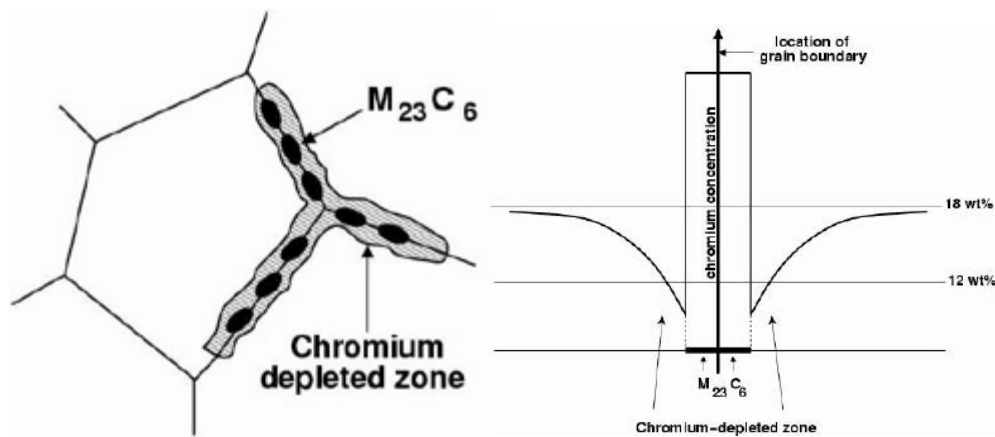


**Figure 4-6** Schematic illustration of sensitisation process and intergranular corrosion (36)

It is possible to avoid and/or limit sensitization by: (26)

- Reducing the carbon content to a very low level (0.03 wt% to 0.08 wt%) so the precipitation of carbides is limited
- Using strong carbide formers as alloying elements such as Nb, Ti, V or Ta in conjunction with heat treatment to allow the formation of these carbides
- Performing a high temperature heat treatment to re-dissolve the chromium carbides completely

Sensitization and intergranular corrosion are often associated to welding of stainless steels due to the temperature increase in and around the weld. Those steels can often be desensitized with a post-weld heat treatment (37).

Thermal cycling can also be an issue when temperatures cycle through the sensitization range. In CSP technology, temperatures cycle from room temperature at night up to > 900 °C when exposed to the sun. This exposes the austenitic stainless steel pipes and tubes to the sensitization temperature-range everyday, leading to intergranular corrosion. The stainless steel composition in and around the grain boundaries

---

becomes depleted in chromium and as the temperatures cycle. The chromium-depleted area is then oxidized as a result of the formation of less-protective oxides such as iron-chromium spinel oxides or destructive oxides such as iron oxides.

The composition change within the stainless steel intergranular areas coupled with thermal cycling can also trigger phase transformations, such as from austenite to martensite. The austenitic structure obtained by heat treatment is stable above 800 °C. By quenching the steel after heat treatment the full austenitic structure can exist at room temperature. However, the austenitic structure below 800 °C is metastable and a phase transformation or precipitation can take place (38). The phase transformation from austenite to martensite can occur in austenitic steels when the temperature decreases to a critical value, the martensite-start temperature (Ms). The Ms temperature is affected by the solute content in the austenite and can be predicted by empirical formulae such as the following: (38)

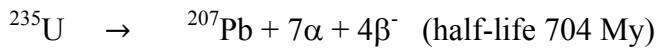
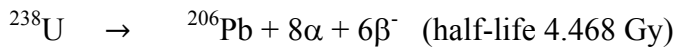
$$M_s(^{\circ}\text{C}) = 502 - 810(\text{C}) - 1230(\text{N}) - 13(\text{Mn}) - 30(\text{Ni}) - 12(\text{Cr}) - 54(\text{Cu}) - 6(\text{Mo}) \text{ wt\%} \quad (38)$$

Martensite that forms below the Ms temperature is called athermal martensite. The martensitic transformation occurs “instantaneously” at a fixed temperature Ms, rather than being a gradual transformation over a finite time. The Ms temperature is usually in the cryogenic level for austenitic stainless steels. However the composition change within intergranular areas after sensitization can potentially lead to Ms temperatures above room temperature, triggering the phase transformation. Previous studies have reported the formation of martensite in sensitization-induced chromium-depleted zones of austenitic stainless steels due to the raised Ms temperature (39, 40). However only little attention has been paid to such phase transformations within intergranular corrosion, and the implication for austenitic stainless steels used in high temperature thermal cycling conditions.

## 4.2 Silicate mineral zircon

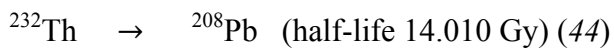
### 4.2.1 Mineral zircon: a uranium-lead geochronometer

Knowledge of the ages of rocks is indispensable to understand the origin of Earth, as well as to record geological processes such as extinction episodes or the formation of mountains (41). First discovered by Boltwood about one century ago, the uranium-lead (U-Pb) decay is one of the most established ways of dating rocks (42). It is based on the following decay system: (43)



The U-Pb decay system is unique. The half-life of  $^{238}\text{U}$  is long enough to date all of Earth's history. Using the ratios  $^{206}\text{Pb}/^{238}\text{U}$  and  $^{207}\text{Pb}/^{235}\text{U}$ , this system enables two age determinations from the same two elements, improving the measurement accuracy by checking both dates against each other. There is also the possibility of determining the age from the daughter ions using the ratio  $^{207}\text{Pb}/^{206}\text{Pb}$  without knowing the daughter-parent ratio (43).

It is important to note that the U-Pb decay system is also referred as the U-Pb-Thorium (Th) system due to the following decay:



For the U-Pb decay system to give an accurate age, the principal assumption is that the material hosting U and Pb must be a closed system for those elements. In other words, the mobility of Pb and U has to be minimal. This is one of the many properties of the accessory mineral zircon that makes it the material of choice for geochronological application (figure 4.7). Zircon is an orthosilicate mineral with the composition  $\text{ZrSiO}_4$ . This accessory mineral can be found in a wide range of rocks, usually in very small amount. It occurs in igneous rocks, metamorphic rocks and it has even been extracted from meteorites and lunar rocks (45).

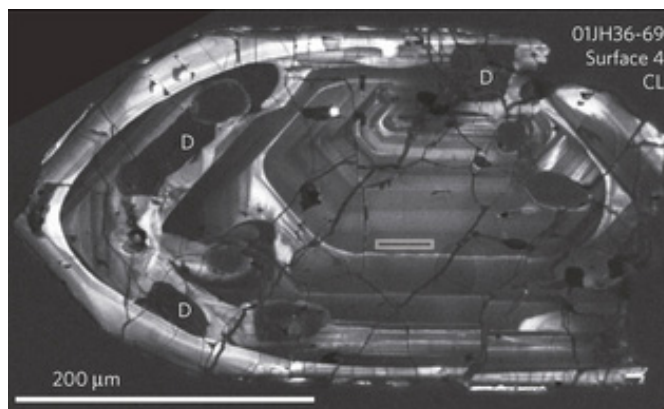


**Figure 4-7** SEM image by cathodoluminescence (photon emission induced by incident electron beam) of the surface of zircon from Jack Hills, Australia. Adapted from (46)

The typical size of a zircon crystal is hundreds of microns. When an igneous rock crystallizes from magma, zircon crystal grows and small amount of many elements such as radioactive U and Th as well as Y, Hf and rare earth elements (REE) are incorporated into the crystal lattice (44).

U and Th amongst other elements are usually present in the melt in the form of the cations  $U^{4+}$  and  $Th^{4+}$ . These cations can easily substitute for  $Zr^{4+}$  ions during the crystallization of the zircon. The ionic radii of the cations largely control this substitution process. The ionic radius of  $Zr^{4+}$  is 0.083 nm. With an ionic radius of 0.083 nm, Hf can heavily substitute for  $Zr^{4+}$  explaining the large amount of Hf found in zircons. The ionic radii of  $U^{4+}$  and  $Th^{4+}$  are respectively 0.10 nm and 0.105 nm. They can be accommodated in the crystal lattice but are usually found in lower amount (maximum of 5000 ppm for U and 1000 ppm for Th). Due to the large ionic radius of  $Pb^{2+}$  (0.129 nm) and its less positively charged character, Pb is not incorporated at all in the growing zircon crystal (or only a few ppb) (41, 44, 47).

The ability of zircon to incorporate U (and other elements) but exclude Pb during crystallization enables the use of the U-Pb decay system as geochronometer without the need for a complex non-radiogenic Pb correction. The lattice structure of zircon, composed of isolated  $SiO_4$  tetrahedra, results in its refractory and weather resistant nature. It also allows the zircon crystal to stay a closed system even at lower Earth crust temperatures (600°C - 800°C) (48, 49).

In 1956, Wetherill introduced the Concordia diagram, a graphical procedure allowing the assessment of zircon U-Pb decay (Figure 4.8) (50). It is obtained by plotting  $^{206}Pb/^{238}U$  vs  $^{207}Pb/^{235}U$ . As a result of the two different half-lives and the constant decay, a curve is obtained as shown in figure 4.7. For a single  $^{206}Pb/^{238}U$  ratio there is a corresponding  $^{207}Pb/^{235}U$  ratio and an age derived from the half-lives.

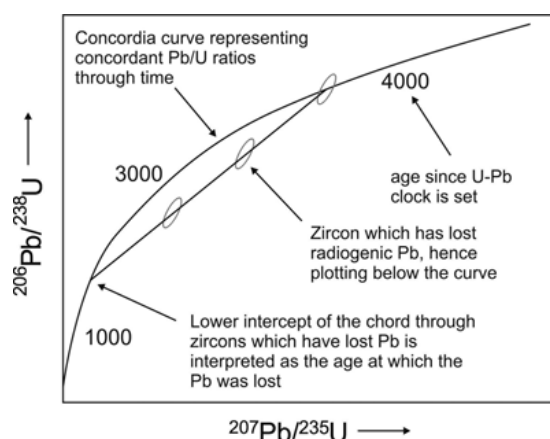


**Figure 4-8** Wetherill Concordia diagram showing Pb/U isotope ratios of zircons and how to interpret data where the two ratios are discordant. (48)

---

If the two ratios measured in a zircon fall on the Concordia curve, it means that they correspond to the same age, which can directly be measured. This is a concordant zircon grain. However, there are cases when the two ratios do not agree on the same age. In such case the zircon grain is said discordant. If the ratios are below the curve, the zircon is normally discordant. If they are above the curve, the zircon is said reverse discordant.

In the case of normal discordance, the zircon has lost some lead, usually through a geological event that allowed lead to diffuse out. Generally, the loss of Pb in zircon after such an event is not homogeneous throughout the grain with some microscopic parts of the grain retaining most of it and some losing a lot of it. This effect leads to several points in the concordia diagram and a series of discordant analysis generating a discordant line.

The lower intercept of this line with the Concordia curve will give the age of the geological event that provoked the lead loss while the upper intercept is a measure of the original age of the zircon formation (41, 48).

Mass spectrometry is the technique of choice for the measurement of the isotopic ratios of U and Pb. The spatial resolution for zircon dating using mass spectrometers has evolved from hundreds of microns (in the 1950s) to microns (10 – 20  $\mu\text{m}$ ) with high-resolution ion microprobe (SIMS) or sensitive high-resolution ion microprobe (SHRIMP) (51, 52). The improvement in spatial resolution of isotopic ratio measurement coupled with scanning electron microscopy techniques such as cathodoluminescence or backscattered imaging allow the analysis of microscopic areas within a single zircon grain. The accuracy of dating zircon greatly improved as it allowed avoiding damaged parts of the crystal, leading to lead loss and inaccurate dates. It is well understood that zircon grains can be damaged by the radioactive decay of U. This process is called metamictization (53). As a result, lead and other trace elements can diffuse in or out of the metamict grain making this part of the zircon an open system unsuitable for accurate dating.

#### 4.2.2 Deformation in zircons and trace elements diffusion

As described earlier, the physical and chemical robustness of zircon is the reason for its wide use in a large range of geological disciplines. A study of Pb diffusion within pristine zircons shows that it can only occur at extreme temperatures (54). However, diffusion at lower temperatures than experimentally predicted was revealed by a few studies in metamict areas (55, 56).

---

Over the last decade a number of studies have documented significant changes in trace elements contents and ratios in a range of zircons (4-7, 57, 58). In these studies, deformation microstructures (Figure 4.9) such as low-angle boundaries formed during crystal plastic deformation, show a clear correlation with changes in U, Pb, Th and associated deformation.

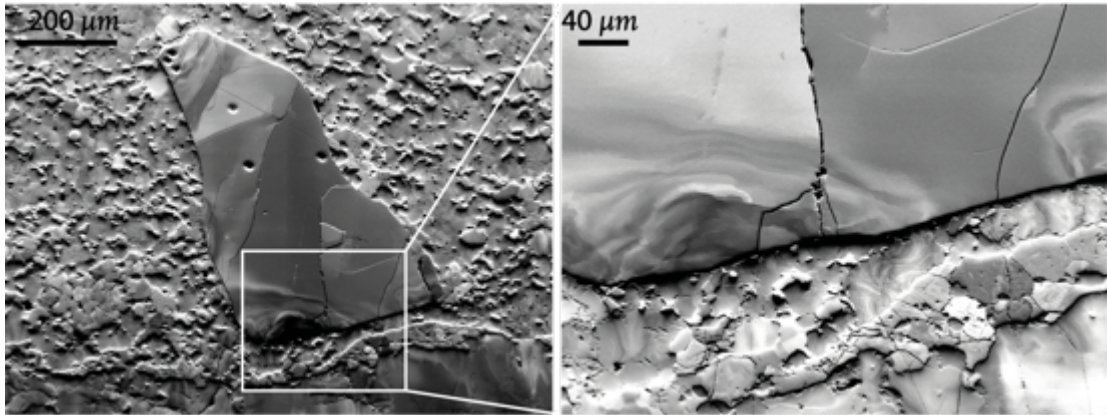


**Figure 4-9** Deformation in zircon imaged by foreshatter orientation contrast map in a scanning electron microscope (Courtesy Patrick Trimby)

The most common explanation for the isotopic ratios changes is that deformation microstructures provide pathways for fast diffusion along dislocation cores. Such processes have been suggested for minerals including zircon (4, 6, 7). However, unequivocal evidence and in-depth understanding of the diffusion rate enhancement is still lacking.

Lead isotope and trace element mobility due to deformation structures has not previously been studied at the atomic scale and the details of the relationship between deformation microstructures and Pb migration, loss and / or enrichment remain poorly understood.

## 4.3 Human dental enamel hydroxyapatite

### 4.3.1 Hierarchical structure of enamel

Human dental enamel is the hardest tissue of the human body. It covers the crown protecting the tooth from daily use. Its thickness varies from 0.1 mm to up to 2.5 mm at the cusp (59).

Dental enamel consists of a mineral phase (96 wt %), mainly in the form of highly oriented carbonated hydroxyapatite (HAP) ribbon-like nanowires with cross-sectional dimensions of about 50 x 25 nm that

are up to several millimeters long (60). These crystallites are packed into bundles, known as rods or *prisms*.

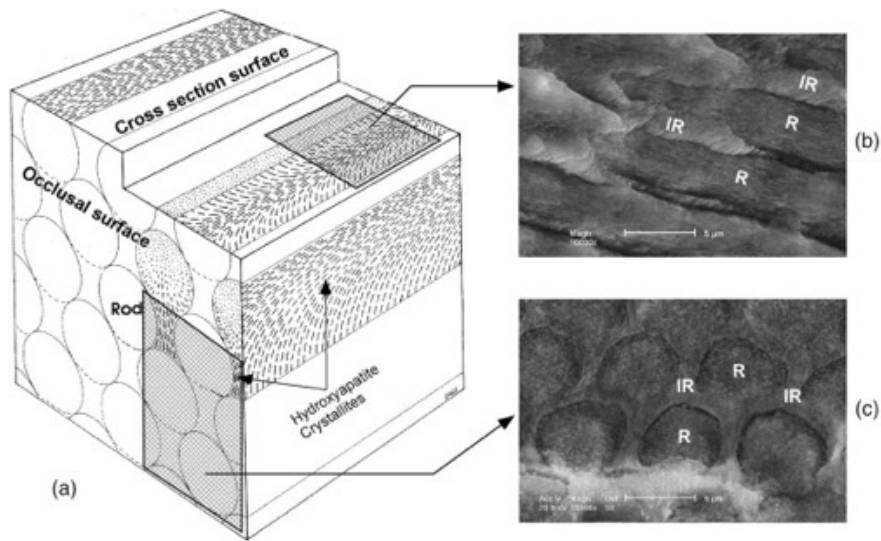


**Figure 4-10** “(a) Schematic illustration of enamel’s hierarchical structure. The occlusal surface is equal to the natural tooth surface in which the cc-axis of the rods is parallel to the chewing force. (b) and (c) SEM images of different faces. (Samples were etched in 37% H<sub>3</sub>PO<sub>4</sub> for 5 s and observed by secondary electron detector.)” (61, 62)

Each prism contains about 40,000 nanowires at a density of roughly 550 crystallites per  $\mu\text{m}^2$  (63, 64). A mineral phase present between the enamel prisms is referred as interprismatic enamel (Figure 4.10). The prisms extend in an interwoven pattern through the entire thickness of the enamel, from the dentine-enamel junction to the outer surface of the tooth (65).

Dental enamel is a bio-composite. Apart from a mineral phase, it contains enamel proteins (1 wt %) and water (3 wt %). This combination of proteins, water and a highly anisotropic nano-structured mineral phase lead to a unique combination of strength and toughness (66), visco-elastic properties (67, 68), wear (69) and erosion (70) resistance, and resistance to carious attack (71). These features enable dental enamel to last a lifetime in the harsh and variable environment of the oral cavity.

### 4.3.2 Formation of hydroxyapatite

The HAP composition in enamel differs slightly from the perfect HAP crystal ( $\text{Ca}_{10}(\text{PO}_4)_6(\text{OH})_2$ ). Dental enamel HAP is carbonated and contains trace elements such as magnesium and sodium (72). Naturally occurring peptides of the enamel-specific proteins, *i.e.* amelogenin, ameloblastin, and enamelin have been



---

identified in mature human enamel (73). These proteins play an essential role in enamel formation i.e. amelogenesis. During amelogenesis, ameloblast cells secrete an organic matrix containing enamel-specific proteins, which is followed immediately by mineralization. As the HAP crystallization progresses, specific enzymes degrade and eliminate most of the remaining organic matrix (74). HAP crystallization is initiated by the mineralization of an amorphous calcium phosphate (ACP) precursor (75). It was recently proposed that Mg ions play a critical role in the stabilization of this ACP phase and the formation of the HAP mineral, where surface Mg ions retard the growth of HAP crystals, leading to the nanometer-sized HAP crystallites (76). Knowledge of the distribution of Mg ions and the presence of the precursor ACP in mature human dental enamel would provide much needed information for a better understanding of amelogenesis, and may eventually allow the development of strategies to enhance remineralisation, to slow or prevent caries, or even to restore lost dental enamel. However, until recently, it has not been possible to observe the distribution of Mg ions within HAP nanowires at the nanoscale in human dental enamel.

In a recent study of rodent tooth enamel, nanoscale heterogeneities in the distribution of Mg ions and organic materials, as well as the presence of intergranular ACP, were revealed using the atomic-scale 3-dimensional visualization and chemical analysis enabled by atom probe tomography (77, 78).

## **5 Advanced microscopy techniques**

The rapid development of advanced microscopy techniques has enabled the characterization of materials at the nanometer length scale. Transmission electron microscopy (TEM) is the most established technique for atomic scale characterization of materials. High-resolution aberration corrected TEM can indeed image individual atomic columns (79). When coupled with X-ray spectroscopy (1) or energy loss electron spectroscopy (EELS), TEM is a powerful technique enabling precise chemical, electrical and physical analyses of materials at the atomic scale. While TEM only gives access to 2-d information, the recent development of transmission electron tomography allows imaging of 3-d nanostructures (80). However, this technique is limited by the maximum analysis depth of ~20 nm corresponding to the sample thickness. Atom probe tomography (APT) is a unique technique in that is able to achieve atomic-scale tomography with large field of view (hundreds of nm) (78, 81). Section 5.1 is dedicated to introducing APT.

---

While TEM and APT are the ultimate techniques for atomic scale characterization, scanning electron microscopy (SEM) has seen some interesting development in the past years with better instrumentation leading to dramatic improvements in the spatial and chemical resolutions. One particular technique was developed 4 years ago that uses electron-backscattered diffraction (EBSD) in transmission mode: transmission Kikuchi diffraction (TKD). TKD gives access to structural information of a material at the nano-scale and is proving to be to be an excellent complimentary technique to APT. TKD technique will be introduced in Section 5.2.

## 5.1 Introduction to atom probe tomography

### 5.1.1 Overview of APT

APT is a microscopy technique that enables 3-dimensional visualization and chemical identification of materials at the atomic scale. In this technique, ions are successively field-ionised from the tip of a needle shaped sample, collected by a position sensitive detector and their mass-to-charge ratios are recorded by time-of-flight spectrometry (78, 81). In a typical APT analysis chamber, the sample is cooled to cryogenic temperatures ( $\sim 50$  K) and maintained at ultra-high vacuum ( $\sim 10^{-11}$  Torr).

For APT the sample has to be a sharp hemispherical-shaped tip with a typical diameter of  $< 100$  nm. When a DC voltage (typically between 2 and 10 kV) is applied to such specimen, a high electric field can be achieved at the surface of the tip according to this equation:

$$F = \frac{V}{k_f R}$$

Where  $F$  is the electric field at the apex of the tip,  $V$  is the applied voltage,  $k_f$  is the field factor (a correction parameter accounting for experimental aspects such as sample shank angle) and  $R$  is the radius of curvature of the tip.

The DC voltage applied to the sample is usually just below the value required to initiate field evaporation. In the case of electrically conductive materials, high voltage pulses are applied to the tip creating an electrical field strong enough to enable field ionization. For less conductive samples, laser pulses are applied enabling thermal evaporation of the tip. Laser pulsing is generally used for higher resistivity materials such as semi-conductors or minerals where high voltage pulses are inefficient (82-85). Laser-assisted APT applied to high resistivity materials will be discussed in more detail in the next chapter.

APT originates from the work of Erwin Müller, with the development of the field ion microscope (FIM) in the 1950s (86). In 1967, the first time-of-flight atom probe was developed as a combination of time-of-flight mass spectrometer and FIM (87). Today, the most common design for APT is the local electrode atom probe (LEAP<sup>®</sup>), manufactured by Cameca<sup>®</sup>.

In a LEAP<sup>®</sup>, the voltage is applied between the sample (positively charged) and a counter electrode (local electrode). Once field ionised, the positively charged ions fly through a small aperture in the local electrode toward a micro-channel plate detector (MCP) that converts the ions into a cloud of electrons. The electron cloud then hits a delay-line position-sensitive detector and the detector position  $X_d$  and  $Y_d$  of each “hit” is recorded (78, 88).

Using the simple flight path geometry and the assumption that the sample is a hemispherical cap on a truncated cone, the ions detector coordinates can then be used to determine the lateral positions ( $x$  and  $y$ ) of the atoms in the sample, and the in-depth coordinates ( $z$ ) may be directly obtained from the sequence of evaporation (Figure 5.1). The most common APT reconstruction algorithm is based on the work from Bas et al., Geiser et al. and Gault et al. (89-91).

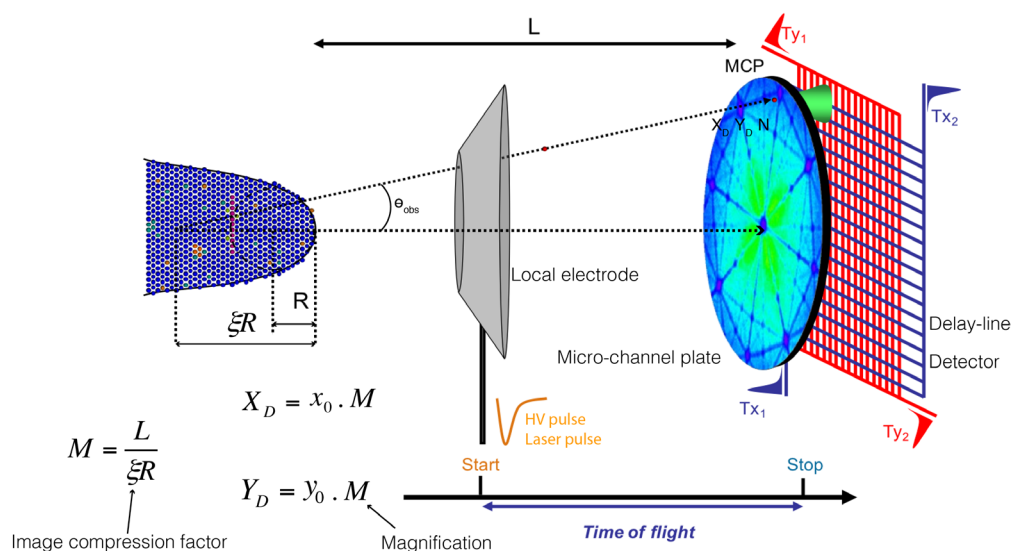


**Figure 5-1** Basic schematic of a straight flight path LEAP. Note  $x_0$  and  $y_0$  are ions coordinates in original sample (Courtesy B. Gault and M. Moody)

The high-voltage or laser pulse that triggered the evaporation event is correlated to the corresponding ion(s) detection and its time-of-flight is recorded. The time-of-flight is converted into a mass-to-charge

ratio ( $m/q$ ) that is used to chemically identify each ion.  $m/q$  is simply derived from the time-of-flight according to:

$$\frac{m}{q} = 2eV \frac{t_{TOF}^2}{L^2}$$

where  $q$  is the charge state of the ion (e.g. +1, +2, +3),  $m$  is the mass of the ion,  $e$  is the charge of an electron (69),  $V$  is the voltage applied to the specimen,  $L$  is the flight path (distance from specimen to detector, e.g. 90 mm),  $t_{TOF}$  is the time-of-flight ( $t_{TOF} = t_1 - t_0$ , where  $t_1$  is the time at which ion reaches the detector and  $t_0$  is the time at which pulse was applied).

As a result, a histogram of the resulting  $m/q$  of ions can be created resulting in a mass-to-charge spectrum, commonly referred to as an APT mass spectrum (Figure 5.2).

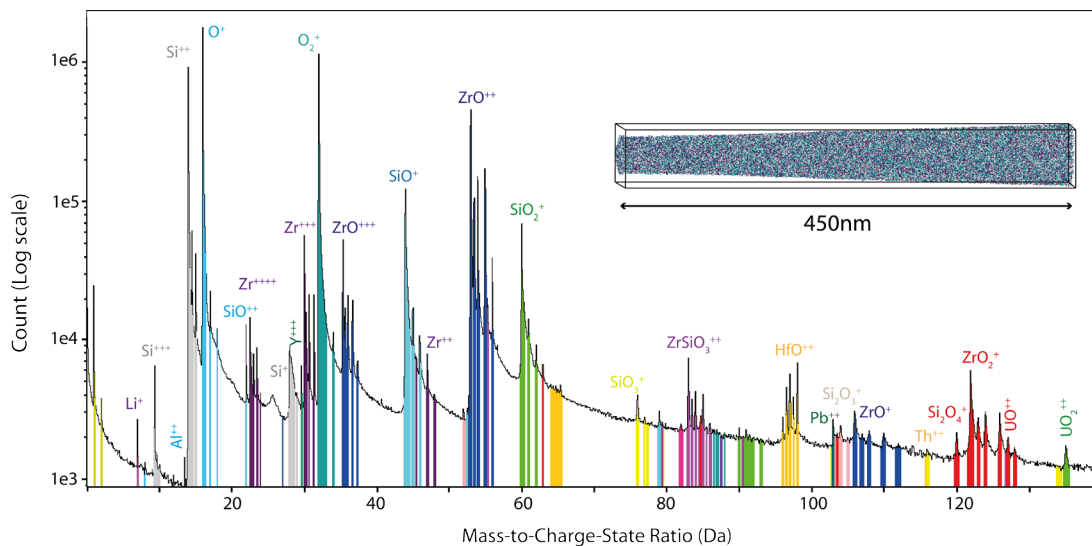


**Figure 5-2** Typical indexed APT mass spectrum of a Zircon sample. Data obtained with laser-assisted APT.

A typical APT experiment results in a large number of collected ions (up to several hundred million). The most prevalent software package to visualize APT data is the Interactive Visualization and Analysis Software (IVAS<sup>®</sup>) which is the Cameca<sup>®</sup> LEAP<sup>®</sup> commercial software (92). This commercial software enables the reconstruction of APT data through semi-automated steps and the 3-dimensional data visualization capabilities. Once the data is reconstructed in IVAS<sup>®</sup> a POS file is created containing (x, y, z and  $m/q$ ) information. The information contained in the POS file can then be opened in IVAS<sup>®</sup> and the 3-d data visualized and manipulated. Several data analysis techniques are available in IVAS<sup>®</sup> such as

---

isosurfaces, proximity histograms (93), ion range selections, clipping and so on. Here we briefly introduce the grid-based methods (or voxel-based analysis), as it is the most relevant for this work.

Grid-based data analysis techniques are based on dividing the whole dataset into small 3-dimensional volumes. This is called voxelisation and it facilitates the management of large datasets (94). Each atom is assigned to a voxel, which is a rectangular prism with a user-defined size. Typically, a voxel size can be based on volume (defined size) or population (same number of atoms). The voxel size should be optimized keeping in consideration the analysis time and the statistical significance.

Density or concentration analysis is one of the most common techniques that uses voxelisation by volume. The concentration of a particular species can be calculated for each voxel. As a result, a 3-dimensional density map can be used to visualize variations in density or composition through the whole dataset. Microstructural features present within the whole volume such as precipitates or grain boundaries can be revealed by this technique.

Isosurfaces or isoconcentration surfaces is a similar approach that can also be used to reveal microfeatures within an APT reconstructed volume. An isosurface defines surfaces in the reconstruction that join up adjacent blocks of a pre-defined concentration or density of one element. It allows a direct visualization of elemental partitioning within the reconstructed volume of data. Isoconcentration surfaces and isodensity surfaces are interfaces between regions of different concentration or density respectively.. Graphs, called proximity histograms (proxigrams), can subsequently be used to plot the variation of composition or density away from the defined interface (93). This is extremely useful for the study of matrix-precipitate interface for example (2). An example of isosurfaces and a proxigram is given in figure 5.3.

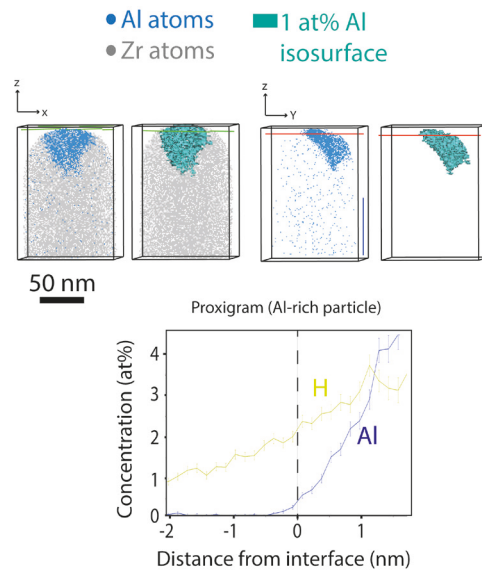


**Figure 5-3** Example of an isosurface used to highlight an Al-rich particle in a zircon mineral. The variation of Al and H content within the precipitate is obtained through a proxigram analysis.

### 5.1.2 Spatial and mass resolution of APT

APT is a unique 3-dimensional technique providing one of the best combinations of chemical and spatial resolution. However, there are limitations. The spatial and mass resolution, as well as the detector efficiency, are limited by different factors. Here we briefly discuss the spatial and mass resolution limitations.

The optimum spatial resolution of APT is estimated to be better than 0.06 nm in depth ( $z$ ) and the lateral resolution ( $x, y$ ) below 0.2 nm (95-97). However, several factors can affect the spatial resolution. Variations in the local geometry and composition on the surface of the tip can cause trajectory aberrations in the flight path degrading the spatial resolution (98). The effect of atoms moving at the surface of the tip just before field ionisation is known as surface migration and is a limiting factor for spatial resolution (99). Trajectory aberrations can occur as a result of the tip becoming mis-shaped by the retention of, for example, a high field precipitate. The local radius of curvature is thus decreased at the location of the precipitate resulting in local increase in the magnification. Local magnification usually involves preferential evaporation or non-evaporation of particular elements due to the difference of evaporation field that typically occurs with the presence of precipitates. It results in a non-uniform sequence of evaporation which is detrimental for the spatial resolution (100). Finally the fact that the reconstruction algorithm is based on several fundamental assumptions is a source of errors that limits the overall accuracy of an APT experiment (2). A calibration protocol based on crystallographic information was developed to calculate essential reconstruction parameters directly from the APT experiment (101, 102).

---

However it can only be used when crystallographic information is visible in the desorption image of the detector, which occurs principally for low-alloyed crystalline materials.

The mass resolving power (MRP) in APT is generally defined as  $m/\Delta m$ , where  $\Delta m$  is measured as the full-width at half-maximum (FWHM) of the peak. MRP is typically up to 500 for voltage-pulsed atom probe and up to 1000 for laser-pulsed atom probe (78). The mass resolution is dependent on many factors such as voltage pulse fraction or laser energy, pulse frequency, temperature, thermal and electrical conductivity of the specimen or the geometry of the tip. The experimental conditions need to be tested for every sample to optimize the mass resolution. We will discuss optimization of laser-pulsed APT applied to high-resistivity materials in the next chapter.

### 5.1.3 Specimen preparation techniques

The specimen preparation is an important and challenging part of a successful APT experiment. Here we briefly introduce the two principal methods, which have been more extensively described elsewhere (2, 78, 103). Requirements for APT specimens include:

- The specimen should be needle-shaped with a radius of curvature at the apex of  $\sim 50$ - $100$  nm
- The specimen length must be  $\sim 20 - 30$   $\mu\text{m}$  and the tip clearance (if several tips)  $\sim 100$   $\mu\text{m}$
- The specimen must have a smooth surface, be free from protrusions or cracks and be clean enough for ultra-high vacuum conditions
- The feature of interest (i.e. grain boundary, precipitate,...) must be within hundreds of nm of the specimen apex

There are two main preparation techniques. Electropolishing suits conductive materials, such as metallic alloys, that do not require site-specific preparation. Focused ion beam (FIB) techniques suit all kind of materials, but are usually applied to high resistivity materials, thin films and site specific preparation (2).

The electrochemical process removes material from the specimen surface within an electrolytic cell. The electrolyte is suspended within a wire loop (cathode). The specimen (anode) is repeatedly pushed through the electrolyte until sufficiently sharp. (Figure 5.4). There are two steps: rough and fine polishing. The choice of electrolyte and specimen voltage is inherent to a specific material and are different for rough (stronger electrolyte, higher voltage) and fine polishing (more diluted electrolyte and smaller voltage).

There are several books available listing recommended electrolyte type for different materials (2, 103-105).

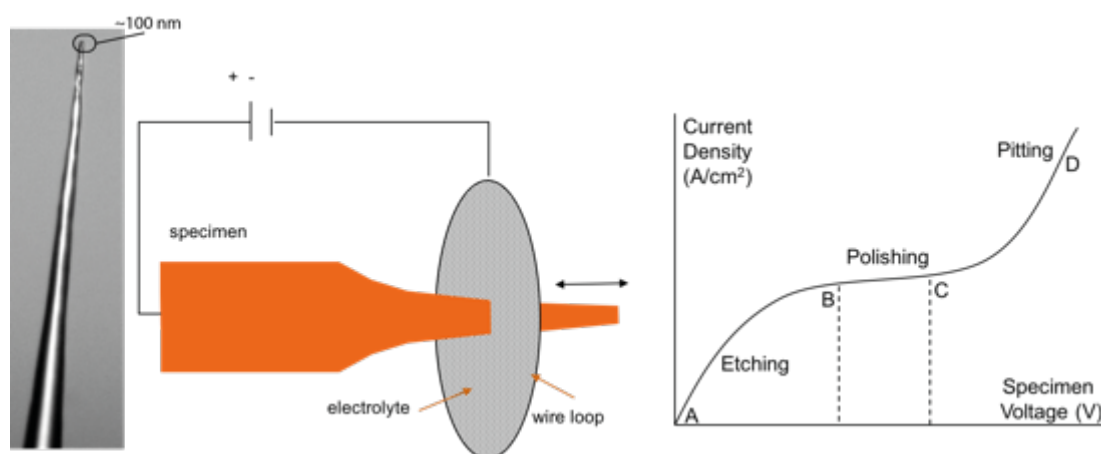


**Figure 5-4** Schematic of electropolishing APT sample preparation. Adapted from (103)

FIB methods rely on the use of a  $\text{Ga}^+$  beam to mill material out in a dual beam (ion/electron) scanning electron microscope. Used for the first time almost 40 years ago, FIB techniques are today routinely used for APT specimen preparation (106-108). A  $\text{Ga}^+$  beam is scanned across the surface of a sample sputtering material exposed to the beam. Conical shapes are easily obtained using ion milling enabling the preparation of needle-shaped samples suitable for APT. The optimum resolution of an ion beam is  $\sim 5$  nm with high acceleration voltage (30kV) and low ion current (30 pA). However, it is recommended to work at lower ion energies during the final stages of APT sample preparation in order to limit ion beam damage. The resolution is consequently reduced to  $\sim 50$  nm. All the final stages of APT sample preparation with FIB involve annular milling enabling the formation of a spherical tip. (Figure 5.5)

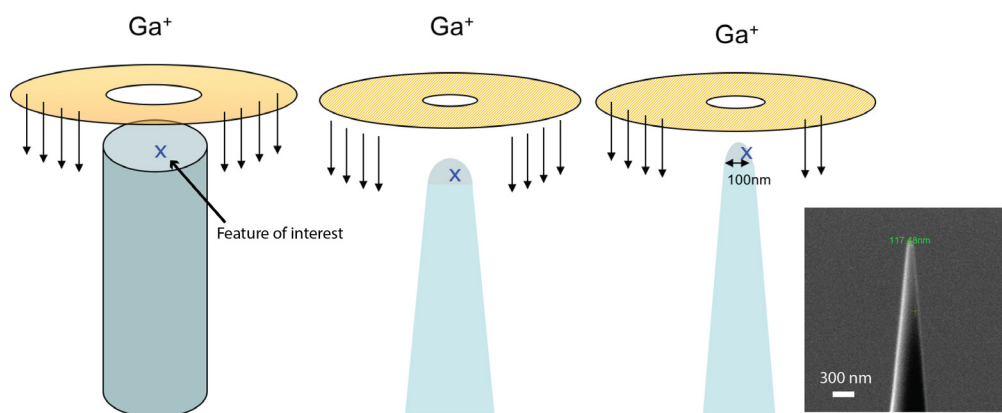


**Figure 5-5** Basics of annular milling to obtain sharp APT tips. (Courtesy J. Cairney)



FIB can be used on an electropolished sample in order to position a feature of interest within the tip. This method is quick and easy but can only be used for conductive materials (suitable to be electropolished) and with a high density of the feature of interest (usually grain boundary). An example is given in figure 5.6 (109).

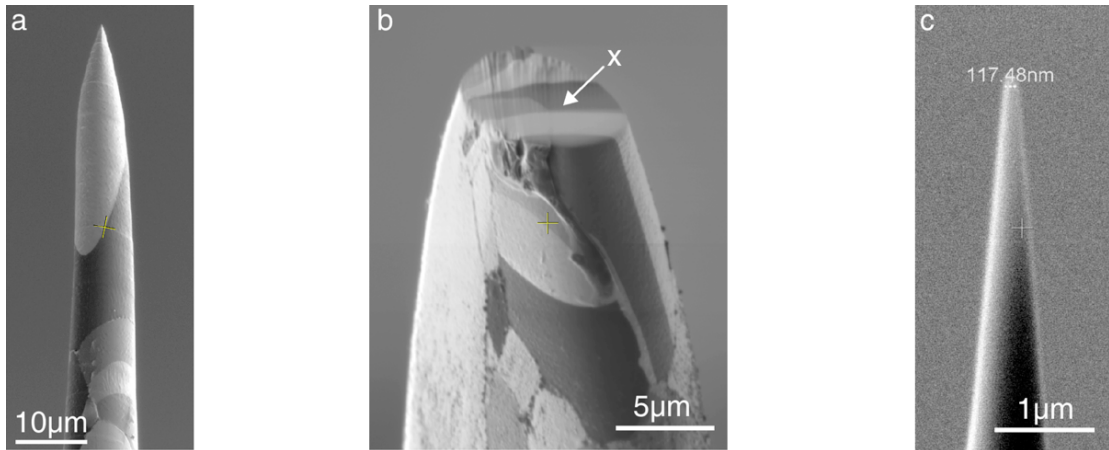


**Figure 5-6** APT tip prepared by annular milling from an electropolished blank. (a and b are ion beam images and c electron beam image) Adapted from (109)

Another method uses a thin wedge usually polished by tripod polishing to produce several tips out of it. The wedge is attached to a support grid and material is removed with the FIB to leave  $\sim 4 \mu\text{m}$  wide posts with  $\sim 50$  to  $100 \mu\text{m}$  opening. (Figure 5.7) APT tips are then milled using annular milling (109, 110).

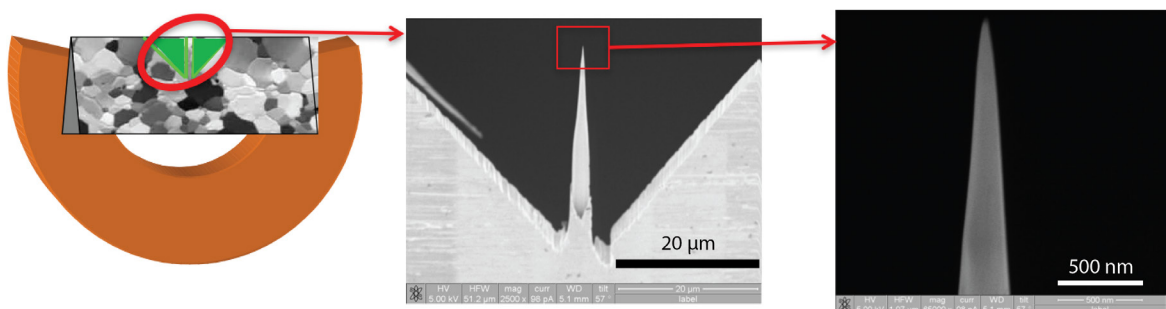


**Figure 5-7** Schematic of the FIB wedge method. Adapted from (109)

Depending on how thin the wedge is, this method can be time consuming due to the large amount of material to mill out.

One great advantage of FIB is the use of gases that can be introduced into the chamber. Under the ion beam (and electron beam) the gas decompose and material can be deposited onto the surface of the

sample. A typical gas source used for deposition is a Platinum (Pt) containing gas. Deposition of Pt onto the sample surface can be used to protect a beam-sensitive region of interest or attach pieces to a micro-manipulator present in the instrument chamber.

The latter enables the lift-out method that was first developed for TEM sample preparation but rapidly was routinely used for APT specimen preparation (111-113). First a wedge from the sample is cut free and attached to a micromanipulator needle with Pt-deposition. Pieces of this wedge are then milled and attached to a support structure (typically electropolished molybdenum grids or a commercial micro-tip array) by ion beam assisted Pt-deposition (Figure 5.8 a). The sample is then milled to form a needle shape. The final milling uses annular patterns to form an APT tip with a typical diameter of  $\sim 100$  nm (Figure 5.8 b) (113, 114).

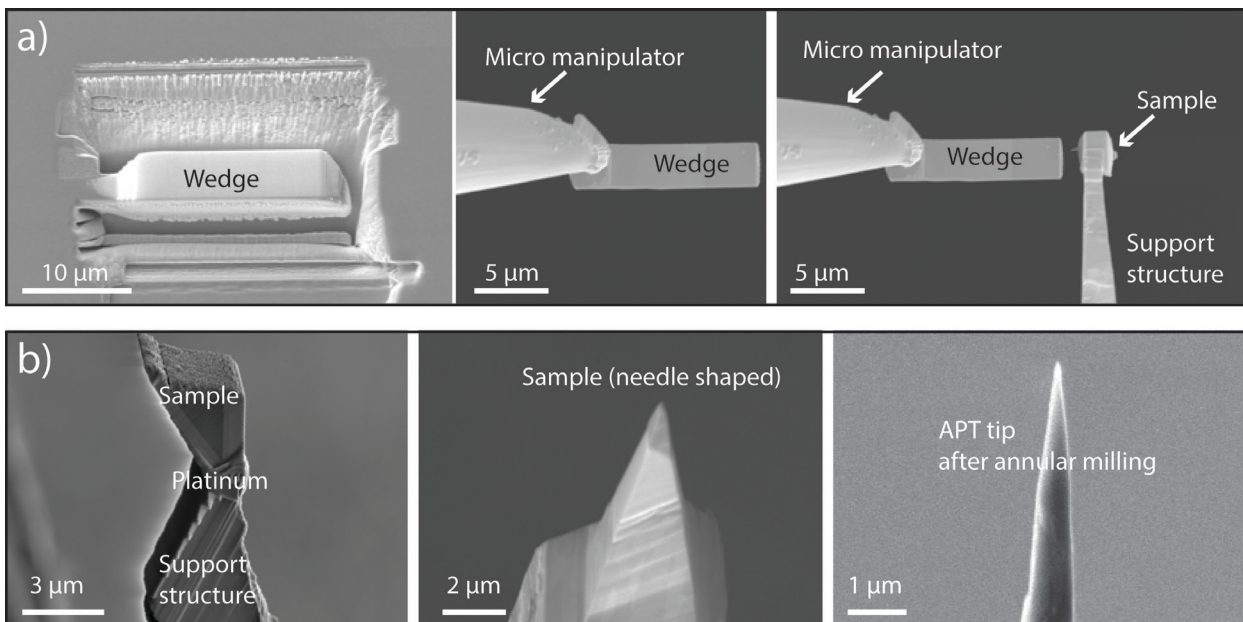


**Figure 5-8** Illustration of the steps involved with in-situ lift out. (Courtesy Limei Yang)

FIB techniques are now routinely used for APT sample preparation and thanks to improved instrumentation and methods, the quality and consistency of specimens prepared by FIB are very high. There are many advantages in using FIB and one of them is imaging the sample during and after preparation. For example, transmission Kikuchi diffraction (TKD) is one recent technique that can be used to map the crystalline orientation of an APT tip during its preparation.

---

## 5.2 Introduction to transmission Kikuchi diffraction

Transmission Kikuchi diffraction (TKD), also known as transmission electron backscattered diffraction (t-EBSD) was introduced by Keller and Geiss a few years ago (115). The basic principles of electron backscattered diffraction (EBSD) are applicable to TKD. In the next section EBSD principle will be briefly introduced and an overview of TKD will be provided.

### 5.2.1 Overview of EBSD and TKD

The type of diffraction on which EBSD is based was discovered by Nishikawa and Kikuchi in 1928 when the first backscattered Kikuchi pattern was observed on calcite (116). In this study, the same Kikuchi pattern appears on a phosphor screen placed behind the sample (transmission) and on a screen in front of the sample (backscattered). Most of the early work on Kikuchi patterns were done using transmission electron microscopes. The first use of an SEM for “EBSD” was not until 1973 (117). The development of EBSD as a useful technique started in the late 1980s and early 1990s when computer aided indexing was developed – since then it has continually improved and EBSD has become a technique of choice for the characterization of the crystallographic structure of materials. EBSD gives access to the grain size, grain orientation, grain boundary character, phase identity and texture of a material (118).

When a beam of electron interacts with the surface of a flat-polished sample some backscattered electrons are reflected out of the sample by elastic scattering of previously inelastically scattered electrons. Some of these electrons can exit near the Bragg condition and as a result diffract to form Kikuchi bands that are directly related to the crystal lattice with which the primary electrons interacted. An EBSD detector, which is typically a phosphor screen equipped with a low light CCD camera detects some of these backscattered electrons thanks to the fluorescence caused by the interaction of the electrons and the phosphor screen (Figure 5.9 a). The Kikuchi bands can be indexed by comparing the angles between Kikuchi bands with a look up table of calculated lattice planes in the relevant materials structure(s), as long as the material structure and geometry is known. With accurate band indexation, the precise crystal orientation of a material can be revealed (Figure 5.9 b).

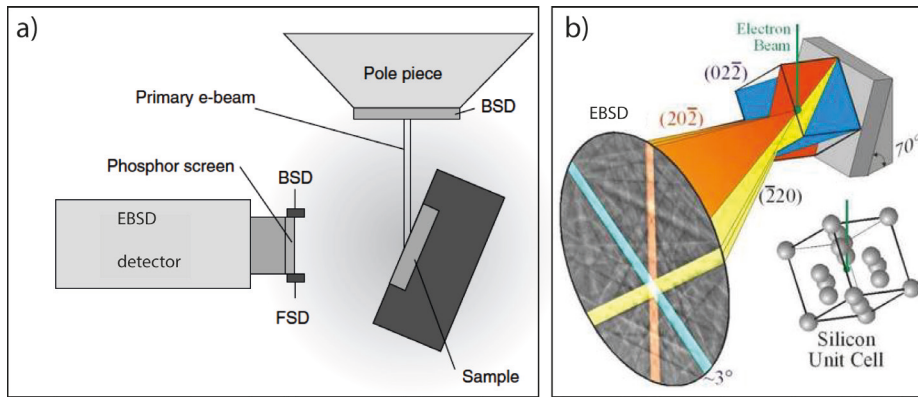


**Figure 5-9** EBSD typical configuration in a SEM and EBSD principle. (Adapted from (118))

The spatial resolution of EBSD is a function of the atomic number of the element and the accelerating voltage of the incident electron beam. An optimum spatial resolution of 30 nm was measured for Cu using a low acceleration voltage (119-121).

The experimental configuration for TKD is almost the same as for EBSD with the main difference being that it requires an electron transparent specimen in a suitable holder, and the EBSD detector is positioned below the sample. The sample is usually positioned in a horizontal position in the microscope with a relatively short distance between the sample and the phosphor screen in order to fill most of the detector (Figure 5.10). Due to the reduced interaction volume, spatial resolution of TKD is much better than EBSD. It has been shown to be in the range of 2-10 nm for a range of materials (122).

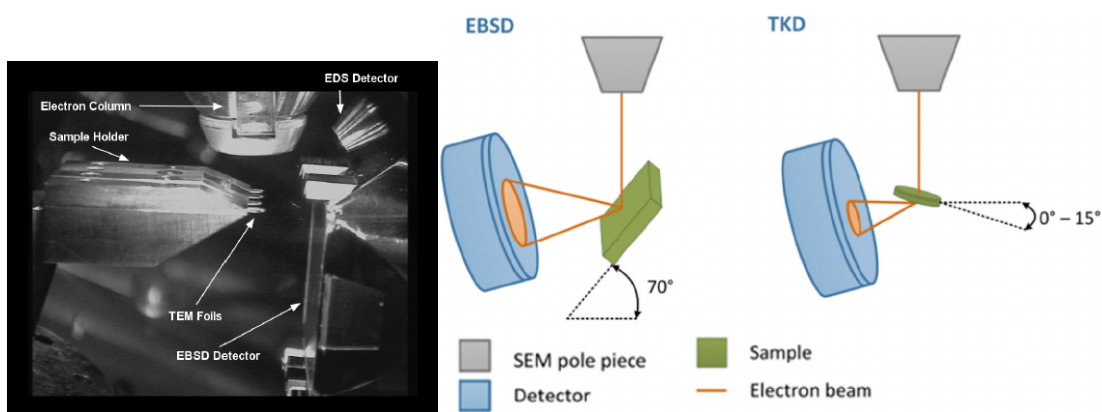


**Figure 5-10** Image of a typical TKD configuration and schematic comparing EBSD and TKD (121, 123)

In order to maximize the penetration of incident electrons and consequently improve the Kikuchi patterns, a high accelerating voltage (typically 30 kV) is usually used. It is however possible to use lower accelerating voltage (down to ~10 kV) with very thin samples to improve the diffracted signal for low

---

atomic numbers (*122, 124, 125*). High resolution TKD with step sizes below  $\sim 5$  nm requires long acquisition times which can lead to the sample contamination and drift. This can be minimized by leaving the sample in the chamber for a few hours, allowing for a better vacuum and stage stabilization.

The sample thickness should be taken into consideration for pattern quality and resolution. High quality patterns are usually obtained for sample thicknesses of  $\sim 100$  to  $200$  nm. However, if the grain size is very small pattern overlap can be an issue and thinner samples should be used. The lower the atomic number, the thicker the sample can be. For example, acceptable diffraction patterns have been obtained for aluminium with a  $3 \mu\text{m}$  thick sample (*122, 126*). However, the spatial resolution will also degrade with a thick sample due to beam broadening. Figure 5.11 illustrates well the degradation of pattern quality with increasing sample thickness. The three diffraction patterns, collected (Figure 5.11 b-d) from three increasingly thick areas of the sample (Figure 5.11 a), show a clear degradation in quality. A very thin sample will minimize beam broadening allowing the resolution to be governed by the incident electron probe size (*125*).

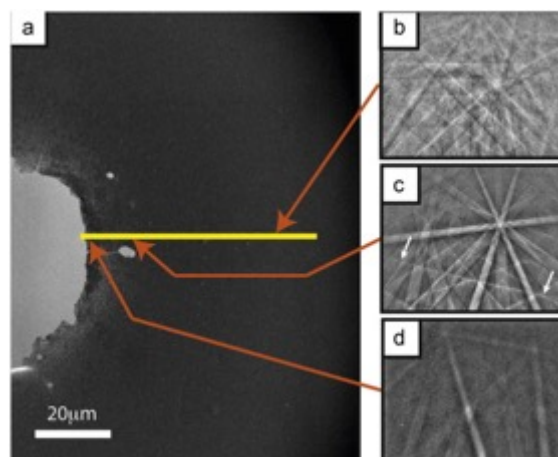


**Figure 5-11** “Pattern quality vs sample thickness (a) Secondary electron (SE) image of the central perforation in an Al-6060 TEM foil. The yellow line marks a transect along which diffraction patterns were stored and analysed. (b) – (d) Example diffraction patterns collected at 22 kV using SEM-TKD from the transect shown in (a).” (*122*)

The results obtained from a typical TKD experiment are usually in the form of different maps: phase map, orientation map, pattern quality map (band contrast), inverse pole figure map and so on. The EBSD detector can also be equipped with up to six foreshattered detectors (*127*). The diodes are fixed around the phosphor screen. For TKD, the lower diodes collect dark field images, as on a TEM. By inverting one diode’s signal and mixing with the other diode’s (normal) signal, the channeling (orientation) contrast can be maximized. The combination of those signals is particularly useful to image thickness, density and/or

---

orientation contrasts of the sample. (121) An example of a forescatter image, band contrast and orientation map from the same region in an Al-alloy sample is shown in figure 5.12.

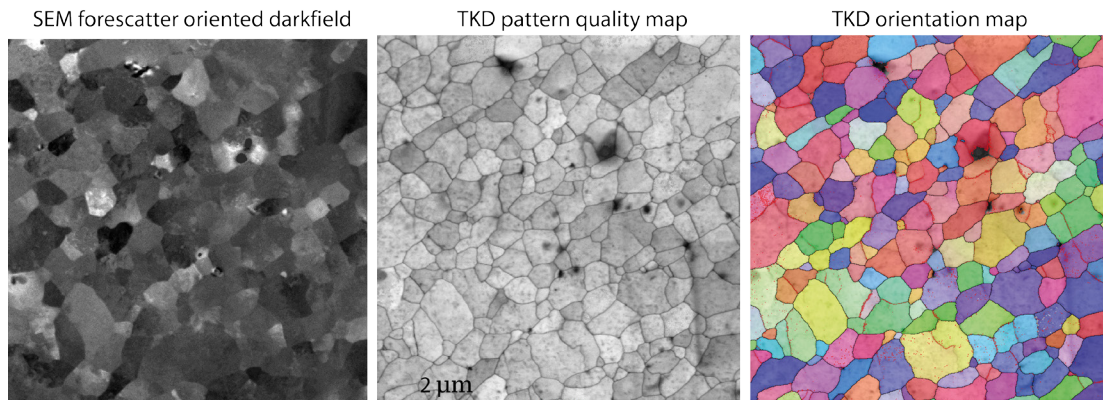


**Figure 5-12** TKD data from a high pressure torsion deformed Al-6060 alloy sample. (Courtesy P. Trimby)

### 5.2.2 Complementarity with other techniques

In a typical EBSD/TKD experimental set-up, the presence of an X-ray energy dispersive spectrometer detector enables the use of energy dispersive spectroscopy (EDS) simultaneously with TKD acquisition. The correlation between the structure and the chemistry of the sample is thus possible. For example, useful insights can be gained into grain boundary segregation or phase transformations induced by elemental partitioning.

Transmission electron microscopy (TEM) and TKD can be performed on the same sample and bring complementary information. TKD is a simpler way of mapping the overall crystallographic structure of a material if high resolution is not required. Different TEM imaging modes such as dark field imaging can be used to image the sample at a higher resolution and reveal features unseen with TKD.

APT sample preparation in a FIB can be a difficult process when small features of interest such as a grain boundary or dislocations need to be within  $\sim 100$  nm of the tip apex. Recently TKD was performed simultaneously with APT sample preparation to locate and position a grain boundary within the APT tip. (128-130) The use of TKD during APT sample preparation in the same instrument not only facilitates site specific APT sample preparation but also allows the crystallographic characterization of features such as grain boundaries, dislocations or phases in an APT tip before its field evaporation. The 3d volume, once

reconstructed, adds to the TKD information an atomic scale 3-dimensional chemical characterization of the tip. A typical set-up is shown in figure 5.13.

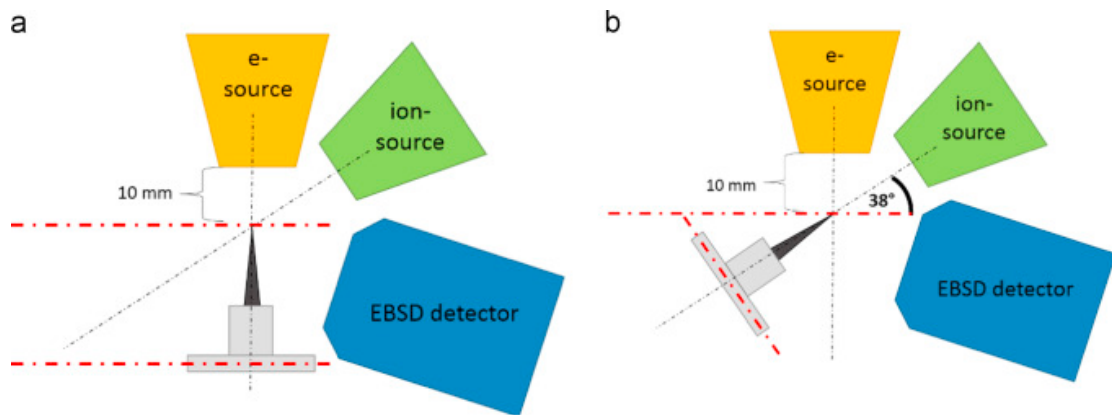


**Figure 5-13** “(a) Schematic set-up in the microscope chamber at a tilt angle of  $0^\circ$ . The ion source (57) is located in an angle of  $52^\circ$  to the electron source. The beams have their intersection point at a working distance of 10 mm; (b) schematic set-up in the microscope chamber at a tilt angle of  $52^\circ$ .” (128, 131)

## 6 Characterization of high resistivity materials using atom probe tomography

In the following sections, we give an overview of laser assisted field evaporation in APT and we review the state of the art of laser-assisted APT applied to high resistivity materials with a focus on the minerals studied in this PhD thesis.

### 6.1 Laser-assisted atom probe tomography

#### 6.1.1 Overview

As described in the APT section of this thesis, the evaporation of the surface atoms of an APT tip relies on field-ionization triggered by a pulse, either voltage or laser, while a DC voltage is applied to the sample. Modern LEAP<sup>®</sup> instruments can now be equipped with UV lasers (355 nm wavelength) and generate ultra-fast pulses (picoseconds) focused on the tip of the sample (16). The use of laser pulses in place of high-voltage pulses to field-ionized surface atoms has opened up the range of materials that can be analyzed by APT. It is now possible to investigate large band gap materials such as mineral oxides or even bio-minerals.

The laser-assisted field ionization mechanism has been the subject of much debate and is still not fully understood. However, thermally-assisted evaporation is now considered by most to be the main mechanism (16, 78, 132, 133). Thermal energy in the form of local temperature spikes is brought to the tip by laser pulsing. The increased temperature has the effect of decreasing the required ionization field (figure 6.1). The combination of DC voltage and local temperature rises allows field ionization of the surface atoms of a tip (16, 82, 83, 133-135).

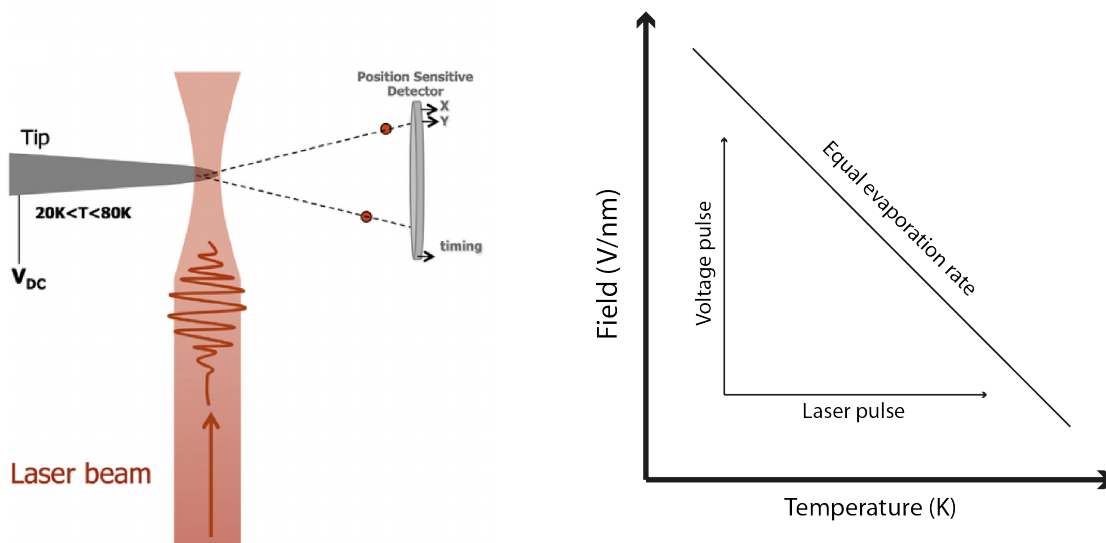


**Figure 6-1** Schematic of laser-assisted APT and the two mechanism (voltage and laser) used for field evaporation of an atom at the tip. (132, 136)

In a modern LEAP<sup>®</sup> equipped with a UV-laser, the spot size of the laser beam is typically  $< 5 \mu\text{m}$  (137). The diffraction effects result in the confinement of the absorption at the apex of the tip, limiting the absorption area of about the wavelength of the laser, which is much smaller than the beam size. The corresponding small heating zone allows for fast heat diffusion in the apex of the tip inducing both fast thermally assisted field ionization and rapid cooling of the tip (132).

The local spike in temperature reached by the tip during laser illumination is typically above  $\sim 200 \text{ K}$  and depends on the laser pulse energy and the material properties. (78) Because of the inhomogeneity in laser absorption by the tip, the side of the tip facing the laser beam becomes hotter much faster than the other side, and can cause preferential evaporation (132, 138) (Figure 6.2).



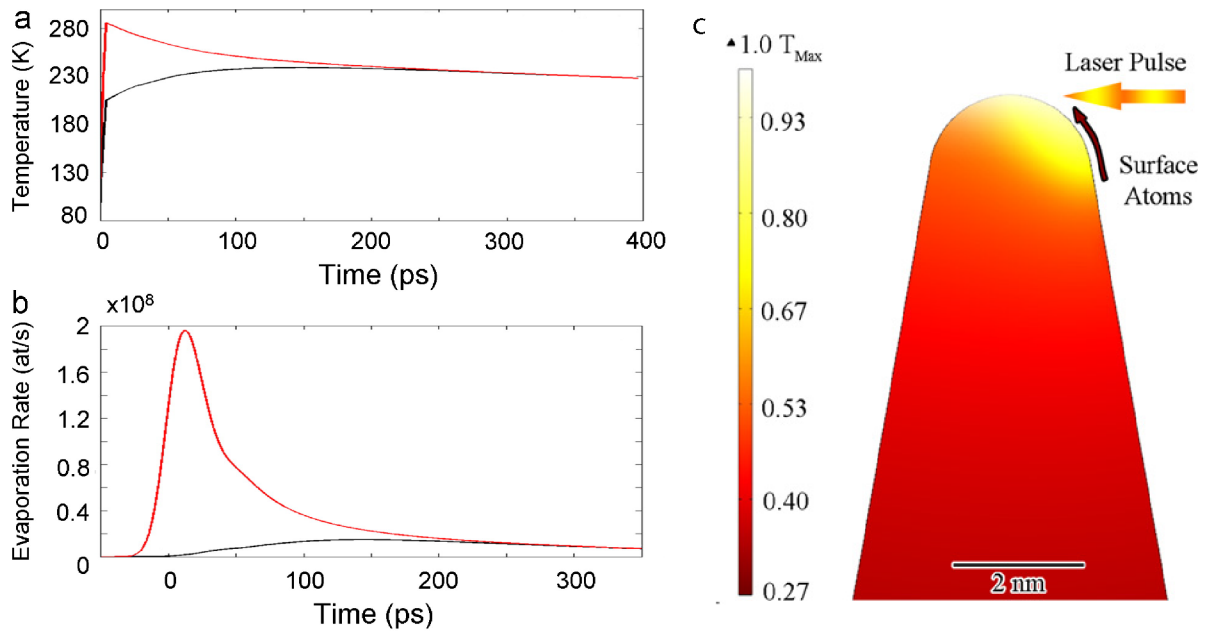


**Figure 6-2** “(a) Temperature evolution (model response) and (b) evaporation rate of a steel tip after the interaction with the laser pulse (red line: the illuminated side of the tip; black line: the opposite side)” (132) (c) “Finite element model of an atom probe specimen showing the temperature distribution due to the laser heating from one side” (136).

### 6.1.2 Common challenges inherent to the APT characterization of high-resistivity materials

The overall data quality is highly dependent on the specimen’s ability to quickly diffuse the heat out. The material thermal conductivity, the sample geometry and the APT acquisition parameters all play an important role (136).

In an insulator (high resistivity material), the thermal conductivity is governed by phonon-phonon interactions. At high temperature, the thermal conductivity of most insulators will decrease due to phonon-phonon scattering (139). For example, the thermal conductivity of pure Si peaks at around 40 K and then decreases quite abruptly at higher temperature (140) (figure 6.3).

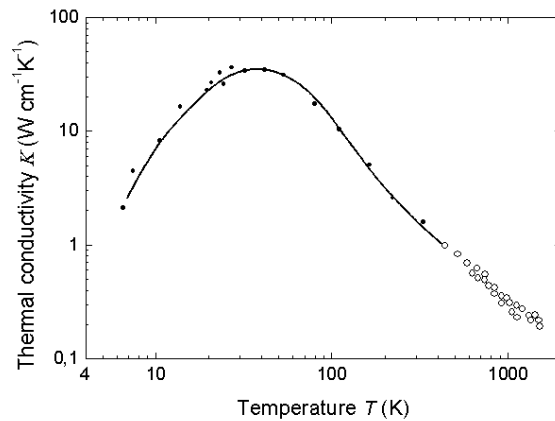


**Figure 6-3** Temperature dependence of thermal conductivity for high purity Si. (140)

The heat after laser illumination of a high resistivity material will diffuse slowly and the sample will stay at high temperature for some time ( $\sim 150$  ps) (136). Consequently, the period during which evaporation of surface atoms may occur will last longer, which in turn impacts the data quality (peak broadening, thermal tail, delayed or DC evaporation and so on).

The specimen geometry also plays a role in how quickly the heat diffuses out. It has been shown that a larger tip radius improves the mass resolution, leads to less ionic clustering and increases the fraction of single event detection (97).

The laser pulse energy intensity is the main factor responsible for the temperature reached at the apex of the sample and plays an important role in determining the mass resolution and the size of the thermal tail. Typically, the lower the energy, the better the mass resolution but the higher the background counts (135). The field applied to the tip is relatively higher with lower laser pulse energy. As a result, ionic clusters that typically evaporate in the case of high resistivity materials are more easily dissociated, which increases the proportion of multiple hits detected (2, 141).

The stoichiometry of high resistivity materials has been shown to be greatly influenced by the laser pulse energy. Preferential evaporation, peak broadening and ionic cluster dissociations all play a role in the measured stoichiometry of the material. This is especially a problem for oxides where a loss of oxygen or particularly wrong stoichiometry was documented in several studies (142-146).

---

‘Minerals’ is such a large class of material that the range of properties (such as mechanical, thermal and chemical) involved is large. From one mineral to another, their suitability for laser-assisted APT and the optimum acquisition parameters need to be separately assessed.

## **6.2 Laser-assisted APT of high-resistivity materials**

### 6.2.1 State of the art

The first analysis of a bulk high-resistivity material by APT was done in 1982 on insulating glass with a UV laser APT (147). In this study, a chromium layer was used to coat the sample in order to facilitate the heat absorption (and diffusion). However, a large number of molecular chromium oxides ions were reported due to the thick chromium coating. It was only later that ultra-fast laser pulsing allowed the evaporation of high-resistivity materials without a coating.

The first successful analyses of high-resistivity materials by APT were done on thin films of oxides. In 2004, the analysis by voltage APT of an alumina oxide tunnel barrier between iron-nickel electrodes was reported (148). Other studies reported the analysis of thin layers of HfO<sub>2</sub> and MgO by laser-assisted APT (149, 150). In 2006, an iron oxide scale grown on a pure iron sample was analyzed by femtosecond laser-assisted APT (151). In 2009, the first laser-assisted APT study of a bulk oxide, zirconia, was reported (152). The last decade saw an increase of APT studies of high resistivity materials such as aluminium oxide (153), cerium oxide (154), zirconium oxide (155), zinc oxide (156) or iron oxides (142, 145). The more frequent successful APT analyses of large band gap materials in the last decade is primarily due to major progress in sample preparation techniques using FIB (108-110, 114, 157-159), the development of commercial laser-assisted APT instrumentation, for instance the use of the new UV-laser in the LEAP<sup>®</sup>, and also a better understanding of the laser-assisted field evaporation. As a result, laser-assisted APT is now starting to be used across a wider range of disciplines, including biology and geosciences.

### 6.2.2 Laser-assisted APT of the selected minerals: a review

A limited number of APT studies of corrosion of metals and alloys have been carried out in the past decade. APT has been used to characterize stress corrosion cracking and intergranular attacks in Ni-based alloys (160-164), oxidation of stainless steels (165, 166) and stress corrosion cracking in stainless steels (157, 167-169). Chromia (170) and alumina (171) scales, which protect stainless steel from further

oxidation have also been studied. However, the intergranular oxides formed during intergranular corrosion of high temperature austenitic stainless steels have never been analyzed by APT.

It is only very recently that the first APT study of the accessory mineral zircon was reported (46, 172). Using laser-assisted APT, the age of the oldest zircon on Earth was confirmed to be  $\sim 4.4$  Gyr. Nano-sized clusters enriched in Pb and other incompatible elements were revealed (figure 6.4).

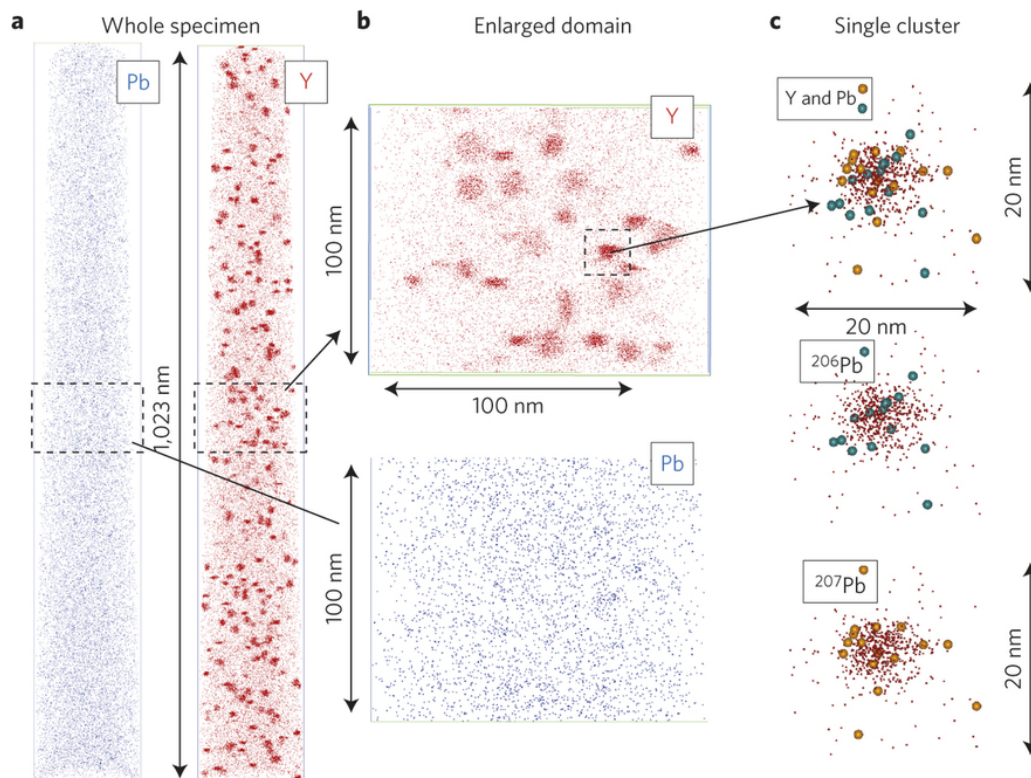


**Figure 6-4** “The clusters of co-localized Y and Pb in Hadean zircon a) Projections of Y and Pb from the same 1,000-nm-long segment. The tip of the specimen points upwards. b) Enlarged view of 100 nm segment of specimen 2. c) Individual Y and Pb atoms for one cluster: small red dots, Y; green dots,  $^{206}\text{Pb}$ ; and yellow dots,  $^{207}\text{Pb}$ . The volume shown in c measures  $20 \times 20$  nm in the plane of the image by 10 nm deep.” (46)

This study demonstrated that the Pb-rich clusters do not lead to age biasing. However, and as described in the zircon section, there is a need for atomic scale analysis of elemental diffusion induced by *deformation* in zircon. There was no laser-APT study of such processes in zircon available prior to this project.

The first APT characterization of bio-minerals was done on chiton tooth in 2011 (173). In 2012, the same group analyzed apatite and bone-type mineralized tissues (174). Laser-assisted APT was also used to analyze a bone-implant interface in 2014 (175). Finally, in 2015 the first atomic scale study of rodent

tooth enamel was published revealing intergranular amorphous phase in rodent tooth enamel (figure 6.5) (77, 176). The discovery of an amorphous intergranular phase in rodent tooth enamel has some major implications in our understanding of demineralization processes. The presence of such intergranular phase in human dental enamel has not been yet investigated.

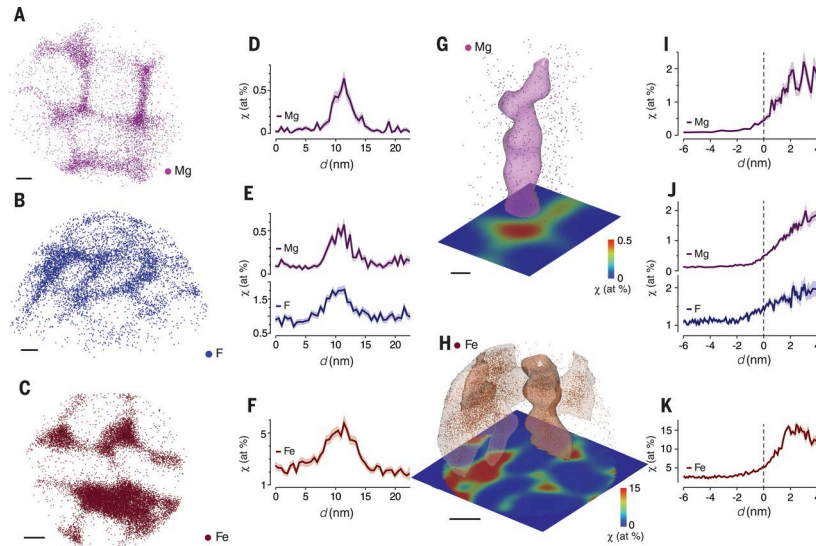


**Figure 6-5** “(A) Mg ( $^{24}\text{Mg}^{2+}$ ) ion positions in mouse outer enamel. (B) F ( $^{40}\text{Ca}^{19}\text{F}^+$ ) ion positions in fluoride-treated mouse inner enamel. (C) Fe ( $^{56}\text{Fe}^{2+}$ ) ions in pigmented rat enamel. Scale bars, 10 nm. The view direction is parallel to the long axis of the nanowires. (D to F) Representative concentration profiles across grain boundaries. (G) Isosurface (0.5 atomic %) surrounding Mg-rich multiple grain boundary in (A). (H) Isosurfaces (5 atomic %) enveloping Fe-rich multiple grain boundary in (C). Scale bars in (G) and (H), 5 nm. (I to K) Representative proxigrams of multiple grain boundaries in (I) mouse outer enamel, (J) fluoride-treated outer mouse enamel, and (K) pigmented rat enamel.” (77)

---

## 7 Aims and scope of this thesis

As described, important characteristics of minerals originate from atomic scale processes and structures. Accessing chemical and physical information at this scale necessitates the use of advanced microscopy techniques such as EBSD, TEM, TKD and APT. The three minerals selected in this PhD thesis were chosen for their scientific, industrial and biological significance. Moreover, atomic scale characterization of minerals using TKD and APT is at its infancy and many challenges remain to be addressed. In the previous chapter, several gaps in the literature were identified for each selected mineral both in terms of material's properties significance and advanced microscopy techniques applied to those minerals.

The scope of this thesis is to develop the necessary skills and methods for the successful atomic scale characterization of minerals using advanced microscopy techniques and apply them to these important scientific problems.

There is a need for a better understanding of microscopic and atomic scale processes that are involved in intergranular corrosion of austenitic stainless steel during high temperature thermal cycling. Particular attention is given to the composition of the oxide minerals formed within the intergranular corrosion areas and an associated martensitic phase transformation. This is addressed in chapter 8, 9 and 10.

One of the principal properties of zircon is its robustness in terms of U-Pb dating and the assumption that it stays a closed system throughout its entire life. However, several studies revealed anomalies in the dating of deformed zircons with the loss of Pb, and suggested that a deformation-induced diffusion mechanism via dislocations and low-angle boundary could be responsible. The high chemical sensitivity and atomic spatial resolution of APT is ideally suited for such investigation. The use of laser-assisted APT combined with EBSD and TKD for the specific study of deformation in zircons was assessed and optimized in order to reveal key trace elements diffusion in deformed zircons. This is addressed in chapter 11 and 12.

Human dental enamel is the essential tissue protecting the tooth from daily chemical and mechanical attacks. However, it can easily decay and be destroyed as a result. The incredible properties of human tooth enamel come from its hierarchical level of organization from nano to micron scale. Heterogeneities in the distribution of magnesium ions and residual organic materials at the atomic scale were recently

---

revealed in rodent tooth. These recent findings have major implications on our understanding of enamel properties and tooth decay. However, human tooth enamel has never been investigated in this way. Laser-assisted APT was used to investigate the atomic scale structure and chemistry of human dental enamel. This is described in chapter 13.

In summary the particular aims of this thesis are as follow:

- Develop new skills and improve existing microscopy methods for the nanoscale characterization of physical processes and the chemical identification of mineral oxides in intergranular corrosion of austenitic stainless steels (chapter 8, 9 and 10)
- Optimize the use of laser-assisted APT combined with EBSD and TKD for the analysis of deformed mineral zircon (chapter 11)
- Apply laser-assisted APT, EBSD and TKD techniques to reveal an important diffusion mechanism in deformed mineral zircons (chapter 12)
- Use laser-assisted APT to characterize for the first time the atomic structure and chemistry of human dental enamel (chapter 13)

---

## PART B Results



---

## **8 New insights on intergranular corrosion of austenitic stainless steel: an oxidation-induced phase transformation**

This publication contributes to the present thesis by using a combination of advanced microscopy techniques to reveal a new and important failure mechanism of an austenitic stainless steel exposed to oxidation during high temperature thermal cycling. A combination of TKD, EBSD and TEM is used to characterize the oxide minerals and the adjacent steel within an intergranular corrosion area. This investigation revealed a displacive martensitic phase transformation occurring in oxidation-induced chromium-depleted zone that is thought to play a major role in the rate at which intergranular corrosion take place. The austenitic stainless steel that was investigated in this work is a key material for the successful development of new generation concentrated solar power, a growing large scale power generation technology. This chapter is the initial part of the investigation of the intergranular corrosion area of the 253MA austenitic stainless steel used in concentrated solar power.

In this publication, the recently developed TKD technique, together with conventional TEM, is applied for the first time to oxide minerals allowing the discovery of an oxidation-induced martensitic phase transformation.

The content of this published letter is largely the product of the work of Alexandre La Fontaine under the supervision of Julie M. Cairney, Simon P. Ringer and Sarah Miller. Hung-Wei Yen revised the manuscript, contributed to the theoretical background of this letter and contributed to the experimental work. Patrick Trimby carried out the EBSD and TKD experiments together with Alexandre La Fontaine and Hung-Wei Yen. He has also significantly contributed to the interpretation of results. Steven Moody assisted in the sample preparation. Martin Chensee provided the material for this investigation.

This letter has been published in *Corrosion Science*, Volume 85, Pages 1-6 (2014)

DOI: 10.1016/j.corsci.2014.04.



Contents lists available at ScienceDirect

## Corrosion Science

journal homepage: [www.elsevier.com/locate/corsci](http://www.elsevier.com/locate/corsci)

## Letter

## Martensitic transformation in an intergranular corrosion area of austenitic stainless steel during thermal cycling



Alexandre La Fontaine<sup>a,b,\*</sup>, Hung-Wei Yen<sup>a,b</sup>, Patrick Trimby<sup>b</sup>, Steven Moody<sup>b</sup>, Sarah Miller<sup>c</sup>, Martin Chensee<sup>c</sup>, Simon Ringer<sup>a,b</sup>, Julie Cairney<sup>a,b</sup>

<sup>a</sup> School of Aerospace, Mechanical, Mechatronic Engineering, The University of Sydney, NSW 2006, Australia

<sup>b</sup> Australian Centre for Microscopy and Microanalysis, The University of Sydney, NSW 2006, Australia

<sup>c</sup> CSIRO Energy Centre, Newcastle, NSW 2304, Australia

## ARTICLE INFO

## Article history:

Received 10 April 2014

Accepted 28 April 2014

Available online 6 May 2014

## Keywords:

A. Stainless steel

B. SEM

B. TEM

B. Thermal cycling

C. Intergranular corrosion

C. High temperature corrosion

## ABSTRACT

An oxidation-assisted martensitic phase transformation was observed in an austenitic stainless steel after thermal cycling up to 970 °C in air in a solar thermal steam reformer. The intergranular corrosion areas were investigated by electron backscatter diffraction (EBSD), transmission Kikuchi diffraction (TKD) and transmission electron microscopy (TEM). The structural-and-chemical maps revealed that within intergranular corrosion areas this martensitic transformation primarily occurs in oxidation-induced chromium-depleted zones, rather than due to only sensitization. This displacive transformation may also play a significant role in the rate at which intergranular corrosion takes place.

© 2014 Elsevier Ltd. All rights reserved.

## 1. Introduction

For high temperature applications, such as in new-generation energy technologies, austenitic stainless steels offer an attractive combination of economy and mechanical/corrosion properties. For example, concentrated solar power (CSP) is a growing renewable energy technology, but its effective use requires cost-effective and corrosion resistant materials for tubing and piping that can operate for extended periods at high temperatures and withstand thermal cycling between around 900 °C in the day and room temperature at night [1]. Like many energy technologies, this application demands affordable alloys characterized by high strength and superior high temperature corrosion resistance. Due to the high cost of Ni-based alloys, austenitic stainless steels (ASSs) are presently the most suitable materials.

However, a major concern affecting the deployment of ASSs in these applications is the well-established fact that they are susceptible to sensitization [2,3]. Sensitization is a phenomenon where intergranular corrosion (IGC) occurs when chromium–nickel (Cr–Ni) ASSs are heated to temperatures between 500 and 800 °C [2]. This kind of IGC usually results from the formation of Cr-rich

M<sub>23</sub>C<sub>6</sub> carbides at the grain boundaries (GBs) leading to a Cr-depleted zone that is vulnerable to corrosion. Although this phenomenon has been well known for many years, new microscopy methods are still providing insight into the complex process via which it occurs [4].

Some studies have reported the formation of martensite in the sensitization-induced Cr-depleted zone [5–8]. The primary cause is an increase in the martensitic transformation start (*M<sub>s</sub>*) temperature due to the depletion of Cr [7,8]. However, little attention has been paid to phase transformation that occurs in the IGC area. Especially, martensite and ferrite may play important roles in the IGC area and hence in the failure mechanism of ASSs at high temperature or during thermal cycling [5–8]. This study investigates the mechanism behind this phase transformation within IGC areas in the ASS during thermal cycling.

## 2. Experimental procedures

The component investigated is the reactor tube of a solar steam reformer made from Sandvik 253 MA. Sandvik 253 MA ASS is a Fe–0.08C–21Cr–10.8Ni–1.64Si–0.58Mn–0.02P–0.44Cu–0.19Mo–0.06V–0.01Ti–0.17N–0.05Ce/La (in wt.%) alloy and it has good high-temperature corrosion resistance and can operate up to 1150 °C [9]. The seamless steel tubes were manufactured by Sandvik with a tube thickness of 3.5 mm and a nominal diameter

\* Corresponding author at: School of Aerospace, Mechanical, Mechatronic Engineering, The University of Sydney, NSW 2006, Australia.

E-mail address: [alex.lafontaine@sydney.edu.au](mailto:alex.lafontaine@sydney.edu.au) (A. La Fontaine).

of 1 inch (2.54 cm). They were used as the outer tube material of a 20 kW prototype solar steam reformer from the CSIRO Energy Centre in Newcastle, Australia. These outer tubes were directly exposed to sun in air with no mechanical stresses. During 100 h service (four day-and-night cycles), the specimen was subjected to thermal cycles between room temperature (without sun exposure) and up to 970 °C (with sun exposure). Each cycle starts from room temperature, ramps up to ~970 °C in about 10 min, stays between 700 °C and 970 °C for around 10 h (sun exposure), slowly cools down in air, and stays at room temperature overnight.

Cross-sectional specimens were sampled from the tube outer surface and cut to a size of approximately 10 mm by 5 mm. Specimens for electron backscatter diffraction (EBSD) mapping were ground with SiC abrasive paper and mechanically polished with a 9 µm diamond suspension for 10 min, a 3 µm diamond suspension for 20 min and finally a 0.05 µm silica suspension for 6 min.

The intergranular corrosion areas were also analysed by transmission Kikuchi diffraction (TKD), a relatively new microscopy technique where an electron transparent specimen is examined in scanning transmission mode in a scanning electron microscope (SEM), dramatically improving the spatial resolution of orientation maps compared to EBSD [10,11]. For TKD, electron transparent specimens for mapping were prepared from the previous SEM-EBSD bulk specimen using a Zeiss-Auriga focused ion beam (FIB) equipped with a Kleindiek micromanipulator system. SEM measurements were performed on a Zeiss Ultra SEM equipped with a Schottky field-emission source with high-current mode capability for extended depth of field and EBSD. Both EBSD and TKD mapping was performed with a Nordlys-NANO EBSD detector. Energy Dispersive X-ray Spectroscopy (EDS) maps were collected using an X-Max 20 mm<sup>2</sup> silicon drift EDS detector. EBSD, TKD and EDS maps were collected and processed using Oxford Instruments Aztec-integrated EBSD/EDS software. TEM bright field imaging and diffraction was also performed on one of the thin samples before and after TKD measurements using a CM12.

### 3. Results and discussion

#### 3.1. Microstructure of intergranular corrosion

A cross section of the tube after 100 h service is shown in Fig. 1a. Extensive intergranular corrosion is present, with several large IGC cracks starting from the outer surface and penetrating beneath the surface by about 1.3 mm, which is almost half the thickness of the tube. Because all of the tubes used were seamless there was little internal stress and there are no welding defects. Hence, the failure of the material is expected to be the result of oxidation, thermal stress, and other phase transformations during the thermal cycling. Fig. 1b shows an EBSD pattern quality map (also known as an Image Quality (IQ) map) of an IGC area. The grey-contrast matrix is austenite (a face-cubic centered (fcc) crystal) and there are extensive chromite-type oxide layers (Fe<sub>x</sub>Cr<sub>1-x</sub>)<sub>3</sub>O<sub>4</sub>, (where  $x \approx 2/3$ ) along the cracks and grain boundaries, which can be seen from the corresponding EDS maps from the Cr–K line and the O–K line [12]. Besides the spinel chromium oxides, thin layers of a body-centered cubic (bcc) phase, highlighted in red in Fig. 1b, were found along the grain boundaries as well as within the corrosion layers. These layers of bcc phase have low Cr contents as marked with arrows in Cr–K line map. In previous studies, the formation of bcc phase along the grain boundary in stainless steels is attributed to a martensitic transformation in a Cr-depleted zone due to sensitization [5–8]. However, as shown in Fig. 1b, the layers of bcc phases are not significantly present in the austenite matrix, but only around the IGC areas. The depletion of Cr can be explained by Cr diffusion towards the carbides along the grain boundaries due to sensitiza-

tion and by Cr diffusion towards the oxides due to oxidation. The fact that bcc layers are extensively observed only around the IGC areas as shown in Fig. 1b implies a possible oxidation-assisted process for the formation of these bcc phases.

#### 3.2. Martensite transformation induced by oxidation

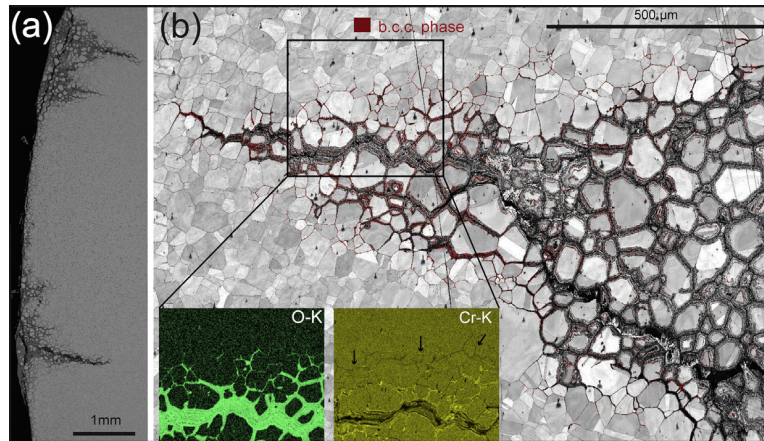
Fig. 2 shows results from an EBSD–EDS analysis along a section of one single IGC crack at higher magnification. The boundaries highlighted in white in Fig. 2b indicate the bcc/fcc interfaces that correspond to the Kurdjumov and Sachs (K–S) orientation relationship (OR):  $[1\ 1\ \bar{1}]_{\alpha} \parallel [1\ 0\ \bar{1}]_{\gamma}$ , and  $(0\ 1\ 1)_{\alpha} \parallel (1\ 1\ 1)_{\gamma}$  [13]. Most of the bcc/fcc interfaces were within 5° of the K–S OR, as shown by the white boundaries in many of the figures of this paper. This relationship originates from the crystallographic nature of the fcc-to-bcc transformation [14,15] and it can occur for both diffusional ferritic and diffusional martensitic transformations. Fig. 2b reveals a thick bcc layer formed between two chromite layers, and two thin bcc layers between the oxides and the austenite. EDS results (Fig. 2c) reveal that the bcc phase occurs in regions that are depleted in Cr. Although austenite and chromite were separated by the bcc phase, the  $\{100\}$  pole figures reveal that they actually hold the cube-on-cube OR:  $[100]_{\text{Chromite}} \parallel [100]_{\gamma}$ , and  $(001)_{\text{Chromite}} \parallel (001)_{\gamma}$  [16] (see Fig. 2d). It is therefore concluded that the formation of chromite along the grain boundary during high-temperature oxidation leads to the Cr-depleted zone. The Cr-depleted zone of the IGC crack is then able to transform into the bcc structure after cooling.

Table 1 shows the average measured composition (by EDS) of Fe, Cr, Ni, Si and O in the fcc, bcc, and chromite phases. The equilibrium phase ratio as functions of temperature were computed by Thermo-Calc software using a TCFE7 database [17,18] for the Cr-depleted bcc zone martensite as shown in Fig. 3. The computation shows that austenite is completely stable in the temperature range between 700 °C and 970 °C. Diffusional ferrite transformation can only occur during cooling but the kinetics of diffusional ferrite transformation can also be suppressed by the high nickel and high nitrogen content [19,20].

Images from higher resolution studies, conducted using TEM and SEM-TKD, of the fine structure of a Cr-depleted bcc zone surrounded by chromite and austenite are displayed in Fig. 4. The grains shown in Fig. 4a are mostly bcc crystals, as shown by the SEM-TKD analysis in Fig. 4b. Fig. 4c shows several bcc laths with a twinning relationship (grain boundaries highlighted in red). Hence, the bcc phase is believed to be lath martensite based on its microstructure [21,22] with the twin-related laths resulting from the self-accommodation by two K–S variants [23]. The two inset TEM images in Fig. 4a show the twinned martensitic laths by the alternating dark and bright contrast. The region with bcc crystals is again Cr-depleted (Fig. 4d) as compared to the austenite. The TEM observations confirm that most of these bcc grains are twinned martensite laths. The austenite in the Cr-depleted zone transformed to martensite when the temperature drops below the  $M_s$  temperature. The  $M_s$  temperature was estimated by the empirical formula derived by Steven and Haynes [24]:

$$M_s(^{\circ}\text{C}) = 561 - 474(w_{\text{C}}\%) - 33(w_{\text{Mn}}\%) - 17(w_{\text{Cr}}\%) - 17(w_{\text{Ni}}\%) - 21(w_{\text{Mo}}\%) \quad (1)$$

where  $w_i\%$  is the content of element  $i$  in martensite region. Based on Table 1, the  $M_s$  temperature for the austenite in a region far from the Cr-depleted zones is around –50 °C, but in the Cr-depleted zone the  $M_s$  temperature is around 265 °C. The martensitic transformation in Cr-depleted zones is therefore due to this increased  $M_s$  temperature. During each thermal cycle, more oxidation occurs, inducing more Cr-depleted zones and upon each pass of cooling,



**Fig. 1.** (a) Z-contrast back-scattered electron image of a cross section of the sample. (b) EBSD pattern quality map of the inter-granular corrosion (IGC) area with the bcc phase highlighted in red. EDS O–K map and Cr–K maps are inset. Note the extensive bcc phase layers in the IGC area and along oxidized and chromium-depleted grain boundaries (marked with arrows in Cr–K map inset). (For interpretation of the references to colour in this figure legend, the reader is referred to the web version of this article.)

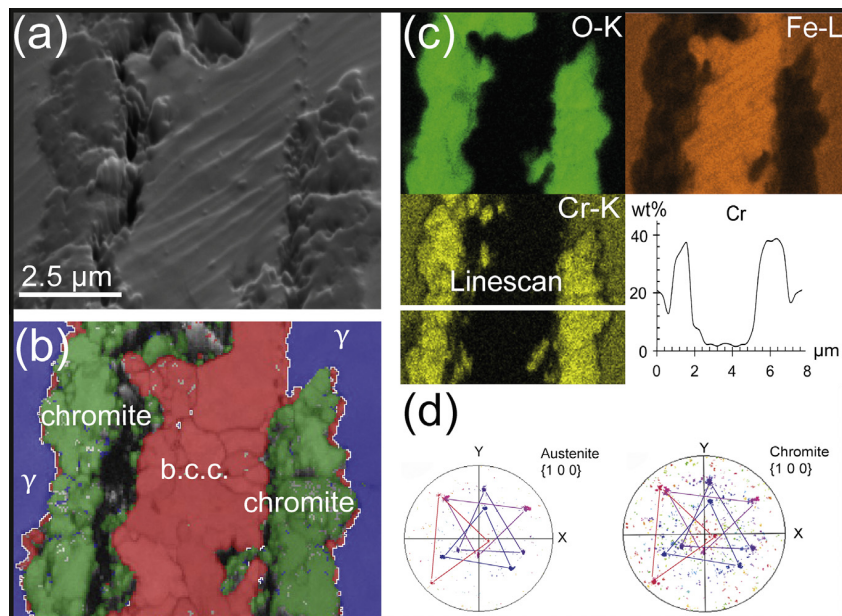


**Fig. 2.** (a) Secondary electron image showing a section of an IGC area. (b) The EBSD phase map shows a large bcc layer (red) between two chromite-type oxide layers (green) and two thinner bcc layers between the oxides and the austenite (blue). The fcc/bcc phase boundaries that correspond to the Kurdjumov and Sachs (K–S) orientation relationship are highlighted in white. (c) EDS elemental maps and Cr concentration profile across the IGC section showing the depletion of Cr in the bcc layers. (d) (100) Austenite pole figure and (100) chromite pole figure showing that they hold the cube-on-cube orientation relationship. (For interpretation of the references to colour in this figure legend, the reader is referred to the web version of this article.)

**Table 1**  
The composition of partitioning elements in austenite, bcc and chromite (in wt.%).

Phase	Fe	Cr	Ni	Si	O
Austenite	57	20.3	12	1.6	0
bcc	78	2.5	11	0.1	1
Chromite	23	36	1	1.8	26

the temperature drops below 265 °C and the martensite layers form.

### 3.3. Role of sensitization

The occurrence of martensitic transformation along the sensitized grain boundaries was also observed in the current study.

However, when it occurs, the martensite layer is usually extremely thin and discontinuous as shown in Fig. 5.  $\text{Cr}_{23}\text{C}_6$  carbides are present at the grain boundaries (marked with arrows in Cr–K and C–K EDS maps) and the Cr-depleted zone is the result of diffusion of Cr toward the carbides along the grain boundary [5–8]. When the grain boundary is oxidized the Cr-depletion is stronger (see O–K and Cr–K EDS maps) and as a result the martensite layer is more pronounced. Although sensitization by  $\text{Cr}_{23}\text{C}_6$  is not responsible for the extensive formation of martensite, which has been shown in Figs. 1, 2 and 4, it is still a critical reaction for the occurrence of the IGC. At high temperature, oxygen diffuses quickly into the sensitized GBs and the GBs are easily attacked by further oxidation due to their lower Cr contents at high temperature. Sensitization is therefore still concluded to be the initial stage for the occurrence of the IGC.

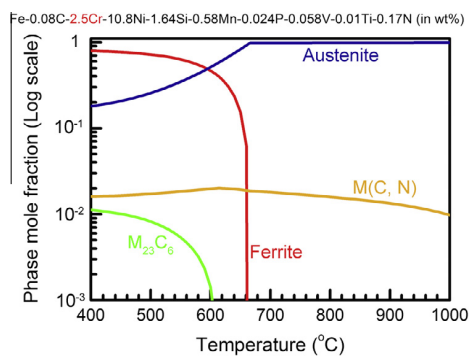


**Fig. 3.** Equilibrium phase ratio as a function of temperature, computed by Thermo-Calc using a TCFe7 database for the Cr-depleted bcc zone. M(C, N) phase represents the vanadium or titanium carbonitrides, (Ti, V)(C, N), in this steel.

### 3.4. Potential failure mode due to martensite

As shown in Fig. 6, the TEM images revealed an interfacial layer between the oxide and the martensite (marked with arrows in Fig. 6a). The interface seems porous and irregular, and no TKD patterns were indexed due to the bad quality of the patterns (as shown in Fig. 6b). The EDS maps in Fig. 6c show that composition of the interface is a mixture of all the elements present (Fe, O, Cr, Si). This is typical of a re-deposition layer formed during FIB milling in porous areas [25,26]. It implies that there are voids or gaps between the martensite and chromite in the sample prior to TEM specimen preparation. Many high temperature alloys including ASSs rely on Cr to form protective chromium-rich oxide scales. At high temperature, a minimum Cr content of nearly 20% is required to develop a continuous and protective chromium-rich oxide scale [27], while Cr contents below 18% will lead to less protective oxides [28]. Sandvik 253MA ASS should have superior oxidation resistance to conventional stainless steels at high temperatures due to formation of a dense oxide layer through silicon and cerium additions [9]. Hence, the formation of martensite as a potential path to failure during the thermal cycling is discussed here.

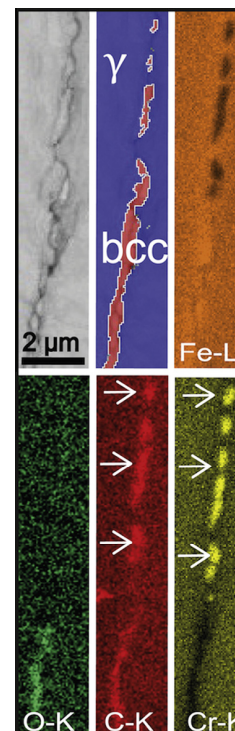


**Fig. 5.** EBSD and EDS maps of a sensitized GB in process of oxidation. Note the more extensive martensite layer in the oxidized and strongly Cr-depleted part of the GB compared to the discontinuous martensite layer around the chromium carbides (marked with arrows).

The martensitic transformation from fcc to bcc (or bct) leads to a rapid volume dilatation and surface relief due to an invariant-plane strain in the displacive transformation [29]. Both of these factors, accompanied by thermal stress, could cause the existing oxides to detach, leaving the steel susceptible to further oxidation attack at high temperature in the next cycle. Although chromite-type oxide

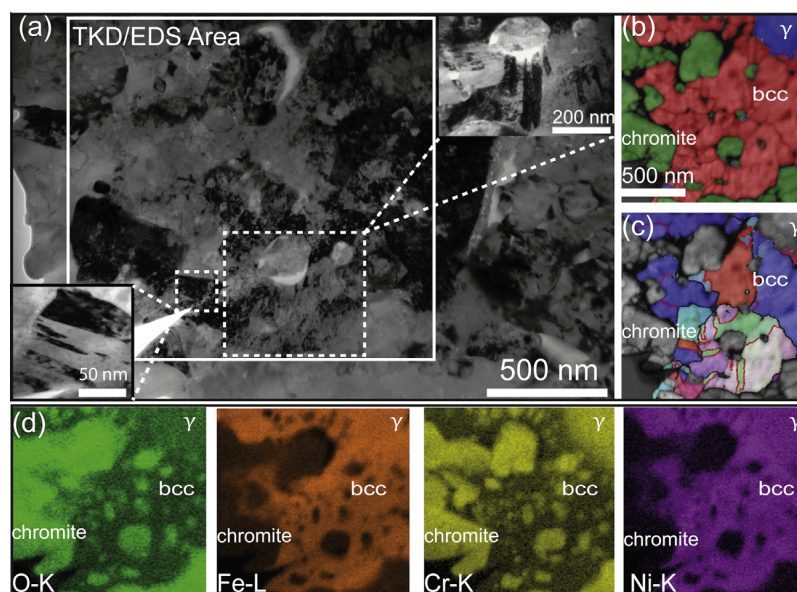


**Fig. 4.** (a) TEM bright field image of a small section of an IGC area containing chromite-type oxide (green), martensite (bcc phase in red) and austenite (blue). (b–d) TKD phase map, IPF-z orientation map and EDS elemental maps. Note the GBs highlighted in red in (c) showing martensitic laths with a twinning relationship. (For interpretation of the references to colour in this figure legend, the reader is referred to the web version of this article.)

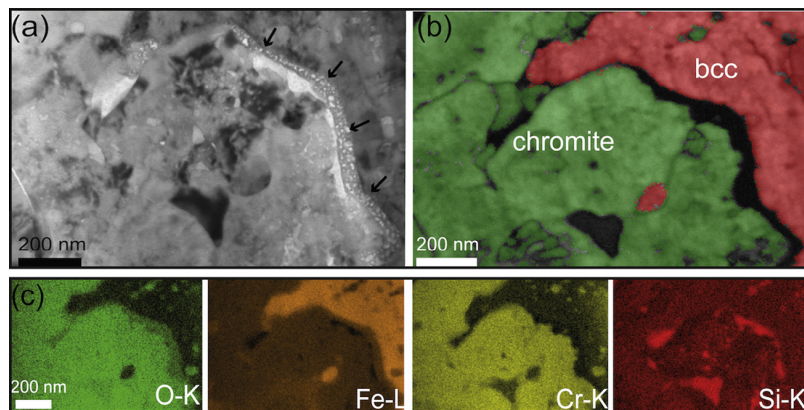


**Fig. 6.** (a) TEM bright field image showing an interface (marked with arrows) between martensite (bcc) and chromite-type oxide. (b) TKD phase map. (c) EDS elemental maps showing a mixture of Fe, Cr, O and Si in the interface marked with arrows. Note the presence of silicon-rich oxide (bright contrast adjacent to the interface layer in (a)) between the chromite and the martensite.

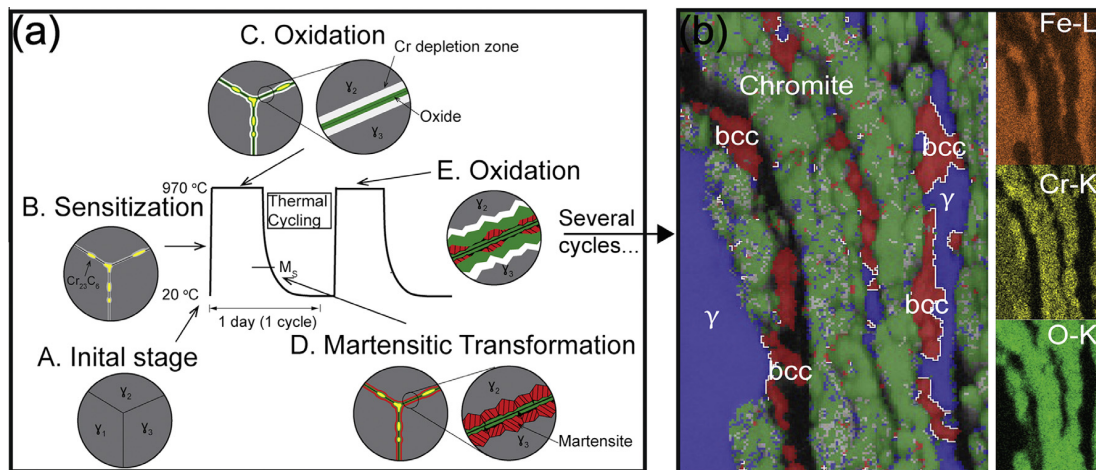


**Fig. 7.** (a) Sketch showing the oxidation cycle at the grain boundary scale. (b) EBSD phase map and EDS elemental of martensitic layers that have invaded into one austenitic grain within an IGC section. bcc/fcc Phase boundaries that correspond to the K-S OR are highlighted in white.

scale can form again at high temperature, martensite then forms again in the Cr-depleted zone during cooling. Fig. 7a illustrates the proposed mechanism based on our observations. After the tube is heated to high temperature, sensitization can occur along GBs (from Stage A to Stage B). The sensitized GBs can be more easily oxidized due to the Cr-depleted zone and these zones appear along the oxide layer (Stage C). After cooling below the  $M_s$  temperature, a martensitic transformation occurs in the Cr-depleted zone (Stage D). The nature of this displacive transformation leads to defects at the martensite/oxide interface or in oxides (black holes in Stage D). When the tube is heated again in the second cycle, the existing martensite is easily oxidized due to its very low Cr content (Stage E) and new oxidation-induced Cr-depleted zones then form. After cooling, the martensitic transformation occurs again. If this reaction repeats with thermal cycling, martensite-oxide corrosion areas invade into the austenite layer-by-layer, parallel to the prior grain boundary. Fig. 7b shows evidence of this mechanism; the phase map and EDS maps reveal three parallel cracking layers, with martensite that has invaded into one austenite grain. Moreover, some martensite regions were embedded into oxide regions. This is also consistent with the proposition that martensite can be oxidized at Stage E.

This martensitic transformation is thought to be detrimental to the corrosion performance of this alloy. A possible alloy design strategy to avoid this transformation may be to either reduce the carbon content, or increase the content of microalloyed elements, such as Ti, V, or Nb, to prevent the occurrence of sensitization. High temperature corrosion resistance still requires the formation of dense and continuous oxide layers. To prevent martensitic transformation after oxidation, Ni or N contents can be increased to suppress the  $M_s$  temperature when the Cr depletion zone forms in austenite. Also, some ferritic stainless steels could be good candidates for solar thermal applications, but higher Cr and lower C contents will be required to prevent the ferrite-to-austenite transformation at high temperatures.

#### 4. Conclusion

Through orientation and compositional maps, the formation of martensite in an IGC region has been explored for thermally cycled ASS. A martensitic transformation occurred, primarily as a result of the Cr-depleted zone created upon chromite-type oxide formation. The displacive characteristics of the martensitic transformation could disrupt the passive oxide layers and is thought to play an

important role contributing toward the rate of failure during thermal cycling. The results shown here have implications for alloy design to avoid such a transformation, possibly improving the corrosion performance of stainless steels for applications in energy production.

### Acknowledgements

Financial support from the Australian Renewable Energy Agency (ARENA) is gratefully acknowledged. Support from Prof. Hongliang Yi with Thermo-Calc software, via the Open Project Program of the State Key Laboratory of Rolling and Automation, Northeastern University, People's Republic of China, is also appreciated. The authors acknowledge the facilities and the scientific and technical assistance of the Australian Microscopy & Microanalysis Research Facility at the Australian Centre for Microscopy & Microanalysis at the University of Sydney.

### References

- [1] O. Behar, A. Khellaf, K. Mohammedi, A review of studies on central receiver solar thermal power plants, *Renew. Sustain. Energy Rev.* 23 (2013) 12–39.
- [2] E. Bain, R. Aborn, J. Rutherford, The nature and prevention of intergranular corrosion in austenitic stainless steels, *Trans. Am. Soc. Steel Treat.* 21 (1933) 481–509.
- [3] M.H. Lewis, B. Hattersley, Precipitation of  $M_{23}C_6$  in austenitic steels, *Acta Metall.* 13 (1965) 1159–1168.
- [4] K. Kaneko, T. Fukunaga, K. Yamada, N. Nakada, M. Kikuchi, Z. Saghi, J.S. Barnard, P.A. Midgley, Formation of  $M_{23}C_6$ -type precipitates and chromium-depleted zones in austenite stainless steel, *Scripta Mater.* 65 (2011) 509–512.
- [5] C.L. Briant, A mechanism for intergranular fracture in type 304 stainless steel, *Scripta Metall.* 12 (1978) 541–542.
- [6] C.L. Briant, Hydrogen assisted cracking of type 304 stainless steel, *Metall Mater. Trans. A* 10 (1979) 181–189.
- [7] E.P. Butler, M.G. Burke, Chromium depletion and martensite formation at grain boundaries in sensitised austenitic stainless steel, *Acta Metall.* 34 (1986) 557–570.
- [8] A.F. Padilha, P.R. Rios, Decomposition of austenite in austenitic stainless steels, *ISIJ Int.* 42 (2002) 325–337.
- [9] <<http://www.smt.sandvik.com>>, (accessed 22.04.14).
- [10] P.W. Trimby, Orientation mapping of nanostructured materials using transmission Kikuchi diffraction in the scanning electron microscope, *Ultramicroscopy* 120 (2012) 16–24.
- [11] P.W. Trimby, Y. Cao, Z. Chen, S. Han, K.J. Hemker, J. Lian, X. Liao, P. Rottmann, S. Samudrala, J. Sun, J.T. Wang, J. Wheeler, J.M. Cairney, Characterizing deformed ultrafine-grained and nanocrystalline materials using transmission Kikuchi diffraction in a scanning electron microscope, *Acta Mater.* 62 (2014) 69–80.
- [12] K. Kruska, S. Lozano-Perez, D.W. Saxey, T. Terachi, T. Yamada, G.D.W. Smith, Nanoscale characterisation of grain boundary oxidation in cold-worked stainless steels, *Corros. Sci.* 63 (2012) 225–233.
- [13] G.V. Kurdjumov, G. Sachs, Über den Mechanismus der Stahlhärtung, *Z. Phys.* 64 (1930) 325–343.
- [14] H.K.D.H. Bhadeshia, Problems in the calculation of transformation texture in steels, *ISIJ Int.* 50 (2010) 1517–1522.
- [15] H.K.D.H. Bhadeshia, Worked Examples in the Geometry of Crystals, Institute of Materials, London, 2001.
- [16] M. Tanino, *Bull. Jpn. Inst. Met.* 11 (1972) 203–220.
- [17] Thermo-Calc version 3.0.
- [18] T. Helander, J.O. Andersson, L. Höglund, P.F. Shi, B. Sundman, Thermo-Calc and DICTRA, computational tools for materials science, *Calphad* 26 (2002) 273–312.
- [19] E. Wilson,  $\gamma \rightarrow \alpha$  transformation in Fe, Fe–Ni, and Fe–Cr alloys, *Met. Sci.* 18 (1984) 471–484.
- [20] R.P. Reed, Nitrogen in austenitic stainless steels, *JOM* 41 (1989) 16–21.
- [21] F.J. Schoen, J.L. Nilles, W.S. Owen, Crystallographic aspects of Fe–Ni and Fe–Ni–C dilute alloy martensites, *Metall. Trans.* 2 (1971) 2489.
- [22] Y. Inokuti, B. Cantor, The microstructure and kinetics of martensite transformations in splat-quenched Fe and Fe–Ni alloys, *Acta Metall.* 30 (1982) 343–356.
- [23] B.P.J. Sandvik, C.M. Wayman, Characteristics of lath martensite: Part I. Crystallographic and substructural features, *MTA* 14 (1983) 809–822.
- [24] A.G. Haynes, W. Steven, The temperature of formation of martensite and bainite in low-alloy steel, *J. Iron Steel Inst.* 183 (1956) 349–359.
- [25] J.M. Cairney, P.R. Munroe, Redeposition effects in transmission electron microscope specimens of FeAl–WC composites prepared using a focused ion beam, *Micron* 34 (2003) 97–107.
- [26] L.A. Giannuzzi, F.A. Stevie, *Introduction to Focused Ion Beams: Instrumentation, Theory, Techniques, and Practice*, Springer, 2005.
- [27] J.R. Davis, *Stainless Steels*, ASM International, Materials Park, Ohio, 1994.
- [28] G.Y. Lai, *High temperature corrosion of engineering alloys*, 1990.
- [29] H.K.D.H. Bhadeshia, Diffusional and displacive transformations, *Scripta Metall.* 21 (1987) 1017–1022.

---

## **9 Optimization and data quality assessment of laser-assisted APT of chromium oxides**

This publication contributes to the present thesis by providing an assessment of the influence of APT analysis parameters on the data quality of chromium oxide scale and chromium-rich oxide spinel. As described in the literature review, there is a need to optimize the laser-assisted APT analysis parameters (essentially laser pulse energy) for each type of mineral, as they all have different thermal, electrical and mechanical properties.

The impact of essential APT analysis parameters (laser pulse energy and frequency, temperature) on data quality was investigated for a chromia scale thermally grown on a model alloy. Parameter tests were also done on iron-chromium spinel from the intergranular corrosion area of the austenitic stainless steel selected in this PhD. It is important to note that laser pulse energies below 20pJ were not reported due to the low specimen yield at such high field conditions.

This publication provides a good base for the high quality investigation of chromium oxides by laser-assisted APT and serves as a preliminary chapter for the atomic scale characterization of the iron-chromium spinel formed during intergranular corrosion of austenitic stainless steel.

The content of this published article is largely the product of the work of Alexandre La Fontaine under the supervision of Julie M. Cairney, Jianqiang Zhang and David Young. Baptiste Gault significantly contributed to the interpretation of results. Andrew Breen, Anna Ceguerra and Leigh Stephenson assisted in the data processing. Limei Yang carried out the chromia sample preparation. Thuan Dinh Nguyen produced and provided the chromia sample.

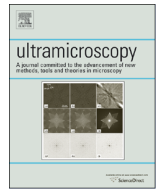
This article has been published in in *Ultramicroscopy*, Volume 159, Pages 354-359 (2015) DOI: 10.1016/j.ultramic.2015.02.005.





Contents lists available at ScienceDirect

## Ultramicroscopy

journal homepage: [www.elsevier.com/locate/ultramic](http://www.elsevier.com/locate/ultramic)

## Interpreting atom probe data from chromium oxide scales



Alexandre La Fontaine<sup>a,b</sup>, Baptiste Gault<sup>c</sup>, Andrew Breen<sup>a,b</sup>, Leigh Stephenson<sup>a,b</sup>,  
Anna V. Ceguerra<sup>a,b</sup>, Limei Yang<sup>a,b</sup>, Thuan Dinh Nguyen<sup>d</sup>, Jianqiang Zhang<sup>d</sup>,  
David J. Young<sup>d</sup>, Julie M. Cairney<sup>a,b,\*</sup>

<sup>a</sup> School of Aerospace, Mechanical, Mechatronic Engineering, The University of Sydney, NSW 2006, Australia

<sup>b</sup> Australian Centre for Microscopy and Microanalysis, The University of Sydney, NSW 2006, Australia

<sup>c</sup> Department of Materials, University of Oxford, Parks Road, Oxford OX1 3PH, UK

<sup>d</sup> School of Materials Science and Engineering, University of New South Wales, Sydney, NSW 2052, Australia

## ARTICLE INFO

## Article history:

Received 9 September 2014

Received in revised form

21 December 2014

Accepted 4 February 2015

Available online 14 February 2015

## Keywords:

Atom probe tomography

Oxides

Corrosion

Field evaporation

## ABSTRACT

Picosecond-pulsed ultraviolet-laser (UV-355 nm) assisted atom probe tomography (APT) was used to analyze protective, thermally grown chromium oxides formed on stainless steel. The influence of analysis parameters on the thermal tail observed in the mass spectra and the chemical composition is investigated. A new parameter termed “laser sensitivity factor” is introduced in order to quantify the effect of laser energy on the extent of the thermal tail. This parameter is used to compare the effect of increasing laser energy on thermal tails in chromia and chromite samples. Also explored is the effect of increasing laser energy on the measured oxygen content and the effect of specimen base temperature and laser pulse frequency on the mass spectrum. Finally, we report a preliminary analysis of molecular ion dissociations in chromia.

© 2015 Elsevier B.V. All rights reserved.

## 1. Introduction

Stainless steels have wide applications in new energy technologies thanks to a combination of high-temperature strength, corrosion resistance and affordability. However, they require improved high-temperature corrosion resistance for extreme conditions, such as within a concentrated solar power plant, where temperature cycles can range from room temperature up to 1000 °C in air or carbonaceous atmosphere. The protective oxide layer that forms on the stainless steels plays a major role in the performance of these components. Investigation of the structure of these oxide layers at the nano-scale is critical for the development of more stable protective layers.

While atom probe tomography (APT) [1] is an excellent technique to the study of the nano-structure of such oxides, the associated data analysis still presents many challenges. In the last ten years, there have been many studies of oxide materials by laser assisted APT [2–10]. However, it is only recently that laser-assisted APT has been used to study the corrosion of stainless steels, providing new insight into the microstructure of the passive oxide

layer that protects the alloy [11–13]. Thermally-assisted field evaporation of oxides leads to data that can be difficult to interpret [14–16]. With increasing interest in applying atom probe to the study of oxides, it is essential to assess the effect of analysis parameters on the data quality. Recent studies reported the influence of analysis parameters on the investigation of wüstite [16] by femtosecond laser assisted APT. The authors recommended that infra-red (IR) laser should be used to analyze wüstite as green and ultra-violet (UV) modes gave a measured oxygen content considerably below its expected value. They showed that an increase of IR-laser energy reduced the oxygen content measured. An increase of the thermal tail was also observed with increase of IR-laser energy.

Here, we aim to understand how atom probe data from thermally grown chromium oxides in stainless steels is affected by analysis conditions (laser pulse energy, laser pulse frequency and base temperature), specifically for data obtained by picosecond UV laser assisted APT. In particular, data from chromia ( $\text{Cr}_2\text{O}_3$ ) was used to test the effect of different analysis parameters on the extent of the thermal tails that follow each peak in the mass-to-charge spectra and the measured composition that results. The results obtained from chromite-type spinel layers ( $\text{Fe}(\text{FeCr})_2\text{O}_4$ ) are then compared to the chromia data.

\* Corresponding author at: School of Aerospace, Mechanical, Mechatronic Engineering, The University of Sydney, NSW 2006, Australia.

E-mail address: [julie.cairney@sydney.edu.au](mailto:julie.cairney@sydney.edu.au) (J.M. Cairney).

<http://dx.doi.org/10.1016/j.ultramic.2015.02.005>

0304-3991/© 2015 Elsevier B.V. All rights reserved.

## 2. Experimental

Two chromium oxide scales were investigated, chromia ( $\text{Cr}_2\text{O}_3$ ) and chromite ( $\text{Fe}(\text{FeCr})_2\text{O}_4$ ). The chromia scale was thermally grown from a Fe–20Cr (wt%) model alloy. The alloy was exposed to Ar–200<sub>2</sub> for 24 h and then to Ar–20CO<sub>2</sub> for 70 h at 650 °C. As a result, a protective scale of chromia was formed on the alloy surface. A more detailed description of the sample and how this data informs corrosion studies can be found in [13]. The chromite-type scale was formed in an intergranular corrosion region in a Sandvik 253MA austenitic stainless steel (ASS). The composition of the scale varies from Fe-rich chromite,  $\text{Fe}(\text{Fe,Cr})_2\text{O}_4$ , to near-stoichiometric chromite,  $\text{FeCr}_2\text{O}_4$ . Details of the material and relevant corrosion studies can be found in [17]. APT samples were prepared using a Zeiss-Auriga focused ion beam (FIB) equipped with a Kleindiek micromanipulator system. Bars of oxide layers were lifted-out from milled cross sections using a micromanipulator. Samples were milled from these bars, attached to electropolished molybdenum grids and finally milled to form APT tips with a typical diameter of around 60 nm [18]. The APT experiments were conducted on a Cameca LEAP 4000 × Si™ atom probe equipped with a picosecond-pulse ultraviolet laser (355 nm, spot size < 4 μm). The data were reconstructed using Cameca IVAS™ 3.6.6. EPOS files were generated using the same software and treated using custom-designed scripts in Matlab (TM, Mathworks), allowing access to the raw detector information collected for each ion, which enabled the study of singles and multiples ions events per pulses [19,20].

## 3. Results and discussion

In this section, we outline the methods used to range the mass spectra, since this is known to have a significant influence on the measured chemical composition [21]. We then focus on the influence of the laser pulse energy and repetition rate, as well as the base temperature, on the overall quality of the mass spectrum, with specific reference to the thermal tailing effect. Finally, we will investigate the influence of molecular ion dissociation events on the overall analysis.

### 3.1. Ion identification and ranging

Correct ion identification in the mass spectrum is critical for compositional accuracy and can be challenging for complex oxides. Two typical mass spectra from chromia and chromite are shown in Fig. 1a and b respectively. These two datasets were collected at a base temperature of 55 K and laser energy of 70 pJ with a laser pulse frequency of 500 kHz. For clarity, the spectra are shown in two parts, each with a different scale. Only minor peaks of  $\text{Cr}_3\text{O}^+$  (173 Da) and  $\text{Cr}_2\text{O}_5^+$  (185 Da) were detected above 105 Da for both oxides. Oxygen was evaporated either as an oxide-ion species or as  $\text{O}^+$  and  $\text{O}_2^+$ . Based on the work of Bachhav et al. [22] the peak at 16 Da was identified as  $\text{O}^+$ , rather than  $\text{O}_2^{2+}$ . Chromium was evaporated as  $\text{Cr}^{2+}$ ,  $\text{CrO}^{+2+}$ ,  $\text{CrO}_2^{+2+}$ ,  $\text{CrO}_3^+$  and  $\text{Cr}_2\text{O}_5^+$ . Iron evaporated as  $\text{Fe}^{+2+}$ ,  $\text{FeO}^+$  and  $\text{Fe}_2\text{O}^{2+}$ .

We have investigated the influence of the ranging method for the chromia dataset used in Fig. 1a. There is still no agreement or standards on how mass ranges should be defined. Hudson et al.

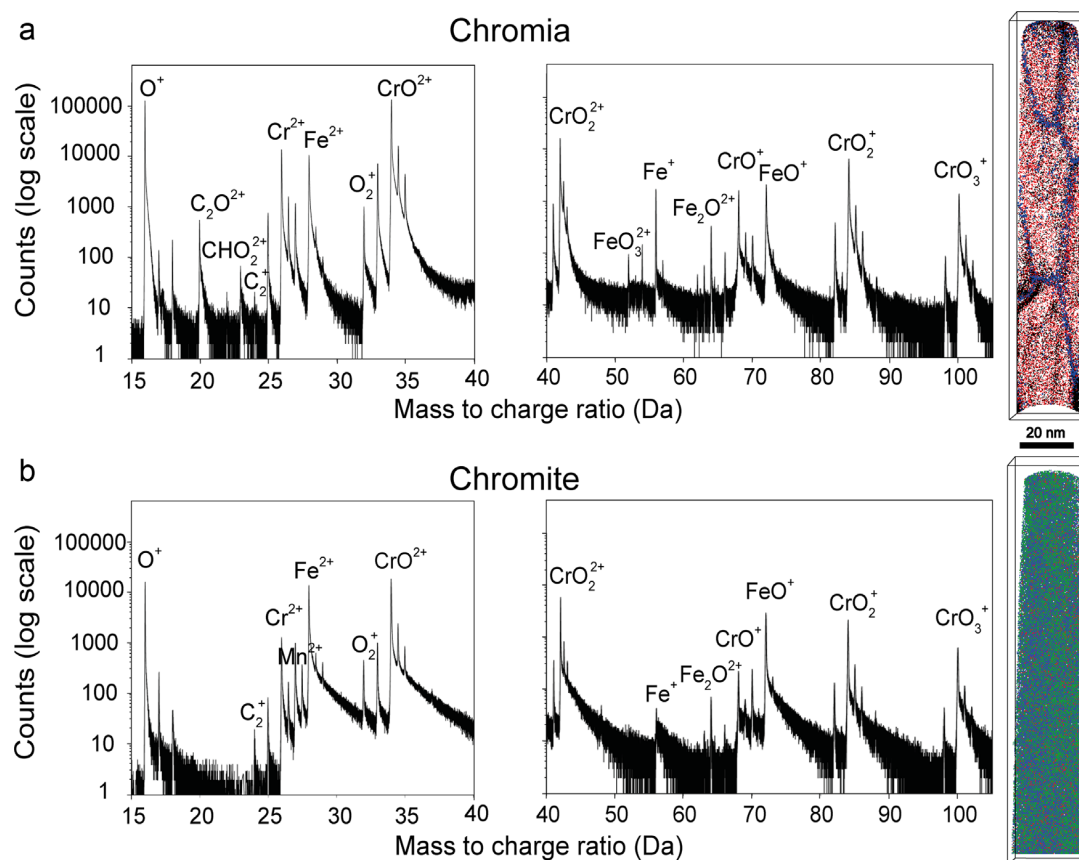


**Fig. 1.** Ion identification. (a) Mass spectrum of chromia ( $\text{Cr}_2\text{O}_3$ ), and a corresponding 5 nm-thick atom probe volume (red: oxygen atoms, blue: carbon atoms and black: iron atoms), the specimen contains grain boundaries decorated with carbon and iron. (b) Mass spectrum of chromite ( $\text{Fe}(\text{FeCr})_2\text{O}_4$ ) and a corresponding 3D atom probe volume (green: oxygen atoms, blue: iron atoms and red: chromium atoms). The chromite sample contains thin layers of Fe-rich chromite type spinels within near-stoichiometric chromite ( $\text{FeCr}_2\text{O}_4$ ). (For interpretation of the references to color in this figure legend, the reader is referred to the web version of this article.)

[19,23] found that ranges defined as full-width nine-tenth maximum gave the most accurate composition for simulated data. With mass ranges defined as full-width nine-tenth maximum, the oxygen and chromium concentrations measured were  $58.2 \pm 0.6$  at% and  $39.8 \pm 0.5$  at% respectively. The measured Cr/O ratio is  $0.68 \pm 0.02$ . With mass ranges including most of the peak tail, the oxygen and chromium concentrations measured were  $57.0 \pm 0.6$  at% and  $39.4 \pm 0.5$  at% respectively, giving a measured Cr/O ratio of  $0.69 \pm 0.02$ . Interestingly, the compositions measured using these two extreme ranging methods are not significantly different.

There is a deficit in the oxygen measured compared to the stoichiometric chromia (60 at% O and Cr/O ratio of 0.67). A deficit in oxygen composition measurements within oxides studied from APT was also reported for the study on haematite by Bachhav et al. [22] as well as alumina by Marquis et al. [5]. However, in this work, the deficit of oxygen measured is less than was noted in the work of Bachhav et al. Care should be taken in interpreting the significance of the extent of the deficit observed here, as it could be affected by the non-stoichiometric character of the chromia used in this work. The sample was heat-treated in a carbon dioxide atmosphere and segregation of carbon and iron was found in the chromia grain boundaries. Due to the carbon dioxide atmosphere, it is likely that oxygen penetrated through the chromia scale, increasing the content of oxygen to a higher level than expected for stoichiometric chromia.

### 3.2. Effect of laser energy

The influence of laser energy on the mass spectra quality was investigated for the two different oxides to provide guidance on selecting the appropriate laser energy. For the experiment on chromia, a single tip was used and the laser energy was progressively increased from 22 to 115 pJ. The base temperature was 50 K, laser pulse frequency 500 kHz and ions were detected at an evaporation rate of 0.5%. Fig. 2a shows several mass spectra of the  $\text{CrO}^{2+}$  peaks (33 Da, 34 Da, 34.5 Da and 35 Da) for data collected at different laser energies. The tail after each peak increases with increasing laser energy. Such effect was also reported by Bachhav et al. on the analysis of wüstite by femtosecond laser-assisted APT [16]. It reflects an increase in the local heating due to the laser pulse, which in turn affects the mass resolution due to a broadening of the thermal tail [24]. By normalizing the mass spectra to sum to unity, the extent of the thermal tail can be quantified and compared more easily for different laser energies. A method was developed to quantify the peak-to-tail ( $P_n/T_n$ ) ratio between the different spectra. A mass-to-charge window for each peak ( $P_n$ ) and tail ( $T_n$ ) was arbitrarily selected, as shown in Fig. 2a, ensuring that the same procedure was applied to all spectra. The normalized counts within each window were then summed together and used to calculate the peak-to-tail ( $P_n/T_n$ ) ratio.

This ratio for the three  $\text{CrO}^{2+}$  peaks is then plotted against the laser energy in Fig. 2b. For all three  $\text{CrO}^{2+}$  peaks the ratio decreases with increasing laser energy, which reflects a more extensive tail. It is important to note that the peak at 34 Da contributes to the tail of the peak at 34.5 Da and both will contribute to the tail at 35 Da. A proper fitting of each peak is necessary to be able to subtract the contribution of the previous peak [25]. However, the method used allows a simple comparison of the influence of the tails under different conditions, or even across different samples.

For example, Fig. 3 shows the evolution of  $^{34}\text{CrO}^{2+}$  peak-to-tail ratio for chromia and chromite with an increase of laser energy. The slope of the curve for a specific peak could be defined as a 'laser energy sensitivity factor' (for the chromite, data from three different specimens with similar tip radii (25–30 nm) were

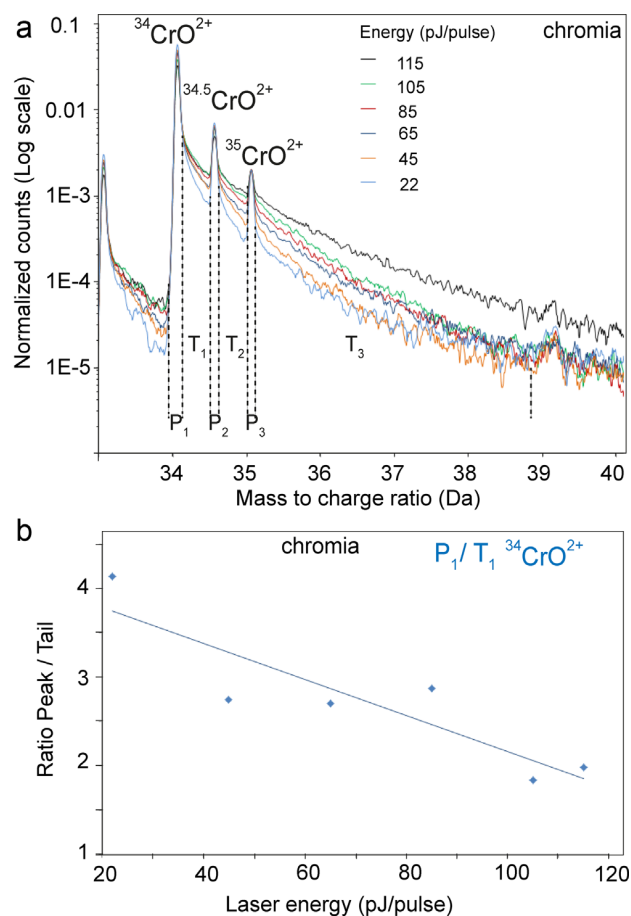


Fig. 2. Effect of laser energy on data quality—Chromia sample. (a) Normalized mass spectrum of  $\text{CrO}^{2+}$  for different laser energies (from 22 pJ to 115 pJ). Note the mass-to-charge windows used to calculate the ratio peak-to-tail ratio. (b) Peak-to-tail ratio as a function of laser energy for three  $\text{CrO}^{2+}$  peaks (34, 34.5 and 35 Da).

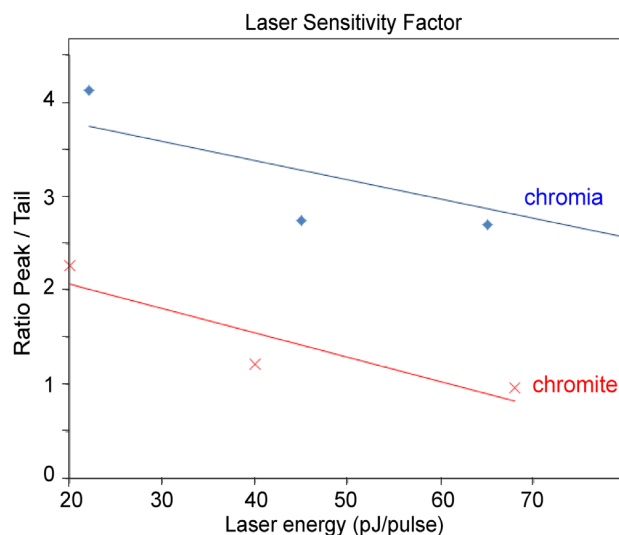


Fig. 3. Laser sensitivity factor for chromia and chromite: Peak-to-tail ratio as a function of laser energy for  $^{34}\text{CrO}^{2+}$  for chromia and chromite. Note the similar slope (laser sensitivity factor) for both samples.

collected with laser energies increasing from 20 pJ to 68 pJ, at a base temperature of 55 K and with a laser pulse frequency of 500 kHz). The peak-to-tail ratios for chromite are nearly half of

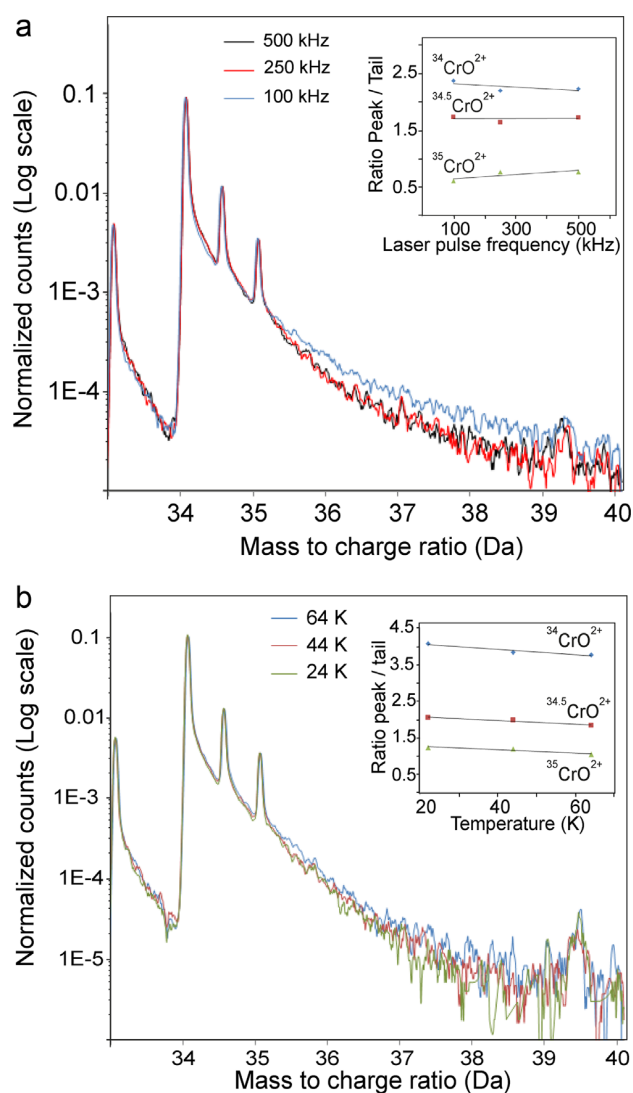


Fig. 4. Measured oxygen content as a function of laser energy.

those for chromia, primarily due to the much larger thermal tail observed for chromite, which can be seen in Fig. 1. This could be the result of different tip geometries, such as the shank angle [26,27] or even the distance from the tip to the underlying metal. For this reason, the laser energy sensitivity factor (i.e. the slope) is an alternative metric and is thought to be independent of the tip geometry. The laser energy sensitivity is quite similar between both materials, which suggests that increasing laser energy is equally detrimental for both materials. This data adds to the existing evidence suggesting that the evaporation process is thermal, and provides evidence that higher laser energy is detrimental for the mass resolution of both chromia and chromite.

Several studies have reported a change in the measured oxygen composition with a variation of laser energy [16,28] so the oxygen composition was investigated here to see if a similar trend was observed. Only the chromia data was used for this part of the study, as the chromite datasets contained heterogeneities that are thought to influence the oxygen content.

Fig. 4 shows the evolution of the oxygen concentration measured in the same chromia tip with laser energy increase but, interestingly, no significant variation of the oxygen content was

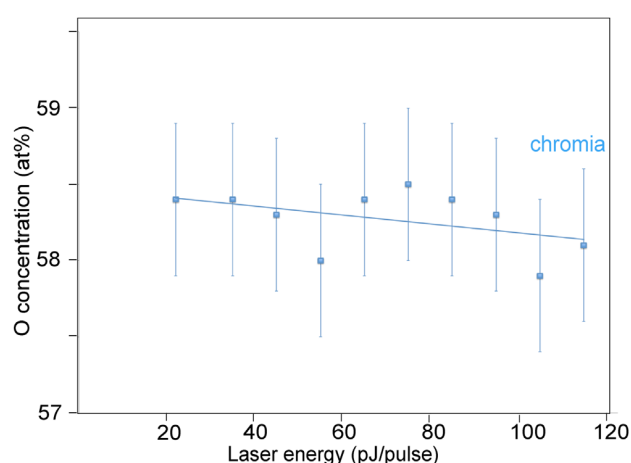


Fig. 5. Effect of laser pulse frequency and base temperature. (a) Normalized mass spectrum (sum to unity) as a function of laser pulse frequency for  $\text{CrO}^{2+}$  ions. Inset is the peak-to-tail ratio as a function of laser pulse frequency. (b) Normalized mass spectrum (sum to unity) as a function of base temperature for  $\text{CrO}^{2+}$ . Inset is the peak-to-tail ratio as a function of base temperature.

observed. The measured oxygen content for all laser energies tested averages  $58.4 \pm 0.5\%$ . These results show that the influence of laser energy on oxygen composition is small for this particular oxide. In this case, the accuracy of the peak identification, and the methods used for peak ranging appears to be of greater importance for accurate compositional measurement.

### 3.3. Effect of laser pulse frequency and base temperature

The effect of laser pulse frequency was also investigated. For this, a single chromia specimen was analyzed with a laser energy of 40 pJ and at a base temperature of 50 K, while the laser pulse frequency was varied from 500 kHz to 250 kHz. There was no major change to the thermal tail with decreasing laser pulse frequency, as shown in Fig. 5a. A slight increase in the size of the tail after the  $^{35}\text{CrO}^{2+}$  peak was observed at 100 kHz. This could be explained by the fact that the sample fractured before the desired number of ions was collected. The data here shows that, for chromia, changing laser pulse frequency does not significantly affect the mass resolution or thermal tailing, since there is more time for the heat to be dissipated from the tip. A possible reason that this was not observed is that there is no build up of heat between the pulses, even at higher frequencies. The thermal tails are relatively short meaning that the heat is sufficiently dissipated between the pulses.

The effect of temperature on the thermal tailing effect was investigated by increasing the base temperature of a single chromia tip from 24 K to 64 K, with constant a laser energy of 40 pJ and a pulse frequency of 500 kHz. Fig. 5b shows the three mass spectra collected. The data demonstrates that, for chromia, there is no major change with increasing base temperature up to 64 K. However, running the chromia tips at higher base temperatures is generally beneficial for decreasing the tip fracture rate due to a lower field and thus a lower electrostatic pressure [29].

### 3.4. Correlation histograms

In order to better understand the complexity of oxide ion evaporation during laser atom probe tomography, which often leads to noise and data loss, we have applied an approach pioneered by Saxey [30] that uses field evaporated ions correlations to reveal in flight molecular ions dissociations. Although

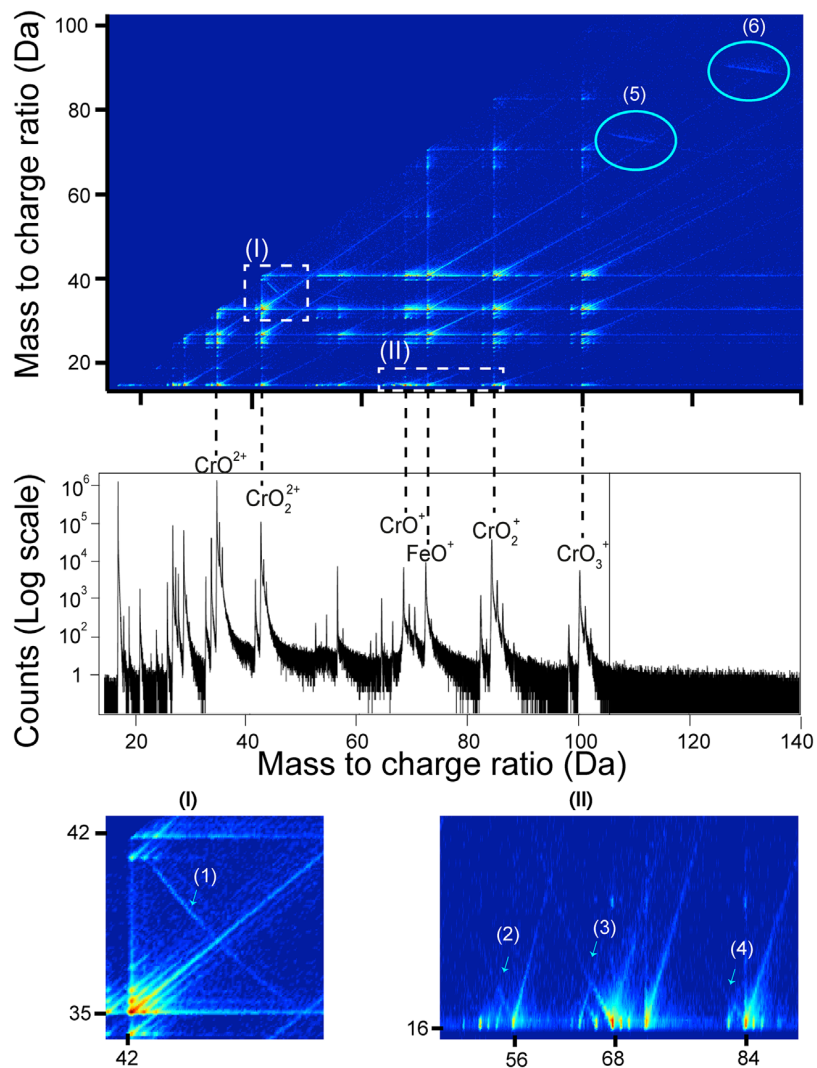


**Fig. 6.** Correlation histogram from chromia with its associated mass spectrum. The two subfigures show details of 4 dissociation tracks as highlighted in the main correlation histogram. (For interpretation of the references to color in this figure, the reader is referred to the web version of this article.)

preliminary, these results are valuable as they highlight the complexity of the field evaporation and molecular ion dissociation process.

A correlation histogram is shown in Fig. 6 for a chromia dataset containing about 20 million atoms with 85% single hits/pulse and 14% double hits/pulse. The rest of the ions detected were either partially detected or formed part of multiple ion hits of 3 or more. For this analysis, only the mass-to-charge information corresponding to multiple events was used (i.e. two or more ions detected from the same pulse). All events were accumulated in a two-dimensional histogram with the largest mass-to-charge value assigned first (the x-coordinate). The corresponding 2D mass-to-charge spectrum (Fig. 6) is displayed below and, as expected, most of the histogram counts are located at coincidences between easily identifiable major peaks [30]. The full graph is symmetrical but everything above  $x=y$  was set to 0 to help with the readability of the graph.

The histogram shows traces of molecular ion dissociation tracks following a parabolic line as described by Saxey [30], pointing either towards the bottom-right or the top-left. These are highlighted in Fig. 6, and specific areas of the plot are enlarged in the subfigures to better reveal this effect. Based on the work of Saxey [30], we have identified some of the possible dissociations

highlighted in the subfigures of Fig. 6 as follows:

- (1)  $^{84}\text{CrO}_2^{2+} \rightarrow ^{52}\text{Cr}^+ + ^{32}\text{O}_2^+$ .
- (2)  $^{72}\text{FeO}^{2+} \rightarrow ^{56}\text{Fe}^+ + ^{16}\text{O}^+$ .
- (3)  $^{84}\text{CrO}_2^{2+} \rightarrow ^{68}\text{CrO}^+ + ^{16}\text{O}^+$ .
- (4)  $^{100}\text{CrO}_3^{2+} \rightarrow ^{84}\text{CrO}_2^+ + ^{16}\text{O}^+$ .

Interestingly the dissociation (1):  $\text{CrO}_2^{2+} \rightarrow \text{Cr}^+ + \text{O}_2^+$  has occurred close to the detector (late in the flight) while all the other dissociations happened quite early (close to the tip). There was no dissociation observed for  $\text{CrO}^{+2+}$  reflecting the higher stability of this ion.

These dissociations have several implications on the mass spectrum. Depending on when the dissociation occurs some of the daughter ions will appear in the mass spectrum with a slightly lower mass and some with a higher mass. As a result the corresponding peak will appear wider or asymmetrical. The graphs showed herein are displayed in log scale, and the number of ions resulting from such dissociative processes is relatively small compared to the amount of ions found along the thermal tails. However, the dissociation of molecular ions does affect, for instance, the relative abundance of various ions or charge states. It is common in the literature to use changes in the charge state ratio

as evidence of tip heating [31], assuming that changes in the electric field linked to the increase in temperature directly affect the probability of post-ionization process and consequently the charge-state ratios. Here, we show that dissociation also plays a role. The actual influence of such processes on the analytical capabilities of APT are still not fully apprehended, but such processes do occur and their in-depth investigation is expected to lead to a better understanding of the field evaporation process of oxide materials. The two traces of dissociations labelled 5 and 6 (circled in light blue in Fig. 6) were particularly interesting. By following the traces back to the parent molecular ions, we identified these two molecular ions as  $\text{CrO}_2^+$  at 84 Da and  $\text{CrO}_3^+$  at 100 Da. However dissociation from these single-charged molecular ions would produce two daughter ions, one singly-charged and the other neutral. We do not fully understand these dissociations, and the role that neutrals may have in the interpretation of atom probe data, but we believe such dissociations could have a potential impact in the form of data loss.

#### 4. Summary and conclusion

We have investigated the influence of laser parameters on the evaporation of chromium oxides by APT. We have shown that the thermal tails after each peak increase in relative size as laser energy is increased, as would be expected for a thermally-assisted process. However, we did not observe a strong effect of laser energy on the measured oxygen concentration. The laser pulse frequency and the base temperature (up to 64 K) had little impact on the data quality. Correlation histograms revealed evidence of ion dissociation, which can affect the charge state ratios, the mass spectrum quality and the overall measured composition.

#### Acknowledgement

The authors acknowledge Dr. Lan Yao for providing the script to compute the correlation histograms. Financial support from the Australian Renewable Energy Agency (ARENA) is gratefully acknowledged. The authors acknowledge the facilities and the scientific and technical assistance of the Australian Microscopy & Microanalysis Research Facility at the Australian Centre for Microscopy & Microanalysis at the University of Sydney. BG acknowledges that he is a full time employee of Elsevier Ltd. but declares no conflict of interest as his contribution to this article corresponds to his activity out of office hours.

#### References

- [1] T.F. Kelly, D.J. Larson, *Atom probe tomography 2012*, *Annu. Rev. Mater. Res.* 42 (2012) 1–31.
- [2] M.N. Bachhav, R. Danoix, F. Vurpillot, B. Hannoyer, S.B. Ogale, F. Danoix, Evidence of lateral heat transfer during laser assisted atom probe tomography analysis of large band gap materials, *Appl. Phys. Lett.* 99 (2011) 084101–084103.
- [3] C. Oberdorfer, P. Stender, C. Reinke, G. Schmitz, Laser-assisted atom probe tomography of oxide materials, *Microsc. Microanal.* 13 (2007) 342–346.
- [4] B. Gault, A. Menand, F. de Geuser, B. Deconihout, R. Danoix, Investigation of an oxide layer by femtosecond-laser-assisted atom probe tomography, *Appl. Phys. Lett.* 88 (2006) 114101.
- [5] E.A. Marquis, N.A. Yahya, D.J. Larson, M.K. Miller, R.I. Todd, Probing the improbable: imaging C atoms in alumina, *Mater. Today* 13 (2010) 34–36.
- [6] D. Larson, R. Alvis, D. Lawrence, T. Prosa, R. Ulfig, D. Reinhard, P. Clifton, S. Gerstl, J. Bunton, D. Lenz, Analysis of bulk dielectrics with atom probe tomography, *Microsc. Microanal.* 14 (2008) 1254–1255.
- [7] K. Hono, T. Ohkubo, Y. Chen, M. Kodzuka, K. Oh-Ishi, H. Sepehri-Amin, F. Li, T. Kinno, S. Tomiya, Y. Kanitani, Broadening the applications of the atom probe technique by ultraviolet femtosecond laser, *Ultramicroscopy* 111 (2011) 576–583.
- [8] B. Mazumder, A. Vella, B. Deconihout, T. Al-Kassab, Evaporation mechanisms of MgO in laser assisted atom probe tomography, *Ultramicroscopy* 111 (2011) 571–575.
- [9] S.-I. Baik, X. Yin, D.N. Seidman, Correlative atom-probe tomography and transmission electron microscope study of a chemical transition in a spinel on an oxidized nickel-based superalloy, *Scr. Mater.* 68 (2013) 909–912.
- [10] A. La Fontaine, H.-W. Yen, P.J. Felfel, S.P. Ringer, J.M. Cairney, Atom probe study of chromium oxide spinels formed during intergranular corrosion, *Scr. Mater.* (2014).
- [11] S. Lozano-Perez, D.W. Saxey, T. Yamada, T. Terachi, Atom-probe tomography characterization of the oxidation of stainless steel, *Scr. Mater.* 62 (2010) 855–858.
- [12] K. Kruska, S. Lozano-Perez, D.W. Saxey, T. Terachi, T. Yamada, G.D.W. Smith, Nanoscale characterisation of grain boundary oxidation in cold-worked stainless steels, *Corros. Sci.* 63 (2012) 225–233.
- [13] D.J. Young, T.D. Nguyen, P. Felfel, J. Zhang, J.M. Cairney, Penetration of protective chromia scales by carbon, *Scr. Mater.* 77 (2014) 29–32.
- [14] M. Tsukada, H. Tamura, K.P. McKenna, A.L. Shluger, Y.M. Chen, T. Ohkubo, K. Hono, Mechanism of laser assisted field evaporation from insulating oxides, *Ultramicroscopy* 111 (2011) 567–570.
- [15] T.F. Kelly, A. Vella, J.H. Bunton, J. Houard, E.P. Silavea, J. Bogdanowicz, W. Vandervorst, Laser pulsing of field evaporation in atom probe tomography, *Curr. Opin. Solid State Mater. Sci.* 18 (2014) 81–89.
- [16] M. Bachhav, R. Danoix, F. Danoix, B. Hannoyer, S. Ogale, F. Vurpillot, Investigation of wüstite ( $\text{Fe}_{1-x}\text{O}$ ) by femtosecond laser assisted atom probe tomography, *Ultramicroscopy* 111 (2011) 584–588.
- [17] A. La Fontaine, H.-W. Yen, P. Trimby, S. Moody, S. Miller, M. Chensee, S. Ringer, J. Cairney, Martensitic transformation in an intergranular corrosion area of austenitic stainless steel during thermal cycling, *Corros. Sci.* 85 (2014) 1–6.
- [18] P.J. Felfel, T. Alam, S.P. Ringer, J.M. Cairney, A reproducible method for damage-free site-specific preparation of atom probe tips from interfaces, *Microsc. Res. Tech.* 75 (2012) 484–491.
- [19] B. Gault, M.P. Moody, J.M. Cairney, S.P. Ringer, *Atom probe microscopy*, Springer, 2012.
- [20] L. Yao, B. Gault, J. Cairney, S. Ringer, On the multiplicity of field evaporation events in atom probe: a new dimension to the analysis of mass spectra, *Philos. Mag. Lett.* 90 (2010) 121–129.
- [21] D. Hudson, G.D.W. Smith, B. Gault, Optimisation of mass ranging for atom probe microanalysis and application to the corrosion processes in Zr-alloys, *Ultramicroscopy* 111 (2011) 480–486.
- [22] M. Bachhav, F. Danoix, B. Hannoyer, J.M. Bassat, R. Danoix, Investigation of O-18 enriched hematite ( $\alpha\text{-Fe}_2\text{O}_3$ ) by laser assisted atom probe tomography, *Int. J. Mass Spectrom.* 335 (2013) 57–60.
- [23] D. Hudson, G. Smith, B. Gault, Optimisation of mass ranging for atom probe microanalysis and application to the corrosion processes in Zr alloys, *Ultramicroscopy* 111 (2011) 480–486.
- [24] F. Vurpillot, J. Houard, A. Vella, B. Deconihout, Thermal response of a field emitter subjected to ultra-fast laser illumination, *J. Phys. D: Appl. Phys.* 42 (2009) 125502.
- [25] L.J.S. Johnson, M. Thuvander, K. Stiller, M. Odén, L. Hultman, Blind deconvolution of time-of-flight mass spectra from atom probe tomography, *Ultramicroscopy* 132 (2013) 60–64.
- [26] J.H. Bunton, J.D. Olson, D.R. Lenz, T.F. Kelly, Advances in pulsed-laser atom probe: instrument and specimen design for optimum performance, *Microsc. Microanal.* 13 (2007) 418–427.
- [27] F. Tang, B. Gault, S.P. Ringer, J.M. Cairney, Optimization of pulsed laser atom probe (PLAP) for the analysis of nanocomposite Ti–Si–N films, *Ultramicroscopy* 110 (2010) 836–843.
- [28] F. Li, T. Ohkubo, Y. Chen, M. Kodzuka, K. Hono, Quantitative atom probe analyses of rare-earth-doped ceria by femtosecond pulsed laser, *Ultramicroscopy* 111 (2011) 589–594.
- [29] T.J. Wilkes, J.M. Titchmarsh, G.D.W. Smith, D.A. Smith, R.F. Morris, S. Johnston, T.J. Godfrey, P. Birdseye, The fracture of field-ion microscope specimens, *J. Phys. D: Appl. Phys.* 5 (1972) 2226.
- [30] D.W. Saxey, Correlated ion analysis and the interpretation of atom probe mass spectra, *Ultramicroscopy* 111 (2011) 473–479.
- [31] F. Vurpillot, B. Gault, A. Vella, M. Bouet, B. Deconihout, Estimation of the cooling times for a metallic tip under laser illumination, *Appl. Phys. Lett.* 88 (2006) 094105.

---

## **10 Atomic scale structure and composition of intergranular chromium oxide spinels**

Austenitic stainless steels can be subject to intergranular corrosion when exposed at high temperature in a corrosive environment. This is especially true for concentrated solar power applications, where the operation temperature cycles every day and night from room temperature up to ~1000 °C in air (see chapter 8 and 4.1). As discussed in the literature review, there are important physical and chemical processes at the micron and nano scale that influence the rate at which intergranular corrosion occurs. For example, in chapter 8, a martensitic phase transformation induced by the formation of chromium-rich oxides was revealed in the intergranular corrosion areas of a commercial austenitic stainless steel.

In this publication, a particular focus is on the structure and composition of the iron-chromium oxides that formed in the same specimen. For the first time, the oxide minerals that constitute the intergranular corrosion areas are characterized by laser-assisted APT. This chapter is the final part of the investigation of the intergranular corrosion area in a commercial austenitic stainless steel by the means of advanced microscopy.

The content of this published article is largely the product of the work of Alexandre La Fontaine under the supervision of Julie M. Cairney and Simon P. Ringer. Hung-Wei Yen revised the manuscript and significantly contributed to the interpretation of results. Peter Felfer carried out the sample preparation for one of the specimens used in this study.

This article has been published in *Scripta Materialia*, Volume 99, Pages 1-4 (2015)

DOI: 10.1016/j.scriptamat.2014.09.028.



## Atom probe study of chromium oxide spinels formed during intergranular corrosion

Alexandre La Fontaine,<sup>\*</sup> Hung-Wei Yen, Peter J. Felfer, Simon P. Ringer and Julie M. Cairney

*School of Aerospace, Mechanical, Mechatronic Engineering, The University of Sydney, NSW 2006, Australia*  
*Australian Centre for Microscopy and Microanalysis, The University of Sydney, NSW 2006, Australia*

Received 27 August 2014; revised 25 September 2014; accepted 25 September 2014  
Available online 3 November 2014

Atom probe microscopy has been used to study the inhomogeneous nature of chromium oxide spinels in intergranular corrosion of a 253 MA austenitic stainless steel after thermal cycling up to 970 °C in air. The results indicate that the non-continuous character of the spinel layers originates from nanoscale phases such as iron-rich oxides along the chromite grain boundaries and silicate particles. Their role in the rate of intergranular corrosion is discussed.

© 2014 Acta Materialia Inc. Published by Elsevier Ltd. All rights reserved.

**Keywords:** Atom probe tomography; Corrosion; Oxidation; Stainless steel; Chromium oxide spinels

For better efficiency, higher operating temperatures are required for thermal energy production technologies such as coal, nuclear, geothermal and solar thermal electric. This will lead to an increasing demand for affordable advanced high-temperature alloys. Austenitic stainless steels (ASSs) are the alloys of choice for high-temperature energy technologies that require a combination of affordability, strength and corrosion resistance. However, the high-temperature corrosion resistance of these stainless steels must be improved if it is to withstand the extreme operating conditions of new high-temperature technologies such as concentrated solar power (CSP), where temperatures can cycle from room temperature to up to 1000 °C [1]. For example, a recent study highlighted the failure of a commercial high-temperature ASS (253 MA) used as a CSP receiver via an oxidation-induced martensitic transformation associated with intergranular corrosion (IGC) [2]. The composition and structure of the intergranular scale formed during CSP operation play a significant role in the rate at which IGC progresses.

It is well established that Cr-rich oxide scales such as Cr<sub>2</sub>O<sub>3</sub> or FeCr<sub>2</sub>O<sub>3</sub> are more protective than Fe-rich oxide scales [3]. Numerous studies have characterized surface oxide scales formed in (Cr–Ni) ASS at high temperature in air [4,5]. These studies were carried out mainly by thermodynamic calculations and by using X-ray diffraction, spectroscopy techniques and analytical electron microscopy

for microscale observations. Characterization of the intergranular oxide scale at an atomic level can provide additional insights useful for the development of alloys with improved high-temperature corrosion resistance. In the last decade, local electrode atom probe (LEAP) has also been applied to study oxide layers. For example, metallic oxide phases, such as wustite [6], hematite [7], chromia [8], as well as surface oxide layers in stainless steels or nickel-based alloys [9–11], have been characterized by using laser-pulsed LEAP. Here we use LEAP to reveal the atomic-scale structure of intergranular oxides that have formed in a commercial ASS (253 MA) used as a receiver in a CSP plant.

A Sandvik 253 MA ASS (Fe–0.08C–21–Cr–10.8Ni–1.64Si–0.58Mn–0.02P–0.44Cu–0.19Mo–0.06V–0.01Ti–0.17N–0.05Ce/La in wt.%) alloy was subjected to thermal cycles in air between room temperature up to 970 °C for four day-and-night cycles [2]. A cross-section of the tube was prepared by mechanically polishing for scanning electron microscopy. The oxides within the IGC region were analyzed by energy-dispersive X-ray spectroscopy (EDS) and electron backscatter diffraction (EBSD) on a Zeiss Ultra scanning electron microscope. APT samples were prepared from IGC layers using a Zeiss-Auriga focused ion beam (FIB) equipped with a Kleindiek micromanipulator system. Two bars of corrosion layers from two different IGC areas were lifted-out. Samples were milled from these bars, attached to electropolished molybdenum grids and finally milled to form APT tips [12]. The APT experiments were conducted on a Cameca LEAP 4000X Si™ atom probe equipped with a picosecond-pulse ultraviolet laser. The data were reconstructed using the Cameca software IVAS 3.6.6. The dataset shown in Figure 2 was collected at a

<sup>\*</sup> Corresponding author at: School of Aerospace, Mechanical, Mechatronic Engineering, The University of Sydney, NSW 2006, Australia; e-mail: [alex.lafontaine@sydney.edu.au](mailto:alex.lafontaine@sydney.edu.au)



temperature of 50 K, with a pulse energy of 75 pJ and a frequency of 250 kHz operating at an evaporation rate of 0.5%. The dataset shown in Figures 3 and 4 was collected at a temperature of 55 K, with a pulse energy of 40 pJ and a frequency of 500 kHz operating at an evaporation rate of 0.5%.

Scanning electron microscopy investigation of a cross-section of the receiver tube after 100 h of service revealed extensive IGC cracks penetrating beneath the surface of the tube by  $\sim 1.3$  mm (Fig. 1a). This IGC is the result of sensitization [13,14] during thermal cycling. Sensitization leads to a depletion of Cr at the grain boundaries (GBs) such that a protective Cr-rich scale cannot be formed and the alloy is preferentially oxidized in and around the GBs. Based on previous studies in which similar alloys were oxidized in air at above 900 °C, possible oxide phases include a mix of spinels ( $\text{FeCr}_2\text{O}_4$ ,  $\text{Fe}_3\text{O}_4$ ,  $\text{Mn}_{0.5}\text{Cr}_{0.5}\text{O}_4$ ,

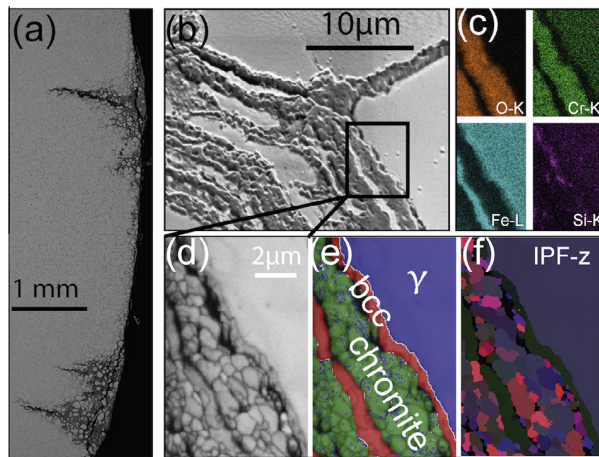


**Fig. 1.** Intergranular corrosion (IGC) in 253MA after thermal cycling. (a) Z-contrast backscattered electron image of a cross-section of the sample showing several large IGC cracks. (b) Secondary electron image of a section of an IGC area. The marked area shows where the EBSD/EDS mapping was done. (c) EDS O-K, Cr-K, Fe-L and Si-K maps. (d) EBSD pattern quality map. (e) EBSD phase map. (f) IPF-z orientation map. Note the multiple grains of chromite revealed by EBSD (d–e).

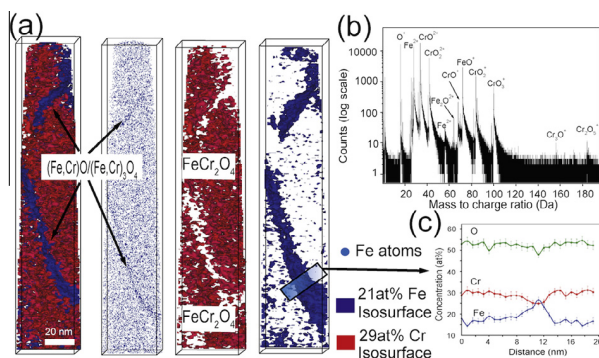


**Fig. 2.** APT reconstructed volumes of Fe-rich oxides within two chromite GBs. (a) Respectively, 29 at.% Cr and 21 at.% Fe isoconcentration map (6 nm slice of data), Fe atoms (3 nm slice), 29 at.% Cr isoconcentration map, and 21 at.% Fe isoconcentration map. (b) Indexed mass spectrum from the dataset (log scale). (c) Concentration profile across a chromite GB (volume marked in the Fe isoconcentration map in (a)).

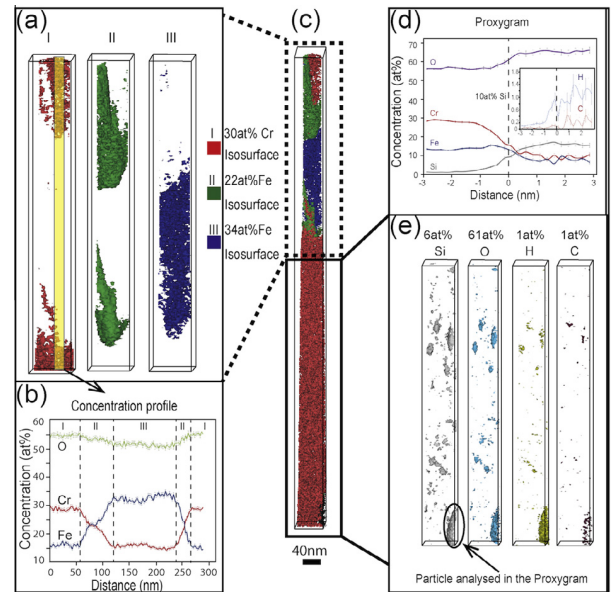


**Fig. 3.** APT reconstructed volumes of an IGC chromite layer containing Fe-rich oxides. (a) Isoconcentration maps of, respectively, 30 at.% Cr, 22 at.% Fe and 34 at.% Fe from the upper part of the reconstructed volume (dashed box). Zone I corresponds to chromite, zone II to a diffusion layer from chromite to Fe-rich oxide and zone III to a mix between ferrous oxide and Fe-rich spinel. (b) Concentration profile in the Z-direction across the upper part of the sample (see highlighted volume in (a)). Zones I, II and III are shown in the graph. (c) Isoconcentration maps of, respectively, 30 at.% Cr, 22 at.% Fe and 34 at.% Fe from the full reconstructed volume. (d) Proximity histogram (proxigram) analysis of a silicate particle (circled in (e)). (e) Isoconcentration maps of Si (6 at.%), O (61 at.%), H (1 at.%) and C (1 at.%) from the bottom part of the reconstructed volume.

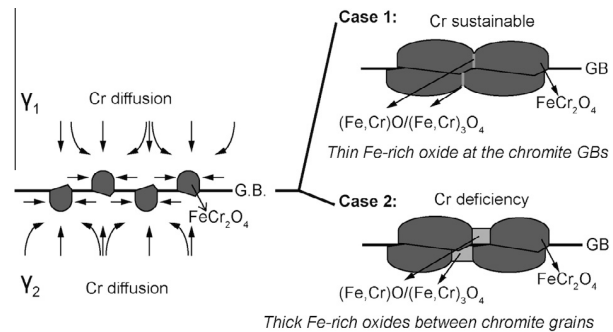


**Fig. 4.** Sketch showing the two proposed mechanisms for the formation of Fe-rich oxides within the chromite.

$\text{SiO}_2$ ) and corundum ( $\text{Cr}_2\text{O}_3\text{--Fe}_2\text{O}_3$ ) [5,15]. Other studies have showed the formation of  $(\text{Fe,Cr,Ni})\text{O}$  [16]. EBSD/EDS maps of a small area within a single IGC layer are shown in Figure 1b–d. The maps reveal that the primary oxide is the chromite-type oxide,  $\text{Fe}(\text{Fe,Cr})_2\text{O}_4$ . The austenite phase is the stainless steel and the body-centered cubic layers are caused by oxidation-induced Cr depletion [2].

With a high Cr content, the 253 MA ASS has been designed to withstand high-temperature corrosion in various environments [17]. However, the Cr depletion due to sensitization along GBs leads to the formation of intergranular Fe–Cr spinels instead of the more protective  $\text{Cr}_2\text{O}_3$  scale [3]. Moreover, some studies done on ASSs in

air + water vapor at high temperature revealed a reduction of the protective  $\text{Cr}_2\text{O}_3$  growth and a loss of Cr through vaporization [16,18].

Based on Figure 1 and our previous results [2], the oxidation layer can be summarized as consisting of spinel-type oxides, such as  $\text{FeCr}_2\text{O}_4$  or  $\text{Fe}(\text{Fe,Cr})_2\text{O}_4$ . Here we reveal a striking nanoscale structure within the spinel layer. Figure 2 displays the APT results of a tip sampled from an intergranular chromite region similar to the chromite region displayed in Figure 1. The sample was prepared from a bar lifted out parallel to the initial ASS GB. This 6 million atom data set contains two grain boundaries, as seen in Figure 2a. Figure 2 shows a series of images from a 6 nm thick slice of data. The different images show isoconcentration surfaces (29 at.% Cr, red; 21 at.% Fe, blue) and a 3 nm slice Fe atom map (second from the left). The mass spectrum from this region is shown in Figure 2b. Chromium was evaporated as  $\text{Cr}^{2+}$ ,  $\text{CrO}^{+,2+}$ ,  $\text{CrO}_2^{+,2+}$ ,  $\text{CrO}_3^+$  and  $\text{Cr}_2\text{O}_5^+$ . Iron was evaporated as  $\text{Fe}^{+,2+}$ ,  $\text{FeO}^+$  and  $\text{Fe}_2\text{O}^{2+}$ . Oxygen was evaporated both as oxide-ion species and as  $\text{O}^+$ ,  $\text{OH}^+$  and  $\text{O}_2^+$ . No Ni was detected in the scales and a trace amount of Mn was detected. The measured composition of the GBs and the chromite is summarized in Table 1 and a concentration profile through a boundary shown in Figure 2c. With a Fe:Cr ratio of 1:1.9 the measured composition is very close to a stoichiometric chromite spinel  $\text{FeCr}_2\text{O}_4$ . There is a deficit in O measured within the chromite. A “loss” of oxygen during APT evaporation has previously been observed, documented and tentatively explained [6,7,10,19]. For example, around 3 at.% O, a deficit was observed in the case of  $\alpha\text{-Fe}_2\text{O}_3$  [7]. The measured composition of the GBs is very close to a spinel  $(\text{Fe,Cr})_x\text{O}_y$ , with  $x/y$  ranging between 0.8 and 1. This grain boundary layer of Fe-rich oxide is thought to be a mixture between ferrous oxide,  $(\text{Fe,Cr})\text{O}$  ( $x/y = 1$ ), and Fe-rich spinel,  $\text{Fe}(\text{Fe,Cr})_2\text{O}_4$  ( $x/y = 0.75$ ). This is similar in composition to the oxide in the Cr diffusion zone in the case of surface oxide scales [16].

In addition to the grain boundary oxides, thicker regions of the Fe-rich oxide are also observed. Figure 3 shows a 10 million atom data set of an oxide layer lifted-out from an IGC area. This reconstructed volume contains several zones, as illustrated in Figure 3a and in the concentration profile (Figure 3b): a Cr-rich spinel (in red, labeled I), which surround san Fe-rich mixed oxide (in blue, labeled III) sandwiched between two gradient zones (in green, labeled II). The composition of the two Cr-rich and Fe-rich regions is summarized in Table 1. Based on their composition, the Cr-rich zone is close to stoichiometric chromite,  $\text{FeCr}_2\text{O}_4$ . The Fe-rich oxide,  $(\text{Fe,Cr})_x\text{O}_y$ , has an  $x/y$  ratio between 0.8 and 1, and is a mixture of ferrous oxide,  $(\text{Fe,Cr})\text{O}$  ( $x/y = 1$ ) and Fe-rich spinel,  $\text{Fe}(\text{Fe,Cr})_2\text{O}_4$ . Thus, the Fe-rich oxide in Figure 3a–c and the oxides along the GBs in Figure 2 are thought to have the same spinel structure with a different Fe:Cr ratio. The thicker spinel contains more Fe.

**Table 1.** The composition of oxides in different regions.

	Fig. 2		Fig. 3	
	Chromite	GBs	Chromite	Fe-rich layer
O (at.%)	53 ± 1.7	50 ± 1.7	55 ± 1.0	51.5 ± 1.0
Cr (at.%)	29.9 ± 1.5	25 ± 1.6	29 ± 1.0	15.5 ± 0.9
Fe (at.%)	15.7 ± 1.3	25 ± 1.4	14.8 ± 0.7	32.4 ± 1.0
Fe:Cr ratio	1:1.9	1:1	1:1.95	2:1:1

Although the chromite layer appears homogeneous on the microscale (Fig. 1), laser-pulsed atom probe reveals nanoscale heterogeneities in the Fe-rich oxides in this layer. The Fe-rich oxides, a mixture of  $(\text{Fe,Cr})\text{O}$  and  $(\text{Fe,Cr})_3\text{O}_4$ , can be classified as (1) thin and (2) thick as shown in Figures 2 and 3a–c, respectively. Their formation mechanism depends on whether sustainable Cr diffusion can be achieved for the growth of  $\text{FeCr}_2\text{O}_4$  chromites. Figure 4 illustrates the proposed mechanism. When the Cr supply is sustainable,  $\text{FeCr}_2\text{O}_4$  spinels can continuously grow toward each other. Hence, a thin Fe-rich/Cr-depleted zone can remain between two  $\text{FeCr}_2\text{O}_4$  chromites. After this zone is oxidized, films of Fe-rich oxide form along the grain boundary of chromite, as shown in Figure 2. On the other hand, when the Cr supply is not sufficient, larger Fe-rich oxides will form before chromite grows over the zone. As a result, blocks of Fe-rich oxide can form between chromites (Fig. 3a–c). The Cr depletion can result from sensitization and prior oxidation during the thermal cycling. This mechanism is also supported by the gradient of Cr between two  $\text{FeCr}_2\text{O}_4$  spinel domains observed in Figure 3b. These Fe-rich oxides are in general less protective than the chromite layer [16]. These nanostructures within the chromite affect the alloy’s high-temperature oxidation behavior. The presence of thicker regions of Fe-rich oxide within the chromite is more detrimental to its protective character than the thin films formed between chromite grains.

These results show the inhomogeneity of the scale formed in IGC during thermal cycling. To limit diffusion of Fe through the Cr-rich protective scale, and to obtain a more adhesive Cr-rich protective scale, 1.64 wt.% Si has been added to the ASS 253MA [17]. The beneficial role of Si in improving the high-temperature corrosion resistance of ASSs has been demonstrated. Above 800 °C, alloys with 1–2 at.% Si can form a thin and continuous layer of  $\text{SiO}_2$  and/or  $\text{Fe}_2\text{SiO}_4$  (fayalite) at the surface of the steel, improving the adherence of the Cr-rich oxide scale and limiting Fe diffusion [20,21]. However, some studies have shown that the Si-rich layer can be subject to spallation during thermal cycling [22]. The Si-L line map in Figure 1b confirms the presence of a Si-rich discontinuous oxide layer between the chromite and the stainless steel as well as some Si-rich particles within the chromite. Close investigation of atom probe data from the chromite phase revealed small Si-rich particles, as shown in Figure 3e. The composition of several silicate particles were measured using a proximity histogram (proxigram) analysis [23]. The proxigram of a typical particle is shown in Figure 3d. Several particles were analyzed and their composition was very similar within experimental error. The composition of a typical particle (circled in Fig. 4a) was 15 ± 1 at.% Si, 64 ± 1.3 at.% O, 8 ± 0.9 at.% Fe, 9 ± 1 at.% Cr. Trajectory aberrations due to the particle–matrix interface are often a concern and can lead to inaccuracy in the measured composition of the particle, so we have investigated further by looking at the density evolution within the whole dataset. The Si-rich particles have a much lower density than the surrounding matrix. Lower-density areas are the result of higher field evaporation. Based on the work of Larson et al. [24] in the case of high evaporation field precipitates with regards to the matrix, the matrix ions will be pushed away from the precipitate. Thus, in our case, there is not thought to be an issue with overlap from the matrix Fe/Cr in the Si-rich precipitate. Most of these particles contained a

non-negligible amount of H ( $1.2 \pm 0.3$  at.%) and C ( $0.3 \pm 0.1$  at.%). Considering that Cr ions can occupy the Fe ions sites, the ratio (Fe,Cr):Si in the silicate particles is 1:1.1, which is very close to the Fe:Si ratio in stoichiometric ferrosilite ( $\text{FeSiO}_3$ ). Ferrosilite is the result of the mix between  $\text{SiO}_2$  and  $\text{Fe}_2\text{SiO}_4$  [25]. However, the measured ratio Si:O is 1:4 instead of 1:3 for stoichiometric ferrosilite. This is due to the high O content measured in the particles. The presence of H and C could be explained by absorption of  $\text{H}_2\text{O}$  and  $\text{CO}_2$  in the silicates. The water and carbon dioxide coming from the atmosphere can diffuse in the IGC through the cracks. Olivines are often used to sequester  $\text{CO}_2$  and can easily react with water [26]. Here we were able to confirm that the protective  $\text{SiO}_2$  layer is not stable in IGC during thermal cycling. If chromium oxide has formed before  $\text{SiO}_2$ , diffusion of Si in oxide will be difficult. It is suggested that the tiny  $\text{SiO}_2$  particles engulfed in the chromium oxide could be internal oxides in the steel matrix from before the matrix was oxidized. The oxygen from the environment can penetrate through the scale of chromium oxide via the iron-rich domain, and diffuse into the austenite.

Laser-pulsed APT revealed additional nano structured phases in the protective chromite layer formed within IGC after thermal cycling. Fe-rich oxides were located between chromite grains. Moreover, small silicate particles are observed within the chromite, instead of a protective  $\text{SiO}_2$  layer, as the sample goes through thermal cycling. These “less protective” in homogeneous nanostructures in the chromite oxide layer may play an important role in the rate of IGC development.

Financial support from the Australian Renewable Energy Agency (ARENA) is gratefully acknowledged. The authors acknowledge the facilities and the scientific and technical assistance of the Australian Microscopy & Microanalysis Research Facility at the Australian Centre for Microscopy & Microanalysis at the University of Sydney.

- [1] O. Behar, A. Khellaf, K. Mohammedi, *Renew. Sustain. Energy Rev.* 23 (2013) 12.
- [2] A. La Fontaine, H.-W. Yen, P. Trimby, S. Moody, S. Miller, M. Chensee, S. Ringer, J. Cairney, *Corros. Sci.* 85 (2014) 1.
- [3] N. Birks, G.H. Meier, F.S. Pettit, *Introduction to the High Temperature Oxidation of Metals*, Cambridge University Press, Cambridge, 2006.
- [4] M. da Cunha Belo, M. Walls, N.E. Hakiki, J. Corset, E. Picquenard, G. Sagon, D. Noël, *Corros. Sci.* 40 (1998) 447.
- [5] I. Saeki, T. Saito, R. Furuichi, H. Konno, T. Nakamura, K. Mabuchi, M. Itoh, *Corros. Sci.* 40 (1998) 1295.
- [6] M. Bachhav, R. Danoix, F. Danoix, B. Hannoyer, S. Ogale, F. Vurpillot, *Ultramicroscopy* 111 (2011) 584.
- [7] M. Bachhav, F. Danoix, B. Hannoyer, J.M. Bassat, R. Danoix, *Int. J. Mass Spectrom.* 335 (2013) 57.
- [8] D.J. Young, T.D. Nguyen, P. Felfer, J. Zhang, J.M. Cairney, *Scripta Mater.* 77 (2014) 29.
- [9] S. Lozano-Perez, D.W. Saxey, T. Yamada, T. Terachi, *Scripta Mater.* 62 (2010) 855.
- [10] K. Kruska, S. Lozano-Perez, D.W. Saxey, T. Terachi, T. Yamada, G.D.W. Smith, *Corros. Sci.* 63 (2012) 225.
- [11] S.-I. Baik, X. Yin, D.N. Seidman, *Scripta Mater.* 68 (2013) 909.
- [12] P.J. Felfer, T. Alam, S.P. Ringer, J.M. Cairney, *Microsc. Res. Tech.* 75 (2012) 484.
- [13] E.C. Bain, R.H. Aborn, J.J.B. Rutherford, *Trans. Am. Soc. Steel Treat* (1933) 481.
- [14] M.H. Lewis, B. Hattersley, *Acta Metall.* 13 (1965) 1159.
- [15] N. Karimi, F. Riffard, F. Rabaste, S. Perrier, R. Cuffe, C. Issartel, H. Buscail, *Appl. Surf. Sci.* 254 (2008) 2292.
- [16] R. Peraldi, B. Pint, *Oxid. Met.* 61 (2004) 463.
- [17] Sandvik. Sandvik 253 MA (Tube and pipe, seamless), 2013.
- [18] M. Halvarsson, J.E. Tang, H. Asteman, J.E. Svensson, L.G. Johansson, *Corros. Sci.* 48 (2006) 2014.
- [19] M. Tsukada, H. Tamura, K.P. McKenna, A.L. Shluger, Y.M. Chen, T. Ohkubo, K. Hono, *Ultramicroscopy* 111 (2011) 567.
- [20] S. Basu, G. Yurek, *Oxid. Met.* 36 (1991) 281.
- [21] R. Jargelius-Pettersson, *Microsc. Oxid.* (1996) 515.
- [22] B. Gleeson, M. Harper, Effects of minor alloying additions on the oxidation behaviour of chromia-forming alloys, *Proc. EFC Workshop* 34 (2001) 167.
- [23] O.C. Hellman, J.A. Vandenbroucke, J. Rüsing, D. Isheim, D.N. Seidman, *Microsc. Microanal.* 6 (2000) 437.
- [24] D.J. Larson, B. Gault, B.P. Geiser, F. De Geuser, F. Vurpillot, *Curr. Opin. Solid State Mater. Sci.* 17 (2013) 236.
- [25] B.J. Wood, O.J. Kleppa, *Geochim. Cosmochim. Acta* 45 (1981) 529.
- [26] O. Qafoku, L. Kovarik, R.K. Kukkadapu, E.S. Ilton, B.W. Arey, J. Tucek, A.R. Felmy, *Chem. Geol.* 332–333 (2012) 124.

---

## **11 Laser-assisted APT analysis parameters influence on zircon minerals data quality**

As described in the literature review and previous chapters, APT is no longer limited to conductive materials due to the use of a pulsed laser to field evaporate ions. The unique resolution of APT, both spatial and chemical, makes this technique an ideal tool for the characterization of atomic scale processes that occur in rock-forming minerals, in particular, zircons. Recently the first successful laser-assisted APT investigation of a zircon confirmed its age as being the oldest zircon ever dated. It also revealed nano-size clusters well dispersed throughout the samples (46, 172). The dating of zircons relies on the assumption that the mineral is a closed system and trace elements such as Pb or U cannot integrate the crystal after its formation, and neither can they diffuse out. As previously described in the literature review, several studies reported a possible diffusion of Pb and other trace elements in deformed regions within zircons. However, such processes have never been characterized due to the scale at which they happen. Laser-assisted APT is ideally suited to characterize such mechanisms. It is thus important to assess the data quality and optimize the laser analysis parameters for the APT study of deformed zircons.

This publication contributes to the present thesis by providing a full assessment of the influence of laser-assisted APT analysis parameters on overall data quality for a range of deformed zircons. Detection limits of key trace elements are also discussed and the use of combined EBSD/TKD to characterize the deformations in zircons is presented.

The content of this article (in submission) is largely the product of the work of Alexandre La Fontaine under the supervision of Julie M. Cairney. Sandra Piazzolo and Patrick Trimby contributed to the interpretation of results and assisted in the writing. Limei Yang carried out the sample preparation.

This article has been submitted the 15<sup>th</sup> of March 2016 to the journal *Microscopy and Microanalysis*.

---

**Title**

Laser-assisted atom probe tomography of deformed minerals: a zircon case study

**Authors**

Alexandre La Fontaine<sup>a, b\*</sup>, Sandra Piazzolo<sup>c</sup>, Patrick Trimby<sup>b</sup>, Limei Yang<sup>b</sup>, Julie M. Cairney<sup>a</sup>,

b

**Affiliations**

- a. School of Aerospace, Mechanical, Mechatronic Engineering, The University of Sydney, NSW 2006, Australia
- b. Australian Centre for Microscopy and Microanalysis, The University of Sydney, NSW 2006, Australia
- c. Department of Earth and Planetary Science, Macquarie University, NSW 2109, Australia

**\* Corresponding Author****Abstract**

The application of atom probe tomography (APT) to the study of minerals is a rapidly growing area. Picosecond-pulsed ultraviolet-laser (UV-355 nm) assisted APT has been used to analyze trace element mobility within dislocations and low-angle boundaries in plastically deformed specimens of the non-conductive mineral zircon ( $ZrSiO_4$ ). Here we discuss important experimental aspects inherent in the APT investigation of this important mineral, providing insights into the challenges in APT characterization of minerals as a whole. We studied the influence of APT analysis parameters on features of the mass spectra, such as the thermal tail, as well as the overall data quality. Three zircon samples with different uranium (U) and lead (Pb) content were analyzed, and particular attention was paid to ion identification in the mass spectra and detection limits of the key trace elements, Pb and U. We also discuss the correlative use of electron backscattered diffraction (EBSD) in a

---

scanning electron microscope (SEM) to map the deformation in the zircon grains, and the combined use of transmission Kikuchi diffraction (TKD) and focused ion beam (FIB) sample preparation to assist preparation of the final APT tip.

### **Keywords**

Atom probe tomography, mineral zircons, lead detection, deformation, dislocations, TKD

### **1. Introduction**

The non-conductive mineral zircon ( $\text{ZrSiO}_4$ ) is ideally suited for radiogenic dating of rocks. Not only does it contain trace amounts of uranium (U) and thorium (Th), enabling radiogenic dating (Hay & Dempster, 2009; Williams, et al., 1984), it is also physically and chemically robust, surviving a range of geological processes such as erosion, deformation and high-grade metamorphism (up to 900 °C) (Harley, et al., 2007). However, several recent studies have suggested that zircons may not be as chemically robust as once believed, especially on the micron and sub-micron scale in regions of the sample that have been affected by deformation (Reddy, et al., 2006). Measuring such chemical variations is a challenge, since the spatial resolution of conventional geochemical analysis techniques such as sensitive high resolution ion microprobe (SHRIMP) and laser – ICPMS is in the range of 5-15  $\mu\text{m}$  and 15- 50  $\mu\text{m}$  respectively,

Atom probe tomography (APT) is a powerful microscopy technique that can provide 3D maps showing the position and atomic mass of individual atoms with sub-nanometre resolution. In the last ten years laser-assisted APT has been increasingly used to analyse oxide-based materials (Bachhav, et al., 2011b; Baik, et al., 2013; Hono, et al., 2011; Kirchhofer, et al., 2014; La Fontaine, et al., 2015a; La Fontaine, et al., 2015b; Larson, et al., 2008; Marquis, et al., 2010; Mazumder, et al., 2011; Oberdorfer, et al., 2007; Stiller, et al., 2016; Stiller, et al., 2013). APT is ideal for studying the spatial distribution of atoms across

---

small volumes. The isotopic sensitivity of APT analysis is also an advantage for its application in the study of geological materials, where isotope ratios are commonly used to derive characteristics of the geological history of a specimen (Davis, et al., 2003). For example, APT has recently been applied for the first time to U/Pb isotope dating in zircon (Valley, et al., 2014; Valley, et al., 2015), where the results were found to agree well with SIMS-based results. APT was also used to reveal the diffusion of trace elements at dislocations and low-angle boundaries in deformed zircons (Piazolo, et al., 2016). However, unanswered questions remain about the distribution of trace elements within zircons, and the unique capabilities of APT applied to the fundamental study of zircons at the atomic level mean that the technique is likely to become a common approach to investigate this important geological mineral.

However, the study of large band gap materials such as oxides with laser assisted APT remains challenging due to their poor thermal conductivity (Balasubramaniam & Callister, 2009). There is a need for more detailed information about the influence of APT analysis parameters on data quality from zircons and the limitations in the quantification and detectability of significant trace elements such as Pb and U. In addition, in order to investigate potential trace element diffusion within dislocations in deformed zircons it is important to be able to identify the nature of local deformation within the region of the sample that is analysed. This may be achieved by correlating electron backscattered diffraction (EBSD) and/or transmission Kikuchi diffraction (TKD) (Trimby, 2012) with APT.

In this paper, we focus on the influence of APT analysis parameters (laser pulse energy and frequency, base temperature) on the overall data quality and mass spectrum thermal tail. We discuss the important topic of ion identification in the APT mass spectrum and assess the Pb and U detection and quantification limits for 2 different zircons. Finally, we present a

---

correlative EBSD, TKD and APT approach for the study of trace element mobility in deformed zircons.

## **2. Materials and methods**

The zircons used in this study come from two different regions: plastically deformed Archean zircons (~2.5 Ga old) from the Napier complex in Antarctica and younger zircons from a decimeter wide high strain zone developed on the island of Krossey within the Bergen Arc of southwest Norway (age range ~ 760 Ma to 405 Ma). The Archean zircons, namely DN5 and DN77 contain ~ 2000 ppma U, ~ 600 ppma Pb and ~150 ppma U, ~ 60 ppma Pb respectively. In contrast, those from the Bergen Arc contain ~10 ppma U and ~1 ppma Pb.

The general microstructure of the zircons was characterized using combined EBSD and energy dispersive X-ray spectroscopy (Arvizu) in a Zeiss Ultra Plus field emission gun (FEG) SEM. Regions of interest (low-angle boundaries with small misorientations, < 4°) were then selected based on the EBSD deformation maps. APT samples were prepared using a Zeiss-Auriga focused ion beam (FIB) SEM equipped with a Kleindiek micromanipulator system. Bars of selected areas were lifted-out from milled cross sections using the micromanipulator. Samples were milled from these bars, attached to electropolished molybdenum grids and finally milled to form APT tips with a typical diameter of around 60 nm. (Felfer, et al., 2012) The deformation structures within each APT tip were analyzed in the FIB-SEM using TKD after the final annular milling. The APT experiments were conducted on a Cameca LEAP 4000X Si<sup>TM</sup> atom probe equipped with a picosecond-pulse ultraviolet laser (355 nm, spot size < 4 µm). The data were reconstructed using Cameca IVAS 3.6.6.



### 3. Results and discussion

#### 3.1 Effect of laser energy

The influence of laser energy on the mass spectra quality was investigated to determine the optimum laser energy for zircon, as an example of a typical mineral. A single tip of the Krossey zircon was used and the laser energy was progressively increased from 25 pJ to 700 pJ. This experiment was carried out at a base temperature of 60 K, a laser pulse repetition rate of 250 kHz and an evaporation rate of 1%. A total of 1 million atoms per laser energy condition were collected. It is important to note that several factors such as tip radius and voltage are changing with laser energy increase. The tip radius is increasing slightly after each million atoms collected. The interaction volume with the laser becomes greater improving the thermal conductivity at the apex. However, this effect is thought to be minimal due to the small volume evaporated between each laser energy. Fig.1a shows the mass spectra of the  $\text{ZrO}^{2+}$  and  $\text{SiO}_2^+$  peaks for data collected at different laser pulse energies.

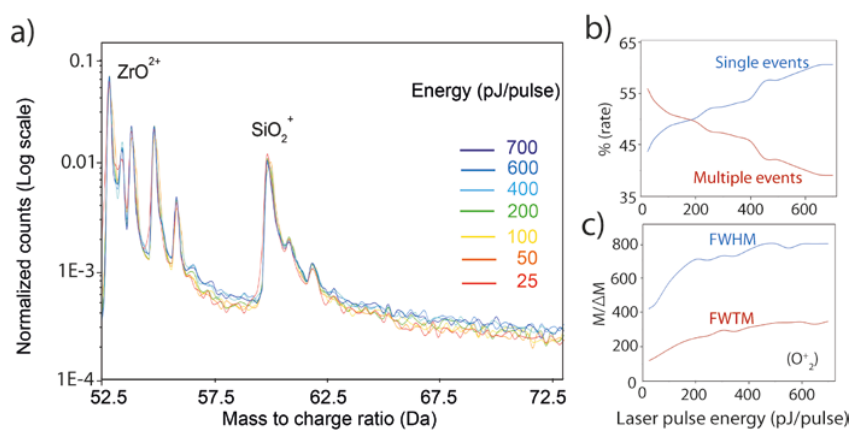


**Fig.1.** Effect of laser pulse energy on zircon data quality. (a) Normalized mass spectrum of  $\text{ZrO}^{2+}$  and  $\text{SiO}_2^+$  for different laser pulse energies (25 pJ to 700 pJ). (b) Evolution of single and multiple events rate with laser pulse energy. (c) Full-width half maximum (FWHM) and full-width tenth maximum (FWTM) calculated at 32 Da ( $\text{O}_2^+$ ) for different laser pulse energies.

Laser-assisted field ionization is a thermal process inducing local heating of the tip, which in turn provokes a broadening of the peak tail (Vurpillot, et al., 2009). The extent of the tail broadening (thermal tail) is function of the local heating intensity and tip cooling rate. The thermal tail after each peak only slightly increases with increasing laser energy. We therefore conclude that the local heating of the tip due to the laser pulse is minimal with only a limited effect on the extent of the tail behind each peak. It shows that mineral zircon has a sufficiently high thermal diffusivity and fast cooling rate when exposed to the picosecond UV laser. The temperature conductivity of zircon was reported to have only a minimal dependency on temperature above 300 K - 400 K (Kingery, et al., 1954). This explains the relatively fast thermal diffusivity of the zircons at high laser energy. The mass resolving power (mass resolution of a specific peak) in APT is usually measured as full-width half maximum (FWHM) and full-width tenth maximum (FWTM) on a peak around 30 Da (Larson, et al., 2013). The FWHM and FWTM measured at 32 Da ( $O_2^+$ ) increases with increasing laser energy and reaches a plateau from  $\sim 400$  pJ with FWHM  $\sim 780$  and FWTM  $\sim 320$ .

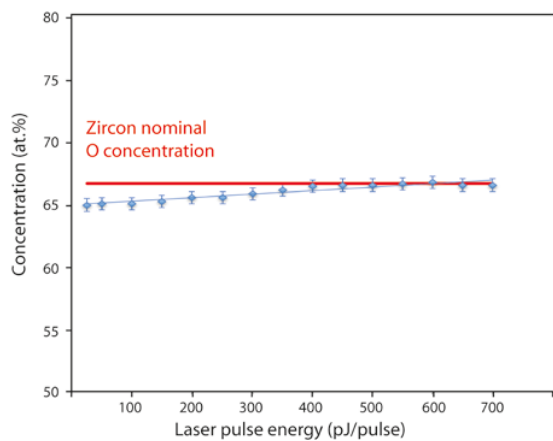


**Fig.2.** Effect of laser pulse energy on measured oxygen content.

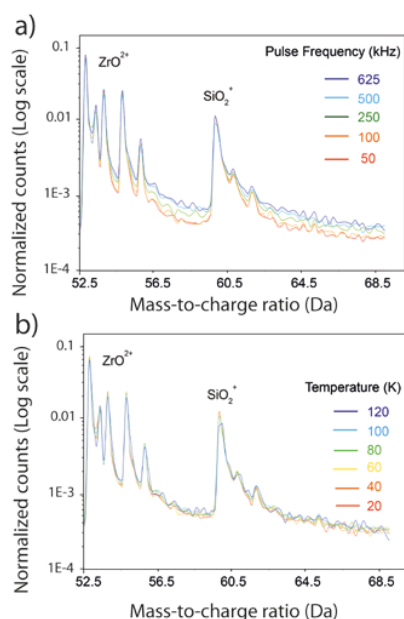
---

Fig.1b shows that increasing laser energy results in an increase in the proportion of single events (and a decrease in the proportion of multiple events). Multiple events often lead to noise and data loss can occur from in-flight molecular ion dissociations. (Saxey, 2011) An increase in the rate of single hits/pulse thus improves APT data quality.

Fig.2 shows the evolution of the measured oxygen content with an increase of laser energy. Between 25 pJ and 400 pJ, the oxygen content increases from 65 at. % to 66.5 at.%. There is no significant variation above 400 pJ. Overall the laser pulse energy has only a very limited effect on measured oxygen concentration with less than 2 at. % variation of measured O content. Here we find that the measured O content is almost identical to the nominal O composition of 66.7 at%. This result contrasts with the observation of O loss with increasing laser energy that was reported in several studies (Bachhav, et al., 2013; Bachhav, et al., 2011a; Kirchhofer, et al., 2014; Kruska, et al., 2012; Tsukada, et al., 2011).

### 3.2 Effect of laser pulse frequency and base temperature

The effect of the laser pulse frequency on the mass spectrum quality was also investigated. A single tip of zircon (Krossey sample) was used with a laser pulse energy of 400 pJ, at a base temperature of 60 K and an evaporation rate of 1%. One million atoms were collected for each laser pulse frequency. Fig.3a shows the mass spectra of the  $\text{ZrO}^{2+}$  and  $\text{SiO}_2^+$  peaks for 5 different laser pulse repetition rate (from 50 kHz to 625 kHz).



**Fig.3.** Effect of laser pulse frequency and sample base temperature. Normalized mass spectrum of  $\text{ZrO}^{2+}$  and  $\text{SiO}_2^+$  (a) for different laser pulse frequencies (50 kHz to 625 kHz) (b) for different specimen base temperatures (20 K to 120 K).

There is a significant increase in the size of the thermal tail with increasing laser pulse frequency. The slower the repetition rate, the more time there is for the heat to dissipate, decreasing the thermal tailing effect. A higher pulsing rate means a shorter time detection window, which could induce a specific loss of the heavier molecular ions due to their time of flight out of the detection time window (Gault, et al., 2012). However, a slower laser pulse frequency increased the experiment duration due to a considerably slower evaporation flux, which potentially increases the probability of sample failure by increasing the length of time under electrostatic pressure.

The effect of sample base temperature on mass spectrum quality was also investigated for a single tip with laser pulse energy of 400 pJ, a laser pulse frequency of 250 kHz and an evaporation rate of 1%. As shown in Fig. 3b there is no change in thermal tail with increasing

---

base temperature up to 120 K. A higher temperature is usually beneficial for a decrease of tip fracture as it lowers the field and the electrostatic pressure (Wilkes, et al., 1972).

### 3.3 Ion identification in zircon

In APT the mass-to-charge ratios of ions are recorded by time-of-flight mass spectroscopy (Gault, et al., 2012). Correct identification of the peaks in the mass spectrum is essential for accurate elemental analysis. High resistivity materials such as complex oxides lead to particularly challenging mass spectra especially when using high laser energy leading to higher probability of molecular ion evaporation but also due to the large number of elements and the potential for peak overlaps. In order to discriminate peaks when they overlap the isotopic ratio is generally used to deconvolve those particular peaks, resulting in a more accurate composition measurement (Kunicki, et al., 2006). However, this method cannot be used with radiogenic elements such as Pb or U in zircons, which limits the isotopes we can use for dating. Three mass spectra from the different zircon samples (DN5, Krossey and DN77) are shown in Fig. 4. The main elements detected were, as expected, Zr, Si and O. Silicon was detected as  $\text{Si}^{2+}$ ,  $\text{SiO}^+$ ,  $\text{SiO}_2^+$ ,  $\text{Si}^{3+}$ ,  $\text{Si}^+$ ,  $\text{SiO}^{2+}$ ,  $\text{SiO}_3^+$ ,  $\text{ZrSiO}_3^{2+}$ ,  $\text{Si}_2\text{O}_4^+$  and  $\text{Si}_2\text{O}_3^+$  (in order of importance). Zirconium was detected as  $\text{ZrO}^{2+}$ ,  $\text{Zr}^{3+}$ ,  $\text{ZrO}^{3+}$ ,  $\text{Zr}^{4+}$ ,  $\text{Zr}^{2+}$ ,  $\text{ZrSiO}_3^{2+}$ ,  $\text{ZrO}^+$  and  $\text{ZrO}_2^+$ . Oxygen was mainly detected as  $\text{O}^+$  and  $\text{O}_2^+$ , as well as in the form of molecular ions combined with Si, Zr and some of the trace elements. The main trace elements detected were U ( $\text{UO}_2^{2+}$ ,  $\text{UO}^{2+}$ ,  $\text{UO}^{3+}$ ,  $\text{U}^{3+}$ ), Pb ( $\text{Pb}^{2+}$ ), Al ( $\text{Al}^+$  and  $\text{Al}^{2+}$ ), Li ( $\text{Li}^+$ ), Y ( $\text{Y}^{3+}$ ), and Hf ( $\text{HfO}^{2+}$ ). The following elements were also detected in some of the samples: Mg, P, Yb, Gd, Ta, Be, Lu. The mass spectra from the 3 different samples were very consistent with only very minor differences. Mg is only detected in DN77. (Fig.4)

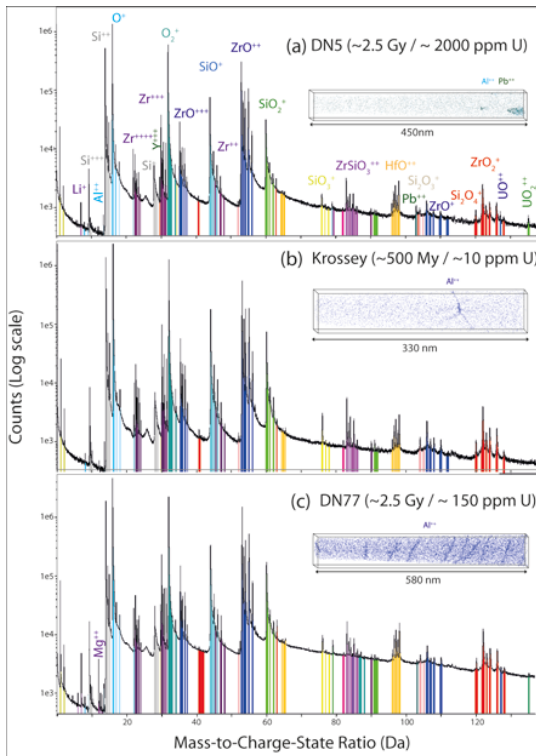


**Fig.4.** Ion identification in mineral zircon. **(a)** Mass spectrum of zircon DN5 (~15M atoms dataset, ~2.5 Ga, ~2000 ppma U, ~600 ppma Pb). Inset is the corresponding APT reconstructed volume ( $\text{Al}^{2+}$  in blue and  $\text{Pb}^{2+}$  in green) **(b)** Mass spectrum of zircon Krossey (~30M atoms dataset, ~500 Ma, ~10 ppma U, ~1 ppma Pb). Inset is the corresponding APT reconstructed volume ( $\text{Al}^{2+}$  in blue) **(c)** Mass spectrum of zircon DN77 (~42M atoms dataset, ~2.5 Ga, ~150 ppma U, ~60 ppma Pb). Inset is the corresponding APT reconstructed volume ( $\text{Al}^{2+}$  in blue)

The high laser energy necessary to thermally ionized zircon could explain the large number of molecular ions detected in the mass spectra (Affatigato, 2015). For the most prominent radiogenic elements (O, Si and Zr), we used isotopic ratios to validate the identification of ions and molecular ions. No major isobaric interference was encountered. While there is always H present in an APT dataset it is found to be reasonably low in all the datasets analyzed, which is indicative of a clean vacuum system. The presence of H during an APT experiment may lead to hydrides after each peak, impacting the composition measurement accuracy. The O content was around 66.5 at.% for all samples, very close to the nominal

---

composition of 66.7 at.%. A small deficit of measured Zr (~ 16 at.% instead of 16.7 at.%) and Si (~ 15.5 at.% instead of 16.7 at.%) was noted.

Some of the key trace elements for dating zircons are U, Pb, Th and Hf. Th was not detected in our datasets. Hf was only detected as  $\text{HfO}^{2+}$ . While it is possible to isolate the relative abundance for each HfO isotopes, most of them overlap. Only  $^{174}\text{Hf}^{16}\text{O}$  at 190 Da,  $^{174}\text{Hf}^{17}\text{O}$  at 191 Da and  $^{180}\text{Hf}^{18}\text{O}$  at 198 Da have no overlaps. However geologists use Hf176/Hf177 ratio (Scherer, et al., 2001), so it is impossible to use the Lutetium-Hafnium clock with APT analysis. The only Pb isotopes detected with no interference are  $^{206}\text{Pb}^{2+}$  and  $^{207}\text{Pb}^{2+}$  at 103 and 103.5 Da respectively, whereas  $^{208}\text{Pb}^{2+}$  overlaps with  $^{104}\text{Si}_2\text{O}_3^+$  at 104 Da (Valley, et al., 2014; Valley, et al., 2015).  $^{238}\text{U}$  and  $^{235}\text{U}$  decay to  $^{206}\text{Pb}$  and  $^{207}\text{Pb}$  respectively, allowing geologists to use the  $^{206}\text{Pb}/^{207}\text{Pb}$  ratios to provide accurate dating of zircons. In the case where both Pb isotope counts can be measured with good confidence, their ratio can be used to date an APT sample.

### 3.4 Key trace element detection and quantification limits

The minimum detection limit of a specific element mainly depends on the position of the peak in the mass spectrum and its associated background or noise level. The detection limit is also function of the number of ions collected, to achieve sampling statistics, and whether the element is homogeneously distributed within the material. Overlapping peaks are also an important factor as it is not always possible to deconvolve them. Generally, where conditions are optimal, the APT detection limit is ~10 ppma (Gault, et al., 2012).

Fig. 5 contains the mass spectra from 102 Da to 105 Da and 126 Da to 136 Da for sample DN5, containing a Pb-rich precipitate and the Krossey sample, containing Al-rich dislocations.

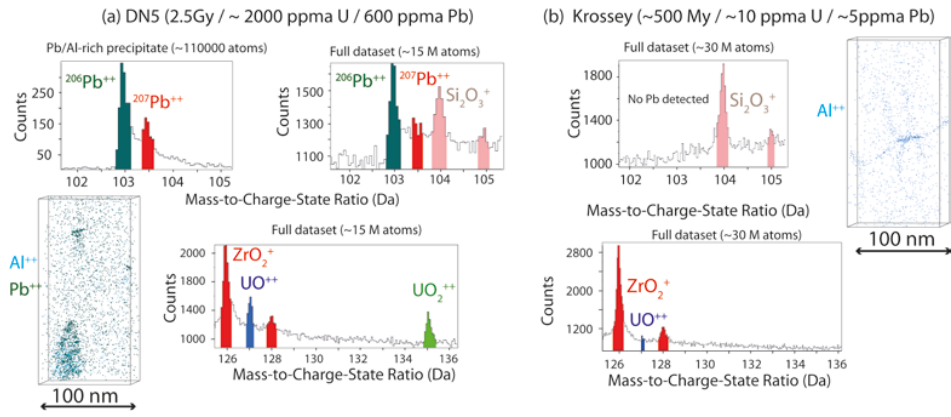


**Fig.5** Pb and U detection limits. (a) Mass spectra from 102 Da to 105 Da and 126 Da to 136 Da for the sample DN5. The first two mass spectra show Pb for the precipitate only and for the full data set. (b) Mass spectra from 102 Da to 105 Da and 126 Da to 136 Da for the Krossey sample.

In the Krossey sample, Pb is below detection limit and U was detected as  $\text{UO}^{++}$  just above the noise level (Fig.5-a), whereas both are able to be detected in the DN5 sample (Fig.5-b). The detection and quantification limits of a peak can be calculated based on the Currie definition (Currie, 1968). For a peak to be detected 95% of the time ( $L_{DL}$ ), its net value in counts should be  $> 4.65$  times the square root of the background. For a peak to be quantified at a satisfactory level ( $L_Q$ ) its net count should be above 14.1 times square root of the background (Larson, et al., 2013). The background should be assessed for each peak.

Pb is not detected in the Krossey sample.  $L_{DL} (^{206}\text{Pb}^{2+})$  and  $L_{DL} (^{207}\text{Pb}^{2+})$  are respectively  $\sim 410$  counts ( $\sim 13$  ppma) and  $\sim 325$  counts ( $\sim 10$  ppma). U is more complicated as it evaporates in the form of molecular ions and all the three peaks should be considered and decomposed. For instance, while  $L_{DL} (^{254}\text{UO}^{2+})$  is  $\sim 320$  counts ( $\sim 14$  ppma) the equivalent  $L_{DL}$  for U corresponding to this peak would be  $\sim 14$  ppma. For the Krossey sample, U was detected but cannot be quantified at a satisfactory level.

Pb and U are detected in the DN5 sample. In the full 16 million atom dataset,  $L_Q (^{206}\text{Pb}^{2+})$  and  $L_Q (^{207}\text{Pb}^{2+})$  are  $\sim 3890$  counts ( $\sim 55$  ppma) and  $\sim 5500$  counts ( $\sim 65$  ppma) respectively. The



---

measured net counts for  $^{206}\text{Pb}^{2+}$  is  $\sim 5660$  ( $\sim 350$  ppma), which is well above the quantification limit. However, the measured net counts for  $^{207}\text{Pb}^{2+}$  is  $\sim 300$  (19 ppma), which means it cannot be satisfactorily quantified. However, when we isolate the precipitate, the net counts for  $^{206}\text{Pb}^{2+}$  and  $^{207}\text{Pb}^{2+}$  are  $\sim 1425$  ( $\sim 13000$  ppma) and  $\sim 310$  (2820 ppma) respectively. In this case the quantification limits are  $\sim 77$  counts ( $\sim 700$  ppma) for  $^{206}\text{Pb}^{2+}$  and  $\sim 235$  counts ( $\sim 2100$  ppma) for  $^{207}\text{Pb}^{2+}$ .

Here we have shown the limits and possibilities of APT for key trace element analysis in zircons. It is necessary for zircons to have a minimum U content ( $> 50$  ppma) and/or to be old enough so the U decay produces enough Pb to be detected and quantified. The number of ions collected in an APT experiment is also of importance and greater sampling will improve the detection and quantification limits. Finally, the clustering of key trace elements in features such as dislocations or precipitates improves their detectability.

### 3.5 Correlative TKD/APT

APT is the only technique that combines sub-nanometer spatial resolution, high chemical sensitivity and isotopic resolution. It is therefore highly suited to the study of trace element distribution about deformation structures such as dislocations and low-angle boundaries in mineral zircons. To identify suitable areas within deformed regions, the use of EBSD is a prerequisite before preparing the APT sample. Fig. 6 illustrates a typical EBSD deformation map of the zircon from Bergen Arc, Norway. A forescatter electron image (fig. 6a), collected using backscatter electron detectors mounted below the EBSD phosphor screen (DAVID, 1996), shows regions of deformation within the zircon grain. These can then be quantified using EBSD orientation mapping (fig. 6b) allowing areas of interest to be identified for APT tip preparation in the FIB-SEM (fig. 6c).

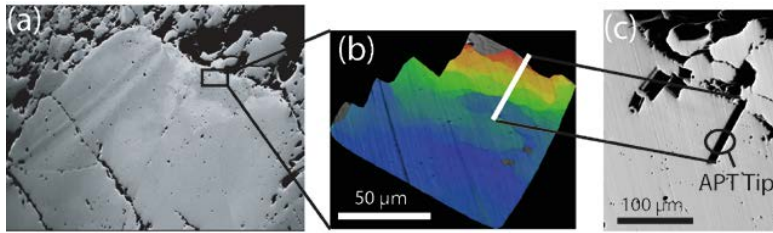


**Fig.6.** EBSD deformation mapping. (a) Forescattered electron image of part of the zircon grain. (b) EBSD relative orientation map (using the lower part of the map as the reference orientation). The colour change from blue to red represents 20° orientation change. (c) Area of APT tip lift-out

Once a sample has been lifted-out and thinned down to a suitable APT tip shape, TKD can be performed on the tip in the FIB/SEM to characterize any deformation structures in the tip (such as low angle boundaries and even the plastic strain associated with individual dislocations) with a spatial resolution below 10 nm and an angular resolution of 0.1-0.5°. If any features of interest are found, the APT tip can be taken out of the FIB/SEM and field evaporated in the APT. If TKD resolves no deformation structures, the tip can be further thinned down and the process repeated until a feature of interest appears. The advantages of using TKD in a FIB/SEM to simultaneously mill and image an APT tip were recently demonstrated (Babinsky, et al., 2014a; Babinsky, et al., 2014b). A highlight is no exchange between microscopes and very quick switchover between the 2 techniques. It is important to note that the TKD information arises dominantly from the lowermost analytical surface meaning that deformation structures that lie close to horizontal in the APT tip during TKD analyses may not be detected. This was the case in a low angle boundary running the length of one of the tips shown in recent work (Piazolo, et al., 2016). For a more complete characterization of the structures in a single tip, it would be better to perform at least 2 TKD scans (top and bottom surfaces of the tip, with a 180° rotation in between) and, ideally, 4 scans with the tip rotated 90° following each TKD scan. With multiple tips mounted on a polished Mo grid, it may only be possible to scan 2 surfaces of each tip using TKD due to

shadowing problems caused by other tips, but this is usually sufficient to detect all deformation structures.

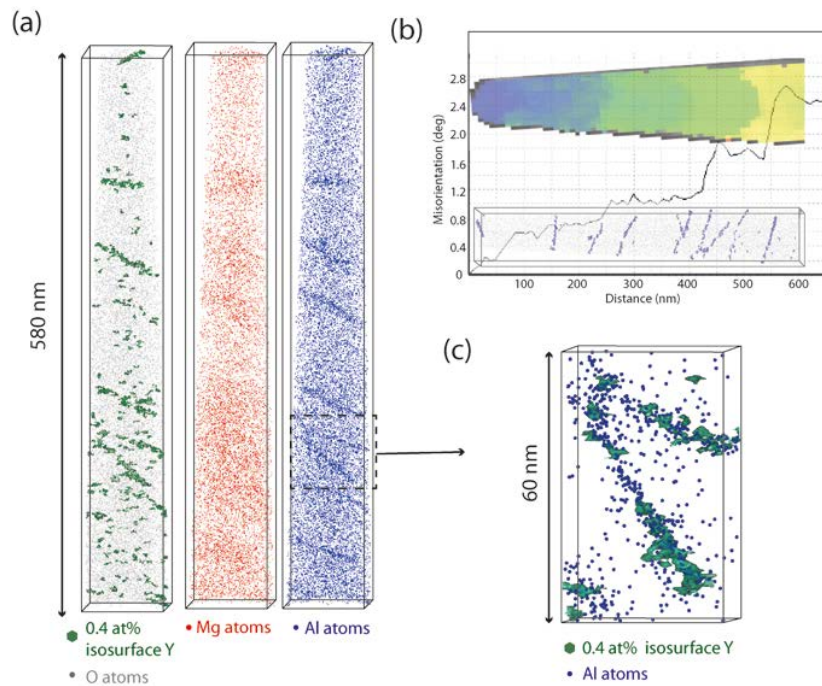


**Fig.7.** Correlative TKD/APT of a deformed zircon DN77. (a) APT atom maps of O (grey) with 0.4 at% isosurface Y (green), Mg (red) and Al (blue). Note the Al and Y segregation in all the dislocations and a cloud of Mg around the dislocations. (b) TKD deformation map (showing misorientations relative to the tip end) and associated misorientation profile. (c) APT 3D volume of 2 dislocations with 0.4 at.% isosurface of Y (green) and Al atoms (blue).

Fig. 7 illustrates correlative TKD/APT microscopy applied to the deformed zircon DN77. Fig. 7a shows the reconstructed 3D volumes for Mg and Al. The dislocations are readily apparent with a strong segregation of Al and Y (Fig. 7a, c and d). Interestingly, there is also segregation of Mg around the dislocations but it is much more spread out compared to Al. Fig. 7b contains both the TKD deformation map and the APT 3D reconstructed volume with the misorientation profile obtained from the TKD data laid over both images. Here we show that high-resolution TKD orientation mapping provides essential structural information on the degree of deformation across the tip due to geometrically necessary dislocations. The use of

---

APT on the same tip completes the nano-scale characterization of the sample deformation by revealing the elemental distribution within the dislocations that accommodate the observed deformation.

#### 4. Conclusion

The optimum acquisition parameters for the mineral zircon using UV-laser-assisted LEAP 400XSi<sup>TM</sup> were found to be ~ 400 pJ laser pulse energy, 250 kHz laser pulse frequency and ~ 60 K base temperature. These parameters generate very limited thermal effects, a good mass resolving power, an acceptable rate of single events per pulse and a good specimen yield. The mass spectra from different zircons were all similar and most of the peaks detected were identified. The detection and quantification limits of the key trace elements, U and Pb, were assessed using 2 different zircons and as expected they were found to be a function of the size of the dataset, the initial U content, the age of the zircon as well as the potential clustering of U or Pb. Finally, we demonstrate the necessity of correlative EBSD/TKD/APT microscopy for the study of the behaviour of trace elements in deformed zircons.

#### **Acknowledgement**

The authors acknowledge the facilities and the scientific and technical assistance of the Australian Microscopy & Microanalysis Research Facility at the Australian Centre for Microscopy & Microanalysis at the University of Sydney. SP acknowledges funding through the Australian Research Council through FT1101100070 and DP120102060.

---

## References

- AFFATIGATO, M. (2015). *Modern Glass Characterization*. Wiley.
- ARVIZU, D., P. BALAYA, L. CABEZA, T. HOLLANDS, A. JÄGER–WALDAU, M. KONDO, C. KONSEIBO, V. MELESHKO, W. STEIN, Y. TAMAURA, H. XU, R. ZILLES, 2011: DIRECT SOLAR ENERGY. IN IPCC SPECIAL REPORT ON RENEWABLE ENERGY SOURCES AND CLIMATE CHANGE MITIGATION [O. EDENHOFER, R. PICHs–MADRUGA, Y. SOKONA, K. SEYBOTH, P. MATSCHOSS, S. KADNER, T. ZWICKEL, P. EICKEMEIER, G. HANSEN, S. SCHLÖMER, C. VON STECHOW (EDS)]. (2011).
- BABINSKY, K., DE KLOE, R., CLEMENS, H. & PRIMIG, S. (2014a). A novel approach for site–specific atom probe specimen preparation by focused ion beam and transmission electron backscatter diffraction. *Ultramicroscopy* **144**, 9–18.
- BABINSKY, K., WEIDOW, J., KNABL, W., LORICH, A., LEITNER, H. & PRIMIG, S. (2014b). Atom probe study of grain boundary segregation in technically pure molybdenum. *Materials Characterization* **87**, 95–103.
- BACHHAV, M., DANOIX, F., HANNOYER, B., BASSAT, J. M. & DANOIX, R. (2013). Investigation of O–18 enriched hematite ( $\alpha$ -Fe<sub>2</sub>O<sub>3</sub>) by laser assisted atom probe tomography. *International Journal of Mass Spectrometry* **335**(0), 57–60.
- BACHHAV, M., DANOIX, R., DANOIX, F., HANNOYER, B., OGALE, S. & VURPILLOT, F. (2011a). Investigation of wüstite (Fe<sub>1-x</sub>O) by femtosecond laser assisted atom probe tomography. *Ultramicroscopy* **111**(6), 584–588.
- BACHHAV, M. N., DANOIX, R., VURPILLOT, F., HANNOYER, B., OGALE, S. B. & DANOIX, F. (2011b). Evidence of lateral heat transfer during laser assisted atom probe tomography analysis of large band gap materials. *Applied Physics Letters* **99**(8), 084101–084103.
- BAIK, S.–I., YIN, X. & SEIDMAN, D. N. (2013). Correlative atom–probe tomography and transmission electron microscope study of a chemical transition in a spinel on an oxidized nickel–based superalloy. *Scripta Materialia* **68**(11), 909–912.
- BALASUBRAMANIAM, R. & CALLISTER, W. D. (2009). *Callisters Materials Science and Engineering*.
- CURRIE, L. A. (1968). Limits for qualitative detection and quantitative determination. Application to radiochemistry. *Analytical chemistry* **40**(3), 586–593.
- DAVID, J. D. (1996). Orientation contrast imaging of microstructures in rocks using foreshatter detectors in the scanning electron microscope. *Mineralogical Magazine* **60**, 859–869.
- DAVIS, D. W., KROGH, T. E. & WILLIAMS, I. S. (2003). Historical development of zircon geochronology. *Reviews in mineralogy and geochemistry* **53**(1), 145–181.
- FELFER, P. J., ALAM, T., RINGER, S. P. & CAIRNEY, J. M. (2012). A reproducible method for damage–free site–specific preparation of atom probe tips from interfaces. *Microscopy Research and Technique* **75**(4), 484–491.

- 
- GAULT, B., MENAND, A., DE GEUSER, F., DECONIHOUT, B. & DANOIX, R. (2006). Investigation of an oxide layer by femtosecond-laser-assisted atom probe tomography. *Applied Physics Letters* **88**(11), 114101.
- GAULT, B., MOODY, M. P., CAIRNEY, J. M. & RINGER, S. P. (2012). *Atom probe microscopy*. Springer.
- HARLEY, S. L., KELLY, N. M. & MÖLLER, A. (2007). Zircon behaviour and the thermal histories of mountain chains. *Elements* **3**(1), 25–30.
- HAY, D. & DEMPSTER, T. (2009). Zircon behaviour during low-temperature metamorphism. *Journal of Petrology*, egp011.
- HONO, K., OHKUBO, T., CHEN, Y., KODZUKA, M., OH-ISHI, K., SEPEHRI-AMIN, H., LI, F., KINNO, T., TOMIYA, S. & KANITANI, Y. (2011). Broadening the applications of the atom probe technique by ultraviolet femtosecond laser. *Ultramicroscopy* **111**(6), 576–583.
- KINGERY, W., FRANCL, J., COBLE, R. & VASILOS, T. (1954). Thermal conductivity: X, Data for several pure oxide materials corrected to zero porosity. *Journal of the American Ceramic Society* **37**(2), 107–110.
- KIRCHHOFER, R., DIERCKS, D. R., GORMAN, B. P., IHLEFELD, J. F., KOTULA, P. G., SHELTON, C. T. & BRENNER, G. L. (2014). Quantifying Compositional Homogeneity in Pb(Zr,Ti)O<sub>3</sub> Using Atom Probe Tomography. *Journal of the American Ceramic Society* **97**(9), 2677–2697.
- KRUSKA, K., LOZANO-PEREZ, S., SAXEY, D. W., TERACHI, T., YAMADA, T. & SMITH, G. D. W. (2012). Nanoscale characterisation of grain boundary oxidation in cold-worked stainless steels. *Corrosion Science* **63**(0), 225–233.
- KUNICKI, T., BEERMANN, D., GEISER, B., OLTMAN, E., ONEILL, R. & LARSON, D. Atom probe data reconstruction, visualization and analysis with the Imago Visualization and Analysis System (IVAS). In *Vacuum Nanoelectronics Conference, 2006 and the 2006 50th International Field Emission Symposium., IVNC/IFES 2006. Technical Digest. 19th International*: IEEE.
- LA FONTAINE, A., GAULT, B., BREEN, A., STEPHENSON, L., CEGUERRA, A. V., YANG, L., NGUYEN, T. D., ZHANG, J., YOUNG, D. J. & CAIRNEY, J. M. (2015a). Interpreting atom probe data from chromium oxide scales. *Ultramicroscopy*.
- LA FONTAINE, A., YEN, H.-W., FELFER, P. J., RINGER, S. P. & CAIRNEY, J. M. (2015b). Atom probe study of chromium oxide spinels formed during intergranular corrosion. *Scripta Materialia* (2015).
- LARSON, D., ALVIS, R., LAWRENCE, D., PROSA, T., ULFIG, R., REINHARD, D., CLIFTON, P., GERSTL, S., BUNTON, J. & LENZ, D. (2008). Analysis of bulk dielectrics with atom probe tomography. *Microscopy and Microanalysis* **14**(S2), 1254–1255.
- LARSON, D. J., PROSA, T. J., ULFIG, R. M., GEISER, B. P., KELLY, T. F. & HUMPHREYS, C. J. (2013). *Local Electrode Atom Probe Tomography: A Users Guide*. Springer New York.

- 
- MARQUIS, E. A., YAHYA, N. A., LARSON, D. J., MILLER, M. K. & TODD, R. I. (2010). Probing the improbable: imaging C atoms in alumina. *Materials Today* **13**(10), 34–36.
- MAZUMDER, B., VELLA, A., DECONIHOUT, B. & AL-KASSAB, T. A. (2011). Evaporation mechanisms of MgO in laser assisted atom probe tomography. *Ultramicroscopy* **111**(6), 571–575.
- OBERDORFER, C., STENDER, P., REINKE, C. & SCHMITZ, G. (2007). Laser-assisted atom probe tomography of oxide materials. *Microscopy and Microanalysis* **13**(5), 342–346.
- PIAZOLO, S., LA FONTAINE, A., TRIMBY, P., HARLEY, S., YANG, L., ARMSTRONG, R. & CAIRNEY, J. M. (2016). Deformation-induced trace element redistribution in zircon revealed using atom probe tomography. *Nat Commun* **7**.
- REDDY, S. M., TIMMS, N. E., TRIMBY, P., KINNY, P. D., BUCHAN, C. & BLAKE, K. (2006). Crystal-plastic deformation of zircon: A defect in the assumption of chemical robustness. *Geology* **34**(4), 257–260.
- SAXEY, D. W. (2011). Correlated ion analysis and the interpretation of atom probe mass spectra. *Ultramicroscopy* **111**(6), 473–479.
- SCHERER, E., MÜNKER, C. & MEZGER, K. (2001). Calibration of the lutetium–hafnium clock. *Science* **293**(5530), 683–687.
- STILLER, K., THUVANDER, M., POVSTUGAR, I., CHOI, P. & ANDRÉN, H.-O. (2016). Atom probe tomography of interfaces in ceramic films and oxide scales. *MRS Bulletin* **41**(01), 35–39.
- STILLER, K., VISKARI, L., SUNDELL, G., LIU, F., THUVANDER, M., ANDRÉN, H.-O., LARSON, D., PROSA, T. & REINHARD, D. (2013). Atom probe tomography of oxide scales. *Oxidation of metals* **79**(3–4), 227–238.
- TIMMS, N. E., REDDY, S. M., GERALD, J. D. F., GREEN, L. & MUHLING, J. R. (2012). Inclusion-localised crystal-plasticity, dynamic porosity, and fast-diffusion pathway generation in zircon. *Journal of Structural Geology* **35**, 78–89.
- TRIMBY, P. W. (2012). Orientation mapping of nanostructured materials using transmission Kikuchi diffraction in the scanning electron microscope. *Ultramicroscopy* **120**, 16–24.
- TSUKADA, M., TAMURA, H., MCKENNA, K. P., SHLUGER, A. L., CHEN, Y. M., OHKUBO, T. & HONO, K. (2011). Mechanism of laser assisted field evaporation from insulating oxides. *Ultramicroscopy* **111**(6), 567–570.
- VALLEY, J. W., CAVOSIE, A. J., USHIKUBO, T., REINHARD, D. A., LAWRENCE, D. F., LARSON, D. J., CLIFTON, P. H., KELLY, T. F., WILDE, S. A., MOSER, D. E. & SPICUZZA, M. J. (2014). Hadean age for a post-magma-ocean zircon confirmed by atom-probe tomography. *Nature Geosci* **7**(3), 219–223.
- VALLEY, J. W., REINHARD, D. A., CAVOSIE, A. J., USHIKUBO, T., LAWRENCE, D. F., LARSON, D. J., KELLY, T. F., SNOEYENBOS, D. R. & STRICKLAND, A. (2015). Presidential Address. Nano- and micro-geochronology in Hadean and Archean zircons by atom-probe tomography and SIMS: New tools for old minerals. *American Mineralogist* **100**(7), 1355–1377.

- 
- VURPILOT, F., HOUARD, J., VELLA, A. & DECONIHOUT, B. (2009). Thermal response of a field emitter subjected to ultra-fast laser illumination. *Journal of Physics D: Applied Physics* **42**(12), 125502.
- WILKES, T. J., TITCHMARSH, J. M., SMITH, G. D. W., SMITH, D. A., MORRIS, R. F., JOHNSTON, S., GODFREY, T. J. & BIRDSEYE, P. (1972). The fracture of field-ion microscope specimens. *Journal of Physics D: Applied Physics* **5**(12), 2226.
- WILLIAMS, I., COMPSTON, W., BLACK, L., IRELAND, T. & FOSTER, J. (1984). Unsupported radiogenic Pb in zircon: a cause of anomalously high Pb-Pb, U-Pb and Th-Pb ages. *Contributions to Mineralogy and Petrology* **88**(4), 322-327.



---

## **12 Laser-assisted APT investigation of the mobility of trace elements in deformed zircons**

Following chapter 11 and the optimization of laser-assisted APT analysis parameters for the study of zircon, this chapter focuses on applying APT to the study of the diffusion of key elements in deformed zircons. As described in the literature review, investigating the deformation-induced diffusion in the mineral zircon has never previously been carried out at the atomic scale and this data is needed to answer critical questions for the particular problem of dating zircons that have undergone deformation events.

This publication is an important contribution to the field of geoscience and demonstrates the new perspective brought by APT to zircon atomic scale structure investigation.

Sandra Piazzolo initiated this project, selected samples, assisted in data reduction and interpretation, and wrote the majority of the paper. Alexandre La Fontaine performed data analysis and data reduction of atom probe tomography data and assisted in interpretation. Patrick Trimby conducted EBSD and TKD analyses and SEM imaging and assisted in interpretation and rewriting. Limei Yang prepared samples by focused ion beam. Simon Harley provided the sample, field and sample description and assisted in SHRIMP data interpretation. Richard Armstrong dated the zircon by SHRIMP. Julie M. Cairney assisted in data reduction, interpretation and rewriting. All authors reviewed and approved this paper.

This article has been published in Nature communications in 2016.

DOI: 10.1038/ncomms10490

ARTICLE

Received 31 Aug 2015 | Accepted 18 Dec 2015 | Published 12 Feb 2016

DOI: 10.1038/ncomms10490

OPEN

# Deformation-induced trace element redistribution in zircon revealed using atom probe tomography

Sandra Piazzolo<sup>1</sup>, Alexandre La Fontaine<sup>2</sup>, Patrick Trimby<sup>2</sup>, Simon Harley<sup>3</sup>, Limei Yang<sup>2</sup>, Richard Armstrong<sup>4</sup> & Julie M. Cairney<sup>2</sup>

Trace elements diffuse negligible distances through the pristine crystal lattice in minerals: this is a fundamental assumption when using them to decipher geological processes. For example, the reliable use of the mineral zircon ( $\text{ZrSiO}_4$ ) as a U-Th-Pb geochronometer and trace element monitor requires minimal radiogenic isotope and trace element mobility. Here, using atom probe tomography, we document the effects of crystal-plastic deformation on atomic-scale elemental distributions in zircon revealing sub-micrometre-scale mechanisms of trace element mobility. Dislocations that move through the lattice accumulate U and other trace elements. Pipe diffusion along dislocation arrays connected to a chemical or structural sink results in continuous removal of selected elements (for example, Pb), even after deformation has ceased. However, in disconnected dislocations, trace elements remain locked. Our findings have important implications for the use of zircon as a geochronometer, and highlight the importance of deformation on trace element redistribution in minerals and engineering materials.

<sup>1</sup>Australian Research Council Centre of Excellence for Core to Crust Fluid Systems/GEMOC, Department of Earth and Planetary Sciences, Macquarie University, Sydney, New South Wales 2109, Australia. <sup>2</sup>Australian Centre for Microscopy and Microanalysis, University of Sydney, Sydney, New South Wales 2006, Australia. <sup>3</sup>School of Geosciences, Grant Institute, University of Edinburgh, Edinburgh EH9 3JW, UK. <sup>4</sup>Research School of Earth Sciences, Australian National University, Canberra, Australian Capital Territory 0200, Australia. Correspondence and requests for materials should be addressed to S.P. (email: sandra.piazzolo@mq.edu.au).

The recent development of a range of high-resolution, chemically sensitive analytical techniques has enabled routine geochemical characterization of geological samples; this allows the use of trace element distributions in single grains as indicators of the Earth's large-scale processes<sup>1,2</sup>. Fundamental to these studies is the assumption of element immobility and/or predictable element diffusion. Theoretically, deformation may induce differential element mobility<sup>3</sup> resulting in substantial changes to both absolute and relative element concentrations. However, even though many rocks undergo crystal-plastic deformation, the link between trace element mobility and deformation is still poorly understood.

Zircon is one of the main minerals routinely analysed *in situ* for several trace elements. The ability of the zircon lattice to incorporate U, Th, Hf and a number of geochemically important rare earth elements, while remaining physically and chemically robust<sup>4</sup>, has resulted in the use of zircon geochemistry in many geoscience disciplines (igneous petrology<sup>5</sup>; provenance studies<sup>6</sup>; metamorphic processes<sup>4,7</sup>; Earth evolution<sup>2,8,9</sup>). Although experimental determination of diffusion rates within pristine zircons shows that substantial Pb diffusion should only occur at extreme temperatures<sup>10</sup>, there is some evidence that Pb diffusion can take place at lower temperatures<sup>11</sup>. This is often attributed to the annealing of regions of radiation damage within the crystalline lattice<sup>12,13</sup>. Such damaged (metamict) domains are only partially crystalline, may be porous<sup>12,14</sup>, and are usually cited as the cause of either relative Pb-loss (discordance) or Pb-gain (reverse discordance) recorded on the micrometre scale<sup>13–15</sup>. Recent studies show diffusion only over small distances (<100 nm) resulting in Pb clusters<sup>6</sup> and some micrometre-scale redistribution<sup>16</sup>. Although measurable changes in trace element concentrations have been linked to micrometre-scale deformation structures<sup>17–19</sup>, atomic-scale evidence of the relevant processes is lacking. Consequently, it is not yet possible to predict how these changes may influence the accuracy of dating or our ability to utilize trace element data.

In metals and alloys, solute atoms are observed in higher concentrations in a volume surrounding dislocations, commonly referred to as a Cottrell Atmosphere<sup>20</sup>. Nearby solute atoms are attracted by the strain field associated with the dislocation from a region that we describe here as a 'capture zone'. The size of this zone varies between elements since it depends on the lattice diffusion rate, which is affected by temperature, the relative sizes of the solute and matrix atoms and the bonding type<sup>21</sup>. The solute may follow dislocations as they move through the lattice, but only up to a critical velocity. Above this velocity, the dislocation and

solute become detached<sup>3</sup>. Additional substantial element mobility may occur through pipe diffusion, the process of relatively rapid diffusion of atoms along dislocation cores<sup>22,23</sup>. Although in metals pipe diffusion has been demonstrated to occur along single dislocations<sup>24,25</sup>, evidence for pipe diffusion occurring in minerals is so far only indirect<sup>17–19,26</sup>.

Here we present an atomic-scale study of a ~2.5-Ga-old zircon grain using a range of high-end microanalytical techniques including atom probe tomography (APT)<sup>27</sup>, high-resolution electron backscatter diffraction (EBSD), transmission Kikuchi diffraction (TKD)<sup>28</sup> and sensitive high-resolution ion microprobe (SHRIMP). Our work shows that deformation induced dislocation movement and dislocation structures can significantly influence element mobility and redistribution in a crystalline material. As such, when interpreting local elemental and isotopic variations in both deforming and deformed crystalline materials, a thorough characterization of deformation-related dislocation structures is essential.

## Results

**Sample selection and general sample characteristics.** The zircon selected for this study needed to satisfy three main criteria: (i) a sufficiently high U and Pb content to allow reliable, statistically robust detection of radiogenic isotopes using APT, (ii) a known crystal-plastic deformation history to enable an understanding of the link between deformation and element mobility and (iii) a sufficiently long time after the main deformation event(s) to allow an assessment of the importance of pre-existing deformation structures on trace element/isotope mobility in a static regime. The zircon chosen for this study originates from a garnet-orthopyroxene-sapphirine gneiss from the Archean Napier Complex, Antarctica<sup>29</sup> (Supplementary Note 1). Previous studies show that zircons from this particular area meet the criteria outlined above. Napier complex zircons are generally old (>2 Ga), and have a sufficiently high Pb and U content<sup>30–32</sup>. Deformation occurred in the early history of the zircons at high temperatures ensuring crystal-plastic deformation features with little or no later plastic deformation<sup>29,33,34</sup>.

The analysed grain displays a sub-euhedral shape. EBSD analysis reveals complex-shaped metamict domains, characterized by a complete lack of any diffraction patterns and revealed in foreshatter electron images as featureless, topographic lows (Fig. 1). EBSD-based orientation data show evidence for crystal-plastic deformation. On this basis, a single well-defined, low-angle boundary with a misorientation of 1–1.5° extending ~25 µm between two adjacent metamict domains was selected

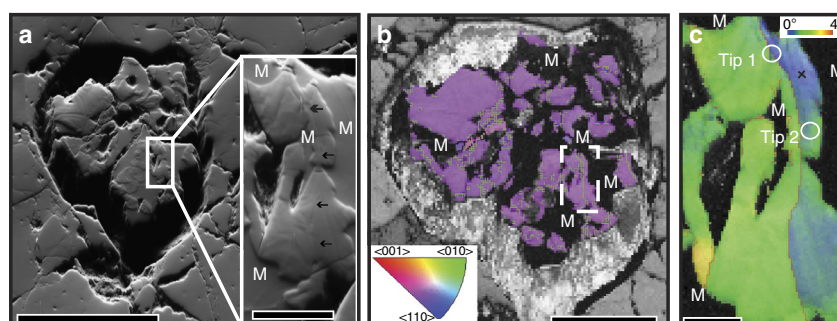


**Figure 1 | Characteristics of the analysed zircon grain.** Metamict domains are marked as M. **(a)** Forescatter electron image; metamict domains are homogeneous, topographic lows; crystalline areas show a complex zonation pattern; scale bar, 100 µm. Inset depicts the analysis area shown in **c**; black arrows point to a low-angle boundary; scale bar, 10 µm. **(b)** Colour-coded orientation EBSD map. Orientation data for the zircon are superimposed on a pattern quality map; low-angle boundaries (>0.8°) are marked in green; white rectangle depicts region of interest shown in **c**; scale bar, 50 µm. **(c)** EBSD relative misorientation map superimposed on a pattern quality map; red lines mark low-angle boundaries (>0.7°); black cross marks the reference point for the relative misorientation colour coding; note location of APT tips 1 and 2; scale bar, 5 µm.

for further analysis (Fig. 1). Detailed misorientation analysis of this boundary shows a rotation about one  $\langle 011 \rangle$  axis consistent with a tilt boundary oriented close to perpendicular to the sample surface (Supplementary Fig. 1). The surrounding zircon lattice shows evidence of minor crystal plastic deformation with distributed lattice bending accumulating to  $1\text{--}2^\circ$  about either  $\langle 111 \rangle$  or  $\langle 011 \rangle$  (Fig. 1b and Supplementary Fig. 1). Two needle-shaped specimens or ‘tips’ were prepared for atomic-scale analysis with APT from the regions indicated in Fig. 1c: one across the low-angle boundary (APT tip 1) and one less than  $1\ \mu\text{m}$  to the side (APT tip 2).

**Atomic-scale analysis.** The dislocation array in tip 1 is immediately visible in the APT reconstruction (Fig. 2a and Supplementary Movie 1). The individual dislocations are highlighted by a very high concentration of Al ( $>2\ \text{at.}\%$ ) and increased concentrations of Y and U (both  $\sim 0.1\text{--}0.2\ \text{at.}\%$ ). The U concentration in the dislocation array is  $\sim 3\text{x}$  that in the matrix (compared with  $17\text{x}$  and  $3,000\text{x}$  for Y and Al, respectively; Table 1). The Pb concentration in the dislocation array is below detection levels ( $<260\ \text{p.p.m.a.}$ ) but the proximity histogram shows that there is no increase in the concentration of Pb in the dislocation array relative to the matrix ( $\sim 50\ \text{p.p.m.a.}$ ; Fig. 2a). The dislocation array is oriented parallel to the tip

(Fig. 2a and Supplementary Figs 1 and 2) and the individual dislocation spacing is  $\sim 50\ \text{nm}$ . Tip 2 shows a very different structure (Fig. 2b and Supplementary Movie 2). In the uppermost  $150\ \text{nm}$  of the data set, numerous clusters are present that are enriched in both Pb ( $1800\ \text{p.p.m.a.}$ ,  $25\text{x}$  matrix) and Y ( $17,420\ \text{p.p.m.a.}$ ,  $>1,700\text{x}$  matrix; Table 2). The elongated morphology of these clusters, their presence in only one part of the volume, and the correlation of this region with a zone of lattice distortion measured by TKD analysis (Supplementary Fig. 2) suggest that these are partially decorated dislocations. There is minor enrichment of U in these dislocations, but no enrichment of Al (Table 2). Tip 2 exhibits additional enrichment of Yb and P in the dislocations, with  $3,740\ \text{p.p.m.a.}$  (not detected in the matrix) and  $9,050\ \text{p.p.m.a.}$  ( $10\text{x}$  matrix), respectively (Table 2).

**Ion microprobe analysis.** SHRIMP-based isotopic analyses show higher U and Pb concentrations and a greater degree of reverse discordance (that is, a relative enrichment in Pb over U) in metamict domains than in crystalline regions (Table 3 and Fig. 3). Because of the size and depth of the analysed volume, signals may originate from variable mixtures of metamict and crystalline domains. The  $^{207}\text{Pb}/^{206}\text{Pb}$  ages for 7 of the 8 analyses are  $2,470 \pm 10\ \text{Ma}$  (Table 3 and Fig. 3).

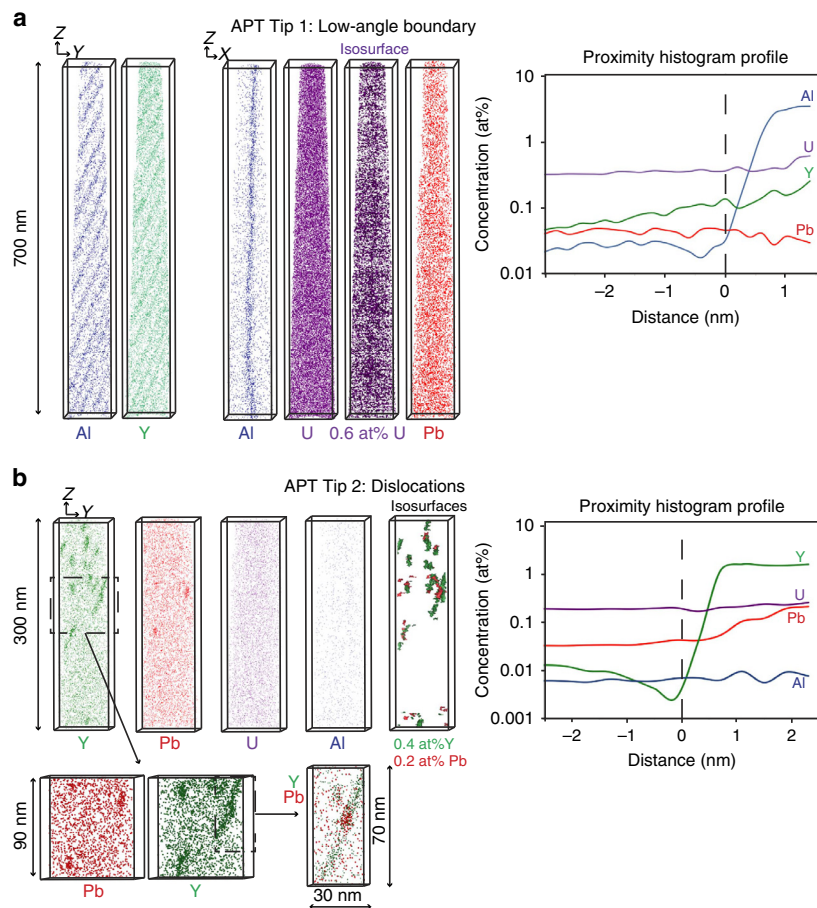


**Figure 2 | Atomprobe Tomography results.** (a) APT tip 1; Al, Y, U and Pb atom maps; note different orientation of maps, see Fig. 1c for tip location. (Upper right) Proximity histogram profile based on 0.1 at% Al isosurface in the vicinity of the low-angle boundary. For compositional data, see Table 1. (b) APT tip 2; see Fig. 1c for tip location: Al, Y, U and Pb atom maps and isosurfaces of 0.4at% Y and 0.2at% Pb. (Lower left) Enlarged views around the dislocations. (Lower middle) Close-up of a single dislocation; note Pb cluster within the Y-enriched dislocation. (Upper right) Proximity histogram profile in the vicinity of a dislocation. For compositional data see Table 2.

**Discussion**

The correlation between the deformation microstructures and the atomic-scale distribution of trace elements in this zircon allows us to determine the mechanisms of trace element movement and segregation in a deformed mineral. The sample analysed is

**Table 1 | Chemical analysis from the APT tips: APT tip 1 for the low-angle boundary (where Al > 0.1 at%) and matrix (where Al < 200 p.p.m.a.).**

APT tip 1	Matrix (~ 68 Mio. atoms)	Low-angle boundary (~120,000 atoms)
O (at%)	68.8 ± 0.02	67.3 ± 0.3
Zr (at%)	15.8 ± 0.01	14.2 ± 0.2
Si (at%)	14.9 ± 0.01	15.3 ± 0.2
Al (p.p.m.a.)	8 ± 3	24,270 ± 520
Y (p.p.m.a.)	110 ± 3	1,830 ± 140
Pb (p.p.m.a.)	50 ± 4	ND*
U (p.p.m.a.)	357 ± 3	965 ± 100
Hf (p.p.m.a.)	1,765 ± 5	1,910 ± 140
Mg (p.p.m.a.)	18 ± 3	ND
P (p.p.m.a.)	378 ± 4	180 ± 40
Li (p.p.m.a.)	67 ± 3	ND
Be (p.p.m.a.)	25 ± 3	ND

APT, atom probe tomography; ND, not detected.  
\*Detection limit over 120,000 atoms: 260 p.p.m.a.

**Table 2 | Chemical analysis from the APT tips: APT tip 2 for dislocations (where Y > 0.1 at%) and the matrix (where Y < 400 p.p.m.a.).**

APT tip 2	Matrix (~23 Mio. atoms)	Dislocations (~198,000 atoms)
O (at%)	66.5 ± 0.02	66.6 ± 0.3
Zr (at%)	16.8 ± 0.01	15.5 ± 0.2
Si (at%)	15.8 ± 0.01	13.9 ± 0.2
Al (p.p.m.a.)	8 ± 3	ND
Y (p.p.m.a.)	10 ± 3	17,420 ± 270
Pb (p.p.m.a.)	71 ± 4	1,800 ± 100
U (p.p.m.a.)	346 ± 3	420 ± 50
Hf (p.p.m.a.)	2,650 ± 7	2,200 ± 140
Yb (p.p.m.a.)	ND	3,740 ± 150
Mg (p.p.m.a.)	10 ± 3	ND
P (p.p.m.a.)	900 ± 5	9,050 ± 200
Ta (p.p.m.a.)	14 ± 3	120 ± 30
Li (p.p.m.a.)	96 ± 3	ND
Be (p.p.m.a.)	15 ± 3	ND

APT, atom probe tomography; ND, not detected.

characterized by a series of high temperature deformation events at common geological strain rates ( $\sim 10^{-11}$ – $10^{-16}$  s $^{-1}$ ) with peak temperatures exceeding 980 °C (refs 29,33–35). The exact timing of these events has been the subject of much discussion, but the general consensus is that there was high temperature formation and deformation of zircons at around 2.55–2.45 Ga, followed by some weaker, lower temperature ( $\sim 500$ – $600$  °C) retrograde deformation. We believe that the dislocation array in tip 1 was formed during the early stages of deformation at relatively high temperatures (>800 °C) enabling dislocation movement through the lattice by both glide and climb. High temperatures result in higher lattice diffusion rates within the crystal lattice, which will enlarge the capture zone, although the bonding of trace elements to the dislocation core may be weakened. At the same time, at high temperatures, the elastic strain may be dissipated by increased dislocation movement. The higher level of dislocation movement, together with an enlarged capture zone (outweighing the effect of a possible weak element-dislocation bond), means that much of the zircon lattice volume was at some point in time in a dislocation capture zone, resulting in large volumes becoming solute depleted (Fig. 4, Stage I). At the same time, the dislocations themselves become enriched (Fig. 4, Stage I) as at the geologically slow strain rates solutes remain captured.

The absence of detectable Pb in the dislocation array in tip 1 is striking. However, the presence of a relatively high amount of U in this array, presumably swept into the array during its formation, would necessitate the presence of a significant amount of radiogenic Pb (Fig. 4, Stage II). Given the age of this zircon and the concentration of U in the array, we would expect  $\sim 550$  ppma of Pb to be present in the array. Pb must diffuse along the dislocation array into the structural sink at either end—namely the porous, metamict domains (Fig. 1). In effect, Pb is ‘successfully’ lost from the dislocation array (Fig. 4, Stage III). SHRIMP analyses of such metamict domains do indeed show a reverse discordance with higher than expected Pb levels (Fig. 3, Table 3). This process must be ongoing throughout the history of this sample, even after the deformation event and at lower temperatures. This is unequivocal evidence for pipe diffusion along a dislocation array in zircon, resulting in relatively fast and continuous redistribution of Pb over >10  $\mu$ m.

Reverse discordance has been the subject of a number of studies<sup>13–15,36,37</sup> and is generally observed in high-U zircons (above a threshold of  $\sim 2,500$  p.p.m. U). The phenomenon has been attributed to possible matrix effects, causing increased relative sputtering of Pb from high-U, metamict regions and resulting in a 1–3% increase in  $^{206}\text{Pb}/^{238}\text{U}$  ages for every 1,000 p.p.m. U (ref. 15). However, in the zircon analysed here, the relationship between U content and reverse discordancy is not simple: several points show a degree of reverse discordance

**Table 3 | Summary of SHRIMP U-Pb zircon data.**

Grain spot	% $^{206}\text{Pb}_c$	p.p.m. U	p.p.m. Th	$^{232}\text{Th}/^{238}\text{U}$	$\pm$ %	( $\dagger$ ) p.p.m. $^{206}\text{Pb}^*$	( $\dagger$ ) $^{206}\text{Pb}/^{238}\text{U}$ Age	( $\dagger$ ) $^{207}\text{Pb}/^{206}\text{Pb}$ Age	% Discordant	( $\dagger$ ) $^{207}\text{Pb}^*/^{206}\text{Pb}^*$	$\pm$ %	( $\dagger$ ) $^{207}\text{Pb}^*/^{235}\text{U}$	$\pm$ %	( $\dagger$ ) $^{206}\text{Pb}^*/^{238}\text{U}$	$\pm$ %	Err corr
2.1	0.01	5,209	1,214	0.24	2.34	2,147	2,527 ± 39	2,471 ± 9	–3	0.161	0.6	10.7	1.9	0.48	1.9	1.0
2.2	0.01	1,615	102	0.07	0.46	661	2,511 ± 30	2,472 ± 14	–2	0.162	0.8	10.6	1.6	0.48	1.4	0.9
2.3	0.02	2,018	331	0.170	2.0	621	2,465 ± 28	2,472 ± 3	+0	0.16156	0.17	10.38	1.4	0.466	1.4	0.99
2.4	0.03	1,900	310	0.169	2.2	597	2,556 ± 25	2,481 ± 12	–4	0.16238	0.68	10.89	1.4	0.487	1.2	0.87
2.6	0.01	4,209	1,019	0.250	1.4	1,211	2,613 ± 24	2,478 ± 6	–7	0.16209	0.36	11.17	1.2	0.500	1.1	0.95
2.7	0.06	2,712	467	0.178	2.4	844	2,486 ± 22	2,483 ± 3	–0	0.16262	0.17	10.55	1.1	0.471	1.0	0.99
2.8	0.15	3,102	847	0.282	0.2	1,138	3,024 ± 31	2,592 ± 8	–21	0.17357	0.46	14.32	1.4	0.598	1.3	0.94

SHRIMP, sensitive high-resolution ion microprobe.

Errors are 1-sigma;  $\text{Pb}_c$  and  $\text{Pb}^*$  indicate the common and radiogenic portions, respectively.

Error in standard calibration was 0.33% (not included in above errors but required when comparing data from different mounts).

$\dagger$ Common Pb corrected using measured  $^{204}\text{Pb}$ .

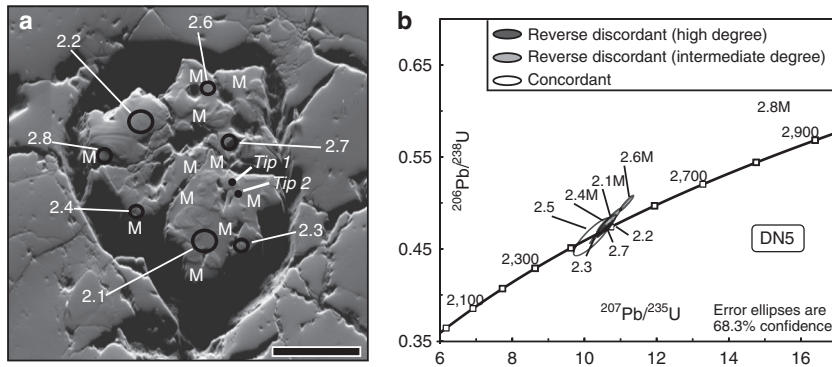


**Figure 3 | Details on the SHRIMP data from analysed zircon.** (a) Forescatter electron image of the zircon grain, showing metamict areas (M), which are homogeneous and topographic lows, SHRIMP analysis spots (black circles) and locations for APT tips 1 and 2 (black dots); scale bar, 50  $\mu\text{m}$ ; refer to Table 3 for results. (b) Conventional Wetherill concordia plot for SHRIMP zircon analyses; spot numbers correspond to those given in a; reverse discordant and concordant analyses are grey scale coded.

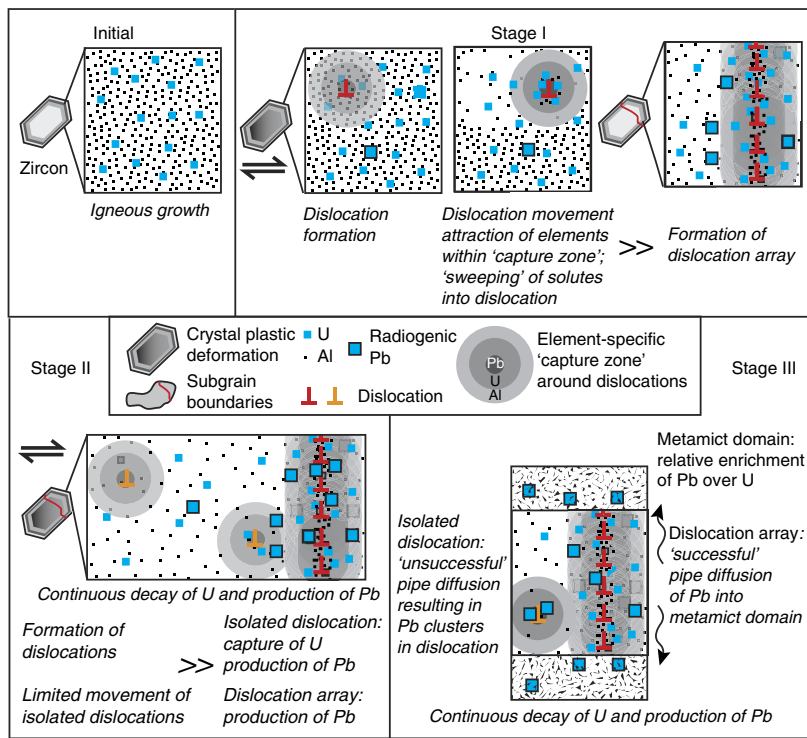


**Figure 4 | Schematic diagram showing the link between element redistribution and dislocations.** This diagram illustrates the proposed stages of dislocation formation and movement and associated trace element mobility within this zircon grain. Only the trace elements U, Pb and Al are considered, with active processes shown in italics. See text for further details.

despite having U concentrations below 2,000 p.p.m. (spots 2.2 and 2.4, Table 3), whereas the highest measured reverse discordancy (21%, spot 2.8, Table 3) is from a location with 3,102 p.p.m. U, only just above the threshold for which reverse discordancy is normally attributable to matrix effects. Different to analyses exhibiting some degree of reverse discordance, we interpret that the chemical signal of spot 2.8 represents a domain that is completely metamict. Although we cannot rule out some matrix effects in high-U, metamict zones, the complex relationship between U content and reverse discordancy in this zircon is further evidence for an additional process of Pb-enrichment—namely the pipe diffusion of Pb along dislocation arrays into adjacent metamict zones.

In tip 2, the dislocations have not formed into well-ordered arrays indicating little, high-temperature recovery took place. The lack of Al in both the matrix and dislocations in tip 2 and its proximity to the low-angle boundary in tip 1 suggests that the dislocations forming the array in tip 1 had already passed through this volume, collecting the majority of the solute atoms, especially Al, and to a lesser extent U and Pb. As a consequence, there is only a slight enrichment of ‘swept’ U in the dislocations of tip 2 (Fig. 4, Stage II). In the dislocations, Pb concentrations are too high to be explained by radioactive decay of U alone. We believe that the Pb clustering in particular areas along the dislocation is further evidence for its localized redistribution through pipe diffusion along dislocation cores (Fig. 4, Stage III). However, in

contrast to tip 1, the lack of a physically continuous connection to a sink leads to ‘unsuccessful’ pipe diffusion: there is no loss of Pb from the dislocation (Fig. 4, Stage III). Consequently, at the micrometre scale, no element redistribution takes place. Radiation damage may enhance this pipe diffusion/clustering behaviour. The phenomena we observe here is quite similar to the segregation and clustering behaviour around dislocations in metals<sup>38</sup>.

Even though, in the field of materials science, pipe diffusion plays a very important role in governing the properties of advanced materials, affecting nucleation, corrosion, creep and dynamic strain-ageing<sup>39,40</sup>, it has proven to be extremely hard to demonstrate or measure its effects experimentally, as processes are too fast to allow a time-resolved study. Our study in zircon provides a unique opportunity to study this phenomenon with a control on timing, as the continuous production of elements through radioactive decay is time dependent. Consequently, this study is as close as possible to an ‘*in situ*’ study allowing the construction of a robust model with regard to ongoing processes through time. Therefore, we are able to provide unprecedented evidence of pipe diffusion along a dislocation array, a process of key interest to the materials community.

Our results demonstrate the importance of deformation processes and microstructures on the localized trace element concentrations and continuous redistribution from the nanometre to micrometre scale in the mineral zircon. Dislocation movement through the zircon lattice can effectively sweep up and concentrate solute atoms at geological strain rates. Dislocation arrays can act as fast pathways for the diffusion of incompatible elements such as Pb across distances of >10 µm if they are connected to a chemical or structural sink. Hence, nominally immobile elements can become locally extremely mobile. Not only does our study confirm recent speculation that an understanding of the deformation microstructures within zircon grains is a necessity for subsequent, robust geochronological analyses but it also sheds light on potential pit-falls when utilizing element concentrations and ratios for geological studies. Our results have far-reaching implications for the interpretation of local elemental variations in not only deformed minerals but also a range of engineering materials.

## Methods

**Scanning electron microscopy.** A thin section from the analysed sample DN5 was mechanically polished down to 1 µm, and subsequently mechano-chemically polished to allow EBSD analysis. The thin section was coated with ~5–10 nm carbon, and then candidate zircon grains were detected using a combination of backscattered electron imaging and energy dispersive X-ray spectroscopy (EDS) using a Zeiss EVO scanning electron microscope (SEM) and an Oxford Instruments INCA EDS system (Australian Centre for Microscopy and Microanalysis, University of Sydney, Australia). The zircon presented in this study was subsequently analysed in a Zeiss Ultra Plus field emission gun SEM using an Oxford Instruments AZtec integrated EBSD/EDS system (Australian Centre for Microscopy and Microanalysis, University of Sydney, Australia). A low-resolution EBSD-EDS map was collected using a step size of 1 µm, indexing the orientations of the zircon grain and the surrounding phases—quartz, orthoclase and antiperthitic feldspar. EBSD data were processed using CHANNEL5 software in order to produce orientation, boundary and relative orientation maps. A region of interest, including low-angle boundaries not associated with brittle fractures, was selected and was further analysed using EBSD at higher resolution, with a step size of 200 nm. EBSD data were cleaned using a single isolated pixel removal process, and then with one pass to remove unindexed pixels with five or more indexed neighbours. Metamict regions exhibited no diffraction because of radiation damage to the crystal lattice; hence, these regions could not be indexed using EBSD and appear black in pattern quality maps.

**Sample preparation for APT and TKD.** Rectangular regions of interest measuring ~3 × 2 µm were selected on the basis of the EBSD data, and cut free using a Zeiss Auriga focused ion beam SEM (Australian Centre for Microscopy and Microanalysis, University of Sydney, Australia). The rectangular prisms were lifted out using a Kleindiek micromanipulator system and welded onto electropolished

molybdenum grids using platinum deposition. The samples were then milled to form atom probe tips, 80–120 nm in diameter, with final milling using a low acceleration voltage (10 kV) in order to minimize Ga implantation and damage. The tip long axes were oriented perpendicular to the original polished grain surface.

**TKD analysis.** TKD analysis provides orientation information with a higher spatial resolution than EBSD<sup>28</sup>, allowing characterization of plastic deformation within the tip and subsequent correlation with atom probe data. The TKD signal arises from the lower surface of the tip, so that a sub-horizontal boundary orientation (such as in APT tip 1) would only be apparent where the boundary intersects the lower surface and at the very tip end (see Supplementary Fig. 3 for details). As for the EBSD measurements, TKD analyses were performed using a Zeiss Ultra Plus field emission gun SEM equipped with an Oxford Instruments AZtec EDS/EBSD system (Australian Centre for Microscopy and Microanalysis, University of Sydney, Australia). Each APT tip was mapped using a step size of 10 nm, an accelerating voltage of 30 kV and a probe current of 10–20 nA. Orientation maps were processed in the same way as for EBSD data.

**APT measurements and analysis.** APT measurements were conducted on a Cameca LEAP 4000X Si atom probe equipped with a picosecond-pulse ultraviolet laser (Australian Centre for Microscopy and Microanalysis, University of Sydney, Australia). In laser-pulsed APT, a sharp needle with a typical diameter of ~100 nm is placed under an intense field produced by a DC voltage of up to 10 kV, in high vacuum and cryogenic temperature (between 20 and 100 °K). Ultra-short laser pulses are then used to field evaporate atoms from the specimen surface. A position-sensitive detector detects the ions and their mass-to-charge ratios are recorded by time-of-flight spectroscopy, synchronized with the laser pulse.

In our study, a 355-nm wavelength laser with a pulse energy of 400 pJ and 250 kHz pulse frequency was used to field evaporate both samples at 50 °K. A total of 68 million atoms in tip 1 and 23 million atoms in tip 2 were detected. The mass-resolving power was around 750 full-width at half-maximum for both samples (measured on O<sup>+</sup> peak; Supplementary Fig. 3).

The minimum detection limit is dependent on the number of atoms considered and the position of the peaks within the mass spectrum and is approximately 10 p.p.m.a. The spatial resolution is generally below 0.3 nm in X, Y and Z.

Molecular species and isobaric interferences are quite common for high-resistivity materials such as zircon and could lead to inaccuracies in compositional measurements<sup>27</sup>. In the case of the two data sets from this study, the molecular species containing the major elements (Zr, Si, O) were easily identified and discriminated using isotopic ratios. No significant isobaric interference was encountered. Al and Y, important trace elements in our study, evaporated principally as single ions without isobaric interferences from other ions. As for radiogenic Pb, there is an isobaric interference between <sup>208</sup>Pb<sup>2+</sup> and <sup>104</sup>Si<sub>2</sub>O<sub>3</sub><sup>+</sup> and as a result only <sup>206</sup>Pb<sup>2+</sup> and <sup>207</sup>Pb<sup>2+</sup> were used to quantify Pb. A deconvolution of the peak was impossible because of the non-radiogenic character of Pb limiting the use of isotopic ratio. The mass spectra obtained for the two data sets in this study were high quality, with a very good mass resolving power (750 full-width at half-maximum for O<sup>+</sup>), limited hydrides and only a minor thermal tail behind peaks. Our results are in excellent agreement with the study of Hadean and Archean zircons from Valley *et al.*, where the mass spectrum full analysis is detailed, providing a benchmark for APT analysis of zircons<sup>41</sup>.

**SHRIMP analysis.** Additional high-resolution chemical analyses on the zircon grain were carried out using a SHRIMP (Australian National University, Canberra, Australia). Two spot sizes (8 and 15 µm diameter) were used (for locations see Fig. 3a). Uncertainties given for individual U-Pb analyses (ratios and ages) are at the 1σ level, however, uncertainties in the calculated weighted mean ages are reported as 95% confidence limits and include the uncertainties in the standard calibrations where appropriate. The standard zircon SL13 (U = 238 p.p.m.)<sup>41</sup> was used for the reference value of U and Th concentrations in zircon. Pb/U ratios were corrected for instrumental interelement fractionation using the ratios measured on the standard zircon Temora 2 (416.8 ± 1.3 Ma)<sup>42</sup>. Common Pb corrections were based on the measured <sup>204</sup>Pb and the relevant common Pb compositions from the Stacey and Kramers model<sup>43</sup>. Data reduction and processing were conducted using the Excel Macros SQUID 2 and ISOPLOT<sup>44,45</sup>.

## References

- Foley, S. F., Prelevic, D., Rehfeldt, T. & Jacob, D. E. Minor and trace elements in olivines as probes into early igneous and mantle melting processes. *Earth Planet. Sci. Lett.* **363**, 181–191 (2013).
- Næraa, T. *et al.* Hafnium isotope evidence for a transition in the dynamics of continental growth 3.2 Gyr ago. *Nature* **485**, 627–630 (2013).
- Ruoff, A. L. & Balluffi, R. W. Strain-enhanced diffusion in metals. II. Dislocation and grain-boundary short-circuiting models. *J. Appl. Phys.* **34**, 1848–1854 (1963).
- Harley, S. L., Kelly, N. M. & Moeller, A. Zircon behaviour and the thermal histories of mountain chains. *Elements* **3**, 25–30 (2007).

5. Hoskin, P. W. O. & Schaltegger, U. The composition of zircon and igneous and metamorphic petrogenesis. *Rev. Mineral. Geochem.* **53**, 27–62 (2003).
6. Gray, M. B. & Zeitler, P. K. Comparison of clastic wedge provenance in the Appalachian foreland using U/Pb ages of detrital zircons. *Tectonics* **16**, 151–160 (1997).
7. Rubatto, D. Zircon trace element geochemistry: partitioning with garnet and the link between U-Pb ages and metamorphism. *Chem. Geol.* **184**, 123–138 (2002).
8. Wilde, S. A., Valley, J. W., Peck, W. H. & Graham, C. M. Evidence from detrital zircons for the existence of continental crust and oceans on the Earth 4.4 Gyr ago. *Nature* **409**, 175–178 (2001).
9. Valley, J. W. *et al.* Hadean age for a post-magma-ocean zircon confirmed by atom-probe tomography. *Nat. Geosci.* **7**, 219–221 (2014).
10. Cherniak, D. J. & Watson, E. B. Diffusion in zircon. *Rev. Mineral. Geochem.* **53**, 113–143 (2003).
11. Geisler, T. Isothermal annealing of partially metamict zircon: evidence for a three-stage recovery process. *Phys. Chem. Minerals* **29**, 420–429 (2002).
12. Mezger, K. & Krogstad, E. J. Interpretation of discordant U-Pb zircon ages: an evaluation. *J. Metamorphic Geol.* **15**, 127–140 (1997).
13. Williams, L. S., Compston, W., Black, L. P., Ireland, T. R. & Foster, J. J. Unsupported radiogenic Pb in zircon: a cause of anomalously high Pb-Pb, U-Pb and Th-Pb ages. *Contrib. Mineral. Petrol.* **88**, 322–327 (1984).
14. Hay, D. C. & Dempster, T. J. Zircon behaviour during low-temperature metamorphism. *J. Petrol.* **50**, 571–589 (2009).
15. White, L. T. & Ireland, T. R. High-uranium matrix effect in zircon and its implications for SHRIMP U-Pb age determinations. *Chem. Geol.* **306**, 78–91 (2012).
16. Kusiak, M. A., Whitehouse, M. J., Wilde, S. A., Nemchin, A. A. & Clark, C. Mobilization of radiogenic Pb in zircon revealed by ion imaging: Implications for early Earth geochronology. *Geology* **41**, 291–294 (2013).
17. Reddy, S. M., Timms, N. E., Pantleon, W. & Trimby, P. Quantitative characterization of plastic deformation of zircon and geological implications. *Contrib. Mineral. Petrol.* **153**, 625–645 (2007).
18. Piazzolo, S., Austrheim, H. & Whitehouse, M. Brittle-ductile microfabrics in naturally deformed zircon: Deformation mechanisms and consequences for U-Pb dating. *Am. Mineral.* **97**, 1544–1563 (2012).
19. Timms, N., Kinny, P. & Reddy, S. Enhanced diffusion of Uranium and Thorium linked to crystal plasticity in zircon. *Geochem. Trans.* **7**, 1–16 (2006).
20. Cottrell, A. H. Theory of dislocations. *Prog. Met. Phys.* **4**, 205–264 (1953).
21. Heitjans, P. & Karger, J. (eds). *Diffusion in condensed matter: Methods, Materials, Models* (Springer, Science & Business Media, 2005).
22. Hart, E. W. On the role of dislocations in bulk diffusion. *Acta Metall.* **5**, 597 (1957).
23. Love, G. R. Dislocation pipe diffusion. *Acta Metall.* **12**, 731–737 (1964).
24. Legros, M., Dehm, G., Arzt, E. & Balk, T. J. Observation of giant diffusivity along dislocation cores. *Science* **319**, 1646–1649 (2008).
25. Huang, C. & Bernstein, I. M. Dislocation transport of hydrogen in iron single crystals. *Acta Metall.* **34**, 1001–1010 (1986).
26. Hirth, G. & Kohlstedt, D. L. The stress dependence of olivine creep rate: Implications for extrapolation of lab data and interpretation of recrystallized grain size. *Earth Planet. Sci. Lett.* **418**, 20–26 (2015).
27. Larson, D. J. *et al.* *Local Electrode Atom Probe Tomography: A User's Guide* (Springer, 2013).
28. Trimby, P. W. Orientation mapping of nanostructured materials using transmission Kikuchi diffraction in the scanning electron microscope. *Ultramicroscopy* **120**, 16–24 (2012).
29. Harley, S. L. Garnet-orthopyroxene bearing granulites from Enderby Land, Antarctica: metamorphic pressure-temperature-time evolution of the Archaean Napier Complex. *J. Petrol.* **26**, 819–856 (1985).
30. Hokada, T., Misawa, K., Yokoyama, K., Shiraishi, K. & Yamaguchi, A. SHRIMP and electron microprobe chronology of UHT metamorphism in the Napier Complex, East Antarctica: implications for zircon growth at > 1,000 °C. *Contrib. Mineral. Petrol.* **147**, 1–20 (2004).
31. Harley, S. L. & Black, L. P. A revised Archaean chronology for the Napier Complex, Enderby Land, from SHRIMP ion-microprobe studies. *Antarctic Sci.* **9**, 74–91 (1997).
32. Kelly, N. M. & Harley, S. L. An integrated microtextural and chemical approach to zircon geochronology: refining the Archaean history of the Napier Complex, east Antarctica. *Contrib. Mineral. Petrol.* **149**, 57–84 (2005).
33. Hokada, T. Feldspar thermometry in ultrahigh-temperature metamorphic rocks: evidence of crustal metamorphism attaining ~ 1100 °C in the Archaean Napier Complex, East Antarctica. *Am. Mineral.* **86**, 932–938 (2001).
34. Lund, M. D., Piazzolo, S. & Harley, S. L. Microtextures and deformation mechanisms in deformed felsic high grade granulites: Insights from EBSD analysis. *Tectonophysics* **427**, 133–151 (2006).
35. Harley, S. L. A pyroxene-bearing meta-ironstone and other pyroxene-granulites from Tonagh Island, Enderby Land, Antarctica: further evidence for very high temperature (> 980 °C) Archaean regional metamorphism in the Napier Complex. *J. Metamorphic Geol.* **5**, 341–356 (1987).
36. McLaren, A. C., Fitzgerald, J. D. & Williams, I. S. The microstructure of zircon and its influence on the age determination from Pb/U ratios measured by the ion microprobe. *Geochim. Cosmochim. Acta.* **58**, 933–100 (1994).
37. Butera, K. M., Williams, I. S., Blevin, P. L. & Simpson, C. J. U-Pb dating of Early Palaeozoic monzonitic intrusives from the Goonumbra area, New South Wales. *Aust. J. Earth Sci.* **48**, 457–464 (2001).
38. Xie, K. Y. *et al.* Strengthening from Nb-rich clusters in a Nb-microalloyed steel. *Scripta Materialia* **66**, 710–713 (2012).
39. Luo, W., Shen, C. & Wang, Y. Nucleation of ordered particles at dislocations and formation of split patterns. *Acta Mater.* **55**, 2579–2586 (2007).
40. Picu, R. C. & Zhang, D. Atomistic study of pipe diffusion in Al-Mg alloys. *Acta Mater.* **52**, 161–171 (2004).
41. Valley, J. W. *et al.* Nano- and micro-geochronology in Hadean and Archaean zircons by atom-probe tomography and SIMS: New tools for old minerals. *Am. Mineral.* **100**, 1355 (2015).
42. Cloué-Long, J. C., Compston, W., Roberts, J. & Fanning, C. M. Two Carboniferous ages: a comparison of SHRIMP zircon dating with conventional zircon ages and <sup>40</sup>Ar/<sup>39</sup>Ar analysis. *SEPM Special Publications* **4**, 3–21 (1995).
43. Black, L. P. *et al.* Improved <sup>206</sup>Pb/<sup>238</sup>U microprobe geochronology by monitoring of a trace-element-related matrix effect; SHRIMP, ID-TIMS, ELA-ICP-MS and oxygen isotope documentation for a series of zircon standards. *Chem. Geol.* **205**, 115–140 (2004).
44. Stacey, J. S. & Kramers, J. D. Approximation of terrestrial lead isotope evolution by a two-stage model. *Earth Planet. Sci. Lett.* **26**, 207–221 (1975).
45. Ludwig, K. R. SQUID 2: A User's Manual. *Berkeley Geochronology Center Special Publication* **5**, 110p (2009).

#### Acknowledgements

This work is supported by the Australian Research Council through DP120102060 and FT1101100070 to S.P. We acknowledge the facilities, and the scientific and technical assistance, of the Australian Microscopy and Microanalysis Research Facility at the Australian Centre for Microscopy and Microanalysis, University of Sydney. This is contribution 688 from the ARC Centre of Excellence for Core to Crust Fluid Systems (<http://www.ccfms.mq.edu.au>) and 1,047 in the GEMOC Key Centre (<http://www.gemoc.mq.edu.au>).

#### Author contributions

S.P. initiated this project, selected samples, assisted in data reduction and interpretation, and wrote the majority of the paper. A.L.F. performed data analysis and data reduction of APT data and assisted in interpretation. P.T. conducted EBSD and TKD analyses and SEM imaging and assisted in interpretation and rewriting. L.Y. prepared samples by focused ion beam. S.H. provided the sample, field and sample description and assisted in SHRIMP data interpretation. R.A. dated the zircon by SHRIMP. J.M.C. assisted in data reduction, interpretation and rewriting. All authors reviewed and approved this paper.

#### Additional information

**Supplementary Information** accompanies this paper at <http://www.nature.com/naturecommunications>

**Competing financial interests:** The authors declare no competing financial interests.

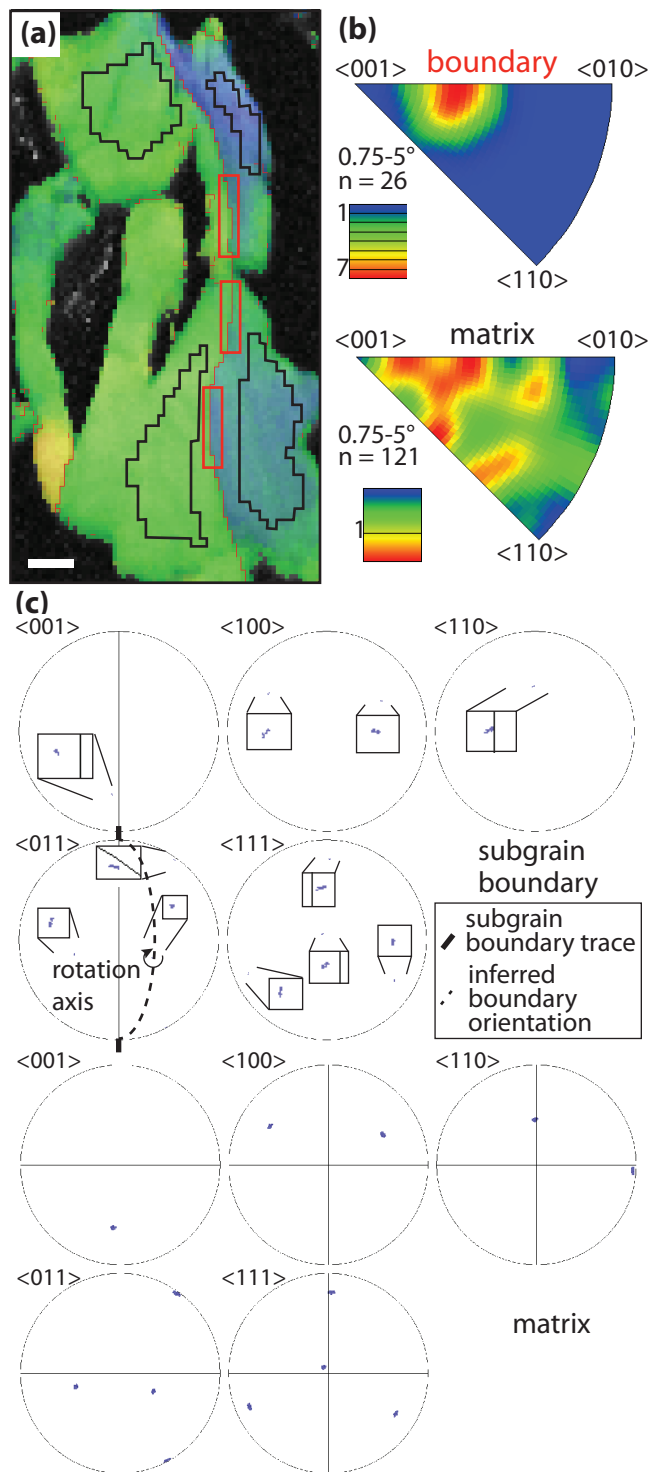
**Reprints and permission** information is available online at <http://npg.nature.com/reprintsandpermissions/>

**How to cite this article:** Piazzolo, S. *et al.* Deformation-induced trace element redistribution in zircon revealed using atom probe tomography. *Nat. Commun.* **7**:10490 doi: 10.1038/ncomms10490 (2016).



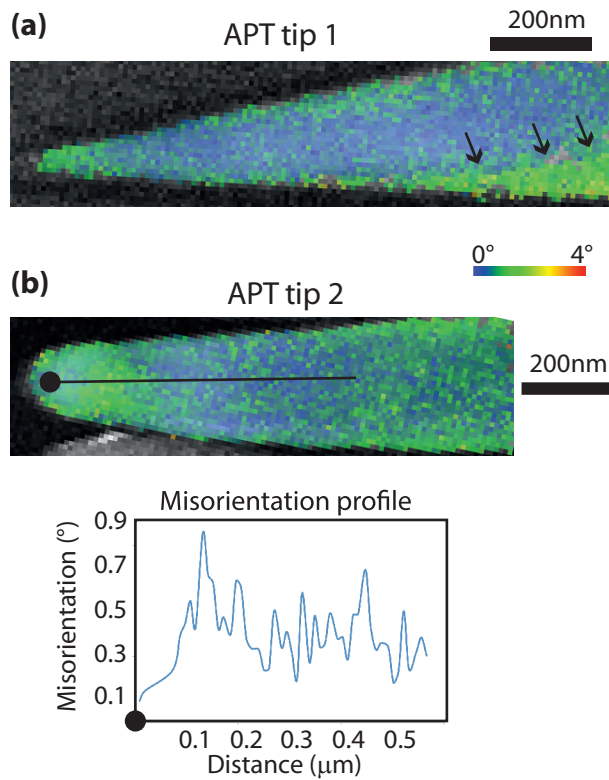
This work is licensed under a Creative Commons Attribution 4.0 International License. The images or other third party material in this article are included in the article's Creative Commons license, unless indicated otherwise in the credit line; if the material is not included under the Creative Commons license, users will need to obtain permission from the license holder to reproduce the material. To view a copy of this license, visit <http://creativecommons.org/licenses/by/4.0/>





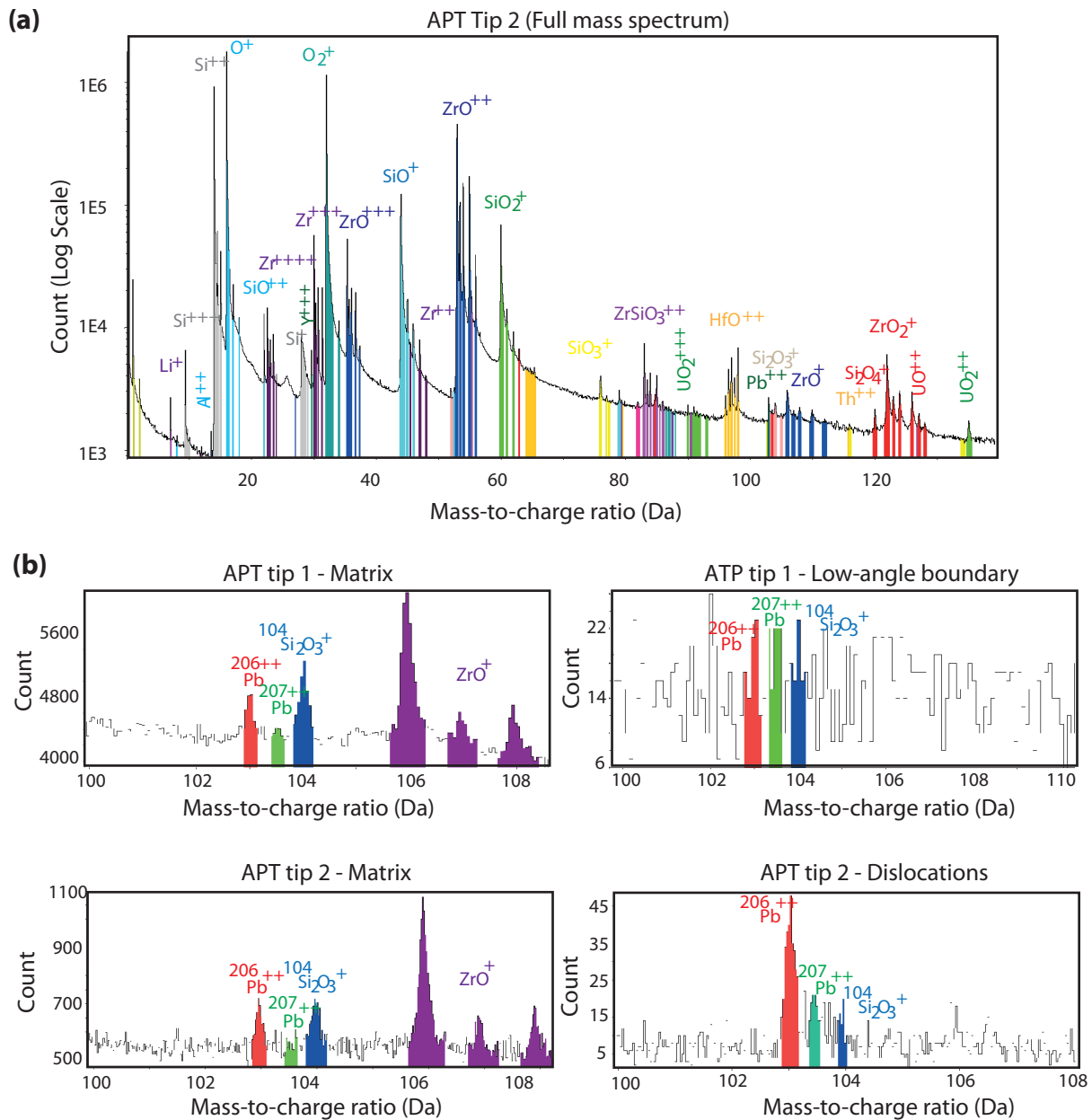
**Supplementary Figure 1: Additional orientation data from the area presented in Fig. 1c**

(a) EBSD map showing the location of two orientation datasets, representing data from the subgrain boundary (red) and in the area of isolated dislocations (black); scale bar represents 2  $\mu\text{m}$ . (b) Misorientation axes for both areas shown in an inverse pole figure; note the cluster of misorientation axes with rotation around  $\langle 011 \rangle$  for the subgrain boundary data set, which is significantly weaker in the matrix. (c) Pole figure of the same two areas; a clear rotation axis is only observed for the subgrain boundary dataset; the boundary trace (solid line) and inferred boundary plane (stippled) are also shown. The fact that the rotation axis lies in the boundary plane is consistent with a tilt boundary.



Supplementary Figure 2:  
Transmission Kikuchi Diffraction results of APT  
tips.

Shown here is the local change in crystallographic orientation of the two analysed tips. Data was acquired after annular milling and before insertion of the tips in the LEAP. Note that only a part of these samples were field evaporated in the LEAP (about a 700 nm length for tip 1 and 350 nm for tip 2). **(a)** APT tip 1; note the low angle boundary in the lower part of the tip (black arrow); step size is 10 nm. **(b)** APT tip 2: note the relative change in orientation along a profile across the first



Supplementary Figure 3: APT mass spectra for the two tips presented in this study.

**(a)** APT tip 1; full mass spectrum (logarithmic scale) from 1 to 140 Da; note many elements are detected as ionic molecules and have multiple charges. **(b)** Enlarged area of the mass spectra (linear scale) for both tips from 100 Da to 108 Da, showing  $206\text{Pb}^{++}$ ,  $207\text{Pb}^{++}$ ,  $104\text{Si}_2\text{O}_3^+$  and  $\text{ZrO}^+$ . Note that no lead is observed in the low-angle boundary (below detection limit) (APT tip 1) and a high lead content is detected in the isolated dislocations (APT tip 2).

---

## Supplementary Note 1: Geological background and sample description

The sample DN5 is from a locality on the lower slopes of Mount Pardoe (67°08'35.6"S, 50°13'27.6"E) which is situated on the south-eastern side of Amundsen Bay in the Napier Complex (66°-68°S, 48°-57° E), Antarctica. The Napier Complex is an Archean granulite facies terrain belonging to the East Antarctic Precambrian Shield and hosts ultrahigh temperature (UHT) metamorphic rocks at a regional scale (1, 2, 3). A general description of the region is provided by (1, 2) and in reviews by (4) and (5). Peak metamorphic conditions across the Napier Complex are >1000 °C at pressures from ~11 kbar in the southern part to ~6 kbar in the northern part (3, 6, 7, 8). Mount Pardoe itself belongs to the central-western part of Napier Complex, within the region of sapphirine-quartz stability and close to Tonagh Island, where pressures of 8-9 kbar have been estimated for the metamorphic peak (3, 4). In this part of the Napier Complex large scale near-isoclinal reclined to recumbent D2 folds fold pre-existing high grade foliations developed during the first deformation event (D1). Such D2 refolding and associated layer-parallel flattening and megaboudinage is observed on metre to 100 metre fold amplitude scales at Mt Pardoe in the vicinity of the DN5 locality. The DN5 locality features a 20 metre thick sequence of pale gneisses including: garnet-quartz-feldspar-bearing massive gneiss; layered quartzofeldspathic felsic gneiss; garnet-rich pods containing sapphirine, orthopyroxene and feldspar with a secondary garnet, and boudinaged garnetite pods and layers. The pale gneisses and associated garnetite pods are considered to have formed from the metamorphism of sedimentary protoliths, based on the range in inferred bulk-rock compositions in the pale gneiss sequence and the geochemistry of comparable paragneisses from the Napier Complex (1, 2). Broadly concordant pods of very coarse grained garnet-orthopyroxene restitic material occurs with and surrounds irregular leucosomes of quartz-feldspar-rutile interpreted to be syn-D1/D2. The restitic pods may

---

contain detrital zircons inherited from the sedimentary protoliths to the gneisses and zircons formed during the crystallisation of the irregular leucosomes.

The sample studied represents such a silica-deficient boudinaged horizon, consisting of garnet, sapphirine (Spr), orthopyroxene (Opx) and feldspar. In thin section, different orthopyroxene (Opx) textures are seen. Opx occurs either as coarse blasts that enclose subhedral and skeletal garnet, or as an Opx+Spr assemblage where Opx is typically xenomorphic on subhedral coarse Spr. Up to 2 cm large garnet blasts are observed. These may contain inclusions and inclusion arrays of: Spr, Opx, biotite, antiperthitic plagioclase, rutile, and in rare cases sillimanite. A second generation of garnet is seen associated with Spr+Opx, next to Spr adjacent to feldspar, and in places it is also associated with minor sillimanite. Both antiperthitic and perthitic (mesoperthite) feldspars are present, though in essentially different domains. Feldspars are invariably deformed and exhibit deformation lamella. Within coarse grains wavy, curved and dispersed extinction is observed. Grain boundaries, originally broadly lobate to subhedral, are sutured to serrated on finer scales, modified by recrystallisation. Seams of similarly finer-grained neoblastic feldspar occur within and between grains and are present at garnet and feldspar contacts where late biotite and sillimanite also occurs. The analysed zircon grain is embedded in quartz, orthoclase and antiperthitic feldspar. The surrounding phases all exhibit irregular boundaries and undulose extinction.

### **Supplementary References**

1. Sheraton, J. W., Tingey, R. J., Black, L. P., Offe, L. A. & Ellis, D. J. Geology of Enderby Land and Kemp Land Antarctica. Aus. Bureau Min. Res. Bull. **223**, 1-51 (1987).

- 
2. Sheraton, J. W., Offe, L. A., Tingey, R. J. & Ellis, D. J. Enderby Land, Antarctica — an unusual Precambrian high-grade metamorphic terrain. *Journal of the Geological Society of Australia* **27**, 1–18 (1980).
  3. Harley, S. L. Garnet–orthopyroxene bearing granulites from Enderby Land, Antarctica: metamorphic pressure–temperature–time evolution of the Archean Napier Complex. *Journal of Petrology* **26**, 819–856 (1985).
  4. Harley, S. L. & Hensen B. J. Archaean and Proterozoic high-grade terranes of East Antarctica (40–80 E): a case study of diversity in granulite facies metamorphism. *High-temperature metamorphism and crustal anatexis*. Springer Netherlands, pp. 320–370 (1990).
  5. Harley, S. L. Ultrahigh temperature granulite metamorphism (1050 °C, 12 kbar) and decompression in garnet (Mg<sub>70</sub>)- orthopyroxene–sillimanite gneisses from Rauer Group, East Antarctica. *Journal of Metamorphic Geology* **16**, 541–562 (1998).
  6. Harley, S. L. & Motoyoshi, Y. Al zoning in orthopyroxene in a sapphirine quartzite: evidence for N1120 °C UHT metamorphism in the Napier Complex, Antarctica, and implications for the entropy of sapphirine. *Contributions to Mineralogy and Petrology* **138**, 293–307 (2000).
  7. Hokada, T. Feldspar thermometry in ultrahigh-temperature metamorphic rocks: evidence of crustal metamorphism attaining ~1100 °C in the Archean Napier Complex, East Antarctica. *American Mineralogist* **86**, 932–938 (2001).
  8. Lund, M. D., Piazzolo, S. & Harley, S. L. Microtextures and deformation mechanisms in deformed felsic high grade granulites: Insights from EBSD analysis. *Tectonophysics* **427**, 133–151 (2006).

---

## **13 Revealing the atomic scale structure and chemistry of human dental enamel by laser-assisted APT**

The last mineral investigated in this work is hydroxyapatite (HAP), the phosphate mineral that is the predominant phase in human dental enamel. In previous studies, laser-assisted APT was used to reveal intergranular amorphous phases between HAP nanowires in rodent tooth (chapter 4.3 and 6.2). However, this type of investigation has never been performed in human dental enamel. The consequences of such phases and the precise knowledge of the atomic scale structure and chemistry of enamel is vital for our understanding of the amazing properties of this mineral. As demonstrated in the previous chapters, laser-assisted APT is the ideal technique to access information at that level.

This publication reveals for the first time the atomic scale structure and composition of human dental enamel. The results detailed in this paper have major implications for our understanding of mechanical properties, acid dissolution and formation of human tooth enamel.

Alexandre La Fontaine prepared the APT samples, performed data analysis and data reduction of APT data, assisted in TEM data interpretation, and wrote the majority of the paper. Alexander Zavgorodniy sourced the samples, prepared the samples for optical and TEM, conducted optical microscopy and assisted in interpretation and writing. Hongwei Liu conducted TEM imaging and performed TEM data reduction and interpretation. Rongkun Zheng participated in the project initiation, assisted in interpretation and rewriting. Michael Swain participated in the project initiation, assisted in data reduction and interpretation and assisted in writing. Julie M. Cairney participated in the project initiation, assisted in data reduction, interpretation and writing. All authors reviewed and approved this paper.

This article has been submitted to Science Advances on the 31<sup>st</sup> of March 2016.

---

**Title: Atomic scale compositional mapping reveals Mg-rich amorphous calcium phosphate in human dental enamel**

**Short title: Amorphous phase responsible for tooth decay**

**Authors:** Alexandre La Fontaine<sup>1,2</sup>, Alexander Zavgorodniy<sup>4,5</sup>, Howgwei Liu<sup>2</sup>, Rongkun Zheng<sup>3</sup>, Michael Swain<sup>4,6</sup>, Julie Cairney<sup>1,2\*</sup>

**Affiliations:**

<sup>1</sup> School of Aerospace, Mechanical, Mechatronic Engineering, The University of Sydney, NSW 2006, Australia

<sup>2</sup> Australian Centre for Microscopy and Microanalysis, The University of Sydney, NSW 2006, Australia

<sup>3</sup> School of Physics, The University of Sydney, NSW 2006, Australia

<sup>4</sup> Faculty of Dentistry, The University of Sydney, NSW 2006, Australia

<sup>5</sup> Institute of Dental Research, Westmead Centre for Oral Health, NSW 2145, Australia

<sup>6</sup> Faculty of Dentistry, Kuwait University, Kuwait

\*Corresponding author: [julie.cairney@sydney.edu.au](mailto:julie.cairney@sydney.edu.au)

**Teaser:** Atomic scale study of human dental enamel reveals an intergranular amorphous phase thought to be responsible for tooth decay.

**Abstract:** Human dental enamel, the hardest tissue in the body, plays a vital role in protecting teeth from wear as a result of daily grinding and chewing as well as from chemical attack. It is well established that its mechanical strength and fatigue resistance is derived from its hierarchical structure, which consists of periodically-arranged bundles of hydroxyapatite



---

(HAP) nanowires. However, we do not yet have a full understanding of the *in vivo* HAP crystallization process that leads to this structure. Mg<sup>2+</sup> ions, present in many biological systems, regulate HAP crystallization by stabilizing its precursor, amorphous calcium phosphate (ACP), but their atomic scale distribution within HAP is unknown. Here we use atom probe tomography (APT) to provide the first direct observations of an intergranular Mg-rich ACP phase between the HAP nanowires in mature human dental enamel. We also observe Mg-rich elongated precipitates and pockets of organic material among the HAP nanowires. These observations support the post-classical theory of amelogenesis (i.e. enamel formation), and suggest that decay occurs via dissolution of the intergranular phase. This information is also useful for the development of more accurate models to describe the mechanical behaviour of teeth.

### **Introduction:**

A staggering 60-90% of children and nearly 100% of adults worldwide suffer from dental decay (caries), which occurs via the progressive dissolution of dental enamel (1). The development of effective treatments requires a basic understanding of the structure of enamel and the processes by which it forms and dissolves. Dental enamel consists of a mineral phase (96 wt.%), mainly in the form of highly oriented carbonated hydroxyapatite (HAP) ribbon-like nanowires with cross-sectional dimensions of about 50 x 25 nm that are up to several millimeters long. (2) (Fig.1D) These crystallites are packed into bundles, known as *rods* or *prisms*. Each rod contains about 40,000 nanowires at a density of roughly 550 crystallites per  $\mu\text{m}^2$  (3, 4). The phase present between the enamel rods is referred as interprismatic enamel. The rods extend in an interwoven pattern through the thickness of the enamel, from the dentine-enamel junction to the outer surface of the tooth (5) (Fig.1 A-C).

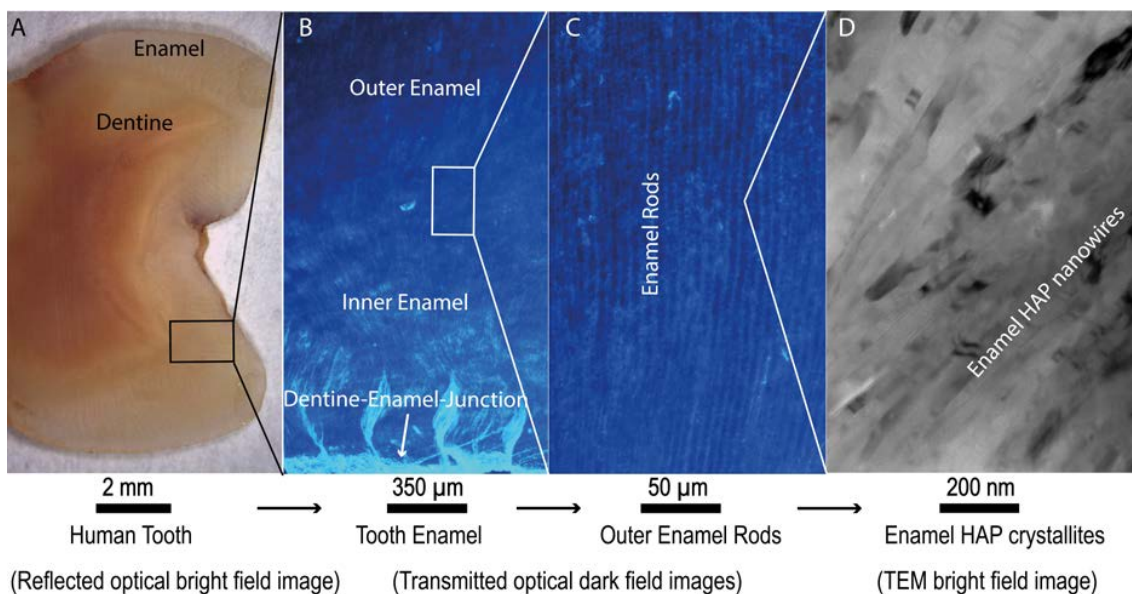


**Fig. 1. Human dental enamel from millimeter to nanometer.**

(A) Reflected optical bright field image of the mature human tooth used in this study. Enamel is the outer layer of this cross section. (B) Transmitted optical dark field image of human tooth enamel showing the junction between dentine and enamel as well as the inner and outer enamel. (C) Transmitted optical dark field image showing outer enamel rods, each composed of thousands of HAP nanowires surrounded by a less dense interprismatic layer. (D) Higher magnification TEM bright field image of aligned HAP nanowires viewed edge on.

Dental enamel is a bio-composite. Apart from a mineral phase, it contains enamel proteins (1 wt.%) and water (3 wt.%). This combination of proteins, water and a highly anisotropic nano-structured mineral phase lead to a unique combination of strength and toughness (6), visco-elastic properties (7, 8), wear (9) and erosion (10) resistance, and resistance to carious attack. (11) These features enable dental enamel to last a lifetime in the harsh and variable environment of the oral cavity.

Under normal physiological conditions, demineralisation and remineralisation processes occur cyclically within the dental biofilm (plaque) layer, but these processes are balanced

---

(12). The first stage of caries occurs when, due to an imbalance of metabolic activity, the biofilm microbial community shifts towards acidogenic species. This causes the pH of the dental biofilm to remain low for prolonged periods of time, resulting in increased dissolution of the dense outermost layer that is normally present at the tooth surface, leaving the tooth susceptible to preferential demineralisation of the nano-wires (thought to occur at the nanowire core (13)) and in the spaces that exist between the enamel rods.

The HAP composition in enamel differs slightly from the perfect HAP crystal ( $\text{Ca}_{10}(\text{PO}_4)_6(\text{OH})_2$ ). Dental enamel HAP is carbonated and contains trace elements such as magnesium and sodium (14). Naturally occurring peptides of the enamel-specific proteins, *i.e.* amelogenin, ameloblastin, and enamelin have been identified in mature human enamel (15). These proteins play an essential role in enamel formation *i.e.* amelogenesis. During amelogenesis, ameloblast cells secrete an organic matrix containing enamel-specific proteins, which is followed immediately by mineralization. As the HAP crystallization progresses, specific enzymes degrade and eliminate most of the remaining organic matrix (16). HAP crystallization is initiated by the mineralization of an amorphous calcium phosphate (ACP) precursor (17). It was recently proposed that Mg ions play a critical role in the stabilization of this ACP phase and the formation of the HAP mineral, where surface Mg ions retard the growth of HAP crystals, leading to the nanometer-sized HAP crystallites (18). Knowledge of the distribution of Mg ions and the presence of the precursor ACP in mature human dental enamel would provide much needed information for a better understanding of amelogenesis, and may eventually allow the development of strategies to enhance remineralisation, to slow or prevent caries, or even to restore lost dental enamel. However, until recently, it has not been possible to observe the distribution of Mg ions within HAP nanowires at the nanoscale in human dental enamel.

---

In recent work on rodent tooth enamel (19, 20), nanoscale heterogeneities in the distribution of Mg ions and organic materials, as well as the presence of intergranular ACP, were revealed using atom probe tomography (APT), a technique that allows 3-dimensional visualization and chemical analysis at the atomic scale (21). Here we use ultra-violet laser-assisted APT to investigate the distribution of trace inorganic (Mg, Na, C ions) and organic (C, H, N ions) materials within HAP nanowires in mature human dental enamel.

In laser-assisted APT, individual atoms (or small molecules) are field-evaporated from a needle-shaped sample (tip) with a diameter of about 100 nm by applying a combination of picosecond laser pulses and high voltage to the sample. A position-sensitive detector records the position of each atom and their mass-to-charge ratio is determined by time-of-flight mass spectrometry. As a result, a 3D reconstruction of the field-evaporated volume (typically millions of atoms) is obtained (21, 22). In a typical APT mass spectrum, direct peak overlaps can lead to erroneous ion identification and composition measurements. (23) For example, in the case of tooth enamel  $^{24}\text{Mg}^{2+}$ ,  $^{12}\text{C}^+$  and  $^{24}\text{C}_2^{2+}$  could directly overlap at 12 Da (and their corresponding isotopes at 12.5 Da and 13 Da). Since there is direct overlap between those species, the combined use of the isotopic distribution and the spatial association with other ions (for example carbon-rich areas) was used to differentiate with a high degree of confidence between Mg and C ions from 12 to 13 Da. Details are provided in the supplementary material (S2 and S3).

### **Results and discussion:**

Six APT tips were prepared from the cusp region of a human permanent molar tooth and a total of approximately 400 million atoms were collected. The APT mass spectra (Fig. S1) were consistent with previous APT studies of HAP. (19, 24, 25) O, Ca and P dominated. Interfaces enriched with Mg and Na were found between the HAP nanowires in all of the samples (Fig. 2-3 and S5, movie S1). Three tips contained Mg-rich elongated precipitates

(Fig. 3 and S6) and two tips contained traces of organic material (Fig. 3-5 and S7). The Ca/P ratios measured within the HAP crystallites in the 6 tips are between 1.48 and 1.59, close to the expected ratio of  $\sim 1.6$  for pure HAP (26) (Table S1).

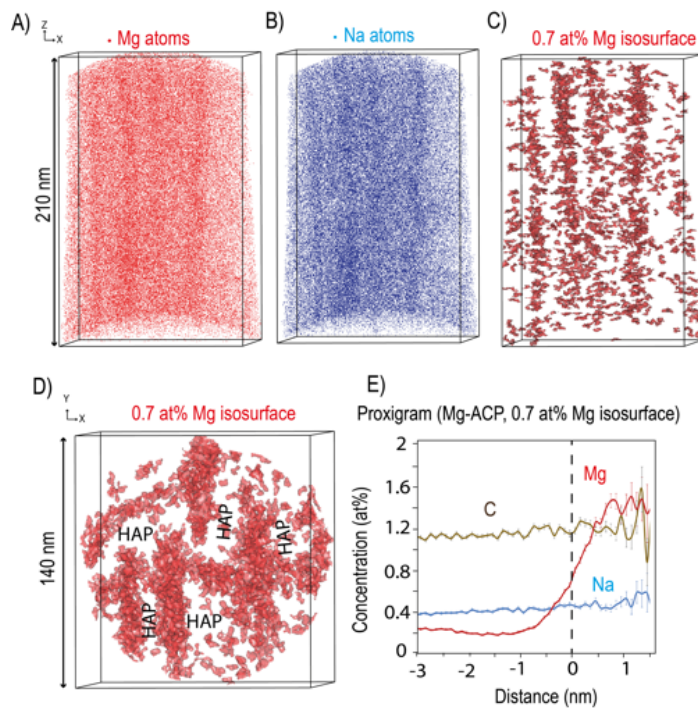


**Fig. 2.** *APT reconstructed volumes of human dental enamel HAP nanowires showing intergranular Mg-rich ACP. (A) Mg atoms, (B) Na atoms distribution and (C) 0.7 at.% Mg isosurface revealing the Mg-rich ACP between HAP nanowires. (D) Cross sectional view of 0.7 at.% Mg isosurface that highlights the ribbon-like shape of the HAP nanowires. (E) Proximity histogram (proxigram) from Mg-rich ACP based on 0.7 at.% Mg isosurface (based on the sum of interfaces shown in D).*

The intergranular Mg-rich phase between the HAP nanowires is a calcium phosphate phase with a Ca/P ratio varying from 1.70 to 1.76 and containing  $\sim 15$  times more Mg and  $\sim 1.5$  times more Na than the bulk of the HAP crystallites (Table S1). Human tooth enamel differs from pure HAP due to the presence of  $\text{CO}_3$ , Mg and Na as its main impurities. Typical human tooth enamel contains between 2.7 - 5 wt.%  $\text{CO}_3$ , 0.2 - 0.6 wt.% Mg and 0.2 - 0.9 wt.% Na.

(27, 28) When measured by APT, the level of Mg in the intergranular phase (from 1.55 – 2.66 wt.%) far exceeds the Mg observed in HAP (~ 0.10 wt.%). Only a disordered calcium phosphate phase could accommodate this level of foreign ions (29). A Mg-rich intergranular phase could accommodate this level of foreign ions (29). A Mg-rich intergranular phase, thought to be ACP, has also been reported in rodent dental enamel (19). The intergranular regions were investigated by TEM. A bright field image of HAP nanowires (Fig. 4) shows thin layers of lighter contrast between nanowires as well as at a triple point. The bright contrast between the crystallites is consistent with the presence of an amorphous phase that appears lighter due to the absence of diffraction. It is assumed to be the Mg-rich phase observed in the atom probe data.

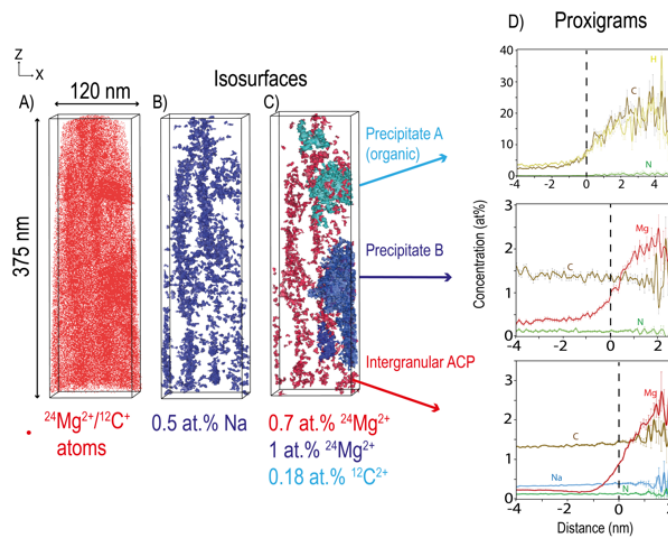


**Fig. 3.** APT 3D reconstructed volumes of human dental enamel HAP nanowires containing a Mg-rich precipitate and organic matter. (A)  $^{24}\text{Mg}^{2+}$  (overlapping with  $^{12}\text{C}^{+}$ ) atoms distribution. (B) 0.5 at.% Na isosurface showing Mg-ACP intergranular phase (C) 0.18 at.% isosurface  $^{12}\text{C}^{2+}$  (precipitate A), 1 at.%  $^{24}\text{Mg}^{2+}$  isosurface (precipitate B) and 0.7 at. %  $^{24}\text{Mg}^{2+}$  (Mg-ACP intergranular phase) (D) Proxigrams of precipitate A, precipitate B and Mg-ACP (based on the sum of ACP interfaces).

The HAP nanowires are mostly parallel and elongated in the z-direction of the atom probe analysis, corresponding to the c-axis of the nanowires. (Fig. 2 and 3) As predicted by theories of enamel formation (30), the HAP nanowires have grown along the c-axis direction while their growth in other directions was inhibited. In two APT tips containing Mg-rich precipitates, the HAP crystallites are bent, suggesting their growth was interrupted (Fig. S6). The ribbon-shape of the nanowires is visible in Fig. 2D. The amorphous ACP phase is homogeneously distributed along all sides of the nanowires. The ACP phase was found to be 2-10 nm thick in all 5 tips. This measurement is based on specific Mg isosurfaces and hence there is some spread in the values recorded. The TEM image (Fig. 4) indicates the width of the amorphous layer is ~2 nm.

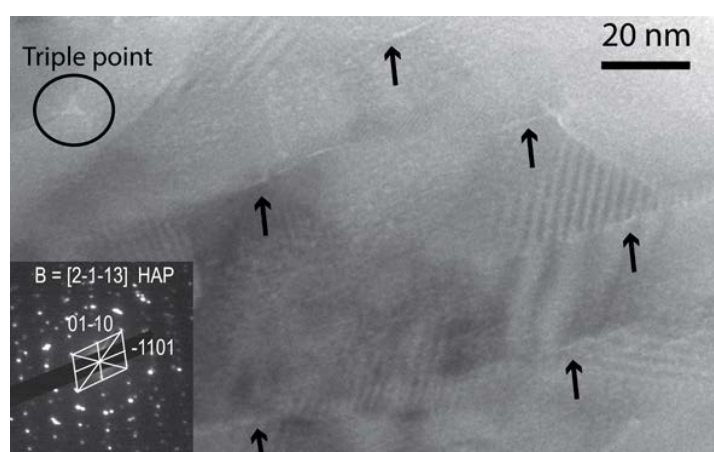


**Fig. 4. TEM image of human dental enamel HAP nanowires.**

*TEM central bright field (CBF) image. Arrows show an intergranular layer (light contrast) between HAP nanowires and a triple point (circled), thought to be amorphous. The electron diffraction pattern is indexed as  $[2-1-13]$ .*

This new finding has important implications for the mechanical and acid corrosion resistance of enamel as well as for the understanding of the HAP growth process. The presence of an intergranular amorphous layer between the HAP crystallites has a strong influence on the mechanical and wear properties of enamel, similar to ceramic nanocomposites (31, 32).

---

Previous studies attributed the observed deformation behavior under nanoindentation to the presence of proteins and peptides at the interface between HAP crystallites (31, 33). Here we show that the interphase regions contain Mg-ACP phase and remnants of proteins rather than proteins alone (Fig.3-5 and S7).

The Mg-rich ACP is also rich in Na (Fig. 2, 4 and 5, Table S1). ACP is known to accommodate foreign ions such as Mg or Na. (29) While not detected here, fluorine ions have been found in intergranular ACP of fluorine-treated rodent enamel (19). In pigmented rodent enamel, an iron-rich ACP phase replaces the Mg-rich ACP improving greatly its resistance to acid attack (19). Here we provide evidence of incorporation of foreign ions in ACP in human dental enamel. This new knowledge highlights the potential for new techniques of remineralization using the intergranular ACP as a conduit for ions known to benefit enamel remineralization such as fluorine.

While the intergranular ACP phase may provide a pathway for beneficial ions, it also has higher dissolution rates in acidic environments compared to the crystalline HAP phase, (34) having been shown to be preferentially etched by acid in rodent tooth. (19)

It has been hypothesized that Na within the ACP may act to balance the charge as a result of an increase of hydroxyl ions. (35) However, we found no clear evidence of H enrichment within the intergranular ACP. (Table S1) Although it is difficult to distinguish the H in the instrument chamber from H present in the sample, sharp localized increases in H in specific features within atom probe data could be interpreted as coming from the sample.



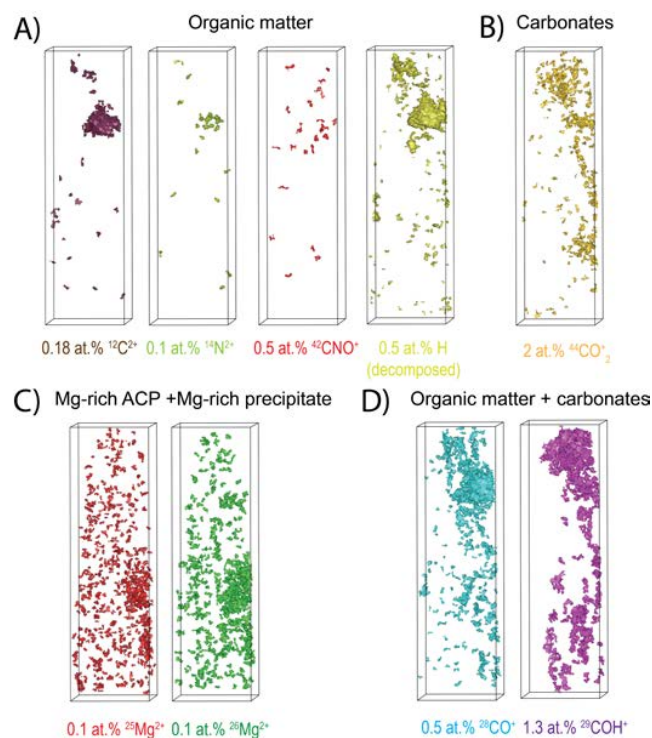


**Fig. 5.** APT 3D reconstructed volumes from sample 2 with isosurfaces from the main species that arise from organic regions, carbonates or Mg-rich phases. A) Isosurfaces of  $^{12}\text{C}^{2+}$ ,  $^{14}\text{N}^{2+}$ ,  $^{42}\text{CNO}^+$  and H (decomposed) highlighting the organic matter. B) Isosurfaces of  $^{44}\text{CO}_2^+$  highlighting the carbonates. C) Isosurfaces of  $^{25}\text{Mg}^{2+}$  and  $^{26}\text{Mg}^{2+}$  highlighting the Mg-rich precipitate and ACP. D) Isosurfaces of  $^{28}\text{CO}^+$  and  $^{29}\text{COH}^+$  highlighting both organic matter and carbonates.

The carbon content measured in HAP and ACP varied greatly between the samples, depending on whether they a) consisted of the HAP/ACP only (e.g. fig. 2), b) contained Mg-rich precipitates (e.g. fig. 3-5) or c) also contained C-rich regions (e.g. fig. 3-5). Samples with no Mg-rich precipitates or organic material contain  $\sim 0.12$  wt.% C in HAP and  $\sim 0.22$  wt.% in ACP. The average carbonate content in bulk HAP is expected to be  $\sim 3 - 5$  wt.%, ( $\sim 1$  wt.% C), higher than the APT results. (36) On the other hand, the samples containing Mg-rich precipitates and signs of organic materials (Fig. 3 and 5) have a total C concentration of  $\sim 0.42$  wt.% in the ACP regions and 0.23 wt.% in the HAP regions. (Table S1)

---

Most of the carbon measured in the ACP and HAP is thought to be inorganic (from carbonates), as no significant enrichment of H,  $^{14}\text{N}^{2+}$ ,  $^{12}\text{C}^{2+}$  and  $^{44}\text{CNO}^+$  was detected (Fig. 5). On the other hand, the precipitates that contain a much larger amount of carbon (15.6 wt.%) are thought to be organic in origin due to the co-presence of H,  $^{14}\text{N}^{2+}$ ,  $^{12}\text{C}^{2+}$  and  $^{44}\text{CNO}^+$  (Fig. S4). The C evaporating as  $^{28}\text{CO}^+$  and  $^{29}\text{COH}^+$  is from both organic and inorganic origin (Fig. 5 D) whereas the C from  $^{44}\text{CO}^{2+}$  is from carbonates only (Fig. 5 B), as highlighted by the respective isosurfaces. The distribution of carbonates and organic carbon is highly heterogeneous. Reconstructed APT volumes also revealed that the Mg-rich precipitates are elongated along the nanowire's c-axis ((Fig. 3, S6 and S7)) and contain  $\sim 2$  wt.% Mg, very close to the Mg content of the ACP intergranular phase.

Our direct observation of these Mg-rich ACP and precipitates supports the post-classical theory of amelogenesis. (37) It has been demonstrated that, during amelogenesis, the enamel mineral nanowires near the mineralisation front initially take the form of the amorphous calcium phosphate (ACP) phase, and then, at a later stage, during the enamel maturation, they crystallise into the HAP phase. Our observations support the hypothesis that ACP ribbon-like nanowires are initially formed following the template provided by the enamel-specific self-assembled protein matrix, mainly composed of the N-terminal amelogenin cleavage products. The ACP nanowires begin to crystallise into the HAP phase only during the maturation stage, which lasts about 5 years for human permanent teeth. This stage is characterised by the secretion of kallikrein 4 (KLK4) proteases, which progressively degrade the enamel protein matrix followed by the reabsorption of the cleaved products into ameloblasts. The removal of the protein matrix allows ribbon-like nanowires to crystallise and to grow in thickness, interlocking with the neighbouring crystallites. Regions of enamel where peptides were not removed remain poorly crystallised. They are characterised by the increased concentration of magnesium, carbon, hydrogen, and nitrogen ions.

---

## **Conclusions:**

Atomic scale observations of an intergranular Mg-rich ACP phase between the enamel rods in human dental enamel contribute to our understanding of how enamel forms, how it decays, and its mechanical behaviour. Understanding how enamel forms is the first step for the development of methods to achieve remineralisation of carious enamel. Our observations verify the mechanism of enamel formation, specifically, the post-classical theory of amelogenesis. Because the Mg-ACP phase at the enamel boundaries is susceptible to dissolution in an acidic environment, we propose that decay occurs via dissolution along the enamel rod boundaries. Finally, these results can be used to improve models of the mechanical properties and wear behaviour of enamel by incorporating the true properties of the intergranular ACP phase.

## **Materials and Methods**

### **Sample preparation**

The collection of the human tooth sample for this study was approved by Western Sydney Local Health District Human Research Ethics Committee, Australia (AU RED HREC/15/WMEAD/142). The tooth used in this study was a molar.

- Tooth cutting

Following the extraction, the tooth was fixed overnight in 0.2M sodium cacodylate buffer overnight at 4°C. The specimen was then placed in Hanks' balanced salts solution (Sigma-Aldrich Co., St. Louis, MO, USA, 9.8 g per 1 L of deionized distilled water) for 24 hours at 4°C, then dried with compressed air. The tooth was cut along the mesio-distal axis at the

---

cement-dentine junction to separate the crown using a low-speed diamond saw (Isomet, Buehler Ltd., Lake Bluff, USA) under constant water irrigation. One millimeter thick sections were prepared from the crown using a low-speed diamond saw.

- Optical imaging

For optical imaging, the tooth section was thinned and polished using the diamond lapping films 30, 9, and 6  $\mu\text{m}$  (Allied High Tech Products, U.S.A.) on a tripod (Allied High Tech Products, U.S.A.). A electron transparent sample was used for transmitted dark field optical imaging.

- Transmission electron microscopy

For transmission electron microscopy (TEM), the specimens were further thinned on a tripod using the diamond lapping films 6, 3, and 1  $\mu\text{m}$  , followed by ion-beam thinning for 2 hours at 3kV in a precision ion-polishing system (Gatan 691, U.S.A.) using a cold stage.

- Atom probe tomography

For atom probe tomography, a small piece (10mm by 10mm) of enamel from the tooth cross section was cut out. It was then tripod polished to a thin wedge (typically below 10  $\mu\text{m}$ ) and attached to a support grid. The sample was then coated with Gold to limit charging effects under the electron beam. Posts about 4  $\mu\text{m}$  wide and with 50 to 100  $\mu\text{m}$  clearance were cut using a Zeiss-Auriga focused ion beam. The samples were then milled to form atom probe tips, 80 – 120 nm in diameter, with final milling using a low acceleration voltage (10 kV) in order to minimize Ga implantation and damage.

### **Optical Microscopy**

A Leica DM6000 optical microscope was used in reflective light and transmitted dark field for the optical images of the tooth.

---

## Transmission electron Microscopy

The transmission electron microscopy was carried out on a microscope CM120 Biofilter running at 120 KV by using JEOL standard high-background double-tilt holder.

## Atom probe tomography

APT measurements were conducted on a Cameca LEAP 4000X Si<sup>TM</sup> atom probe equipped with a picosecond-pulse ultraviolet laser. In laser-assisted APT, individual atoms or small molecules from a needle-shape sample (tip) with a diameter of about 100 nm are field-evaporated by picosecond laser pulses in combination with high voltage applied to the sample. A position-sensitive detector records the position of each atom and their mass-to-charge ratio is determined by time-of-flight mass spectrometry. As a result, a 3-d reconstruction of the volume field-evaporated (typically millions of atoms) is obtained.

In our study, a 355 nm-wavelength laser with a pulse energy of 100 pJ and 250 kHz pulse frequency was used to field evaporate the samples at 50K. A total of 400 million atoms from 6 tips were detected.

## References

1. W. H. Organisation, in *Fact sheet N 318*. (World Health Organisation, 2012), vol. 2015.
2. A. Meckel, W. Griebstein, R. Neal, Structure of mature human dental enamel as observed by electron microscopy. *Archives of oral biology* **10**, 775–783 (1965).
3. J. E. Eastoe, Organic Matrix of Tooth Enamel. *Nature* **187**, 411–412 (1960).
4. B. Kerebel, G. Daculsi, L. Kerebel, Ultrastructural studies of enamel crystallites. *Journal of dental research* **58**, 844–851 (1979).
5. G. Daculsi, J. Menanteau, L. Kerebel, D. Mitre, Length and shape of enamel crystals. *Calcified tissue international* **36**, 550–555 (1984).
6. E. D. Yilmaz, S. Bechtle, H. Özcoban, A. Schreyer, G. A. Schneider, Fracture behavior of hydroxyapatite nanofibers in dental enamel under micropillar compression. *Scripta Materialia* **68**, 404–407 (2013).
7. I. Scheider *et al.*, Damage modeling of small-scale experiments on dental enamel with hierarchical microstructure. *Acta biomaterialia* **15**, 244–253 (2015).
8. J. Zhang, C. Wang, F. Yang, C. Du, Nanoindentation creep behavior of enamel biological nanocomposites. *RSC Advances* **4**, 41003–41009 (2014).

- 
9. O. Borrero-Lopez, A. Pajares, P. J. Constantino, B. R. Lawn, Mechanics of microwear traces in tooth enamel. *Acta biomaterialia* **14**, 146–153 (2015).
  10. T. Baumann, T. Carvalho, A. Lussi, The effect of enamel proteins on erosion. *Scientific reports* **5**, (2015).
  11. G. V. Lubarsky *et al.*, Enamel proteins mitigate mechanical and structural degradations in mature human enamel during acid attack. *Materials Research Express* **1**, 025404 (2014).
  12. N. Takahashi, B. Nyvad, The role of bacteria in the caries process ecological perspectives. *Journal of Dental Research* **90**, 294–303 (2011).
  13. T. Yanagisawa, Y. Miake, High-resolution electron microscopy of enamel-crystal demineralization and remineralization in carious lesions. *Journal of electron microscopy* **52**, 605–613 (2003).
  14. C. Robinson, S. J. Brookes, R. C. Shore, J. Kirkham, The developing enamel matrix: nature and function. *European journal of oral sciences* **106**, 282–291 (1998).
  15. G. A. Castiblanco *et al.*, Identification of proteins from human permanent erupted enamel. *Eur J Oral Sci* **123**, 390–395 (2015).
  16. C. Robinson, H. Briggs, P. Atkinson, J. Weatherell, Matrix and mineral changes in developing enamel. *Journal of dental research* **58**, 871–882 (1979).
  17. E. Beniash, R. A. Metzler, R. S. Lam, P. Gilbert, Transient amorphous calcium phosphate in forming enamel. *Journal of structural biology* **166**, 133–143 (2009).
  18. H. Ding, H. Pan, X. Xu, R. Tang, Toward a detailed understanding of magnesium ions on hydroxyapatite crystallization inhibition. *Crystal Growth & Design* **14**, 763–769 (2014).
  19. L. M. Gordon *et al.*, Amorphous intergranular phases control the properties of rodent tooth enamel. *Science* **347**, 746–750 (2015).
  20. L. M. Gordon, D. Joester, Mapping residual organics and carbonate at grain boundaries and the amorphous interphase in mouse incisor enamel. *Frontiers in Physiology* **6**, 57 (2015).
  21. B. Gault, M. P. Moody, J. M. Cairney, S. P. Ringer, *Atom probe microscopy*. (Springer Science & Business Media, 2012), vol. 160.
  22. T. F. Kelly, D. J. Larson, Atom probe tomography 2012. *Annual review of materials research* **42**, 1–31 (2012).
  23. T. F. Kelly, Kinetic-energy discrimination for atom probe tomography. *Microscopy and Microanalysis* **17**, 1–14 (2011).
  24. L. M. Gordon, L. Tran, D. Joester, Atom probe tomography of apatites and bone-type mineralized tissues. *ACS nano* **6**, 10667–10675 (2012).
  25. L. M. Gordon, D. Joester, Nanoscale chemical tomography of buried organic-inorganic interfaces in the chiton tooth. *Nature* **469**, 194–197 (2011).
  26. C. Robinson, J. A. Weatherell, A. S. Hallsworth, Variation in Composition of Dental Enamel Within Thin Ground Tooth Sections. *Caries Research* **5**, 44–57 (1971).
  27. F. C. M. Driessens, The mineral in bone, dentin and tooth enamel. *Bulletin des Sociétés Chimiques Belges* **89**, 663–689 (1980).
  28. J. Featherstone, I. Mayer, F. Driessens, R. Verbeeck, H. Heijligers, Synthetic apatites containing Na, Mg, and CO<sub>3</sub> and their comparison with tooth enamel mineral. *Calcified Tissue International* **35**, 169–171 (1983).
  29. C. Combes, C. Rey, Amorphous calcium phosphates: synthesis, properties and uses in biomaterials. *Acta Biomaterialia* **6**, 3362–3378 (2010).
  30. L. Addadi, Stereochemical and structural relations between macromolecules and crystals in biomineralization. *Biomineralization, chemical and biochemical perspectives*, 133–152 (1989).

- 
31. L. H. He, M. V. Swain, Understanding the mechanical behaviour of human enamel from its structural and compositional characteristics. *Journal of the Mechanical Behavior of Biomedical Materials* **1**, 18–29 (2008).
  32. P. M. Ajayan, L. S. Schadler, P. V. Braun, *Nanocomposite science and technology*. (John Wiley & Sons, 2006).
  33. Z. H. Xie, M. V. Swain, G. Swadener, P. Munroe, M. Hoffman, Effect of microstructure upon elastic behaviour of human tooth enamel. *Journal of Biomechanics* **42**, 1075–1080 (2009).
  34. R. Legfros, T. Sakae, C. Bautista, M. Retino, J. LeGeros, Magnesium and carbonate in enamel and synthetic apatites. *Advances in Dental Research* **10**, 225–231 (1996).
  35. L. M. Gordon, D. Joester, Mapping residual organics and carbonate at grain boundaries and the amorphous interphase in mouse incisor enamel. *Frontiers in physiology* **6**, (2015).
  36. R. Terpstra, F. Driessens, Magnesium in tooth enamel and synthetic apatites. *Calcified tissue international* **39**, 348–354 (1986).
  37. J. P. Simmer, A. S. Richardson, Y.–Y. Hu, C. E. Smith, J. C.–C. Hu, A post-classical theory of enamel biomineralization&mdash; and why we need one. *International journal of oral science* **4**, 129–134 (2012).

## Acknowledgements

**General:** The authors acknowledge the facilities and the scientific and technical assistance of the Australian Microscopy & Microanalysis Research Facility at the Australian Centre for Microscopy & Microanalysis at the University of Sydney. The authors acknowledge Dr. Anna Ceguerra for providing the theoretical isotopic abundance of the different Carbon and Magnesium molecular ions.

**Funding:** This study was partially supported by the Faculty of Dentistry Research Committee grant, University of Sydney and ARC grant DP160104602.

**Author contributions:** A.L.F. initiated this project, prepared the APT samples, performed data analysis and data reduction of APT data, assisted in TEM data interpretation, and wrote the majority of the paper. A.Z. sourced the samples, prepared the samples for optical and TEM, conducted optical microscopy and assisted in interpretation and writing. H.L. conducted TEM imaging and performed TEM data reduction and interpretation. R.Z. participated in the project initiation, assisted in interpretation and rewriting. M.S. participated

---

in the project initiation, assisted in data reduction and interpretation and assisted in writing. J.C. supervised this project and assisted in data reduction, interpretation and writing. All authors reviewed and approved this paper.

**Competing interests:** The authors declare that we have no competing interests.

**Data availability:** All data needed to evaluate the conclusions in the paper are present in the paper and/or the supplementary materials. Additional data related to this paper may be requested from the authors.

### **Supplementary materials**

Table S1

Fig S1 – S7

Movie S1



---

## Supplementary materials

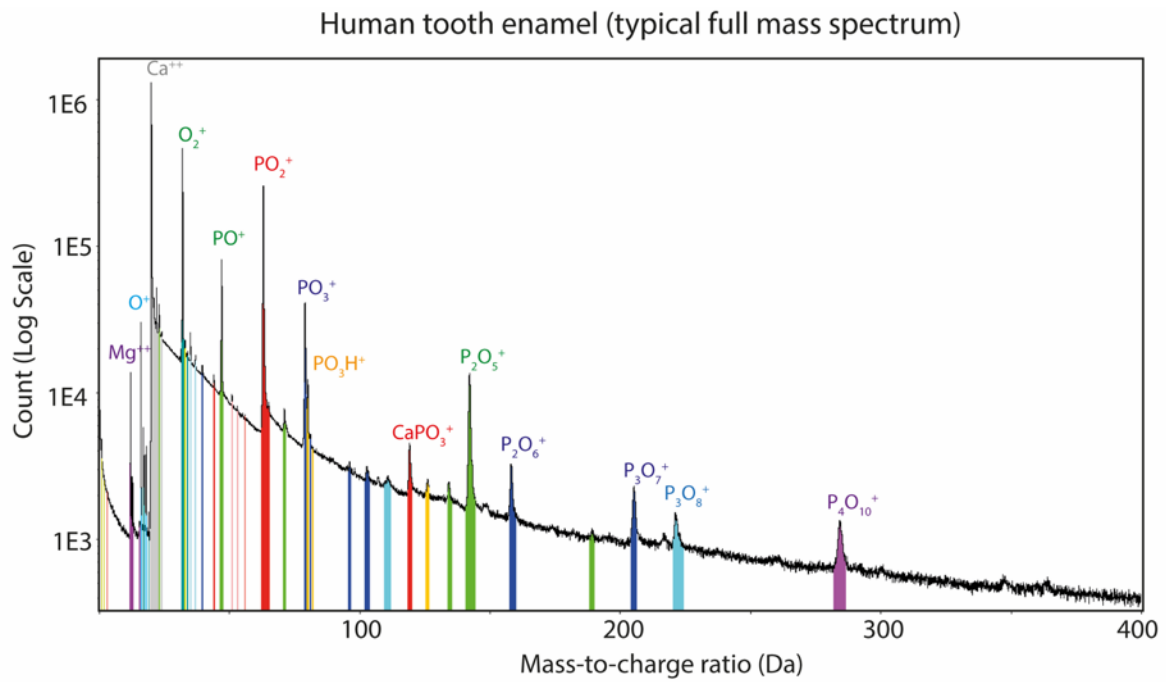


**Figure S1.** Typical APT mass spectrum of human dental enamel containing organic materials (sample 1 – fig.2).

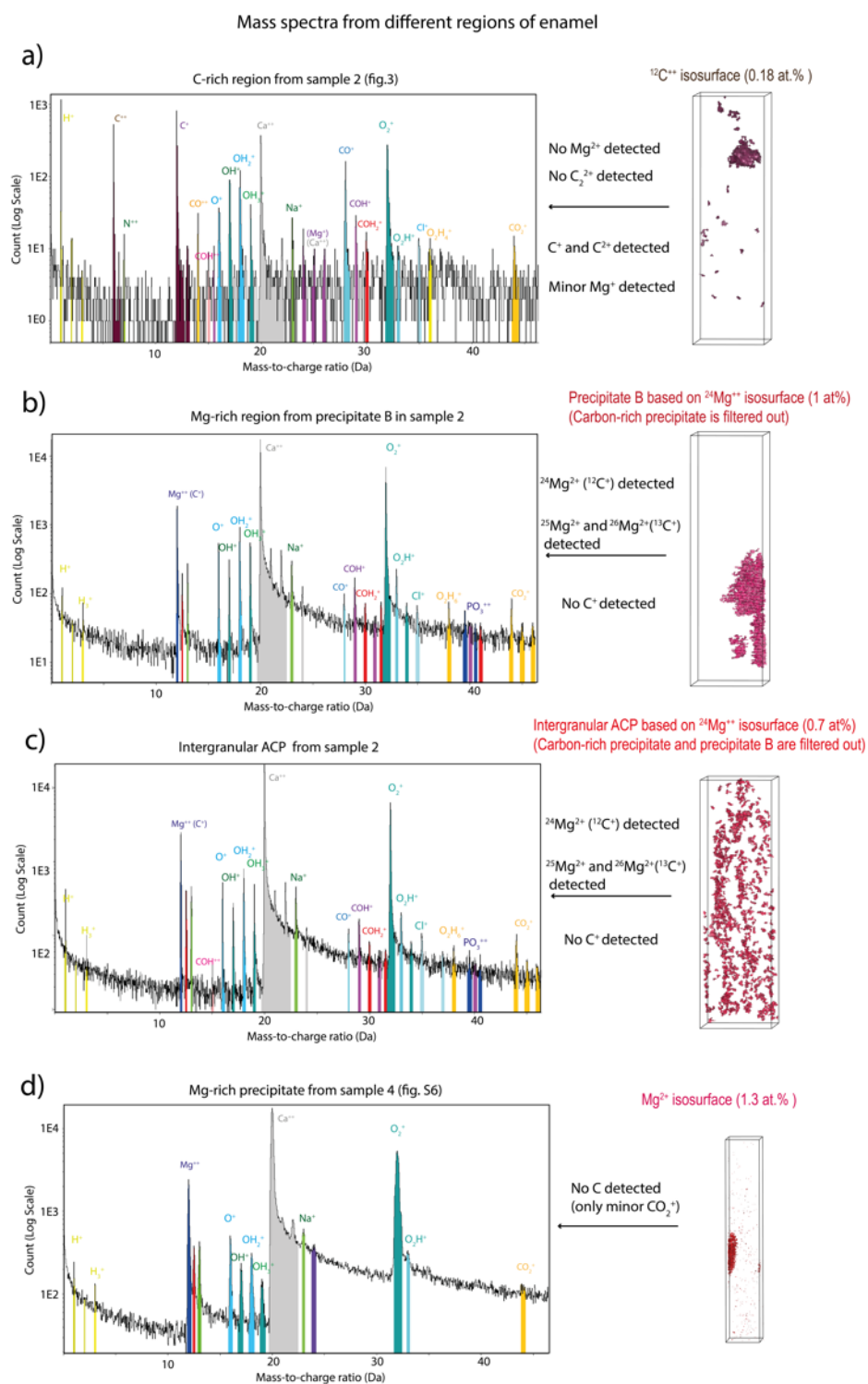


**Figure S2. Mass spectra from different regions of human tooth enamel.**

(a) C-rich region from sample 2 (fig.3) based on 0.18 at.%  $^{12}\text{C}^{2+}$  isosurface. (b) Mg-rich region from precipitate B, sample 2 (fig.3) based on 0.18 at.%  $^{24}\text{Mg}^{2+}$  isosurface. (c) Intergranular Mg-ACP from sample 2 (fig.3) based on 0.7 at.%  $^{24}\text{Mg}^{2+}$  isosurface. (d) Mg-rich precipitate from sample 4 (fig.S6) based on 1.3 at.%  $^{24}\text{Mg}^{2+}$  isosurface.

### S3: Differentiation between Magnesium and Carbon in the enamel APT mass spectra

There is direct overlap between specific Mg and C ions in an atom probe mass-to-charge spectrum at 12, 12.5 and 13 Da, meaning that careful analysis is required to differentiate between Mg and C in the enamel mass spectra.

In this study, Mg is predominantly detected as  $\text{Mg}^{2+}$  (12, 12.5 and 13 Da). The  $\text{Mg}^+$  peaks (24, 25, 26 Da) are minimal (only detected in one mass spectrum just above noise level; see S2-a); If there is any  $\text{Mg}^+$  evaporating, it is too small to be detected above the thermal tail of  $^{24}\text{Ca}^{2+}$ ; the most abundant Mg isotope,  $^{24}\text{Mg}^+$ , also overlaps with  $^{48}\text{Ca}^{2+}$  (and potentially  $^{24}\text{C}^{2+}$ ).

There are different potential overlaps at 12, 12.5 and 13 Da between Mg, C and  $\text{C}_2$ , summarised in table S3-1.

Mass-to-charge (Da)	Possible ions	Theoretical isotopic proportion (at. %)
12	$^{24}\text{Mg}^{2+}$	78.99
	$^{12}\text{C}^+$	98.89
	$^{24}\text{C}_2^{2+}$	97.79
12.5	$^{25}\text{Mg}^{2+}$	10
	$^{25}\text{C}_2^{2+}$	2.19
13	$^{26}\text{Mg}^{2+}$	11
	$^{13}\text{C}^+$	1.11
	$^{26}\text{C}_2^{2+}$	0.01

**Table S3-1:** Theoretical isotope proportion for Mg, C and  $\text{C}_2$  at 12, 12.5 and 13.

H-containing species such as  $^{12}\text{C}^1\text{H}^+$ ,  $^{24}\text{C}_2^1\text{H}^{2+}$  or  $^{24}\text{Mg}^1\text{H}^{2+}$  are potentially able to contribute to the 13 Da peak. However, if this were the case, one would expect a series of ions corresponding to a parent ion and between zero and a maximum number of H atoms to be visible in the mass spectrum, i.e.  $^{12}\text{CH}_{0-3}^+$ ,  $^{24}\text{C}_2\text{H}_{0-4}^{2+}$  or  $^{24}\text{MgH}_{0-3}^{2+}$ . Across all the data collected, there is no evidence for such ions. Moreover, no such peaks were observed in the mass spectra from C-rich and N-rich regions (fig. S2 and S4), which have higher H contents. While a contribution from these species to the peak at 13 Da cannot be entirely ruled out, it is thought to be highly unlikely.

At 12 Da, there are 3 possible overlapping peaks:  $^{24}\text{Mg}^{2+}$ ,  $^{12}\text{C}^+$  and  $^{24}\text{C}_2^{2+}$ . These three isotopes are the most abundant of their series, at abundances of 78.99 at. %, 98.89 at. % and 97.79 at. %, respectively. At 12.5 Da,  $^{25}\text{Mg}^{2+}$  overlaps with  $^{25}\text{C}_2^{2+}$ . However, only 2.19 at. % of the total  $\text{C}_2^{2+}$  would contribute to that peak as  $^{25}\text{C}_2^{2+}$ , which contrasts with 10 at. % of the total  $\text{Mg}^{2+}$  from  $^{25}\text{Mg}^{2+}$ . A similar situation occurs for the peak at 13 Da, with three potential overlaps between  $^{26}\text{Mg}^{2+}$ ,  $^{13}\text{C}^+$  and  $^{26}\text{C}_2^{2+}$ , although there is a substantial difference in the contributions to this peak, with  $^{26}\text{Mg}^{2+}$  accounting for 11 at. % of  $\text{Mg}^{2+}$ ,  $^{13}\text{C}^+$  1.11 at. % of total  $\text{C}^+$  and  $^{26}\text{C}_2^{2+}$  0.01 at. % of total  $\text{C}_2^{2+}$ .

The overlap between these three species is direct. It is thus impossible to use deconvolution techniques to differentiate them. There are however different ways to distinguish between Mg and C:

- Extracting the mass spectrum from carbon-rich regions (using isosurfaces based on  $^{12}\text{C}^{2+}$  at 6 Da) and investigating the presence and amount of  $\text{C}^{2+}$ ,  $\text{C}_2^{2+}$ , and other carbon peaks.
- Extracting the mass spectrum from (supposed) Magnesium-rich regions (based on the absence of  $^{12}\text{C}^{2+}$  at 6 Da) and comparing it with the carbon-rich region mass spectrum.
- Checking the deviation of the measured (supposed)  $\text{Mg}^{2+}$  peaks abundances with the theoretical values for Mg.

**\* Important note on the isotopic proportions measurement method:**

Each peak was ranged from noise to noise. The standard deviations were calculated using the formula  $\sqrt{(\text{Background} + \text{Uncorrected Signal})}$ . The local range-assisted background model was used in IVAS to perform the background correction.

Note that the tail of the peak at 12 Da could contribute to the measured amount of the peak at 12.5 Da and both tails could also contribute to the 13 Da peak. This cannot be perfectly corrected and as a result the calculated standard deviations do not fully reflect the real uncertainties in the measured proportions.

Carbon-rich regions do not contain  $\text{C}_2^{2+}$

In the mass spectrum from the carbon-rich region of sample 2 (fig. S2-a) C peaks are detected as  $^{12}\text{C}^+ / ^{24}\text{C}_2^{2+}$  (12 Da),  $^{13}\text{C}^+$  (13 Da) and  $^{12}\text{C}^{2+}$  (6 Da),  $^{13}\text{C}^{2+}$  (6.5 Da). However, there is no peak detected at 12.5 Da which rules out presence of significant quantities of  $^{25}\text{C}_2^{2+}$ .

Similarly, if significant  $\text{Mg}^{2+}$  was present,  $^{25}\text{Mg}^{2+}$ , accounting for 10 at. % of the whole  $\text{Mg}^{2+}$  should be detected at 12.5 Da. For example, the peak at 12 Da in fig. S2-a is around 1206 counts. The detection limit at 12.5 Da is estimated at around 10 counts. The maximum possible contribution of  $^{24}\text{Mg}^{2+}$  at 12 Da would then be around 79 counts which represents 6.5 % of the total peak at 12 Da. To a lesser extent, the same is valid for  $^{25}\text{C}_2^{2+}$  which accounts for 2.19 at. % of the whole  $\text{C}_2^{2+}$ .

Moreover, the measured isotopic proportion of  $^{12}\text{C}^+$  and  $^{13}\text{C}^+$  is quite close to the theoretical value as shown in table S3-2.

	Mass-to-charge (Da)	Net counts	Measured isotopic proportion (at. %)
<b>Carbon-rich region (sample 2)</b>	12	1206 ± 35	97.9 ± 2.8
	12.5	not detected	n/a
	13	25 ± 6	2.1 ± 0.5

**Table S3-2:** Measured isotopic proportions at 12, 12.5 and 13 in C-rich regions of enamel

The combination of no peak detected at 12.5 Da, a measured isotopic ratio  $^{12}\text{C}^+ / ^{13}\text{C}^+$  within experimental error of its theoretical value and the presence of  $^{12}\text{C}^{2+}$  and  $^{13}\text{C}^{2+}$  leads us to conclude that  $\text{Mg}^{2+}$  and  $\text{C}_2^{2+}$  are absent in the C-rich region mass spectrum.

While the absence of  $\text{Mg}^{2+}$  in the carbon-rich region mass spectrum allows for clear determination of the different carbon peaks, the most important finding is the absence of  $\text{C}_2^{2+}$ . Considering that all the data sets were collected using very similar experimental parameters, equivalent to similar field conditions, we can safely assume that  $\text{C}_2^{2+}$  is not present (at least not detectable) in any of the enamel mass spectra. This allows us to rule out any major overlap at 12.5 Da, so that only  $^{25}\text{Mg}^{2+}$  contributes to this peak.

Magnesium and carbon-rich precipitate:

The precipitate B from sample 2 (fig. 3-5 and S2-b) also contains a significant amount of carbon (presence of  $^{12}\text{C}^{2+}$  at 6 Da), together with, presumably, a large amount of Mg (presence of peaks at 12, 12.5 and 13). Based on the previous discussion,  $\text{C}_2^{2+}$  is ruled out leaving only  $^{12}\text{C}^+$ ,  $^{13}\text{C}^+$  and  $^{24}\text{Mg}^{2+}$ , with  $^{26}\text{Mg}^{2+}$  being the principal contribution to the peaks at 12 and 13 Da. Table S3-3 shows the measured isotopic proportions of the three peaks.

	Mass-to-charge (Da)	Net counts	Measured isotopic proportion (at. %)
<b>Precipitate B (sample 2)</b>	12	6393 ± 83	78.1 ± 1
	12.5	773 ± 36	9.4 ± 0.4
	13	1017 ± 39	12.4 ± 0.5

**Table S3-3:** Measured isotopic proportions at 12, 12.5 and 13 in precipitate B

These proportions are very close to the theoretical values for  $\text{Mg}^{2+}$ . Due to the presence of  $^{12}\text{C}^{2+}$  one would expect some small contribution of  $^{12}\text{C}^+$ . In the mass spectrum from the carbon-rich region (fig. S2-a),  $^{12}\text{C}^{2+}$  was around 1000 counts and  $^{12}\text{C}^+$  around 1206 counts. By extrapolation, we could estimate the  $^{12}\text{C}^+$  contribution around 1.2 times the  $^{12}\text{C}^{2+}$  peak. With  $^{12}\text{C}^{2+}$  at around 50, the contribution of  $^{12}\text{C}^{2+}$  to the peak at 12 Da would be around 60 Da, which is about 1 % of the total peak. As mentioned earlier, there are many sources of uncertainties involved in such measurements such as tail contribution from the previous peak to the next one, the accuracy of background removal model as well as peak ranging. However, these results provide a high degree of confidence in our ability to differentiate between C and Mg.

Intergranular ACP phase:

The mass spectrum from the intergranular region in sample 2 (S2-c) does contain a large amount of Mg (based on the presence of peaks at 12, 12.5 and 13).  $^{12}\text{C}^{2+}$  was not detected at 6 Da. However, carbon is present, detected as molecular ions.

The following table shows the isotopic proportions for  $Mg^{2+}$  at 12, 12.5 and 13 Da. (table S3-4) The measured proportion are again quite close to theoretical  $Mg^{2+}$  isotopic proportions although the  $^{24}Mg^{2+}$  seems a bit smaller than usual. It is worth noting that this trend occurs in most of the intergranular ACP mass spectra. Despite this slight difference, these results are still very convincing, with  $Mg^{2+}$  contributing mostly to the three peaks.

	Mass-to-charge (Da)	Net counts	Measured isotopic proportion (at. %)
<b>Precipitate sample 4</b>	12	7296 ± 90	76.1 ± 1
	12.5	1120 ± 35	11.6 ± 0.4
	13a	1170 ± 36	12.2 ± 0.4

**Table S3-4:** Measured isotopic proportions at 12, 12.5 and 13 in intergranular ACP

Magnesium-rich precipitate:

The precipitate from sample 4 (S6 and S2-d) does contain a large amount of Mg (presence of peaks at 12, 12.5 and 13). Carbon was only detected as  $CO^{2+}$ , and just above noise level. The following table shows the isotopic proportions for  $Mg^{2+}$  at 12, 12.5 and 13 Da. (table S3-3) These results again confirm the principal contribution from  $Mg^{2+}$  to the three peaks.

	Mass-to-charge (Da)	Net counts	Measured isotopic proportion (at. %)
<b>Precipitate sample 4</b>	12	10605 ± 100	77.9 ± 1
	12.5	1344 ± 45	9.9 ± 0.4
	13	1652 ± 50	12.1 ± 0.5

**Table S3-4:** Measured isotopic proportions at 12, 12.5 and 13 in Mg-rich precipitate of sample 4

Conclusions:

We were able to rule out the presence of  $C_2^{2+}$  in enamel mass spectrum. We also were able to demonstrate a good match between the theoretical and experimental isotopic proportions of  $Mg^{2+}$ . While we cannot rule out completely the contribution of any C to the Mg peaks, the evidence presented here leads us to conclude that it is minimal.

**S3. Discussion on differentiating Mg from C in the human tooth enamel mass spectra**

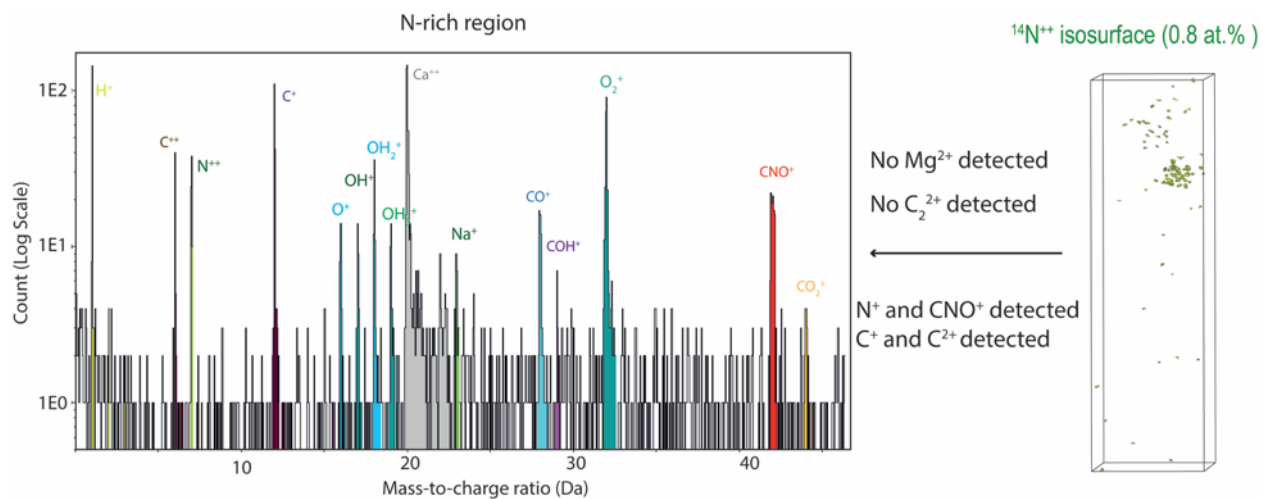


**Figure S4: Mass spectrum from N-rich region (organic)**

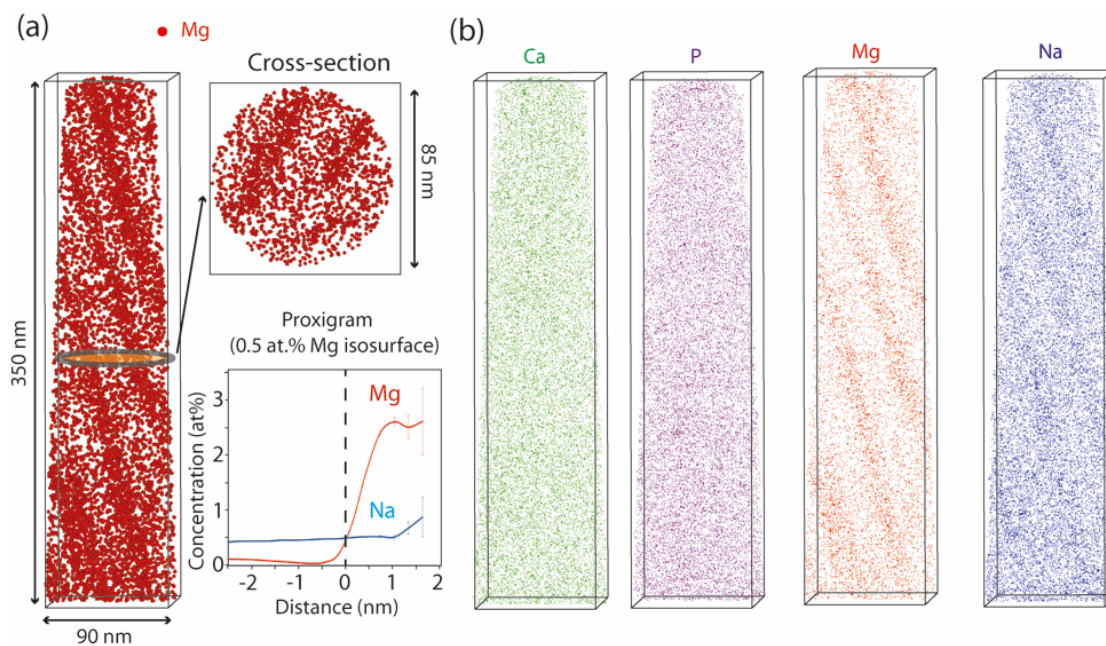


**Figure S5 APT 3d reconstructed volumes of sample 3.**

(a) Atom maps of Mg (8 nm slices) with two orientations (along the tip and cross-section). Proxigram analysis of Mg-ACP based on 0.5 at.% Mg isosurface. (b) atom maps of Ca, P, Mg and Na (8nm slices)

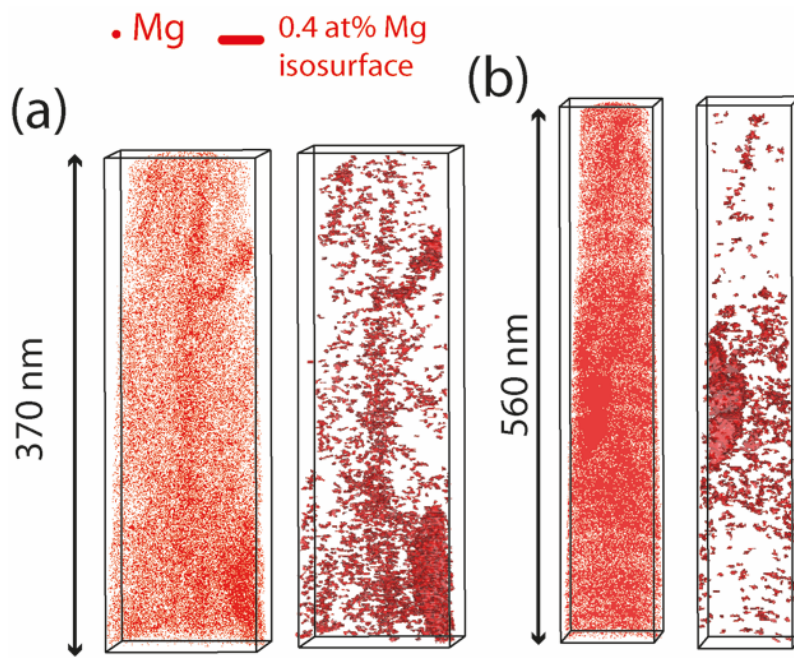


**Figure S6: APT 3d reconstructed volumes of sample 4 and 5.**

Atom maps of Mg and 0.4 at.% Mg isosurface of (a) sample 4 and (b) sample 5. Note the two elongated Mg-rich precipitates.

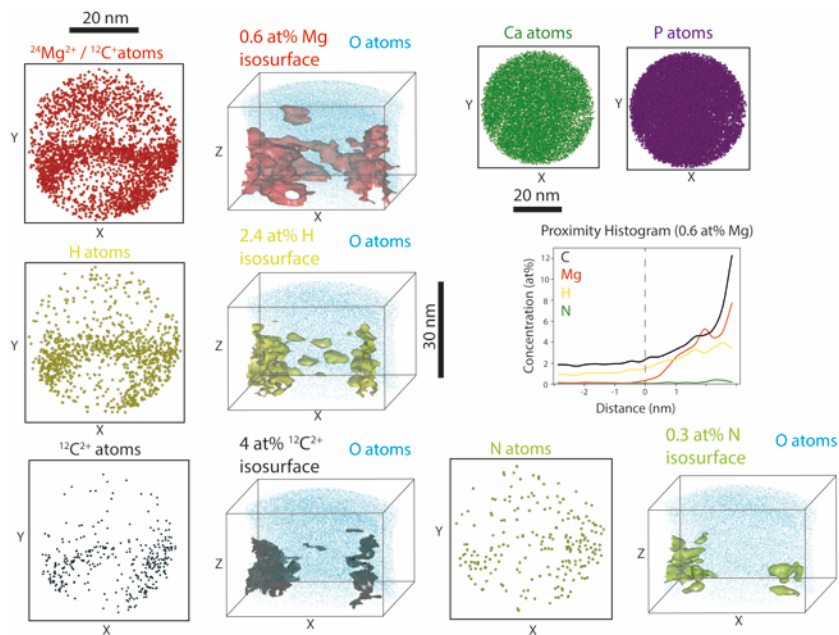


**Figure S7: APT 3d reconstructed volumes of sample 6.**

Atom maps of Mg, H, C and N. Volumes with isosurfaces of Mg (0.6 at%), H (2.4 at%), C (4 at%) and N (0.3 at%) and O atoms. Note the organic materials remnants (C, H, N). This APT data-set is limited in size due to the rapid fracture of the tip.



Sample 1 (fig.2)			Sample 2 (fig.3)			
Element (wt%)	Mg-rich ACP	HAP crystallites	Mg-rich ACP	HAP crystallites	Precipitate A	Precipitate B
Ca	38.5 ± 0.1	37.1 ± 0.02	37.1 ± 0.1	35.3 ± 0.02	18.9 ± 0.1	31.3 ± 0.1
P	21.8 ± 0.1	23.4 ± 0.02	21.7 ± 0.1	23.9 ± 0.02	16.4 ± 0.1	24.7 ± 0.1
O	37.0 ± 0.1	38.6 ± 0.02	37.3 ± 0.2	39.8 ± 0.04	46.1 ± 0.2	40.7 ± 0.2
Mg	1.55 ± 0.02	0.15 ± 0.002	2.66 ± 0.02	0.11 ± 0.002	0.10 ± 0.05	2.24 ± 0.02
Na	0.51 ± 0.02	0.26 ± 0.002	0.35 ± 0.02	0.24 ± 0.002	0.51 ± 0.02	0.33 ± 0.01
C	0.22 ± 0.02	0.14 ± 0.004	0.42 ± 0.005	0.23 ± 0.004	15.60 ± 0.02	0.39 ± 0.01
N	not detected	not detected	not detected	not detected	0.16 ± 0.02	not detected
H	0.13 ± 0.02	0.10 ± 0.01	0.14 ± 0.02	0.10 ± 0.02	1.00 ± 0.02	0.13 ± 0.01
Cl	0.25 ± 0.02	0.32 ± 0.002	0.29 ± 0.02	0.34 ± 0.002	1.31 ± 0.02	0.15 ± 0.02
Ca/P ratio	1.76	1.59	1.70	1.48	1.15	1.26

**Table S1.** Typical composition of ACP, HAP and Mg-rich precipitates in human dental enamel measured by APT.

**Movie S1.** Animation showing the 3D distribution of Mg and Na atoms in human dental enamel; APT sample 3.

---

## PART C Conclusions

---

## 14 Conclusions

In this thesis, existing advanced microscopy techniques were used and optimized to push the limits of the structural and chemical investigation in minerals at the sub-micron scale. The combined use of TEM, TKD and EBSD revealed a new oxidation-induced phase transformation in intergranular corrosion area of a stainless steel while the oxide minerals that formed around the grain boundaries were characterized by APT. The unrivaled spatial and chemical resolutions of APT coupled with TKD and EBSD allowed a new level of characterization in zircons. The atomic scale structure and chemistry of human dental enamel was investigated for the first time and revealed features that have major implications in our understanding of its incredible properties.

### 14.1 Advanced microscopy techniques applied to minerals

In the course of this thesis, methods were developed and optimised to overcome the numerous challenges in specimen preparation and data acquisition associated to the intrinsic properties of minerals.

#### 14.1.1 Specimen preparation for TKD and APT

Sample preparation procedures were adapted to the properties of each type of mineral (electrical and thermal conductivity, porosity...) and analysis constraints (density of features of interest for example). The common challenge in the sample preparation was limiting the charging effects and damages under the electron or ion beam in the FIB as a result of the non-conductive character of the minerals.

In chapter 8 the intergranular corrosion area containing the iron-chromium oxides and the steel was carefully thinned down to an electron transparent thin layer in order to carry out the TKD / TEM correlative analysis. The difference in milling rate between the steel and the oxides necessitated a careful adjustment of the ion milling parameters in order to obtain a high quality sample suitable for TKD and TEM. The samples used in this study were all prepared by Alexandre la Fontaine with the exception of one sample prepared by a co-author.

In chapters 11 and 12, the APT needle-shaped zircon samples were used for both TKD and APT. The site-specific constraints of the study (i.e. positioning dislocations within the APT tip) added a degree of complexity to the lift-out and milling procedures considering the difficult imaging of such small deformations in the FIB and image drift due to charging effect under the beam. The samples used in this study were all prepared by a co-author in collaboration with Alexandre La Fontaine.

---

The APT sample preparation for the tooth enamel was also a challenge with charging and sample damage occurring under the electron beam due to the presence of the organic materials embedded within in the HAP. As described in chapter 13, the samples were coated with a thin layer of gold several times during the preparation in the FIB. This allowed for minimal charging and also limited the damage to the sample until the last stage of annular milling. The micrometre-long HAP nanowires bundling together to form the enamel renders easy their positioning in an APT tip and as a result the wedge method could be used instead of lift-out. The samples used in this study were all prepared by Alexandre La Fontaine.

Over the course of this PhD, information was acquired about the specific APT preparation of the selected minerals required to achieve the best results in the APT. The geometry of the samples is thought to play an essential role in the success rate of the APT experiment. In particular, long, thin samples ( $\sim 60$  nm diameter,  $\sim 1\text{-}2$   $\mu\text{m}$  long) with a small shank angle, on a larger and bulkier base on top of the support grid was optimal. In the case of human dental enamel, the relatively thick gold coating applied on the whole sample (including the support grid) during the FIB preparation was found to greatly improve the thermal and electric conductivity of the tip.

#### 14.1.2 Data acquisition and analysis

The same difficulties encountered in mineral sample preparation apply to their investigation with electron microscopy as a result of poor electrical conductivity. Charging effects and electron beam damage limit the analysis parameters that can be used. This is particularly a problem with TKD, where the incident electron beam has to generate sufficient scattering without “burning” the sample. It can also be a problem for correlative microscopy, where the same area of a sample needs to be analysed by more than one technique, but remain undamaged. In chapter 8, the successful correlative TKD / TEM analysis of a chromium-rich oxide is demonstrated.

In this thesis, particular attention was paid to laser-assisted APT of minerals. Chapter 9 is dedicated to the understanding of the field evaporation of chromium oxides in laser-assisted APT. Specifically, this chapter assesses the degree of influence of analysis parameters on chromium oxide field evaporation. As a result, optimum analysis parameters for chromium oxides were determined. The identification of ions in the mass spectrum is also discussed and recognized as an essential part of high quality analysis.

---

In a similar fashion, chapter 11 addresses the influence of APT analysis parameters on the data quality of zircons. The optimum parameters were found to be very different compared to the chromium oxides, re-asserting the need for individual assessment for different minerals. The detection and quantification limits of the key trace elements, U and Pb, were assessed using 2 different zircons and as expected they were found to be a function of the size of the dataset, the initial U content, the age of the zircon as well as the potential clustering of U or Pb.

## **14.2 Analysis of selected minerals**

The skills and methods developed throughout this PhD in advanced microscopy techniques applied to minerals have allowed the successful investigation of important questions in engineering, geological and biological minerals.

### **14.2.1 Iron-chromium spinel oxides in intergranular corrosion area of austenitic stainless steel**

In chapter 8, a martensitic phase transformation is revealed within an intergranular corrosion area of a commercial austenitic stainless steel used in CSP technology. This displacive phase transformation is a result of oxidation-induced chromium depletion and high temperature thermal cycling. This new mechanism is thought to play an important role in the rate at which intergranular corrosion occurs in high temperature austenitic stainless steel when used under thermal cycling conditions. In addition to this phase transformation, the discontinuous character of the protective chromite spinel that formed around the grain boundaries is also thought to play a role in the intergranular corrosion. As described in chapter 10, this is due to the presence of non-protective iron-rich oxides and silicon-rich oxide particles within the chromite.

### **14.2.2 Trace elements diffusion in deformed zircons**

In chapter 12, the important question of whether or not trace elements diffuse non negligible distances through the zircon lattice is addressed. It was found that during plastic deformation key trace elements such as U, Pb or Al accumulate at the dislocations. When the dislocation arrays are connected to structural or chemical sinks (metamict areas for instance), Pb was found to be removed from the dislocations via pipe diffusion. However, in isolated dislocations (not connected) trace Pb remained locked. These findings have major implications in the field of geoscience, where zircon is used as a geochronometer.

---

### 14.2.3 Human dental enamel hydroxyapatite

In chapter 13, the atomic scale structure and composition of human dental enamel is revealed for the first time. Layers of Mg-rich amorphous calcium phosphate phase are found between the hydroxyapatite nanowires. Pockets of organic materials and Mg-rich precipitates are also present. The findings verify the mechanism by which enamel forms, specifically, the post-classical theory of amelogenesis. Understanding how enamel forms is essential for the development of methods to achieve remineralisation of carious enamel. There are also important implications for understanding how decay occurs. The Mg rich phase at the enamel boundaries is susceptible to dissolution in an acidic environment. The knowledge of the structure contributes to the understanding of the mechanical properties and models describing the mechanical behaviour can now incorporate the existence of this intergranular phase.

## 14.3 Future outlook

In this work, advanced microscopy techniques have been employed to understand critical atomic scale processes and mechanisms in a variety of minerals. These techniques are going to play an increasingly important role in materials engineering.

The work on the 253MA stainless steel will certainly lead to more oxidation studies in various conditions eventually leading to alloy design for better corrosion resistance. The diffusion study in deformed zircons can be extended to similar processes that happen in various geological minerals such as garnet or amphibolites. The first ever three dimensional atomic scale characterization of human tooth enamel revealed an intergranular amorphous phase thought to be responsible for tooth decay. This work will lead to atomic scale studies of caries formation or enamel re-mineralisation.

---

## 15 Bibliography

1. D. Arvizu, P. Balaya, L. Cabeza, T. Hollands, A. Jäger-Waldau, M. Kondo, C. Konseibo, V. Meleshko, W. Stein, Y. Tamaura, H. Xu, R. Zilles, 2011: Direct Solar Energy. In IPCC Special Report on Renewable Energy Sources and Climate Change Mitigation [O. Edenhofer, R. Pichs-Madruga, Y. Sokona, K. Seyboth, P. Matschoss, S. Kadner, T. Zwickel, P. Eickemeier, G. Hansen, S. Schlömer, C. von Stechow (eds), (2011).
2. D. J. Larson *et al.*, *Local Electrode Atom Probe Tomography: A User's Guide*. (Springer New York, 2013).
3. K. Babinsky *et al.*, Atom probe study of grain boundary segregation in technically pure molybdenum. *Materials Characterization* **87**, 95-103 (2014).
4. S. Piazzolo, H. Austrheim, M. Whitehouse, Brittle-ductile microfibrils in naturally deformed zircon: Deformation mechanisms and consequences for U-Pb dating. *American Mineralogist* **97**, 1544-1563 (2012).
5. S. M. Reddy, N. E. Timms, P. J. Hamilton, H. R. Smyth, Deformation-related microstructures in magmatic zircon and implications for diffusion. *Contributions to Mineralogy and Petrology* **157**, 231-244 (2009).
6. S. M. Reddy, N. E. Timms, W. Pantleon, P. Trimby, Quantitative characterization of plastic deformation of zircon and geological implications. *Contributions to Mineralogy and Petrology* **153**, 625-645 (2007).
7. S. M. Reddy *et al.*, Crystal-plastic deformation of zircon: A defect in the assumption of chemical robustness. *Geology* **34**, 257-260 (2006).
8. W. D. W. D. Nesse, *Introduction to mineralogy*. (2012).
9. W. G. Ernst, *Earth Materials*. (Prentice-Hall, 1969).
10. <http://www.csp-world.com/>. (2015).
11. C. Rossi, in *The Genius of Archimedes--23 Centuries of Influence on Mathematics, Science and Engineering*. (Springer, 2010), pp. 113-131.
12. <http://www.saint-gobain-solar-power.com/>. (2015)
13. J. A. Duffie, W. A. Beckman, *Solar engineering of thermal processes*. (John Wiley & Sons, 2013).
14. O. Behar, A. Khellaf, K. Mohammedi, A review of studies on central receiver solar thermal power plants. *Renewable and Sustainable Energy Reviews* **23**, 12-39 (2013).
15. <http://www.brightsourceenergy.com/>. (2014).
16. T. F. Kelly *et al.*, Laser pulsing of field evaporation in atom probe tomography. *Current Opinion in Solid State and Materials Science* **18**, 81-89 (2014).
17. <http://www.iresen.org/>. (2015)
18. J. A. Crook, L. A. Jones, P. M. Forster, R. Crook, Climate change impacts on future photovoltaic and concentrated solar power energy output. *Energy & Environmental Science* **4**, 3101-3109 (2011).
19. I. Power, "Realising the Potential of Concentrating Solar Power in Australia - Summary for Stakeholders. Australian Solar institute.," (2012).
20. B. C. Jim Hinkley, Jenny Hayward, Alex Wonhas (CSIRO), Rod Boyd, Charles Grima, Amir Tadros, Ross Hall, Kevin Naicker, Adeeb Mikhail (Aurecon Australia Pty Ltd), "Concentrating solar power drivers and opportunities for cost competitive electricity," (CSIRO, 2011).
21. A. H. P. Peter Heller (DLR), Philippe Malbranche (CEA-INES), Olivier Mal (AGC Solar), Luisa F. Cabeza (Universitat de Lleida) – JRC Coordination: N. Taylor, E. Tzimas, Strategic Energy

- 
- Technology Plan – Scientific Assessment in support of the material roadmap enabling low carbon technologies: Concentrated Solar Technology. (2011).
22. L. C. WEINER, Kinetics and mechanism of hydrogen attack of steel. *Corrosion* **17**, 137t-143t (1961).
  23. G. Y. Lai, *High-temperature corrosion and materials applications*. (ASM International, 2007).
  24. <http://www.worldstainless.org/>. (2012).
  25. P.-J. Cunat, "Alloying Elements in Stainless Steel and Other Chromium-Containing Alloys," (Euro Inox, 2004).
  26. <http://thomas-sourmail.net/stainless/index.html>. (2004).
  27. M. F. McGuire. (ASM International).
  28. D. B. Miracle *et al.*, *ASM handbook*. (ASM international Materials Park, OH, USA, 2001), vol. 21.
  29. P. Marshall, *Austenitic stainless steels: microstructure and mechanical properties*. (Springer, 1984).
  30. Sandvick. (2013).
  31. A. Australia, "Aurecon Australia report No.: MET 6858 revision 2," (2012).
  32. O. group. (Finland, 2012).
  33. K. Sieradzki, R. Newman, Stress-corrosion cracking. *Journal of physics and chemistry of solids* **48**, 1101-1113 (1987).
  34. J. R. Davis, *Heat-resistant materials*. (Asm International, 1997).
  35. E. Bain, R. Aborn, J. Rutherford, The nature and prevention of intergranular corrosion in austenitic stainless steels. *Transactions of American Society for Steel Treating* **21**, 481-509 (1933).
  36. C. H. Too, University of Cambridge, (2002).
  37. W. D. Callister, D. G. Rethwisch, *Materials science and engineering: an introduction*. (Wiley New York, 2007), vol. 7.
  38. T. Sourmail. (2001).
  39. E. P. Butler, M. G. Burke, Chromium depletion and martensite formation at grain boundaries in sensitised austenitic stainless steel. *Acta Metallurgica* **34**, 557-570 (1986).
  40. A. F. Padilha, P. R. Rios, Decomposition of austenite in austenitic stainless steels. *Isij International* **42**, 325-337 (2002).
  41. S. L. Harley, N. M. Kelly, Zircon tiny but timely. *Elements* **3**, 13-18 (2007).
  42. B. B. Boltwood, Ultimate disintegration products of the radioactive elements; Part II, Disintegration products of uranium. *American Journal of Science*, 78-88 (1907).
  43. D. W. Davis, T. E. Krogh, I. S. Williams, Historical development of zircon geochronology. *Reviews in mineralogy and geochemistry* **53**, 145-181 (2003).
  44. V. Cilek, *Earth System: History and Natural Variability-Volume I*. (Encyclopedia of Life Support Systems (EOLSS), 2009), vol. 1.
  45. A. Marfunin. (Springer-Verlag, Berlin-Heidelberg-New York, 1995).
  46. J. W. Valley *et al.*, Hadean age for a post-magma-ocean zircon confirmed by atom-probe tomography. *Nature Geosci* **7**, 219-223 (2014).
  47. J. M. Hanchar, P. W. Hoskin, *Reviews in Mineralogy and Geochemistry*. (Mineralogical Society of America, 2003), vol. 53.
  48. J. MacDonald, Zircon—Earth's timekeeper. *Geology Today* **29**, 113-117 (2013).
  49. A. Möller, P. O'brien, A. Kennedy, A. Kröner, Polyphase zircon in ultrahigh-temperature granulites (Rogaland, SW Norway): Constraints for Pb diffusion in zircon. *Journal of metamorphic Geology* **20**, 727-740 (2002).
  50. G. W. Wetherill, Discordant uranium-lead ages, I. *Eos, Transactions American Geophysical Union* **37**, 320-326 (1956).
-



- 
51. A. Radionova, I. Filippov, P. J. Derrick, In pursuit of resolution in time-of-flight mass spectrometry: A historical perspective. *Mass Spectrometry Reviews*, n/a-n/a (2015).
  52. D. J. Cherniak, E. B. Watson, Diffusion in zircon. *Reviews in mineralogy and geochemistry* **53**, 113-143 (2003).
  53. J. A. Woodhead, G. R. Rossman, L. T. Silver, The metamictization of zircon: radiation dose-dependent structural characteristics. *American Mineralogist;(United States)* **76**, (1991).
  54. D. Cherniak, E. Watson, T. Harrison, M. Grove, Pb diffusion in monazite: a progress report on a combined RBS/SIMS study. *Trans Am Geophys Union* **81**, S25 (2000).
  55. D. Gebauer, M. Grünenfelder, U-Pb zircon and Rb-Sr whole-rock dating of low-grade metasediments example: Montagne Noire (southern France). *Contributions to Mineralogy and Petrology* **59**, 13-32 (1976).
  56. T. Geisler, R. Pidgeon, W. Van Bronswijk, R. Kurtz, Transport of uranium, thorium, and lead in metamict zircon under low-temperature hydrothermal conditions. *Chemical Geology* **191**, 141-154 (2002).
  57. N. E. Timms, S. M. Reddy, J. D. F. Gerald, L. Green, J. R. Muhling, Inclusion-localised crystal-plasticity, dynamic porosity, and fast-diffusion pathway generation in zircon. *Journal of Structural Geology* **35**, 78-89 (2012).
  58. N. E. Timms *et al.*, Relationship among titanium, rare earth elements, U–Pb ages and deformation microstructures in zircon: Implications for Ti-in-zircon thermometry. *Chemical Geology* **280**, 33-46 (2011).
  59. J. Arends, J. M. Ten Cate, Tooth enamel remineralization. *Journal of Crystal Growth* **53**, 135-147 (1981).
  60. A. Meckel, W. Griebstein, R. Neal, Structure of mature human dental enamel as observed by electron microscopy. *Archives of oral biology* **10**, 775-783 (1965).
  61. L. H. He, M. V. Swain, Understanding the mechanical behaviour of human enamel from its structural and compositional characteristics. *Journal of the Mechanical Behavior of Biomedical Materials* **1**, 18-29 (2008).
  62. E. DR. (1998), pp. pp 218–235.
  63. J. E. Eastoe, Organic Matrix of Tooth Enamel. *Nature* **187**, 411-412 (1960).
  64. B. Kerebel, G. Daculsi, L. Kerebel, Ultrastructural studies of enamel crystallites. *Journal of dental research* **58**, 844-851 (1979).
  65. G. Daculsi, J. Menanteau, L. Kerebel, D. Mitre, Length and shape of enamel crystals. *Calcified tissue international* **36**, 550-555 (1984).
  66. E. D. Yilmaz, S. Bechtle, H. Özcoban, A. Schreyer, G. A. Schneider, Fracture behavior of hydroxyapatite nanofibers in dental enamel under micropillar compression. *Scripta Materialia* **68**, 404-407 (2013).
  67. I. Scheider *et al.*, Damage modeling of small-scale experiments on dental enamel with hierarchical microstructure. *Acta biomaterialia* **15**, 244-253 (2015).
  68. J. Zhang, C. Wang, F. Yang, C. Du, Nanoindentation creep behavior of enamel biological nanocomposites. *RSC Advances* **4**, 41003-41009 (2014).
  69. O. Borrero-Lopez, A. Pajares, P. J. Constantino, B. R. Lawn, Mechanics of microwear traces in tooth enamel. *Acta biomaterialia* **14**, 146-153 (2015).
  70. T. Baumann, T. Carvalho, A. Lussi, The effect of enamel proteins on erosion. *Scientific reports* **5**, (2015).
  71. G. V. Lubarsky *et al.*, Enamel proteins mitigate mechanical and structural degradations in mature human enamel during acid attack. *Materials Research Express* **1**, 025404 (2014).
  72. C. Robinson, S. J. Brookes, R. C. Shore, J. Kirkham, The developing enamel matrix: nature and function. *European journal of oral sciences* **106**, 282-291 (1998).
  73. G. A. Castiblanco *et al.*, Identification of proteins from human permanent erupted enamel. *European journal of oral sciences*, (2015).
-

- 
74. C. Robinson, H. Briggs, P. Atkinson, J. Weatherell, Matrix and mineral changes in developing enamel. *Journal of dental research* **58**, 871-882 (1979).
  75. E. Beniash, R. A. Metzler, R. S. Lam, P. Gilbert, Transient amorphous calcium phosphate in forming enamel. *Journal of structural biology* **166**, 133-143 (2009).
  76. H. Ding, H. Pan, X. Xu, R. Tang, Toward a detailed understanding of magnesium ions on hydroxyapatite crystallization inhibition. *Crystal Growth & Design* **14**, 763-769 (2014).
  77. L. M. Gordon *et al.*, Amorphous intergranular phases control the properties of rodent tooth enamel. *Science* **347**, 746-750 (2015).
  78. B. Gault, M. P. Moody, J. M. Cairney, S. P. Ringer, *Atom probe microscopy*. (Springer, 2012), vol. 160.
  79. O. L. Krivanek, N. Dellby, R. J. Keyse, M. F. Murfitt, Z. S. Szilagy, Advances in aberration-corrected scanning transmission electron microscopy and electron energy-loss spectroscopy. *Advances in Imaging and Electron Physics: Aberration-corrected microscopy* **153**, 121 (2009).
  80. M. Weyland, P. A. Midgley, Electron tomography. *Materials Today* **7**, 32-40 (2004).
  81. M. Miller, Analysis at the atomic level: The atom probe field-ion microscope. *Journal of Research of the National Bureau of Standards* **93**, 374-376 (1988).
  82. G. Kellogg, T. Tsong, Pulsed-laser atom-probe field-ion microscopy. *Journal of Applied Physics* **51**, 1184-1193 (1980).
  83. B. Gault *et al.*, Design of a femtosecond laser assisted tomographic atom probe. *Review of Scientific Instruments* **77**, 043705 (2006).
  84. J. H. Bunton, J. D. Olson, D. R. Lenz, T. F. Kelly, Advances in pulsed-laser atom probe: Instrument and specimen design for optimum performance. *Microscopy and Microanalysis* **13**, 418-427 (2007).
  85. T. F. Kelly *et al.*, Atom probe tomography of electronic materials. *Annu. Rev. Mater. Res.* **37**, 681-727 (2007).
  86. E. W. Müller, Field desorption. *Physical Review* **102**, 618 (1956).
  87. E. W. Müller, J. A. Panitz, S. B. McLane, The atom-probe field ion microscope. *Review of Scientific Instruments* **39**, 83-86 (1968).
  88. D. J. Larson, T. J. Prosa, R. M. Ulfing, B. P. Geiser, T. F. Kelly, Local electrode atom probe tomography. *New York, US: Springer Science*, (2013).
  89. B. Geiser *et al.*, Wide-field-of-view atom probe reconstruction. *Microscopy and Microanalysis* **15**, 292-293 (2009).
  90. P. Bas, A. Bostel, B. Deconihout, D. Blavette, A general protocol for the reconstruction of 3D atom probe data. *Applied Surface Science* **87**, 298-304 (1995).
  91. B. Gault *et al.*, Advances in the reconstruction of atom probe tomography data. *Ultramicroscopy* **111**, 448-457 (2011).
  92. T. Kunicki *et al.*, in *Vacuum Nanoelectronics Conference, 2006 and the 2006 50th International Field Emission Symposium., IVNC/IFES 2006. Technical Digest. 19th International.* (IEEE, 2006).
  93. O. C. Hellman, J. A. Vandenbroucke, J. Rüsing, D. Isheim, D. N. Seidman, Analysis of three-dimensional atom-probe data by the proximity histogram. *Microscopy and Microanalysis* **6**, 437-444 (2000).
  94. O. C. Hellman, J. B. du Rivage, D. N. Seidman, Efficient sampling for three-dimensional atom probe microscopy data. *Ultramicroscopy* **95**, 199-205 (2003).
  95. T. F. Kelly, B. P. Geiser, D. J. Larson, Definition of spatial resolution in atom probe tomography. *Microscopy and Microanalysis* **13**, 1604-1605 (2007).
  96. E. Cadel, F. Vurpillot, R. Lardé, S. Duguay, B. Deconihout, Depth resolution function of the laser assisted tomographic atom probe in the investigation of semiconductors. *Journal of Applied Physics* **106**, 044908 (2009).
-

- 
97. B. Gault *et al.*, Spatial resolution in atom probe tomography. *Microscopy and Microanalysis* **16**, 99-110 (2010).
  98. W. Lefebvre *et al.*, 3DAP measurements of Al content in different types of precipitates in aluminium alloys. *Surface and interface analysis* **39**, 206-212 (2007).
  99. T. T. Tsong, Atom-probe field ion microscopy. *Physics Today* **46**, 24-24 (1993).
  100. E. A. Marquis, J. M. Hyde, Applications of atom-probe tomography to the characterisation of solute behaviours. *Materials Science and Engineering: R: Reports* **69**, 37-62 (2010).
  101. B. Gault *et al.*, Estimation of the reconstruction parameters for atom probe tomography. *Microscopy and Microanalysis* **14**, 296-305 (2008).
  102. B. Gault *et al.*, Advances in the calibration of atom probe tomographic reconstruction. *Journal of Applied Physics* **105**, 034913 (2009).
  103. M. K. Miller, *Atom probe tomography: analysis at the atomic level*. (Springer Science & Business Media, 2012).
  104. A. J. Melmed, The art and science and other aspects of making sharp tips. *Journal of Vacuum Science & Technology B* **9**, 601-608 (1991).
  105. K. Thompson-Russell, J. W. Edington, *Electron microscope specimen preparation techniques in materials science*. (Springer, 1977).
  106. D. Larson *et al.*, Focused ion-beam milling for field-ion specimen preparation:: preliminary investigations. *Ultramicroscopy* **75**, 147-159 (1998).
  107. D. Larson *et al.*, Advances in atom probe specimen fabrication from planar multilayer thin film structures. *Microscopy and Microanalysis* **7**, 24-31 (2001).
  108. M. K. Miller, K. F. Russell, K. Thompson, R. Alvis, D. J. Larson, Review of atom probe FIB-based specimen preparation methods. *Microscopy and Microanalysis* **13**, 428-436 (2007).
  109. D. Saxey, J. Cairney, D. McGrouther, T. Honma, S. Ringer, Atom probe specimen fabrication methods using a dual FIB/SEM. *Ultramicroscopy* **107**, 756-760 (2007).
  110. H. O. Colijn, T. F. Kelly, R. Ulfig, R. G. Buchheit, Site-specific FIB preparation of atom probe samples. *Microscopy and Microanalysis* **10**, 1150-1151 (2004).
  111. M. Overwijk, F. Van den Heuvel, C. Bulle-Lieuwma, Novel scheme for the preparation of transmission electron microscopy specimens with a focused ion beam. *Journal of Vacuum Science & Technology B* **11**, 2021-2024 (1993).
  112. M. Miller, K. Russell, G. Thompson, Strategies for fabricating atom probe specimens with a dual beam FIB. *Ultramicroscopy* **102**, 287-298 (2005).
  113. K. Thompson *et al.*, In situ site-specific specimen preparation for atom probe tomography. *Ultramicroscopy* **107**, 131-139 (2007).
  114. P. J. Felfer, T. Alam, S. P. Ringer, J. M. Cairney, A reproducible method for damage-free site-specific preparation of atom probe tips from interfaces. *Microscopy research and technique* **75**, 484-491 (2012).
  115. R. Keller, R. Geiss, Transmission EBSD from 10 nm domains in a scanning electron microscope. *Journal of Microscopy* **245**, 245-251 (2012).
  116. S. Nishikawa, S. Kikuchi, The diffraction of cathode rays by calcite. *Proceedings of the Imperial Academy* **4**, 475-477 (1928).
  117. J. Venables, C. Harland, Electron back-scattering patterns—a new technique for obtaining crystallographic information in the scanning electron microscope. *Philosophical Magazine* **27**, 1193-1200 (1973).
  118. T. Maitland, S. Sitzman, *Electron backscatter diffraction (EBSD) technique and materials characterization examples*. (Springer Berlin, 2007), vol. 14.
  119. F. Humphreys, Y. Huang, I. Brough, C. Harris, Electron backscatter diffraction of grain and subgrain structures—resolution considerations. *Journal of Microscopy* **195**, 212-216 (1999).
  120. D. Chen, J.-C. Kuo, W.-T. Wu, Effect of microscopic parameters on EBSD spatial resolution. *Ultramicroscopy* **111**, 1488-1494 (2011).
-

- 
121. P. W. Trimby *et al.*, Characterizing deformed ultrafine-grained and nanocrystalline materials using transmission Kikuchi diffraction in a scanning electron microscope. *Acta Materialia* **62**, 69-80 (2014).
122. P. W. Trimby, Orientation mapping of nanostructured materials using transmission Kikuchi diffraction in the scanning electron microscope. *Ultramicroscopy* **120**, 16-24 (2012).
123. I. Hilger *et al.*, Fabrication and characterization of oxide dispersion strengthened (ODS) 14Cr steels consolidated by means of hot isostatic pressing, hot extrusion and spark plasma sintering. *Journal of Nuclear Materials*, (2015).
124. P. W. Trimby, J. M. Cairney, Transmission Kikuchi diffraction in the scanning electron microscope: Orientation mapping on the nanoscale. *ADVANCED MATERIALS & PROCESSES* **172**, 13-15 (2014).
125. K. P. Rice, R. R. Keller, M. P. Stoykovich, Beam Broadening in Transmission EBSD. *Microscopy Today* **23**, 32-37 (2015).
126. K. Rice, R. Keller, M. Stoykovich, Specimen-thickness effects on transmission Kikuchi patterns in the scanning electron microscope. *Journal of microscopy* **254**, 129-136 (2014).
127. J. D. DAVID, Orientation contrast imaging of microstructures in rocks using foreshatter detectors in the scanning electron microscope. *Mineralogical Magazine* **60**, 859-869 (1996).
128. K. Babinsky, R. De Kloe, H. Clemens, S. Primig, A novel approach for site-specific atom probe specimen preparation by focused ion beam and transmission electron backscatter diffraction. *Ultramicroscopy* **144**, 9-18 (2014).
129. K. Babinsky *et al.*, Grain boundary study of technically pure molybdenum by combining APT and TKD. *Ultramicroscopy* **159**, 445-451 (2015).
130. T. Klein *et al.*, Carbon distribution in multi-phase  $\gamma$ -TiAl based alloys and its influence on mechanical properties and phase formation. *Acta Materialia* **94**, 205-213 (2015).
131. K. Babinsky *et al.*, Grain boundary study of technically pure molybdenum by combining APT and TKD. *Ultramicroscopy* **159**, Part 2, 445-451 (2015).
132. A. Vella, On the interaction of an ultra-fast laser with a nanometric tip by laser assisted atom probe tomography: A review. *Ultramicroscopy* **132**, 5-18 (2013).
133. A. Vella, B. Mazumder, G. Da Costa, B. Deconihout, Field evaporation mechanism of bulk oxides under ultra fast laser illumination. *Journal of Applied Physics* **110**, 044321 (2011).
134. B. Gault, A. Menand, F. De Geuser, B. Deconihout, R. Danoix, Investigation of an oxide layer by femtosecond-laser-assisted atom probe tomography. *Applied Physics Letters* **88**, 114101 (2006).
135. F. Vurpillot, J. Houard, A. Vella, B. Deconihout, Thermal response of a field emitter subjected to ultra-fast laser illumination. *Journal of Physics D: Applied Physics* **42**, 125502 (2009).
136. R. Kirchhofer *et al.*, Quantifying Compositional Homogeneity in Pb(Zr,Ti)O<sub>3</sub> Using Atom Probe Tomography. *Journal of the American Ceramic Society* **97**, 2677-2697 (2014).
137. J. Bunton, J. Olson, D. Lenz, D. Larson, T. Kelly, Optimized Laser Thermal Pulsing of Atom Probe Tomography: LEAP 4000X™. *Microscopy and Microanalysis* **16**, 10-11 (2010).
138. G. Sha, A. Cerezo, G. Smith, Field evaporation behavior during irradiation with picosecond laser pulses. *Applied Physics Letters* **92**, 043503 (2008).
139. N. W. Ashcroft, N. D. Mermin, Solid state phys. *Saunders, Philadelphia* **293**, (1976).
140. C. Glassbrenner, G. A. Slack, Thermal conductivity of silicon and germanium from 3 K to the melting point. *Physical Review* **134**, A1058 (1964).
141. R. Kirchhofer, M. C. Teague, B. P. Gorman, Thermal effects on mass and spatial resolution during laser pulse atom probe tomography of cerium oxide. *Journal of Nuclear Materials* **436**, 23-28 (2013).
142. M. Bachhav *et al.*, Investigation of wüstite (Fe<sub>1-x</sub>O) by femtosecond laser assisted atom probe tomography. *Ultramicroscopy* **111**, 584-588 (2011).
143. K. Kruska *et al.*, Nanoscale characterisation of grain boundary oxidation in cold-worked stainless steels. *Corrosion Science* **63**, 225-233 (2012).
-

- 
144. M. Tsukada *et al.*, Mechanism of laser assisted field evaporation from insulating oxides. *Ultramicroscopy* **111**, 567-570 (2011).
  145. M. Bachhav, F. Danoix, B. Hannoyer, J. M. Bassat, R. Danoix, Investigation of O-18 enriched hematite ( $\alpha$ -Fe<sub>2</sub>O<sub>3</sub>) by laser assisted atom probe tomography. *International Journal of Mass Spectrometry* **335**, 57-60 (2013).
  146. A. Devaraj *et al.*, Visualizing nanoscale 3D compositional fluctuation of lithium in advanced lithium-ion battery cathodes. *Nature communications* **6**, (2015).
  147. G. L. Kellogg, Field ion microscopy and pulsed laser atom-probe mass spectroscopy of insulating glasses. *Journal of Applied Physics* **53**, 6383-6386 (1982).
  148. M. Kuduz, G. Schmitz, R. Kirchheim, Investigation of oxide tunnel barriers by atom probe tomography (TAP). *Ultramicroscopy* **101**, 197-205 (2004).
  149. D. Blavette *et al.*, Laser-assisted atom probe tomography and nanosciences. *International Journal of Materials Research* **99**, 454-460 (2008).
  150. T. E. Kelly *et al.*, in *Annual Review of Materials Research*. (2007), vol. 37, pp. 681-727.
  151. B. Gault, A. Menand, F. d. Geuser, B. Deconihout, R. Danoix, Investigation of an oxide layer by femtosecond-laser-assisted atom probe tomography. *Applied Physics Letters* **88**, 114101 (2006).
  152. Y. Chen, T. Ohkubo, M. Kodzuka, K. Morita, K. Hono, Laser-assisted atom probe analysis of zirconia/spinel nanocomposite ceramics. *Scripta Materialia* **61**, 693-696 (2009).
  153. E. A. Marquis, N. A. Yahya, D. J. Larson, M. K. Miller, R. I. Todd, Probing the improbable: imaging C atoms in alumina. *Materials Today* **13**, 34-36 (2010).
  154. F. Li, T. Ohkubo, Y. Chen, M. Kodzuka, K. Hono, Quantitative atom probe analyses of rare-earth-doped ceria by femtosecond pulsed laser. *Ultramicroscopy* **111**, 589-594 (2011).
  155. Y. Dong, A. T. Motta, E. A. Marquis, Atom probe tomography study of alloying element distributions in Zr alloys and their oxides. *Journal of Nuclear Materials* **442**, 270-281 (2013).
  156. N. Dawahre *et al.*, Atom probe tomography of zinc oxide nanowires. *Journal of electronic materials* **41**, 801-808 (2012).
  157. S. Lozano-Perez, A guide on FIB preparation of samples containing stress corrosion crack tips for TEM and atom-probe analysis. *Micron* **39**, 320-328 (2008).
  158. P. Felfer, S. Ringer, J. Cairney, Shaping the lens of the atom probe: Fabrication of site specific, oriented specimens and application to grain boundary analysis. *Ultramicroscopy* **111**, 435-439 (2011).
  159. P. Felfer, I. McCarroll, C. Macauley, J. M. Cairney, A simple approach to atom probe sample preparation by using shadow masks. *Ultramicroscopy* **160**, 163-167 (2016).
  160. D. K. Schreiber *et al.*, Examinations of oxidation and sulfidation of grain boundaries in alloy 600 exposed to simulated pressurized water reactor primary water. *Microscopy and Microanalysis* **19**, 676-687 (2013).
  161. M. J. Olszta, D. K. Schreiber, L. E. Thomas, S. M. Bruemmer, in *15th International Conference on Environmental Degradation of Materials in Nuclear Power Systems-Water Reactors*. (Wiley Online Library, 2011), pp. 331-342.
  162. S.-I. Baik, M. Olszta, S. Bruemmer, D. N. Seidman, Grain-boundary structure and segregation behavior in a nickel-base stainless alloy. *Scripta Materialia* **66**, 809-812 (2012).
  163. L. Viskari, M. Hörnqvist, K. Moore, Y. Cao, K. Stiller, Intergranular crack tip oxidation in a Ni-base superalloy. *Acta Materialia* **61**, 3630-3639 (2013).
  164. J. K. Kim, B.-J. Lee, B. H. Lee, Y. H. Kim, K. Y. Kim, Intergranular segregation of Cr in Ti-stabilized low-Cr ferritic stainless steel. *Scripta Materialia* **61**, 1133-1136 (2009).
  165. S. Lozano-Perez, D. W. Saxey, T. Yamada, T. Terachi, Atom-probe tomography characterization of the oxidation of stainless steel. *Scripta Materialia* **62**, 855-858 (2010).
  166. K. Kruska *et al.*, Nanoscale characterisation of grain boundary oxidation in cold-worked stainless steels. *Corrosion Science* **63**, 225-233 (2012).
-

- 
167. K. Kruska *et al.*, in *15th International Conference on Environmental Degradation of Materials in Nuclear Power Systems-Water Reactors*. (Wiley Online Library, 2011), pp. 939-946.
  168. M. Meisnar, M. Moody, S. Lozano-Perez, Atom probe tomography of stress corrosion crack tips in SUS316 stainless steels. *Corrosion Science* **98**, 661-671 (2015).
  169. S. Lozano-Perez *et al.*, Multi-scale characterization of stress corrosion cracking of cold-worked stainless steels and the influence of Cr content. *Acta Materialia* **57**, 5361-5381 (2009).
  170. D. J. Young, T. D. Nguyen, P. Felfer, J. Zhang, J. M. Cairney, Penetration of protective chromia scales by carbon. *Scripta Materialia* **77**, 29-32 (2014).
  171. F. Liu, K. Stiller, Atom probe tomography of thermally grown oxide scale on FeCrAl. *Ultramicroscopy* **132**, 279-284 (2013).
  172. J. W. Valley *et al.*, Presidential Address. Nano-and micro-geochronology in Hadean and Archean zircons by atom-probe tomography and SIMS: New tools for old minerals. *American Mineralogist* **100**, 1355-1377 (2015).
  173. L. M. Gordon, D. Joester, Nanoscale chemical tomography of buried organic-inorganic interfaces in the chiton tooth. *Nature* **469**, 194-197 (2011).
  174. L. M. Gordon, L. Tran, D. Joester, Atom probe tomography of apatites and bone-type mineralized tissues. *ACS nano* **6**, 10667-10675 (2012).
  175. J. Karlsson, G. Sundell, M. Thuvander, M. Andersson, Atomically Resolved Tissue Integration. *Nano Letters* **14**, 4220-4223 (2014).
  176. L. M. Gordon, D. Joester, Mapping residual organics and carbonate at grain boundaries and the amorphous interphase in mouse incisor enamel. *Frontiers in physiology* **6**, (2015).